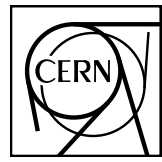


# EUROPEAN ORGANIZATION FOR NUCLEAR RESEARCH



ALICE-ANA-2018-xxx  
February 20, 2019

## **$\Lambda K$ and $\Xi^- K^\pm$ Femtoscopy in Pb-Pb Collisions at $\sqrt{s_{NN}} = 2.76$ TeV from the LHC ALICE Experiment**

Jesse T. Buxton<sup>1</sup>

1. Department of Physics, The Ohio State University, Columbus, Ohio, USA

Email: jesse.thomas.buxton@cern.ch

### **Abstract**

I present the first femtoscopic analysis of  $\Lambda K$  correlations in Pb-Pb collisions at  $\sqrt{s_{NN}} = 2.76$  TeV measured by the ALICE experiment at the Large Hadron Collider (LHC). All pair combinations of  $\Lambda$  and  $\bar{\Lambda}$  with  $K^+$ ,  $K^-$  and  $K_S^0$  are analyzed. The femtoscopic correlations result from strong final-state interactions, and are fit with a parametrization allowing us to both characterize the emission source and measure the scattering parameters for the particle pairs. We observe a large difference in the  $\Lambda K^+$  and  $\Lambda K^-$  correlations in pairs with low relative momenta ( $k^* \lesssim 100$  MeV/c). This might suggest an effect arising from different quark-antiquark interactions within the pairs ( $s\bar{s}$  in  $\Lambda K^+$  and  $u\bar{u}$  in  $\Lambda K^-$ ), or from different net strangeness for each system. To gain further insight into this hypothesis, we are currently conducting a  $\Xi^- K^\pm$  femtoscopic analysis, for which I present preliminary results.



## Contents

<b>1</b>	<b>Introduction</b>	<b>7</b>
<b>2</b>	<b>Data Sample and Software</b>	<b>7</b>
2.1	Data Sample . . . . .	7
2.2	Software . . . . .	7
<b>3</b>	<b>Data Selection</b>	<b>7</b>
3.1	Event Selection and Mixing . . . . .	7
3.2	$K^\pm$ Track Selection . . . . .	8
3.3	V0 Selection . . . . .	8
3.3.1	$\Lambda$ Reconstruction . . . . .	10
3.3.2	$K_S^0$ Reconstruction . . . . .	12
3.3.3	V0 Purity Background Estimation . . . . .	14
3.4	$\Xi$ Reconstruction . . . . .	15
3.5	Pair Selection . . . . .	16
<b>4</b>	<b>Correlation Functions</b>	<b>21</b>
4.1	Typical Correlation Function Construction . . . . .	21
4.2	Stavinskiy Correlation Function Construction . . . . .	23
<b>5</b>	<b>Fitting</b>	<b>26</b>
5.1	Model: $\Lambda K_S^0$ , $\Lambda K^\pm$ , $\Xi^- K_S^0$ . . . . .	26
5.2	Model: $\Xi^- K^\pm$ . . . . .	26
5.3	Momentum Resolution Corrections . . . . .	27
5.4	Residual Correlations . . . . .	32
5.5	Non-Flat Background . . . . .	40
5.6	LednickyFitter . . . . .	43
5.7	Coulomb Fitter . . . . .	46
<b>6</b>	<b>Systematic Errors</b>	<b>47</b>
6.1	Systematic Errors: $\Lambda K_S^0$ . . . . .	47
6.1.1	Particle and Pair Cuts . . . . .	47
6.1.2	Non-Flat Background . . . . .	47
6.1.3	Fit Range . . . . .	47

6.2	Systematic Errors: $\Lambda K^\pm$	48
6.2.1	Particle and Pair Cuts	48
6.2.2	Non-Flat Background	48
6.2.3	Fit Range	48
6.3	Systematic Errors: $\Xi K^\pm$	48
6.3.1	Particle and Pair Cuts	48
<b>7</b>	<b>Results and Discussion</b>	<b>50</b>
7.1	Results: $\Lambda K_S^0$ and $\Lambda K^\pm$	50
7.1.1	3 Residual Correlations Included in Fit	51
7.1.2	10 Residual Correlations Included in Fit	58
7.1.3	No Residual Correlations Included in Fit	65
7.1.4	Fit Method Comparisons	71
7.1.5	Discussion of $m_T$ -Scaling	76
7.2	Results: $\Xi K^\pm$	81
<b>8</b>	<b>To Do</b>	<b>82</b>
<b>9</b>	<b>Additional Figures</b>	<b>87</b>
9.1	Residuals	87
9.1.1	$\Lambda K^+$ Residuals	87
9.1.2	$\Lambda K^-$ Residuals	93
9.1.3	$\Lambda K_S^0$ Residuals	99
9.2	Spherical Harmonics	105

## List of Figures

1	V0 Reconstruction	10
2	$K_S^0$ contamination in $\Lambda(\bar{\Lambda})$ collection	12
3	$\Lambda$ and $\bar{\Lambda}$ Purity	12
4	$\Lambda(\bar{\Lambda})$ contamination in $K_S^0$ collection	14
5	$K_S^0$ Purity	14
6	V0 Purity Background Estimation	15
7	$\Xi$ Reconstruction	17
8	$\Xi^-(\bar{\Xi}^+)$ Purity	17
9	Average Separation of $\Lambda(\bar{\Lambda})$ and $K_S^0$ Daughters	19
10	Average Separation of $\Lambda(\bar{\Lambda})$ Daughter and $K^\pm$	19
11	Average Separation of $\Xi$ Daughters and $K^\pm$	20
12	$\Lambda K$ Correlation Functions	22
13	Correlation Functions: $\Lambda K^+$ vs $\Lambda K^-$ for 0-10% Centrality	22
14	$\Lambda K$ Stavinskiy Correlation Functions (Correct)	24
15	$\Lambda K$ Stavinskiy Correlation Functions (Correct and Incorrect)	25
16	Momentum Resolution: Sample $k_{\text{True}}^*$ vs. $k_{\text{Rec}}^*$	28
17	Particle Contaminations Visible in $k_{\text{True}}^*$ vs. $k_{\text{Rec}}^*$	29
18	Momentum Resolution Corrections: Methods Comparison	31
19	Residual Contributions Cartoon	32
20	Sample Transform Matrices for $\Lambda K^+$ Analysis	33
21	Sample Transform Matrices for $\bar{\Lambda} K^+$ Analysis	34
22	Reconstruction Efficiencies	35
23	$\Sigma^0 K^+$ Transform	38
24	$\Lambda K^{*0}$ Transform	39
25	Compare Non-Femtoscopic Backgrounds	40
26	Backgrounds with THERMINATOR, $K_S^0$ Tweak	41
27	Backgrounds with THERMINATOR	42
28	Correlation with background decomposition (THERM)	43
29	Background reduction methods with THERMINATOR	44
30	Extracted Scattering Parameters: 3 Residuals in Fit	51
31	$m_T$ Scaling of Radii: 3 Residuals in Fit	51
32	$\Lambda(\bar{\Lambda})K_S^0$ Fits with 3 Residuals	52

33	$\Lambda K^+(\bar{\Lambda}K^-)$ Fits with 3 Residuals . . . . .	53
34	$\Lambda K^-(\bar{\Lambda}K^+)$ Fits with 3 Residuals . . . . .	54
35	$\Lambda(\bar{\Lambda})K_S^0$ Fits showing 3 Residuals . . . . .	55
36	$\Lambda K^+(\bar{\Lambda}K^-)$ and $\Lambda K^-(\bar{\Lambda}K^+)$ Fits with 3 Residuals . . . . .	56
37	Extracted Scattering Parameters: 3 Residuals in Fit . . . . .	58
38	$m_T$ Scaling of Radii: 10 Residuals in Fit . . . . .	58
39	$\Lambda K_S^0(\bar{\Lambda}K_S^0)$ Fits with 10 Residuals . . . . .	59
40	$\Lambda K^+(\bar{\Lambda}K^-)$ Fits with 10 Residuals . . . . .	60
41	$\Lambda K^-(\bar{\Lambda}K^+)$ Fits with 10 Residuals . . . . .	61
42	$\Lambda(\bar{\Lambda})K_S^0$ Fits showing 10 Residuals . . . . .	62
43	$\Lambda K^+(\bar{\Lambda}K^-)$ and $\Lambda K^-(\bar{\Lambda}K^+)$ Fits with 10 Residuals . . . . .	63
44	Extracted Scattering Parameters: No Residuals in Fit . . . . .	65
45	$m_T$ Scaling of Radii: No Residuals in Fit . . . . .	66
46	$\Lambda K_S^0(\bar{\Lambda}K_S^0)$ Fits with No Residuals . . . . .	67
47	$\Lambda K^+(\bar{\Lambda}K^-)$ Fits, with NO residual correlations included, with No Residuals . . . . .	68
48	$\Lambda K^-(\bar{\Lambda}K^+)$ Fits with No Residuals . . . . .	69
49	Compare Fit Parameters: Background treatment . . . . .	71
50	Compare Fit Parameters: Number of residuals . . . . .	72
51	Compare Fit Parameters: Free vs fixed $\lambda$ . . . . .	73
52	Compare Fit Parameters: Shared vs unique $\lambda$ . . . . .	74
53	Compare Fit Parameters: Shared vs. Separate Radii . . . . .	75
54	$m_T$ Scaling of Radii: 3 Residuals in Fit (with individual $m_T$ highlighted) . . . . .	76
55	$\Lambda K^+$ $C_{00}$ and $\Im C_{11}$ Spherical Harmonic Components (0-10%) . . . . .	78
56	Short Overall . . . . .	79
57	Short Caption . . . . .	80
58	Short Caption . . . . .	80
59	$\Xi K^\pm$ Results . . . . .	81
60	$\Xi K^\pm$ Data with Coulomb-Only Bands, 0-10% Centrality . . . . .	82
61	Effect of Strong Force Inclusion on Coulomb-Only Curve for $\Xi K^\pm$ systems . . . . .	83
62	$\Xi K^\pm$ Global Coulomb-Only Fit (Set 1) . . . . .	84
63	$\Xi K^\pm$ Global Coulomb-Only Fit (Set 2) . . . . .	85
64	$\Xi^- K^+$ Coulomb-Only Fit . . . . .	85
65	$\Xi^- K^-$ Coulomb-Only Fit . . . . .	86

66	Residuals: $\Sigma^0 K^+$ to $\Lambda K^+$ (0-10% Centrality) . . . . .	87
67	Residuals: $\Xi^0 K^+$ to $\Lambda K^+$ (0-10% Centrality) . . . . .	88
68	Residuals: $\Xi^- K^+$ to $\Lambda K^+$ (0-10% Centrality) . . . . .	88
69	Residuals: $\Sigma^{*+} K^+$ to $\Lambda K^+$ (0-10% Centrality) . . . . .	89
70	Residuals: $\Sigma^{*-} K^+$ to $\Lambda K^+$ (0-10% Centrality) . . . . .	89
71	Residuals: $\Sigma^{*0} K^+$ to $\Lambda K^+$ (0-10% Centrality) . . . . .	90
72	Residuals: $\Lambda K^{*0}$ to $\Lambda K^+$ (0-10% Centrality) . . . . .	90
73	Residuals: $\Sigma^0 \bar{K}^{*0}$ to $\Lambda K^+$ (0-10% Centrality) . . . . .	91
74	Residuals: $\Xi^0 \bar{K}^{*0}$ to $\Lambda K^+$ (0-10% Centrality) . . . . .	91
75	Residuals: $\Xi^- \bar{K}^{*0}$ to $\Lambda K^+$ (0-10% Centrality) . . . . .	92
76	Residuals: $\Sigma^0 K^-$ to $\Lambda K^-$ (0-10% Centrality) . . . . .	93
77	Residuals: $\Xi^0 K^-$ to $\Lambda K^-$ (0-10% Centrality) . . . . .	94
78	Residuals: $\Xi^- K^-$ to $\Lambda K^-$ (0-10% Centrality) . . . . .	94
79	Residuals: $\Sigma^{*+} K^-$ to $\Lambda K^-$ (0-10% Centrality) . . . . .	95
80	Residuals: $\Sigma^{*-} K^-$ to $\Lambda K^-$ (0-10% Centrality) . . . . .	95
81	Residuals: $\Sigma^{*0} K^-$ to $\Lambda K^-$ (0-10% Centrality) . . . . .	96
82	Residuals: $\Lambda \bar{K}^{*0}$ to $\Lambda K^-$ (0-10% Centrality) . . . . .	96
83	Residuals: $\Sigma^0 \bar{K}^{*0}$ to $\Lambda K^-$ (0-10% Centrality) . . . . .	97
84	Residuals: $\Xi^0 \bar{K}^{*0}$ to $\Lambda K^-$ (0-10% Centrality) . . . . .	97
85	Residuals: $\Xi^- \bar{K}^{*0}$ to $\Lambda K^-$ (0-10% Centrality) . . . . .	98
86	Residuals: $\Sigma^0 K_S^0$ to $\Lambda K_S^0$ (0-10% Centrality) . . . . .	99
87	Residuals: $\Xi^0 K_S^0$ to $\Lambda K_S^0$ (0-10% Centrality) . . . . .	100
88	Residuals: $\Xi^- K_S^0$ to $\Lambda K_S^0$ (0-10% Centrality) . . . . .	100
89	Residuals: $\Sigma^{*+} K_S^0$ to $\Lambda K_S^0$ (0-10% Centrality) . . . . .	101
90	Residuals: $\Sigma^{*-} K_S^0$ to $\Lambda K_S^0$ (0-10% Centrality) . . . . .	101
91	Residuals: $\Sigma^{*0} K_S^0$ to $\Lambda K_S^0$ (0-10% Centrality) . . . . .	102
92	Residuals: $\Lambda K^{*0}$ to $\Lambda K_S^0$ (0-10% Centrality) . . . . .	102
93	Residuals: $\Sigma^0 \bar{K}^{*0}$ to $\Lambda K_S^0$ (0-10% Centrality) . . . . .	103
94	Residuals: $\Xi^0 \bar{K}^{*0}$ to $\Lambda K_S^0$ (0-10% Centrality) . . . . .	103
95	Residuals: $\Xi^- \bar{K}^{*0}$ to $\Lambda K_S^0$ (0-10% Centrality) . . . . .	104
96	$\Lambda K^+$ $C_{00}$ and $\Im C_{11}$ Spherical Harmonic Components . . . . .	105
97	$\Lambda K^+$ First Six Components of Spherical Harmonic Decomposition (0-10%) . . . . .	106
98	$\Lambda K^-$ $C_{00}$ and $\Im C_{11}$ Spherical Harmonic Components . . . . .	107

99	$\Lambda K^-$ First Six Components of Spherical Harmonic Decomposition (0-10%) . . . . .	108
100	$\Lambda K_S^0 C_{00}$ and $\Im C_{11}$ Spherical Harmonic Components . . . . .	109
101	$\Lambda K_S^0$ First Six Components of Spherical Harmonic Decomposition (0-10%) . . . . .	110

---

## 10 1 Introduction

11 We present results from a femtoscopic analysis of  $\Lambda K$  and  $\Xi^- K^\pm$  correlations in Pb-Pb collisions at  
 12  $\sqrt{s_{NN}} = 2.76$  TeV by the ALICE experiment at the LHC. All pair combinations of  $\Lambda$  and  $\bar{\Lambda}$  with  $K^+$ ,  
 13  $K^-$  and  $K_S^0$  are analyzed. The femtoscopic correlations are the result of strong final-state interactions,  
 14 and are fit with a parametrization based on a model by R. Lednicky and V. L. Lyuboshitz [1]. This  
 15 allows us to both characterize the emission source and measure the scattering parameters for the particle  
 16 pairs. We observe a large difference in the  $\Lambda K^+(\bar{\Lambda} K^-)$  and  $\Lambda K^-(\bar{\Lambda} K^+)$  correlations in pairs with low  
 17 relative momenta ( $k^* \lesssim 100$  MeV). The results suggest an effect arising from different quark-antiquark  
 18 interactions in the pairs, i.e.  $s\bar{s}$  in  $\Lambda K^+(\bar{\Lambda} K^-)$  and  $u\bar{u}$  in  $\Lambda K^-(\bar{\Lambda} K^+)$ , or from different net strangeness for  
 19 each system. To gain further insight into this hypothesis, we currently are conducting a  $\Xi K$  femtoscopic  
 20 analysis.

## 21 2 Data Sample and Software

### 22 2.1 Data Sample

23 The analysis used “pass 2” reconstructed Pb-Pb data from LHC11h (AOD145). The runlist was selected  
 24 from runs with global quality tag “1” in the ALICE Run Condition Table. Approximately 40 million  
 25 combined central, semi-central, and minimum bias events were analyzed. Runs from both positive (++)  
 26 and negative (--) magnetic field polarity settings were used.

27 Run list: 170593, 170572, 170388, 170387, 170315, 170313, 170312, 170311, 170309, 170308, 170306,  
 28 170270, 170269, 170268, 170230, 170228, 170207, 170204, 170203, 170193, 170163, 170159, 170155,  
 29 170091, 170089, 170088, 170085, 170084, 170083, 170081, 170040, 170027, 169965, 169923, 169859,  
 30 169858, 169855, 169846, 169838, 169837, 169835, 169591, 169590, 169588, 169587, 169586, 169557,  
 31 169555, 169554, 169553, 169550, 169515, 169512, 169506, 169504, 169498, 169475, 169420, 169419,  
 32 169418, 169417, 169415, 169411, 169238, 169167, 169160, 169156, 169148, 169145, 169144, 169138,  
 33 169099, 169094, 169091, 169045, 169044, 169040, 169035, 168992, 168988, 168826, 168777, 168514,  
 34 168512, 168511, 168467, 168464, 168460, 168458, 168362, 168361, 168342, 168341, 168325, 168322,  
 35 168311, 168310, 168315, 168108, 168107, 168105, 168076, 168069, 167988, 167987, 167985, 167920,  
 36 167915

37 Analysis was also performed on the LHC12a17a\_fix (AOD149) Monte Carlo HIJING events for certain  
 38 checks. THERMINATOR2 was also used for certain aspects, such as generation of transform matrices  
 39 describing feed-down contributions, estimation of  $\lambda$  parameters, and non-femtoscopic background  
 40 modeling.

### 41 2.2 Software

42 The analysis was performed on the PWGCF analysis train using AliRoot v5-09-29-1 and AliPhysics  
 43 vAN-20180505-1.

44 The main classes utilized include: AliFemtoVertexMultAnalysis, AliFemtoEventCutEstimators, AliFemto  
 45 toESDTrackCutNSigmaFilter, AliFemtoV0TrackCutNSigmaFilter, AliFemtoXiTrackCut, AliFemtoV0PairCut,  
 46 AliFemtoV0TrackPairCut, AliFemtoXiTrackPairCut, and AliFemtoAnalysisLambdaKaon. All of these  
 47 classes are contained in /AliPhysics/PWGCF/FEMTOSCOPY/AliFemto and .../AliFemtoUser.

## 48 3 Data Selection

### 49 3.1 Event Selection and Mixing

50 The events used in this study were selected with the class AliFemtoEventCutEstimators according to the  
 51 following criteria:

- 52     – Triggers
- 53       – minimum bias (kMB)
- 54       – central (kCentral)
- 55       – semi-central (kSemiCentral)
- 56     – z-position of reconstructed event vertex must be within 10 cm of the center of the ALICE detector
- 57     – the event must contain at least one particle of each type from the pair of interest

58 The event mixing was handled by the AliFemtoVertexMultAnalysis class, which only mixes events with  
 59 like vertex position and centrality. The following criteria were used for event mixing:

- 60     – Number of events to mix = 5
- 61     – Vertex position bin width = 2 cm
- 62     – Centrality bin width = 5

63 The AliFemtoEventReaderAODChain class is used to read the events. Event flattening is not currently  
 64 used. FilterBit(7). The centrality is determined by the “V0M” method of AliCentrality, set by calling  
 65 AliFemtoEventReaderAOD::SetUseMultiplicity(kCentrality). We utilize the SetPrimaryVertexCorrec-  
 66 tionTPCPoints switch, which causes the reader to shift all TPC points to be relative to the event vertex.

### 67 3.2 $K^\pm$ Track Selection

68 Charged kaons are identified using the AliFemtoESDTrackCutNSigmaFilter class. The specific cuts used  
 69 in this analysis are as follows:

70 The purity of the  $K^\pm$  collections was estimated using the HIJING MC data, for which the true identity  
 71 of each reconstructed  $K^\pm$  particle is known. Therefore, the purity may be estimated as:

$$Purity(K^\pm) = \frac{N_{true}}{N_{reconstructed}} \quad (1)$$

72 Purity( $K^+$ )  $\approx$  Purity( $K^-$ )  $\approx$  97%

### 73 3.3 V0 Selection

74  $\Lambda(\bar{\Lambda})$  and  $K_S^0$  are neutral particles which cannot be directly detected, but must instead be reconstructed  
 75 through detection of their decay products, or daughters. This process is illustrated in Figure 1. In  
 76 general, particles which are topologically reconstructed in this fashion are called V0 particles. The  
 77 class AliFemtoV0TrackCutNSigmaFilter (which is an extension of AliFemtoV0TrackCut) is used to  
 78 reconstruct the V0s.

79 In order to ensure a true and reliable signal, one must ensure good purity of the V0 collection. The purity  
 80 of the collection is calculated as:

$$Purity = \frac{Signal}{Signal + Background} \quad (2)$$

81 To obtain both the signal and background, the invariant mass distribution ( $m_{inv}$ ) of all V0 candidates must  
 82 be constructed immediately before the final invariant mass cut. Examples of such distributions can be  
 83 found in Figures 3 and 5. It is vital that the distribution be constructed immediately before the final  $m_{inv}$

<b>K<sup>±</sup> selection</b>	
<b>Kinematic range</b>	
$ \eta $	< 0.8
$p_T$	$0.14 < p_T < 1.5 \text{ GeV}/c$
<b>Track quality and selection</b>	
FilterBit	7
Number of clusters in the TPC	> 80
$\chi^2/N_{DOF}$ for ITS clusters	< 3.0
$\chi^2/N_{DOF}$ for TPC clusters	< 4.0
XY impact parameter	< 2.4 cm
Z impact parameter	< 3.0 cm
Remove particles with any kink labels	true
N $\sigma$ to primary vertex	< 3.0
<b>K<sup>±</sup> identification</b>	
PID Probabilities	
K	> 0.2
$\pi$	< 0.1
$\mu$	< 0.8
p	< 0.1
Most probable particle type	Kaon (fMostProbable=3)
TPC and TOF N $\sigma$ Cuts	
$p < 0.4 \text{ GeV}/c$	$N_{\sigma K, \text{TPC}} < 2$
$0.4 < p < 0.45 \text{ GeV}/c$	$N_{\sigma K, \text{TPC}} < 1$
$0.45 < p < 0.80 \text{ GeV}/c$	$N_{\sigma K, \text{TPC}} < 3 \& N_{\sigma K, \text{TOF}} < 2$
$0.80 < p < 1.0 \text{ GeV}/c$	$N_{\sigma K, \text{TPC}} < 3 \& N_{\sigma K, \text{TOF}} < 1.5$
$p > 1.0 \text{ GeV}/c$	$N_{\sigma K, \text{TPC}} < 3 \& N_{\sigma K, \text{TOF}} < 1$
<b>Misidentification cuts</b>	
Electron Rejection	Reject if $N_{\sigma e^-, \text{TPC}} < 3$
Pion Rejection: Reject if:	
if TOF and TPC available	$N_{\sigma \pi, \text{TPC}} < 3 \& N_{\sigma \pi, \text{TOF}} < 3$
$p < 0.65 \text{ GeV}/c$	$p < 0.5 \text{ GeV}/c$
else	$N_{\sigma \pi, \text{TPC}} < 3$
	$0.5 < p < 0.65 \text{ GeV}/c$
	$N_{\sigma \pi, \text{TPC}} < 2$
$0.65 < p < 1.5 \text{ GeV}/c$	$N_{\sigma \pi, \text{TPC}} < 5 \& N_{\sigma \pi, \text{TOF}} < 3$
$p > 1.5 \text{ GeV}/c$	$N_{\sigma \pi, \text{TPC}} < 5 \& N_{\sigma \pi, \text{TOF}} < 2$

**Table 1:** K<sup>±</sup> selection

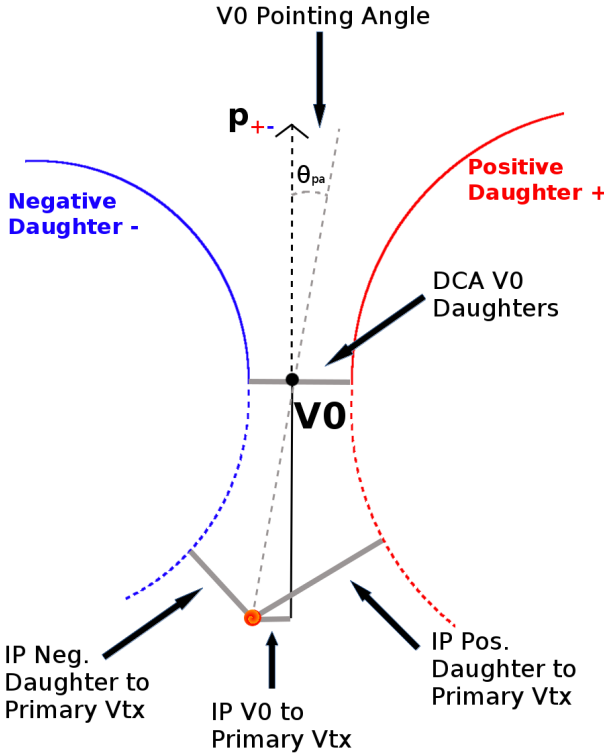


**Fig. 1:** V0 Reconstruction

84 cut, otherwise, it would be impossible to estimate the background. As demonstrated in Figures 3 and 5,  
 85 the background is fit with a polynomial outside of the peak region of interest in order to extrapolate an  
 86 estimate for the background within the region. Within the  $m_{inv}$  cut limits, the background is the region  
 87 below the fit while the signal is the region above the fit.

88 **3.3.1  $\Lambda$  Reconstruction**

89 The following cuts were used to select good  $\Lambda(\bar{\Lambda})$  candidates:

90 1. Shared Daughter Cut for V0 Collection

91 – Iterate through V0 collection to ensure that no daughter is used in more than one V0 candidate

92 Figure 2a shows the mass assuming  $K_S^0$  hypothesis for the  $\Lambda$  collection, i.e. assume the daughters are  
 93  $\pi^+\pi^-$  instead of  $p^+\pi^-$ . Figure 2b is a similar plot, but is for the  $\bar{\Lambda}$  collection, i.e. assume the daughters  
 94 are  $\pi^+\pi^-$  instead of  $p^+\bar{p}^-$ . The  $K_S^0$  contamination is visible, although not profound, in both, in the slight  
 95 peaks around  $m_{inv} = 0.497 \text{ GeV}/c^2$ . If one simply cuts out the entire peak, good  $\Lambda$  particles will be lost.  
 96 Ideally, the  $\Lambda$  selection and  $K_S^0$  misidentification cuts are selected such that the peak is removed from this  
 97 plot while leaving the underlying distribution continuous. To attempt to remove these  $K_S^0$  contaminations  
 98 without throwing away good  $\Lambda$  and  $\bar{\Lambda}$  particles, the following misidentification cuts are imposed; a  $\Lambda(\bar{\Lambda})$   
 99 candidate is rejected if all of the following criteria are satisfied:

- 100 –  $|m_{inv, K_S^0 \text{ Hypothesis}} - m_{PDG, K_S^0}| < 9.0 \text{ MeV}/c^2$   
 101 – Positive and negative daughters pass  $\pi$  daughter cut implemented for  $K_S^0$  reconstruction  
 102 –  $|m_{inv, K_S^0 \text{ Hypothesis}} - m_{PDG, K_S^0}| < |m_{inv, \Lambda(\bar{\Lambda}) \text{ Hypothesis}} - m_{PDG, \Lambda(\bar{\Lambda})}|$

<b>Λ selection</b>	
$ \eta $	< 0.8
$p_T$	> 0.4 GeV/c
$ m_{\text{inv}} - m_{\text{PDG}} $	< 3.8 MeV
DCA to prim. vertex	< 0.5 cm
Cosine of pointing angle	> 0.9993
OnFlyStatus	false
Decay Length	< 60 cm
Shared Daughter Cut	true
Misidentification Cut	true
<b>Daughter Cuts (<math>\pi</math> and p)</b>	
$ \eta $	< 0.8
Number of clusters in the TPC	> 80
Daughter status	kTPC $\chi$ fit
DCA $\pi p$ Daughters	< 0.4 cm
<b><math>\pi</math>-specific cuts</b>	
$p_T$	> 0.16 GeV/c
DCA to prim vertex	> 0.3 cm
TPC and TOF N $\sigma$ Cuts	
$p < 0.5 \text{ GeV}/c$	$N\sigma_{\text{TPC}} < 3$
$p > 0.5 \text{ GeV}/c$	if TOF & TPC available else
	$N\sigma_{\text{TPC}} < 3 \& N\sigma_{\text{TOF}} < 3$ $N\sigma_{\text{TOF}} < 3$
<b>p-specific cuts</b>	
$p_T$	> $0.5(p) [0.3(\bar{p})] \text{ GeV}/c$
DCA to prim vertex	> 0.1 cm
TPC and TOF N $\sigma$ Cuts	
$p < 0.8 \text{ GeV}/c$	$N\sigma_{\text{TPC}} < 3$
$p > 0.8 \text{ GeV}/c$	if TOF & TPC available else
	$N\sigma_{\text{TPC}} < 3 \& N\sigma_{\text{TOF}} < 3$ $N\sigma_{\text{TOF}} < 3$

**Table 2:** Λ selection

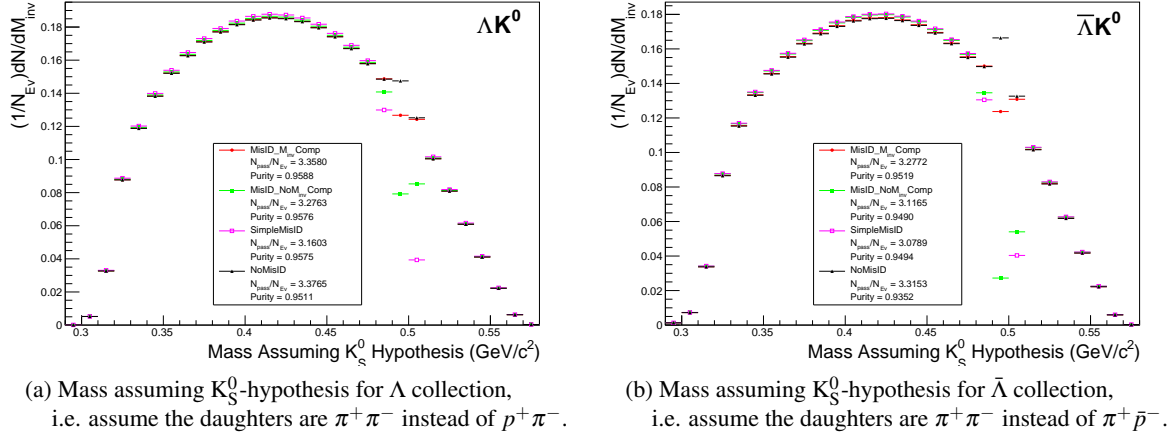


**Fig. 2:** Mass assuming  $K_S^0$ -hypothesis for V0 candidates passing all  $\Lambda$  (2a) and  $\bar{\Lambda}$  (2b) cuts. The “NoMisID” distribution (black triangles) uses the V0 finder without any attempt to remove misidentified  $K_S^0$ . The slight peak in the “NoMisID” distribution around  $m_{inv} = 0.5 \text{ GeV}/c^2$  contains misidentified  $K_S^0$  particles in our  $\Lambda(\bar{\Lambda})$  collection. “SimpleMisID” (pink squares) simply cuts out the entire peak, which throws away some good  $\Lambda$  and  $\bar{\Lambda}$  particles. “MisID\_NoM<sub>inv</sub>Comp” (green squares) uses the misidentification cut outlined in the text, but does not utilize the final invariant mass comparison step. “MisID\_M<sub>inv</sub>Comp” (red circles) utilizes the full misidentification methods, and is currently used for this analysis. “ $N_{pass}/N_{ev}$ ” is the total number of  $\Lambda(\bar{\Lambda})$  particles found, normalized by the total number of events. The purity of the collection is also listed.

103 Figure 3 shows the invariant mass ( $m_{inv}$ ) distribution of all  $\Lambda(\bar{\Lambda})$  candidates immediately before the final  
 104 invariant mass cut. These distributions are used to calculate the collection purities. The  $\Lambda$  and  $\bar{\Lambda}$  purities  
 105 are found to be: Purity( $\Lambda$ )  $\approx$  Purity( $\bar{\Lambda}$ )  $\approx$  95%.

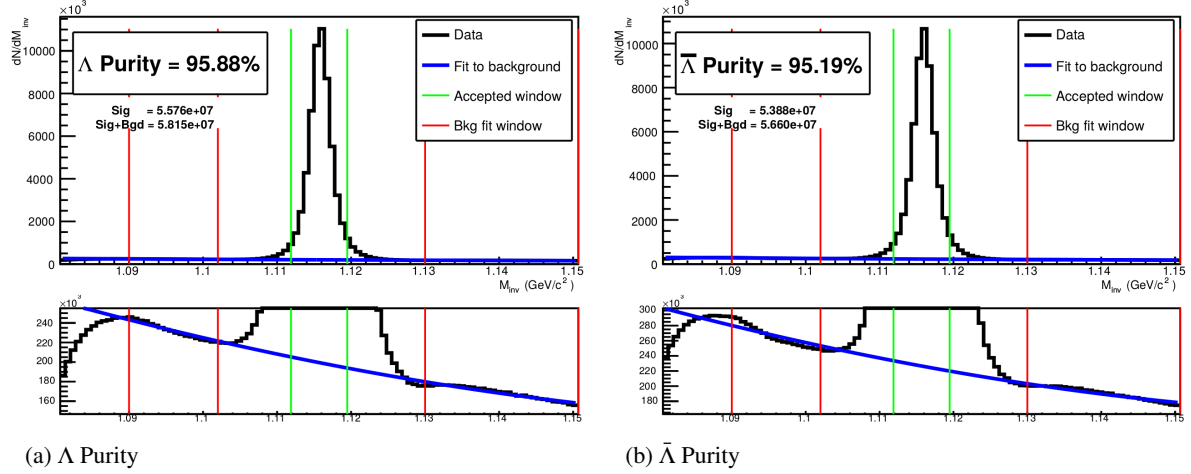


**Fig. 3:** Invariant mass ( $m_{inv}$ ) distribution for all  $\Lambda$  (a) and  $\bar{\Lambda}$  (b) candidates immediately before the final invariant mass cut. The bottom figures are zoomed to show the background with fit. The vertical green lines represent the  $m_{inv}$  cuts used in the analyses, the red vertical lines delineate the regions over which the background was fit, and the blue line shows the background fit. These distributions are used to calculate the collection purities, Purity( $\Lambda$ )  $\approx$  Purity( $\bar{\Lambda}$ )  $\approx$  95%.

### 106 3.3.2 $K_S^0$ Reconstruction

107 The following cuts were used to select good  $K_S^0$  candidates:

## 108 1. Shared Daughter Cut for V0 Collection

- 109 – Iterate through V0 collection to ensure that no daughter is used in more than one V0 candidate

<b>K<sub>S</sub><sup>0</sup> selection</b>	
$ \eta $	< 0.8
$p_T$	> 0.2 GeV/c
$m_{PDG} - 13.677 \text{ MeV} < m_{\text{inv}} < m_{PDG} + 2.0323 \text{ MeV}$	
DCA to prim. vertex	< 0.3 cm
Cosine of pointing angle	> 0.9993
OnFlyStatus	false
Decay Length	< 30 cm
Shared Daughter Cut	true
Misidentification Cut	true

<b><math>\pi^\pm</math> Daughter Cuts</b>	
$ \eta $	< 0.8
Number of clusters in TPC	> 80
Daughter Status	kTPCrefit
DCA $\pi^+\pi^-$ Daughters	< 0.3 cm
$p_T$	> 0.15 GeV/c
DCA to prim vertex	> 0.3 cm

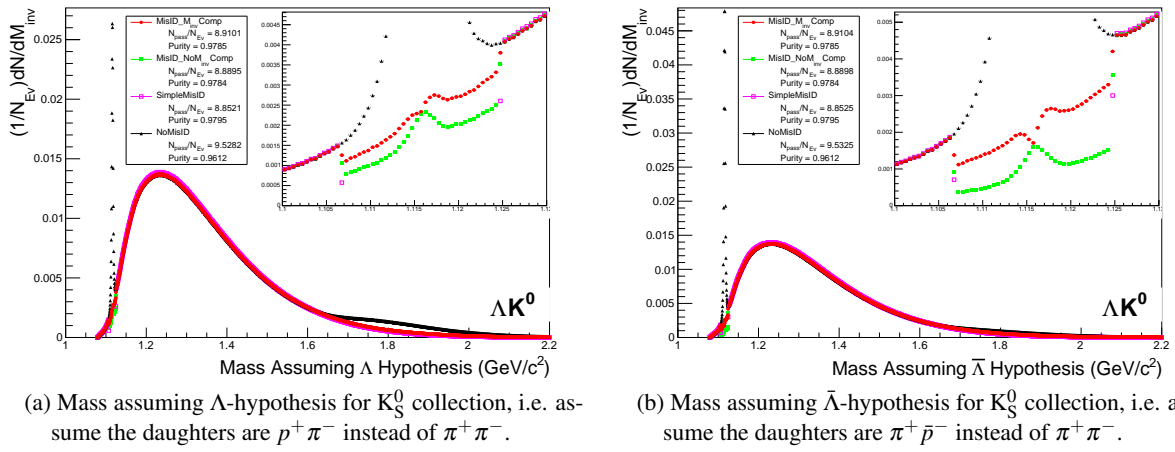
TPC and TOF N $\sigma$ Cuts					
$p < 0.5 \text{ GeV}/c$	$N\sigma_{\text{TPC}} < 3$				
$p > 0.5 \text{ GeV}/c$	<table border="1"> <tr> <td>if TOF &amp; TPC available</td><td><math>N\sigma_{\text{TPC}} &lt; 3 \text{ \&amp; } N\sigma_{\text{TOF}} &lt; 3</math></td></tr> <tr> <td>else</td><td><math>N\sigma_{\text{TOF}} &lt; 3</math></td></tr> </table>	if TOF & TPC available	$N\sigma_{\text{TPC}} < 3 \text{ \& } N\sigma_{\text{TOF}} < 3$	else	$N\sigma_{\text{TOF}} < 3$
if TOF & TPC available	$N\sigma_{\text{TPC}} < 3 \text{ \& } N\sigma_{\text{TOF}} < 3$				
else	$N\sigma_{\text{TOF}} < 3$				

Table 3: K<sub>S</sub><sup>0</sup> selection

110 As can be seen in Figure 4, some misidentified  $\Lambda$  and  $\bar{\Lambda}$  particles contaminate our K<sub>S</sub><sup>0</sup> sample. Figure  
 111 4a shows the mass assuming  $\Lambda$ -hypothesis for the K<sub>S</sub><sup>0</sup> collection, i.e. assume the daughters are  $p^+\pi^-$   
 112 instead of  $\pi^+\pi^-$ . Figure 4b is similar, but shows the mass assuming  $\bar{\Lambda}$ -hypothesis for the collection,  
 113 i.e. assume the daughters are  $\pi^+\bar{p}^-$  instead of  $\pi^+\pi^-$ . The  $\Lambda$  contamination can be seen in 4a, and the  
 114  $\bar{\Lambda}$  contamination in 4b, in the peaks around  $m_{\text{inv}} = 1.115 \text{ GeV}/c^2$ . Additionally, the  $\bar{\Lambda}$  contamination is  
 115 visible in Figure 4a, and the  $\Lambda$  contamination visible in Figure 4b, in the region of excess around 1.65  
 116  $< m_{\text{inv}} < 2.1 \text{ GeV}/c^2$ . This is confirmed as the number of misidentified  $\Lambda$  particles in the sharp peak  
 117 of Figure 4a (misidentified  $\bar{\Lambda}$  particles in the sharp peak of Figure 4b) approximately equals the excess  
 118 found in the  $1.65 < m_{\text{inv}} < 2.1 \text{ GeV}/c^2$  region of Figure 4a (Figure 4b).

119 The peaks around  $m_{\text{inv}} = 1.115 \text{ GeV}/c^2$  in Figure 4 contain both misidentified  $\Lambda(\bar{\Lambda})$  particles and good K<sub>S</sub><sup>0</sup>.  
 120 If one simply cuts out the entire peak, some good K<sub>S</sub><sup>0</sup> particles will be lost. Ideally, the K<sub>S</sub><sup>0</sup> selection and  
 121  $\Lambda(\bar{\Lambda})$  misidentification cuts can be selected such that the peak is removed from this plot while leaving  
 122 the underlying distribution continuous. To attempt to remove these  $\Lambda$  and  $\bar{\Lambda}$  contaminations without  
 123 throwing away good K<sub>S</sub><sup>0</sup> particles, the following misidentification cuts are imposed; a K<sub>S</sub><sup>0</sup> candidate is  
 124 rejected if all of the following criteria are satisfied (for either  $\Lambda$ - or  $\bar{\Lambda}$ -hypothesis):

- 125 –  $|m_{\text{inv}, \Lambda(\bar{\Lambda}) \text{ Hypothesis}} - m_{PDG, \Lambda(\bar{\Lambda})}| < 9.0 \text{ MeV}/c^2$
- 126 – Positive daughter passes  $p^+(\pi^+)$  daughter cut implemented for  $\Lambda(\bar{\Lambda})$  reconstruction
- 127 – Negative daughter passes  $\pi^-(\bar{p}^-)$  daughter cut implemented by  $\Lambda(\bar{\Lambda})$  reconstruction
- 128 –  $|m_{\text{inv}, \Lambda(\bar{\Lambda}) \text{ Hypothesis}} - m_{PDG, \Lambda(\bar{\Lambda})}| < |m_{\text{inv}, K_S^0 \text{ Hypothesis}} - m_{PDG, K_S^0}|$



**Fig. 4:** Mass assuming  $\Lambda$ -hypothesis (4a) and  $\bar{\Lambda}$ -hypothesis (4b) for  $K_S^0$  collection. The “NoMisID” distribution (black triangles) uses the V0 finder without any attempt to remove misidentified  $\Lambda$  and  $\bar{\Lambda}$ . The peak in the “NoMisID” distribution around  $m_{\text{inv}} = 1.115 \text{ GeV}/c^2$  contains misidentified  $\Lambda$  (4a) and  $\bar{\Lambda}$  (4b) particles in our  $K_S^0$  collection. “SimpleMisID” (pink squares) simply cuts out the entire peak, which throws away some good  $K_S^0$  particles. “MisID\_NoM<sub>inv</sub>Comp” (green squares) uses the misidentification cut outlined in the text, but does not utilize the final invariant mass comparison step. “MisID\_M<sub>inv</sub>Comp” (red circles) utilizes the full misidentification methods, and is currently used for this analysis. “N<sub>pass</sub>/N<sub>ev</sub>” is the total number of  $K_S^0$  particles found, normalized by the total number of events. The purity of the collection is also listed. Also note, the relative excess of the “NoMisID” distribution around  $1.65 < m_{\text{inv}} < 2.1 \text{ GeV}/c^2$  shows misidentified  $\bar{\Lambda}$  (4a) and  $\Lambda$  (4b) particles in our  $K_S^0$  collection.

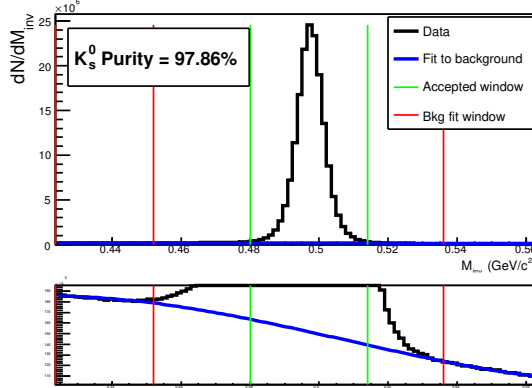


**Fig. 5:** Invariant mass ( $m_{\text{inv}}$ ) distribution for all  $K_S^0$  candidates immediately before the final invariant mass cut. The bottom figure is zoomed to show the background with fit. The vertical green lines represent the  $m_{\text{inv}}$  cut used in the analyses, the red vertical lines delineate the regions over which the background was fit, and the blue line shows the background fit. This distribution is used to calculate the collection purity, Purity( $K_S^0$ )  $\approx 98\%$ .

### 129 3.3.3 V0 Purity Background Estimation

130 As previously stated, the backgrounds in the  $m_{\text{inv}}$  distributions are modeled by a polynomial which is  
 131 fit outside of the final cut region in an attempt to estimate the background within the cut region. As  
 132 this estimate of the background under the mass peak is vital for our estimate of our V0 purity, it is  
 133 important for us to ensure that our estimate is accurate. More specifically, it is necessary that we ensure  
 134 the background is well described by a polynomial fit within the cut region.

135 To better understand our background, we studied V0 candidates reconstructed with daughters from dif-

136 ferent events. These mixed-event V0s certainly do not represent real, physical V0s (a single V0 cannot  
 137 have daughters living in two different events!), but, rather, represent a large portion of the background  
 138 creeping into our analysis.

139 The standard AliFemto framework is not equipped to handle this situation, as most are not interested in  
 140 these fake-V0s. Therefore, we built the AliFemtoV0PurityBgdEstimator class to handle our needs. In ad-  
 141 dition to finding fake-V0s using mixed-event daughters, we also used our AliFemtoV0PurityBgdEstimator  
 142 class to find real-V0s using same-event daughters. The purpose here was to compare our simple V0 finder  
 143 (in AliFemtoV0PurityBgdEstimator) to the established V0 finder used in standard AliFemto analyses.

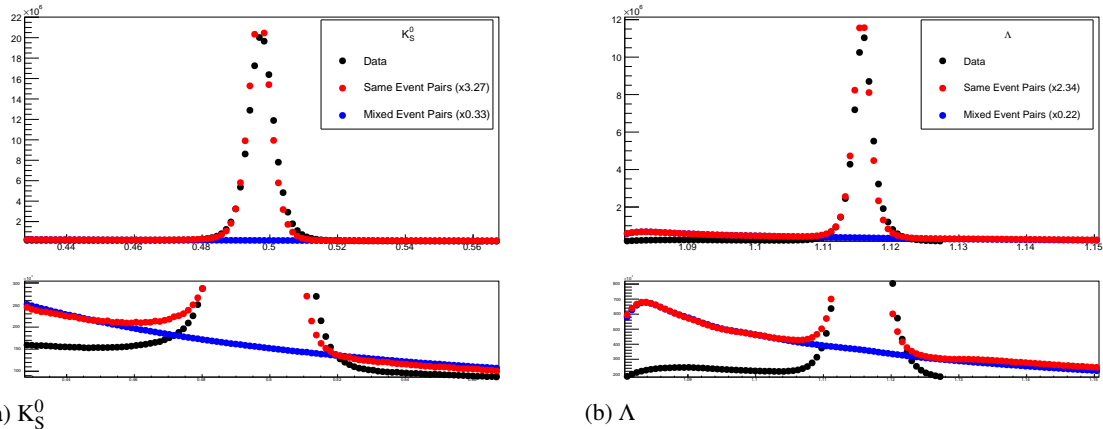


**Fig. 6:** V0 Purity Background Estimation. The black points, marked "Data", correspond to real V0s found using the standard V0-finder (i.e. the V0s used in my analyses). The red points, marked "Same Event Pairs", show real V0s reconstructed with our personal V0-finder in AliFemtoV0PurityBgdEstimator. These data are scaled by a factor (listed in the legend) to match their *Signal + Background* value in the cut region with that of the data. The blue points, marked "Mixed Event Pairs", show fake-V0s reconstructed with our personal V0-finder using mixed-event daughters. The blue points are scaled by a factor (listed in the legend) to closely match the red points in the side-band region.

144 Figure 6 shows the results of our study. In the figures, the black points, marked "Data", correspond to  
 145 V0s found using the standard V0-finder, and to the V0s used in my analyses. The red points show real  
 146 V0s reconstructed with our personal V0-finder (in AliFemtoV0PurityBgdEstimator) using same-event  
 147 daughters, and the blue points show fake-V0s reconstructed with our personal V0-finder using mixed-  
 148 event daughters. Both the red and blue points have been scaled by different factors (listed in the figure's  
 149 legends) to nicely align all three data on a single plot.

150 Figure 6 shows that our personal V0-finder does a good, but not perfect, job of matching the shape of the  
 151  $m_{inv}$  plots obtained from the data. The scale factor listed in the legend reveals that we are only finding  
 152 1/3 - 1/2 of the V0s found by the standard V0-finder. These two points are not of concern, as our purpose  
 153 here was to gain a sense of the broad shape of the background. It is revealed in Fig. 6, when studying  
 154 the red and blue points, that the background distribution within the mass peak region is simply a smooth  
 155 connection of the backgrounds outside of the cut region, as we assumed. Therefore, our method of fitting  
 156 the background outside of the cut region, fitting with a smooth polynomial, and extrapolating to the cut  
 157 region is justified.

### 158 3.4 $\Xi$ Reconstruction

159 Our motivation for studying  $\Xi^- K^\pm$  systems is to attempt to better understand the striking difference in  
 160 the  $\Lambda K^+$  and  $\Lambda K^-$  data at low  $k^*$  (Figure 13).

161 The reconstruction of  $\Xi$  particles is one level above V0 reconstruction. V0 particles are topologically

<sup>162</sup> reconstructed by searching for the charged daughters' tracks into which they decay. With  $\Xi$  particles, we  
<sup>163</sup> search for the V0 particle and charged daughter into which the  $\Xi$  decays. In the case of  $\Xi^-$ , we search  
<sup>164</sup> for the  $\Lambda$  (V0) and  $\pi^-$  (track) daughters. We will refer to this  $\pi$  as the “bachelor  $\pi$ ”.

<sup>165</sup> The following cuts were used to select good  $\Xi^-$  ( $\bar{\Xi}^+$ ) candidates:

<sup>166</sup> 1. Shared Daughter Cut for  $\Xi$  Collection

- <sup>167</sup> – Iterate through  $\Xi$  collection to ensure that no daughter is used in more than one  $\Xi$  candidate
- <sup>168</sup> – Remove any candidate in which the bachelor  $\pi$  is also a daughter of the  $\Lambda$  (implemented in
- <sup>169</sup> AliFemtoXiTrackPairCut class)

<b><math>\Xi</math> selection</b>	
$ \eta $	< 0.8
$p_T$	> 0.8 GeV/c
$ m_{\text{inv}} - m_{\text{PDG}} $	< 3.0 MeV
DCA to prim. vertex	< 0.3 cm
Cosine of pointing angle	> 0.9992
<b><math>\Lambda</math> daughter cuts</b>	
DCA to prim. vertex	> 0.2 cm
Cosine of pointing angle	> 0.0
Cosine of pointing angle to $\Xi$ decay vertex	> 0.9993
OnFlyStatus	false

All other  $\Lambda$  and corresponding ( $\pi$  and p) daughter cuts are same as in primary  $\Lambda$  selection, and can be found in Sec. 3.3.1

<b>Bachelor <math>\pi</math> cuts</b>	
$ \eta $	< 0.8
$p_T$	> 0.0 GeV/c
DCA to prim. vertex	> 0.1 cm
Number of clusters in the TPC	> 70
Daughter status	kTPCrefit

TPC and TOF N $\sigma$  Cuts

$p < 0.5 \text{ GeV}/c$	N $\sigma_{\text{TPC}} < 3$
$p > 0.5 \text{ GeV}/c$	if TOF & TPC available else N $\sigma_{\text{TOF}} < 3$

**Table 4:**  $\Lambda$  selection

<sup>170</sup> The purity of our  $\Xi$  and  $\bar{\Xi}$  collections are calculated just as those of our V0 collections 3.3. Figure 8,  
<sup>171</sup> which is used to calculate the purity, shows the  $m_{\text{inv}}$  distribution of our  $\Xi(\bar{\Xi})$  candidates just before the  
<sup>172</sup> final  $m_{\text{inv}}$  cut. Currently, we have Purity( $\Xi^-$ )  $\approx 90\%$  and Purity( $\bar{\Xi}^+$ )  $\approx 92\%$ .

<sup>173</sup> 3.5 Pair Selection

<sup>174</sup> It is important to obtain true particle pairs in the analysis. In particular, contamination from pairs constructed with split or merged tracks, and pairs sharing daughters, can introduce an artificial signal into the correlation function, obscuring the actual physics. We impose the following pair cuts to combat these issues:

<sup>178</sup> 1. Shared Daughter Cut for Pairs

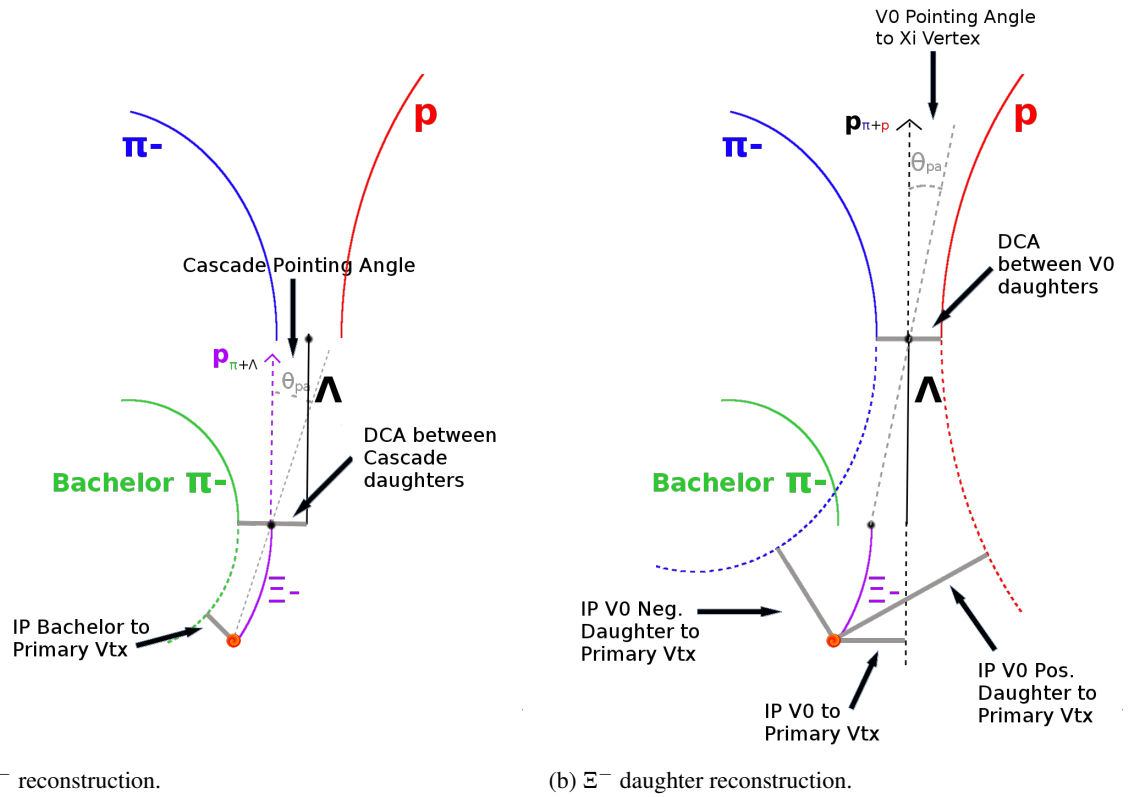


**Fig. 7:** (Left)  $\Xi^-$  reconstruction (DCA to primary vertex for  $\Xi^-$  not shown). (Right)  $\Xi^-$  daughter reconstruction.

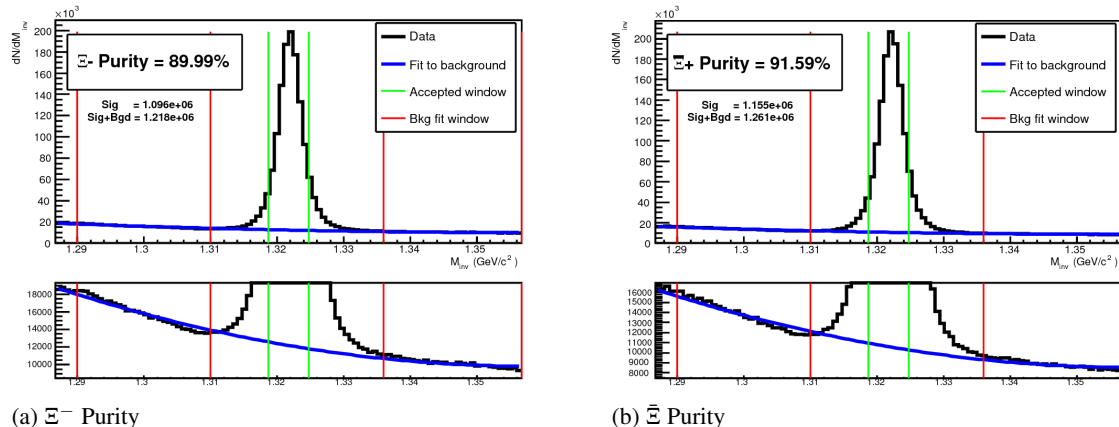


**Fig. 8:** Invariant mass ( $m_{\text{inv}}$ ) distribution for all  $\Xi^-$  (a) and  $\Xi^+$  (b) candidates immediately before the final invariant mass cut. The bottom figures are zoomed to show the background with fit. The vertical green lines represent the  $m_{\text{inv}}$  cuts used in the analyses, the red vertical lines delineate the regions over which the background was fit, and the blue line shows the background fit. These distributions are used to calculate the collection purities,  $\text{Purity}(\Xi^-) \approx 90\%$  and  $\text{Purity}(\Xi^+) \approx 92\%$ .

- 179                   (a) V0-V0 Pairs (i.e.  $\Lambda K_S^0$  analyses)
- 180                   – Remove all pairs which share a daughter
- 181                   – Ex.  $\Lambda$  and  $K_S^0$  particles which share a  $\pi^-$  daughter are not included
- 182                   (b) V0-Track Pairs (i.e.  $\Lambda K^\pm$  analyses)
- 183                   – Remove pairs if Track is also used as a daughter of the V0

- 184           – In these analyses, this could only occur if, for instance, a K is misidentified as a  $\pi$   
185           or p in the V0 reconstruction

186           (c)  $\Xi$ -Track Pairs

- 187           – Remove pairs if Track is also used as a daughter of the  $\Xi$   
188           – In these analyses, this could only occur if, for instance, a K is misidentified as a  $\pi$   
189           or p in the V0 reconstruction, or misidentified as bachelor  $\pi$ .

190           2. Average Separation Cuts (AvgSep)

- 191           – Used to cut out splitting and merging effects  
192           – The motivation for these cuts can be seen in Figures 9, 10, and 11, in which average separa-  
193           tion correlation functions are presented

194           (a)  $\Lambda K_S^0$  Analyses

- 195           – AvgSep  $> 6.0$  cm for like charge sign daughters  
196           – ex. p daughter of  $\Lambda$  and  $\pi^+$  daughter of  $K_S^0$   
197           – No cut for unlike-sign daughters

198           (b)  $\Lambda K^\pm$  Analyses

- 199           – AvgSep  $> 8.0$  cm for daughter of  $\Lambda(\bar{\Lambda})$  sharing charge sign of  $K^\pm$   
200           – ex. in  $\Lambda K^+$  analysis, p daughter of  $\Lambda$  with  $K^+$   
201           – No cut for unlike signs

202           (c)  $\Xi^- K^\pm$  Analyses

- 203           – AvgSep  $> 8.0$  cm for any daughter of  $\Xi$  sharing charge sign of  $K^\pm$   
204           – ex. in  $\Xi^- K^-$  analysis,  $\pi^-$  daughter of  $\Lambda$  daughter with  $K^-$ , and bachelor  $\pi^-$  daugh-  
205           ter with  $K^-$   
206           – No cut for unlike signs

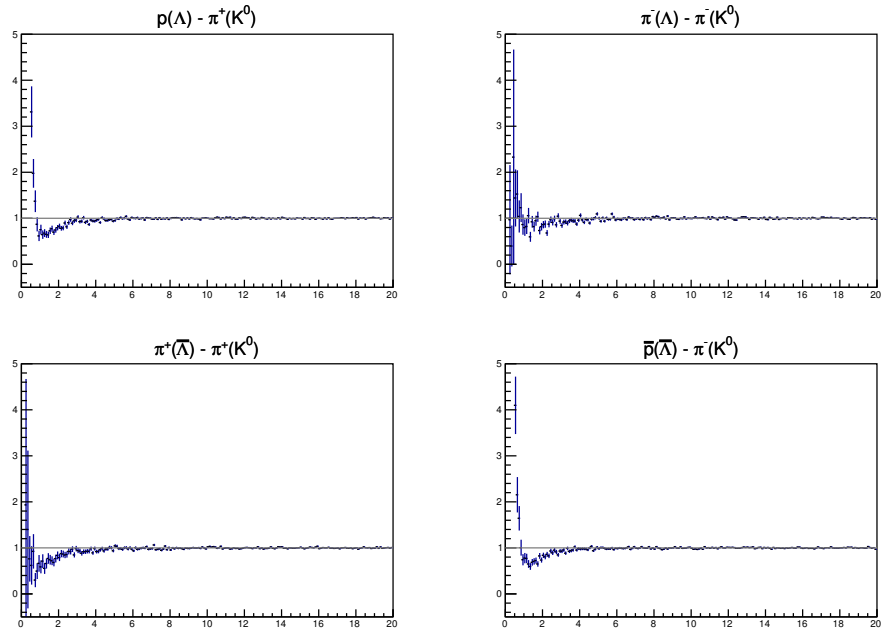


**Fig. 9:** Average separation (cm) correlation functions of  $\Lambda(\bar{\Lambda})$  and  $K_S^0$  Daughters. Only like-sign daughter pairs are shown (the distributions for unlike-signs were found to be flat). The title of each subfigure shows the daughter pair, as well as the mother of each daughter (in “()”), ex. top left is  $p$  from  $\Lambda$  with  $\pi^+$  from  $K_S^0$ .

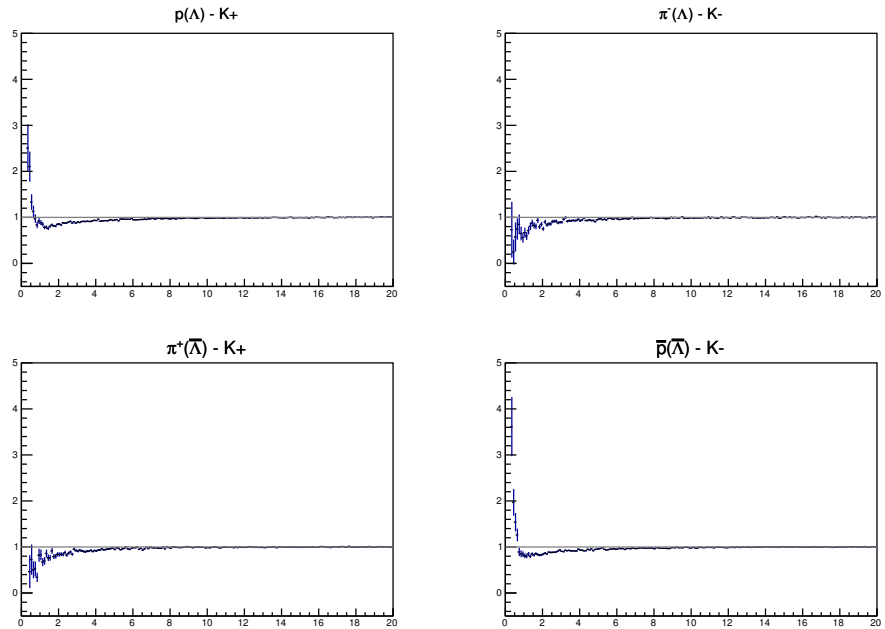


**Fig. 10:** Average separation (cm) correlation functions of  $\Lambda(\bar{\Lambda})$  Daughter and  $K^\pm$ . Only like-sign pairs are shown (unlike-signs were flat). In the subfigure titles, the particles in “()” represent the mothers, ex. top left is  $p$  from  $\Lambda$  with  $K^+$ .

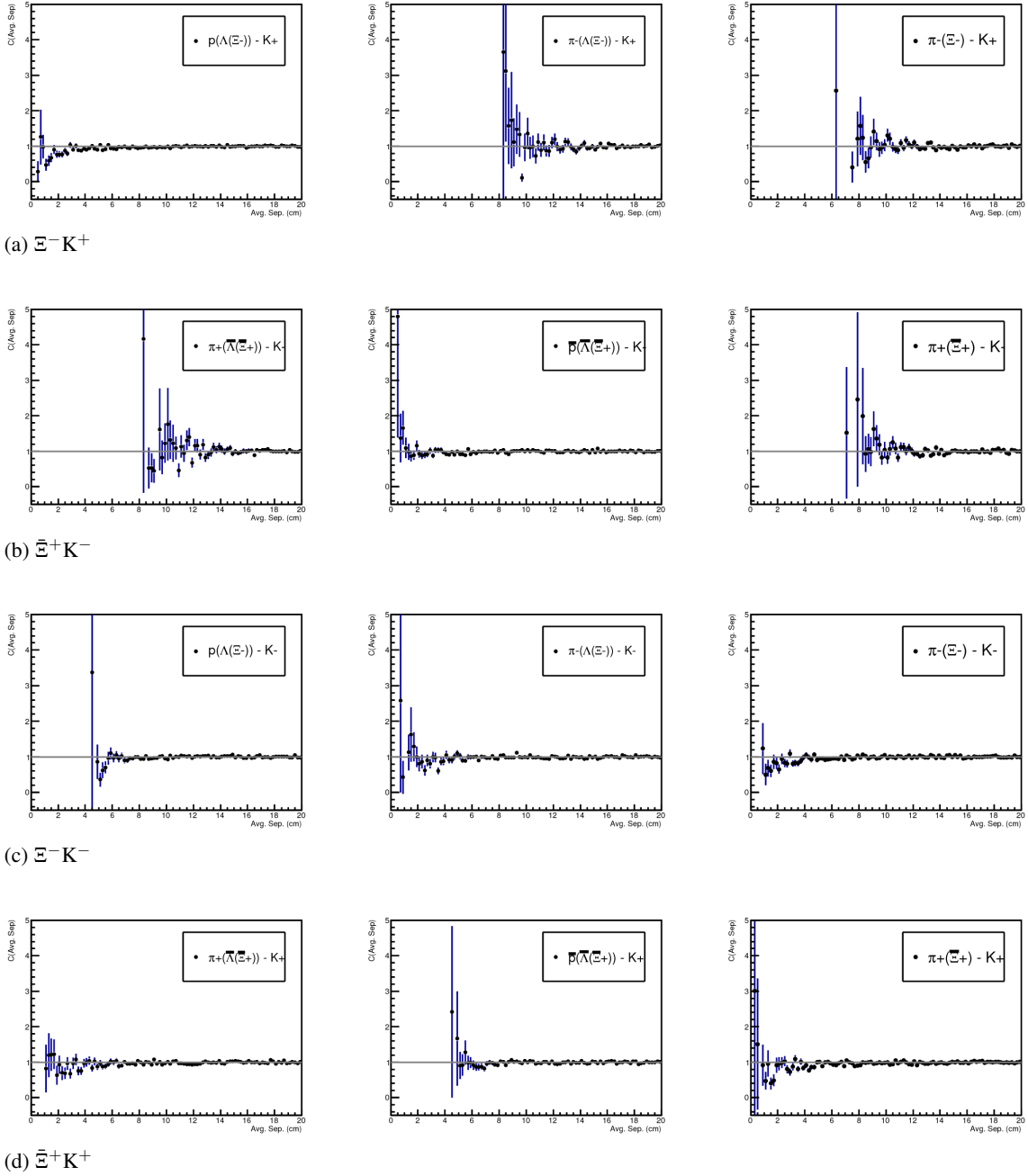


**Fig. 11:** Average separation (cm) correlation functions of  $\Xi$  Daughter and  $K^\pm$ . In the subfigure titles, the particles in “()” represent the mothers, ex. top left is p from  $\Lambda$  from  $\Xi^-$  with  $K^+$ .

207 **4 Correlation Functions**

208 This analysis studies the momentum correlations of both  $\Lambda K$  and  $\Xi^- K^\pm$  pairs using the two-particle  
 209 correlation function, defined as  $C(k^*) = A(k^*)/B(k^*)$ , where  $A(k^*)$  is the signal distribution,  $B(k^*)$  is the  
 210 reference (or background) distribution, and  $k^*$  is the momentum of one of the particles in the pair rest  
 211 frame. In practice,  $A(k^*)$  is constructed by binning in  $k^*$  pairs from the same event. Ideally,  $B(k^*)$  is  
 212 similar to  $A(k^*)$  in all respects excluding the presence of femtoscopic correlations [2]; as such,  $B(k^*)$   
 213 is used to divide out the phase-space effects, leaving only the femtoscopic effects in the correlation  
 214 function.

215 This analysis presents correlation functions for three centrality bins (0-10%, 10-30%, and 30-50%), and  
 216 is currently pair transverse momentum ( $k_T = 0.5|\mathbf{p}_{T,1} + \mathbf{p}_{T,2}|$ ) integrated (i.e. not binned in  $k_T$ ). The  
 217 correlation functions are constructed separately for the two magnetic field configurations, and, after  
 218 assuring consistency, are combined using a weighted average:

$$C_{combined}(k^*) = \frac{\sum_i w_i C_i(k^*)}{\sum_i w_i} \quad (3)$$

219 where the sum runs over the correlation functions to be combined, and the weight,  $w_i$ , is the number of  
 220 numerator pairs in  $C_i(k^*)$ . Here, the sum is over the two field configurations (++ and - -).

221 **4.1 Typical Correlation Function Construction**

222 In practice,  $B(k^*)$  is typically obtained by forming mixed-event pairs, i.e. particles from a given event  
 223 are paired with particles from  $N_{mix}(= 5)$  other events, and these pairs are then binned in  $k^*$ . In forming  
 224 the background distribution, it is important to mix only similar events; mixing events with different  
 225 phase-spaces can result in an unreliable background distribution, and can introduce artificial signals in  
 226 the correlation function. Therefore, in this analysis, we bin our events both in primary vertex location (2  
 227 cm bin width) and in centrality (5% bin width), and we only mix events within a given bin; i.e. we only  
 228 mix events of like centrality and of like primary vertex location. Also note, a vertex correction is also  
 229 applied to each event, which essentially recenters the the primary vertices to  $z = 0$ .

230 Figures 12a, 12b, 12c show the correlation functions for all centralities studied for  $\Lambda K^+(\bar{\Lambda} K^-)$ ,  $\Lambda K^-(\bar{\Lambda} K^+)$ ,  
 231 and  $\Lambda(\bar{\Lambda}) K_S^0$ , respectively. All were normalized in the range  $0.32 < k^* < 0.4$  GeV/c. It is interesting to  
 232 note that the average of the  $\Lambda K^+(\bar{\Lambda} K^-)$  and  $\Lambda K^-(\bar{\Lambda} K^+)$  correlation functions is consistent with our  
 233  $\Lambda K_S^0(\bar{\Lambda} K_S^0)$  measurement.

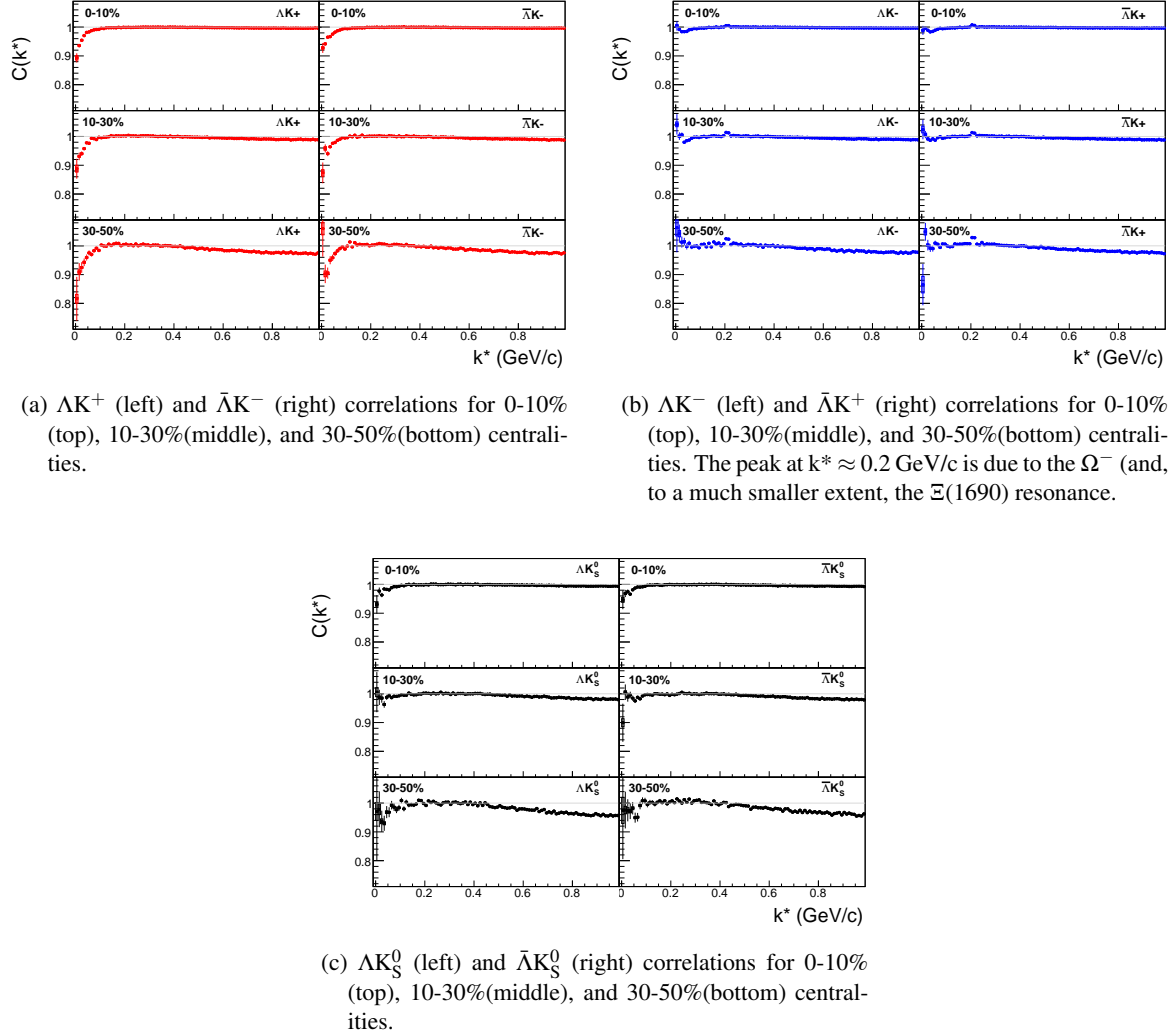


**Fig. 12:**  $\Lambda K$  and  $\bar{\Lambda}K$  correlation functions for 0-10%, 10-30%, and 30-50% centralities. The lines represent the statistical errors, while the boxes represent the systematic errors.

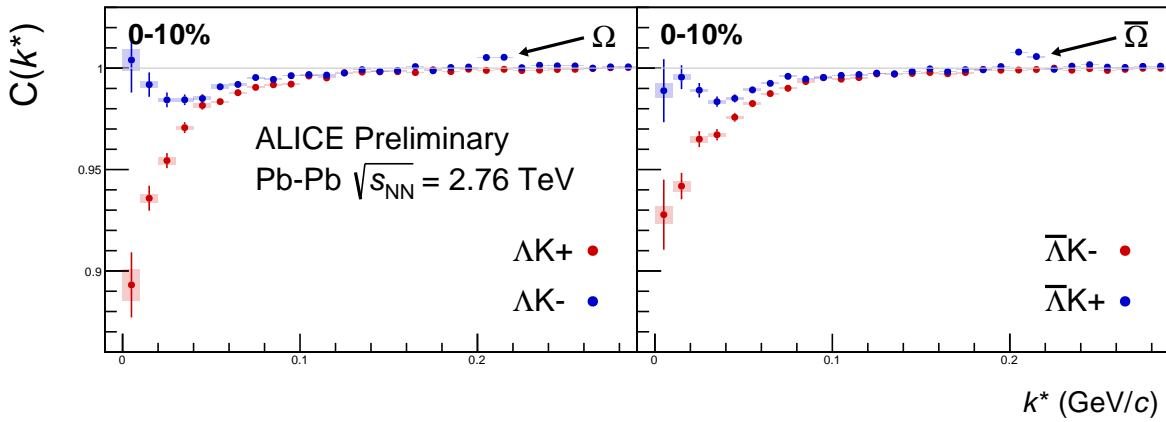


**Fig. 13:** Correlation Functions:  $\Lambda K^+$  vs  $\Lambda K^-$  ( $\bar{\Lambda}K^+$  vs  $\bar{\Lambda}K^-$ ) for 0-10% centrality. The peak in  $\Lambda K^-$  ( $\bar{\Lambda}K^+$ ) at  $k^* \approx 0.2$  GeV/c is due to the  $\Omega^-$  (and, to a much smaller extent, the  $\Xi(1690)$ ) resonance. The lines represent the statistical errors, while boxes represent systematic errors.

---

**234 4.2 Stavinskiy Correlation Function Construction**

235 The purpose of the Stavinskiy method is to rid the correlation functions of the non-femtoscopic back-  
236 ground. More specifically, this method is intended to handle background contributions from elliptic  
237 flow, and other sources having reflection symmetry in the transverse plane. With the Stavinskiy method,  
238 mixed-event pairs are not used for the background ( $B(k^*)$ ); instead, same-event pseudo-pairs, formed  
239 by rotating one particle in a real pair by  $180^\circ$  in the transverse plane, are used as a background. This  
240 rotation rids the pairs of any femtoscopic correlation, while maintaining correlations due to elliptic flow  
241 (and other suitably symmetric contributors).

242 The results of correctly implementing such a procedure are shown in Figure 14. The figure shows the  
243 Stavinskiy method does a very good job of ridding the  $\Lambda K^\pm$  correlations of their non-femtoscopic back-  
244 grounds. We also see the procedure does not work as well on the  $\Lambda K_S^0$  system.

245 Now, one must be somewhat careful when applying this Stavinskiy method. We found that, in order to  
246 obtain correct results, we had to run our pseudo-pairs through the same pair cuts used in our analyses.  
247 In an ideal world, our pair cut would only remove truly bad pairs results from splitting, merging, etc. In  
248 the real world, the pair cut always throws out some of the good with the bad. For the pseudo-pairs to  
249 form a reliable background, they too must experience the pair cut, and the loss of “good” pseudo-pairs.  
250 We found this issue affected mainly our  $\Lambda K^+$  &  $\bar{\Lambda} K^-$  analysis, as can be seen in Figure 15, which shows  
251 both a correct implementation of the Stavinskiy method, and an incorrect implementation lacking the  
252 additional pair cut on the pseudo-pairs.

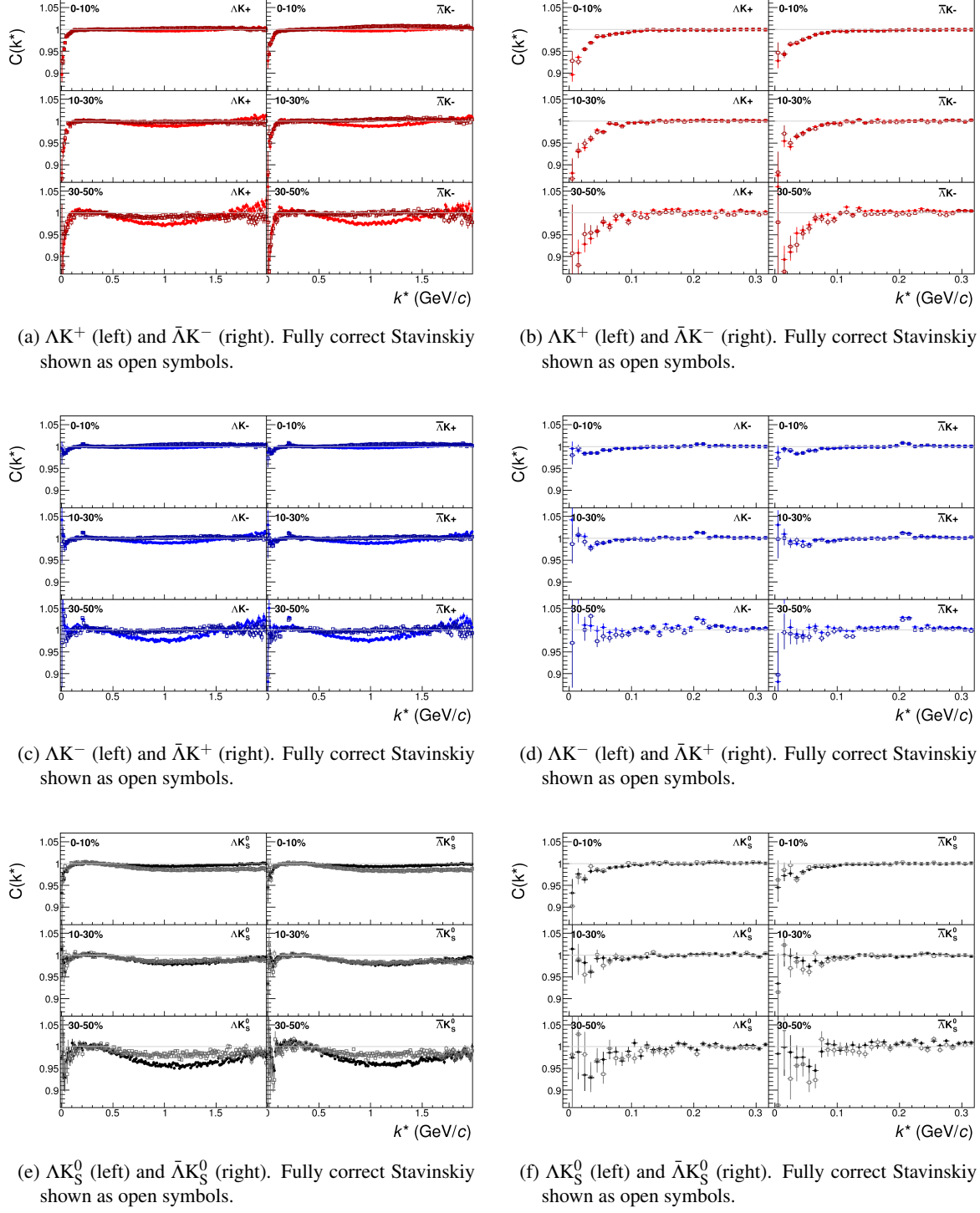


**Fig. 14:**  $\Lambda K$  and  $\bar{\Lambda} K$  correlation functions built using the fully correct Stavinskiy method for 0-10%, 10-30%, and 30-50% centralities. In the fully correct method, the pseudo-pairs (same-event pairs with one particle rotated by  $180^\circ$  in the transverse plane) are also run through the pair cuts used in the analysis (an example of an incorrect implementation is shown in Fig. 15. Closed symbols represent correlations built using the normal mixed-event background, while open symbols represent correlations formed using the Stavinskiy same-event pseudo-pairs as a background. Figures in the right column are zoomed-in versions of figures in the left column.

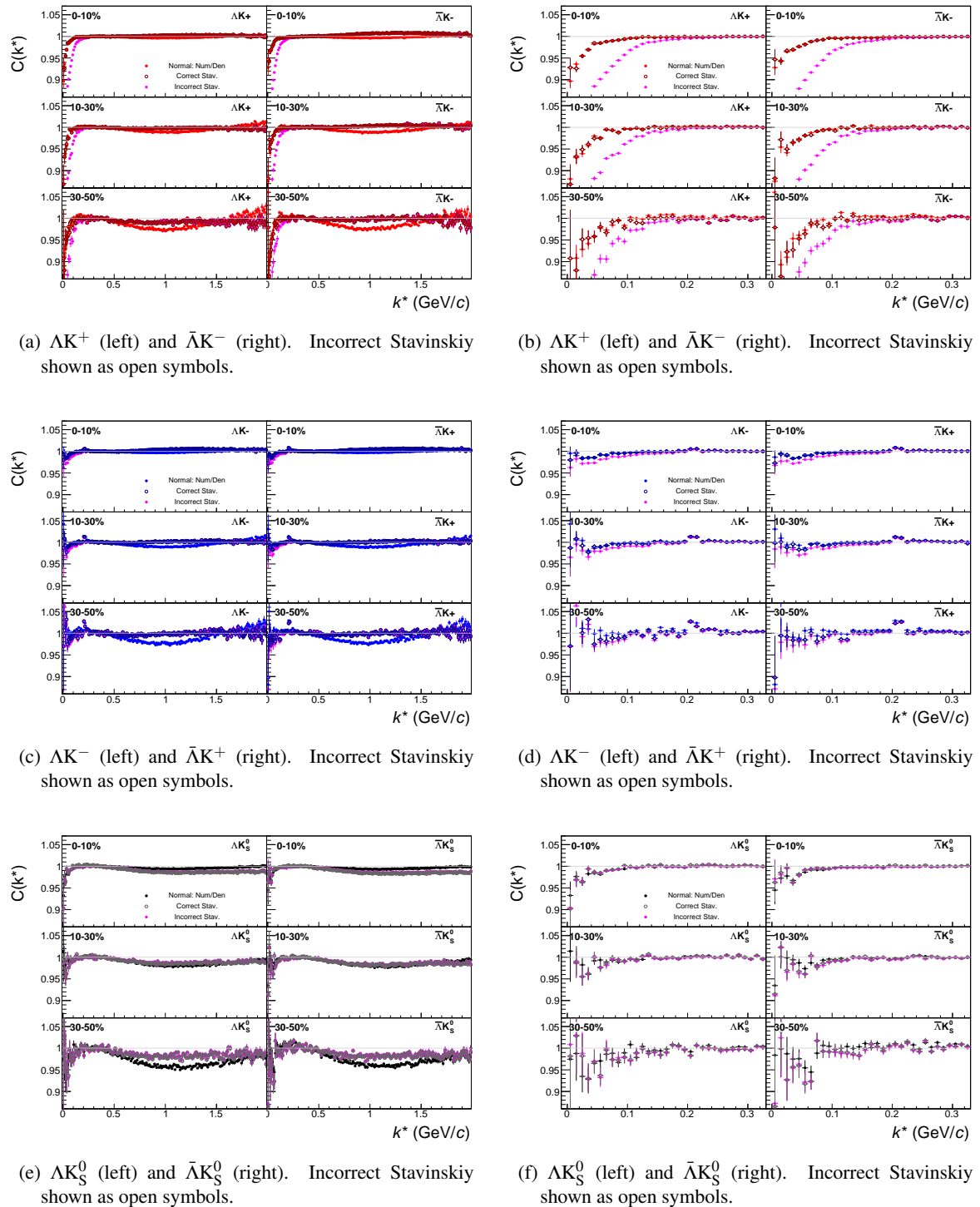


**Fig. 15:**  $\Lambda K$  and  $\bar{\Lambda}K$  correlation functions built, both correctly and incorrectly, using the Stavinskiy method for 0-10%, 10-30%, and 30-50% centralities. This figure is the same as Fig. 14, but with results from the incorrect Stavinskiy implementation shown in magenta. The closed, (red, blue, black) symbols represent correlation functions formed using the normal method with mixed-event background pairs. The open, cyan symbols represent correlation functions formed using the correct Stavinskiy method. The closed, magenta symbols represent correlation functions formed using the incorrect Stavinskiy method. In the correct method, the pseudo-pairs (same-event pairs with one particle rotated by  $180^\circ$  in the transverse plane) are also run through the pair cuts used in the analysis; in the incorrect method, they are not. Figures in the right column are zoomed-in versions of figures in the left column.

253 **5 Fitting**

254 **5.1 Model:  $\Lambda K_S^0, \Lambda K^\pm, \Xi^- K_S^0$**

255 The two-particle relative momentum correlation function may be written theoretically by the Koonin-  
256 Pratt equation [3, 4]:

$$C(\mathbf{k}^*) = \int S(\mathbf{r}^*) |\Psi_{\mathbf{k}^*}(\mathbf{r}^*)|^2 d^3 \mathbf{r}^* \quad (4)$$

257 where  $S(\mathbf{r}^*)$  is the pair source distribution,  $\Psi_{\mathbf{k}^*}(\mathbf{r}^*)$  is the two-particle wave-function, and  $k^*$  is the  
258 momentum of one particle in the pair rest frame. In the absence of Coulomb effects, and assuming a  
259 spherically Gaussian source of width  $R$ , and s-wave scattering, the 1D femtoscopic correlation function  
260 can be calculated analytically using:

$$C(k^*) = 1 + C_{QI}(k^*) + C_{FSI}(k^*) \quad (5)$$

261  $C_{QI}$  describes plane-wave quantum interference:

$$C_{QI}(k^*) = \alpha \exp(-4k^{*2}R^2) \quad (6)$$

262 where  $\alpha = (-1)^{2j}/(2j+1)$  for identical particles with spin  $j$ , and  $\alpha = 0$  for non-identical particles. For  
263 all analyses presented in this note,  $\alpha = 0$ .  $C_{FSI}$  describes the s-wave strong final state interaction between  
264 the particles:

$$\begin{aligned} C_{FSI}(k^*) &= (1 + \alpha) \left[ \frac{1}{2} \left| \frac{f(k^*)}{R} \right|^2 \left( 1 - \frac{d_0}{2\sqrt{\pi}R} \right) + \frac{2\Re f(k^*)}{\sqrt{\pi}R} F_1(2k^*R) - \frac{\Im f(k^*)}{R} F_2(2k^*R) \right] \\ f(k^*) &= \left( \frac{1}{f_0} + \frac{1}{2} d_0 k^{*2} - ik^* \right)^{-1}; \quad F_1(z) = \int_0^z \frac{e^{x^2-z^2}}{z} dx; \quad F_2(z) = \frac{1-e^{-z^2}}{z} \end{aligned} \quad (7)$$

265 where  $R$  is the source size,  $f(k^*)$  is the s-wave scattering amplitude,  $f_0$  is the complex scattering length,  
266 and  $d_0$  is the effective range of the interaction.

267 An additional parameter  $\lambda$  is typically included in the femtoscopic fit function to account for the purity  
268 of the pair sample. In the case of no residual correlations (to be discussed in Section 5.4), the fit function  
269 becomes:

$$C(k^*) = 1 + \lambda [C_{QI}(k^*) + C_{FSI}(k^*)] \quad (8)$$

270 **5.2 Model:  $\Xi^- K^\pm$**

271 The two-particle correlation function may be written as:

$$C(\mathbf{k}^*) = \sum_S \rho_S \int S(\mathbf{r}^*) |\Psi_{\mathbf{k}^*}^S(\mathbf{r}^*)|^2 d^3 \mathbf{r}^* \quad (9)$$

272 where  $\rho_S$  is the normalized emission probability of particles in a state with spin  $S$ ,  $S(\mathbf{r}^*)$  is the pair  
273 emission source distribution (assumed to be Gaussian), and  $\Psi_{\mathbf{k}^*}^S(\mathbf{r}^*)$  is the two-particle wave-function  
274 including both strong and Coulomb interactions [5]:

$$\Psi_{\mathbf{k}^*}(\mathbf{r}^*) = e^{i\delta_c} \sqrt{A_c(\eta)} [e^{i\mathbf{k}^* \cdot \mathbf{r}^*} F(-i\eta, 1, i\xi) + f_c(k^*) \frac{\tilde{G}(\rho, \eta)}{r^*}] \quad (10)$$

where  $\rho = k^* r^*$ ,  $\eta = (k^* a_c)^{-1}$ ,  $\xi = \mathbf{k}^* \cdot \mathbf{r}^* + k^* r^* \equiv \rho(1 + \cos \theta^*)$ , and  $a_c = (\mu z_1 z_2 e^2)^{-1}$  is the two-particle Bohr radius (including the sign of the interaction).  $\delta_c$  is the Coulomb s-wave phase shift,  $A_c(\eta)$  is the Coulomb penetration factor,  $\tilde{G} = \sqrt{A_c}(G_0 + iF_0)$  is a combination of the regular ( $F_0$ ) and singular ( $G_0$ ) s-wave Coulomb functions.  $f_c(k^*)$  is the s-wave scattering amplitude:

$$f_c(k^*) = \left[ \frac{1}{f_0} + \frac{1}{2} d_0 k^{*2} - \frac{2}{a_c} h(\eta) - ik^* A_c(\eta) \right]^{-1} \quad (11)$$

where, the “h-function”,  $h(\eta)$ , is expressed through the digamma function,  $\psi(z) = \Gamma'(z)/\Gamma(z)$  as:

$$h(\eta) = 0.5[\psi(i\eta) + \psi(-i\eta) - \ln(\eta^2)] \quad (12)$$

In this case, the  $\lambda$  parameter may be included as:

$$C(\mathbf{k}^*) = (1 - \lambda) + \lambda \sum_S \rho_S \int S(\mathbf{r}^*) |\Psi_{\mathbf{k}^*}^S(\mathbf{r}^*)|^2 d^3 \mathbf{r}^* \quad (13)$$

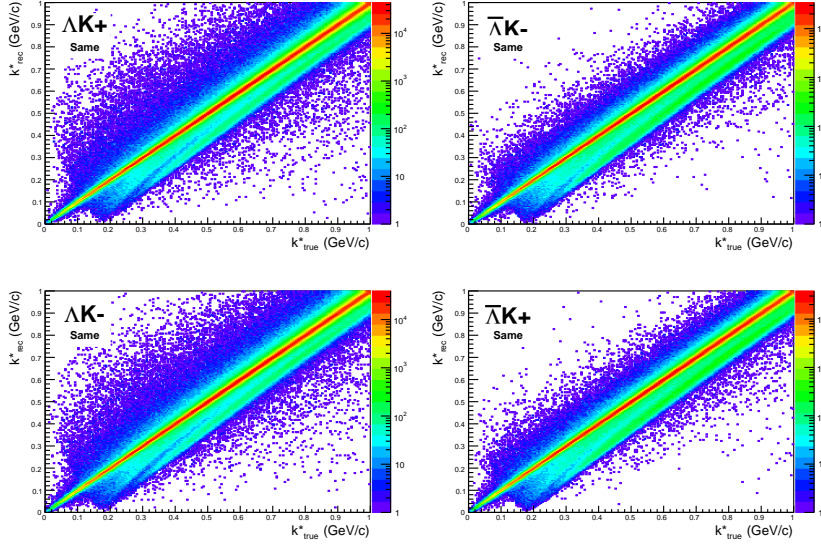
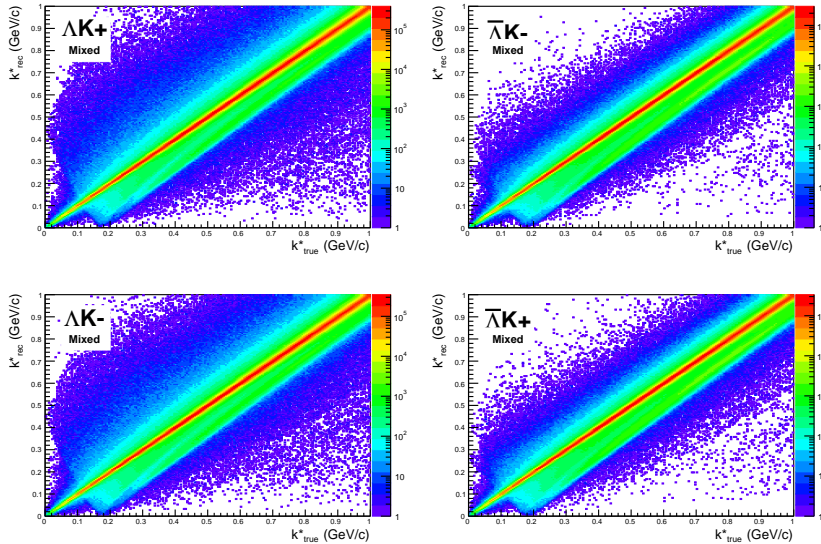
### 5.3 Momentum Resolution Corrections

Finite track momentum resolution causes the reconstructed momentum of a particle to smear around the true value. This, of course, also holds true for V0 particles. The effect is propagated up to the pairs of interest, which causes the reconstructed relative momentum ( $k_{\text{Rec}}^*$ ) to differ from the true momentum ( $k_{\text{True}}^*$ ). Smearing of the momentum typically will result in a suppression of the signal. More specifically, the smearing will broaden the signal, which would cause a decrease in the extracted radius of the system.

The effect of finite momentum resolution can be investigated using the HIJING MC data, for which both the true and reconstructed momenta are available. Figure 16 shows sample  $k_{\text{True}}^*$  vs.  $k_{\text{Rec}}^*$  plots for  $\Lambda K^\pm$  0-10% analyses; Figure 16a was generated using same-event pairs, while Figure 16b was generated using mixed-event pairs (with  $N_{\text{mix}} = 5$ ).

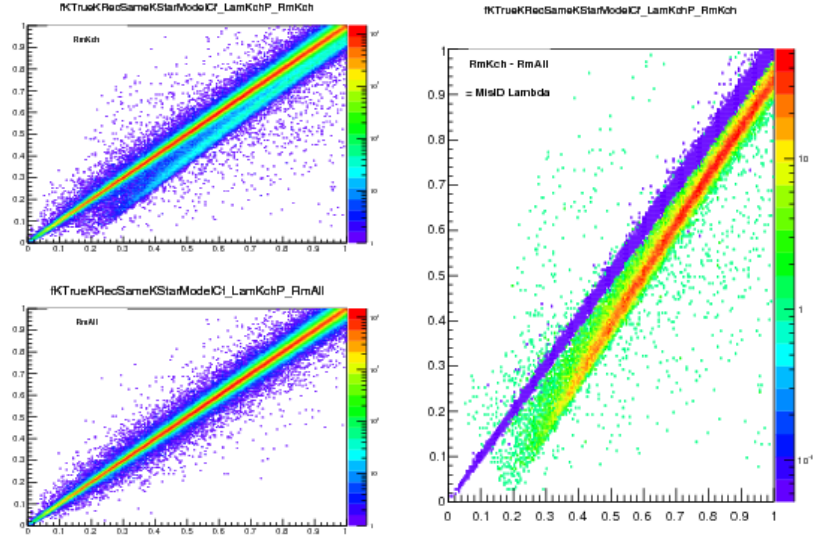
If there are no contaminations in our particle collection, the plots in Figure 16 should be smeared around  $k_{\text{True}}^* = k_{\text{Rec}}^*$ ; this is mostly true in our analyses. However, there are some interesting features of our results which demonstrate a small (notice the log-scale on the z-axis) contamination in our particle collection. The structure around  $k_{\text{Rec}}^* = k_{\text{True}}^* - 0.15 \text{ GeV}/c$  is mainly caused by  $K_S^0$  contamination in our  $\Lambda(\bar{\Lambda})$  sample. The remaining structure not distributed about  $k_{\text{Rec}}^* = k_{\text{True}}^*$  is due to  $\pi$  and  $e$  contamination in our  $K^\pm$  sample. These contaminations are more visible in Figure 17, which show  $k_{\text{Rec}}^*$  vs.  $k_{\text{True}}^*$  plots (for a small sample of the  $\Lambda K^\pm$  0-10% central analysis), for which the MC truth (i.e. true, known identity of the particle) was used to eliminate misidentified particles in the  $K^+(a)$  and  $\Lambda(b)$  collections. (NOTE: This is an old figure and is for a small sample of the data. A new version will be generated shortly. It, nonetheless, demonstrates the point well).

Information gained from looking at  $k_{\text{Rec}}^*$  vs  $k_{\text{true}}$  can be used to apply corrections to account for the effects of finite momentum resolution on the correlation functions. A typical method (“Ratio” method) involves using the MC HIJING data to build two correlation functions,  $C_{\text{Rec}}(k^*)$  and  $C_{\text{True}}(k^*)$ , using the generator-level momentum ( $k_{\text{True}}^*$ ) and the measured detector-level momentum ( $k_{\text{Rec}}^*$ ). The data is then corrected by multiplying by the ratio,  $C_{\text{True}}/C_{\text{Rec}}$ , before fitting. This essentially unsmears the data, which then can be compared directly to theoretical predictions and fits. Although this is conceptually simple, there are a couple of big disadvantages to this method. First, HIJING does not incorporate final-state interactions, so weights must be used when building same-event (numerator) distributions. These weights account for the interactions, and, in the absence of Coulomb interactions, can be calculated using Eq. 5. Of course, these weights are valid only for a particular set of fit parameters. Therefore, in the fitting process, during which the fitter explores a large parameter set, the corrections will not remain valid. As

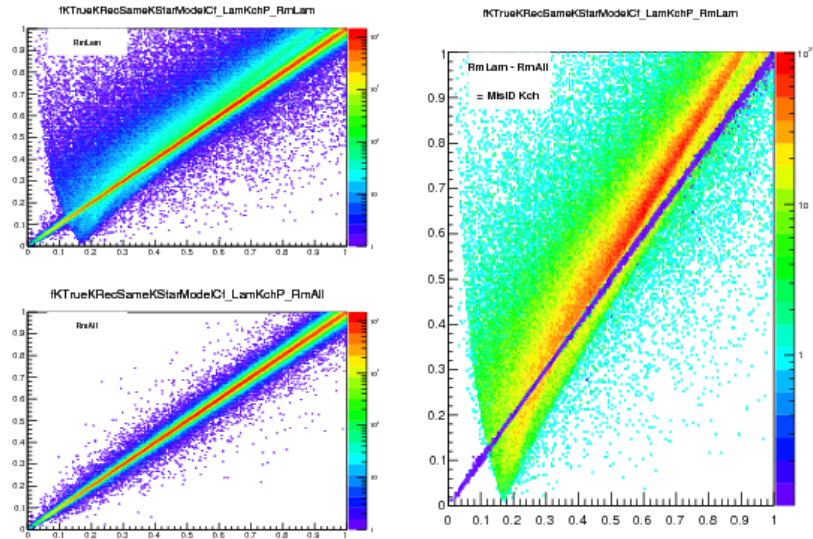
(a) Same Event Pairs ( $\Lambda K^\pm$ , 0-10% Centrality)(b) Mixed Event Pairs ( $\Lambda K^\pm$ , 0-10% Centrality)

**Fig. 16:** Sample  $k^*_{\text{True}}$  vs.  $k^*_{\text{Rec}}$  plots from MC HIJING events for  $\Lambda K^\pm$  0-10% analyses. The structure which appears around  $k^*_{\text{Rec}} = k^*_{\text{True}} - 0.15 \text{ GeV}/c$  is mainly caused by  $K_S^0$  contamination in our  $\Lambda(\bar{\Lambda})$  sample. The remaining structure not distributed about  $k^*_{\text{Rec}} = k^*_{\text{True}}$  is due to  $\pi$  and  $e$  contamination in our  $K^\pm$  sample. These contaminations are more clearly visible in Figure 17

such, applying the momentum resolution correction and fitting becomes a long and drawn out iterative process. An initial parameter set is obtained (through fitting without momentum resolution corrections, theoretical models, or a good guess), then the MC data is analyzed to obtain correlation functions needed to calculate the correction factor, the data is fit using the correction factor, a refined parameter set is extracted, the MC data is analyzed again to obtain the new correction factor, etc. This process continues until the parameter set stabilizes. The second issue concerns statistics. With the MC data available on the grid, we were not able to generate the statistics necessary to use the raw  $C_{\text{True}}/C_{\text{Rec}}$  ratio. The ratio was not stable, and when applied to the data, obscured the signal. Attempting to fit the ratio to use to generate the corrections also proved problematic. However, as HIJING does not include final-state interactions, the same-event and mixed-event pairs are very similar (with the exception of things like



(a) (Top Left) All misidentified  $K^+$  excluded. (Bottom Left) All misidentified  $\Lambda$  and  $K^+$  excluded. (Right) The difference of (Top Left) - (Bottom Left), which reveals the contamination in our  $\Lambda$  collection. The structure which appears around  $k_{\text{Rec}}^* = k_{\text{True}}^* - 0.15 \text{ GeV}/c$  is mainly caused by  $K_S^0$  contamination in our  $\Lambda(\bar{\Lambda})$  sample.



(b) (Top Left) All misidentified  $\Lambda$  excluded. (Bottom Left) All misidentified  $\Lambda$  and  $K^-$  excluded. (Right) The difference of (Top Left) - (Bottom Left), which reveals the contamination in our  $K^-$  collection. The structure not distributed about  $k_{\text{Rec}}^* = k_{\text{True}}^*$  is due to  $\pi$  and  $e^-$  contamination in our  $K^\pm$  sample.

**Fig. 17:** In the figure, the y-axis =  $k_{\text{Rec}}^*$ , and the x-axis =  $k_{\text{True}}^*$ . (Left)  $k_{\text{Rec}}^*$  vs.  $k_{\text{True}}^*$  plots for a small sample of the  $\Lambda K^+$  0-10% central analysis, MC truth was used to eliminate misidentified particles in the  $K^+$  (a) and  $\Lambda$  (b) collections. (Right) The difference of the top left and bottom left plots. Contaminations in our particle collections are clearly visible. Figure (a) demonstrates a  $K_S^0$  contamination in our  $\Lambda$  collection; Figure (b) demonstrates a  $\pi$  and  $e^-$  contamination in our  $K^\pm$  collection.

322 energy and momentum conservation, etc). Therefore, one may build the numerator distribution using  
 323 mixed-event pairs. This corresponds, more or less, to simply running the weight generator through the  
 324 detector framework.

325 A second approach (“Matrix” method) is to use information gained from plots like those in Figure 16,

which can be considered response matrices. The response matrix describes quantitatively how each  $k_{\text{Rec}}^*$  bin receives contributions from multiple  $k_{\text{True}}^*$  bins, and can be used to account for the effects of finite momentum resolution. With this approach, the resolution correction is applied on-the-fly during the fitting process by propagating the theoretical correlation function (fit) through the response matrix, according to:

$$C_{\text{Fit}}(k_{\text{Rec}}^*) = \frac{\sum_{k_{\text{True}}^*} M_{k_{\text{Rec}}^*, k_{\text{True}}^*} C_{\text{Fit}}(k_{\text{True}}^*)}{\sum_{k_{\text{True}}^*} M_{k_{\text{Rec}}^*, k_{\text{True}}^*}} \quad (14)$$

where  $M_{k_{\text{Rec}}^*, k_{\text{True}}^*}$  is the response matrix (Figure 16),  $C_{\text{Fit}}(k_{\text{True}}^*)$  is the fit binned in  $k_{\text{True}}^*$ , and the denominator normalizes the result.

Equation 14 describes that, for a given  $k_{\text{Rec}}^*$  bin, the observed value of  $C(k_{\text{Rec}}^*)$  is a weighted average of all  $C(k_{\text{True}}^*)$  values, where the weights are the normalized number of counts in the  $[k_{\text{Rec}}^*, k_{\text{True}}^*]$  bin. As seen in Figure 16, overwhelmingly the main contributions comes from the  $k_{\text{Rec}}^* = k_{\text{True}}^*$  bins. Although the correction is small, it is non-negligible for the low- $k^*$  region of the correlation function.

Here, the momentum resolution correction is applied to the fit, not the data. In other words, during fitting, the theoretical correlation function is smeared just as real data would be, instead of unsmeareding the data. This may not be ideal for the theorist attempting to compare a model to experimental data, but it leaves the experimental data unadulterated. The current analyses use this second approach to applying momentum resolution corrections because of two major advantages. First, the MC data must be analyzed only once, and no assumptions about the fit are needed. Secondly, the momentum resolution correction is applied on-the-fly by the fitter, delegating the iterative process to a computer instead of the user.

The two methods described above, Ratio and Matrix, should reproduce the same results at the parameter set used to generate the  $C_{\text{True}}/C_{\text{Rec}}$  needed for the Ratio method. Figure 18 shows that the two methods converge as the binning size is decreased.

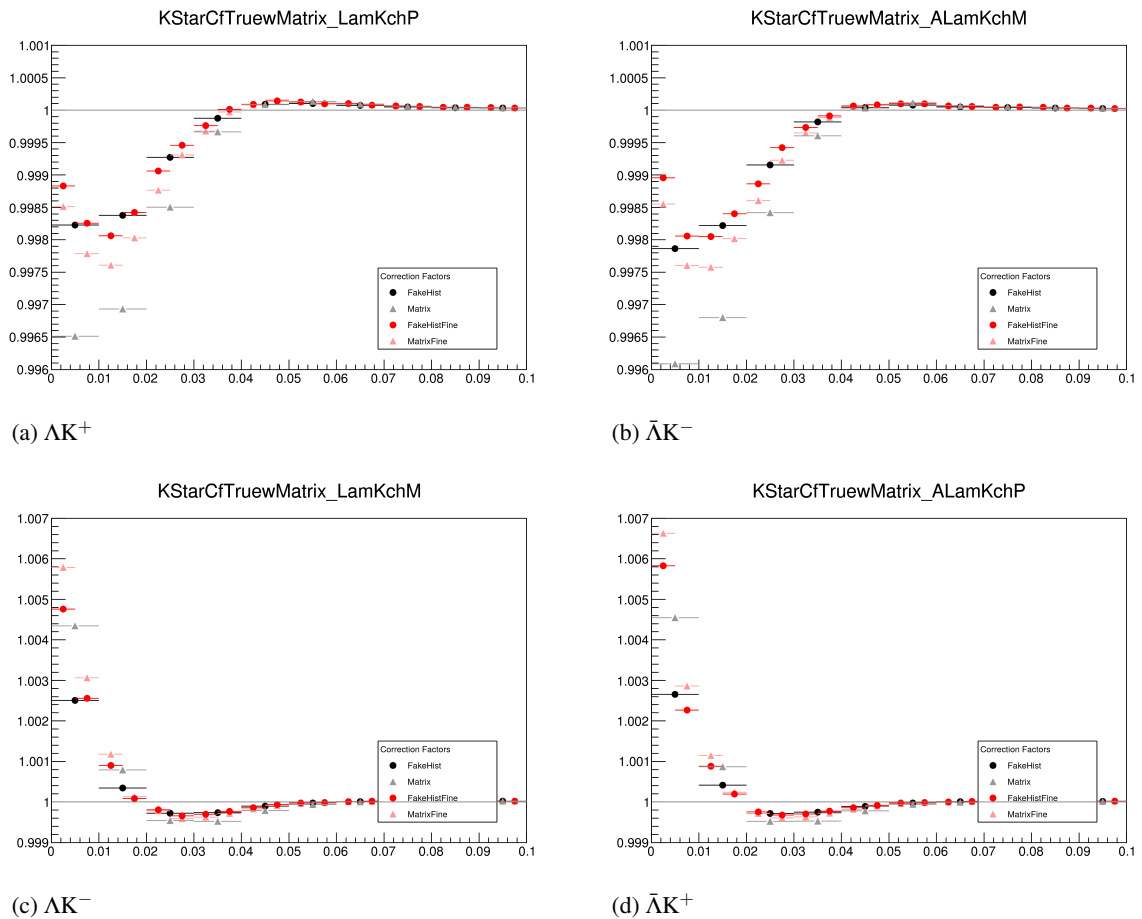


**Fig. 18:** Comparison of the two methods, Ratio and Matrix, for accounting for momentum resolution effects with HIJING. The Ratio method corresponds to the “FakeHist” histograms (circles), while the Matrix method corresponds to the “Matrix” histograms (triangles). Black shows a course binning, while red shows a finer binning.

347 **5.4 Residual Correlations**

348 The purpose of this analysis is to study both the interaction, and the scale of the emitting source, of  
 349 the pairs. In order to obtain correct results, it is important for our particle collections to consist of  
 350 primary particles. In practice, this is difficult to achieve for our  $\Lambda$  and  $\bar{\Lambda}$  collections. Many of our  $\Lambda$   
 351 particles are not primary, but originate as decay products from other hyperons, including  $\Sigma^0$ ,  $\Xi^0$ ,  $\Xi^-$  and  
 352  $\Sigma^{*(+,-,0)}(1385)$ . Additionally, many of our K particles are not primary, but decay from  $K^{*(+,-,0)}(892)$   
 353 parents. In these decays, the daughter  $\Lambda$  or  $K_S^0$  carries away a momentum very similar to that of its parent.  
 354 As a result, the correlation function between a secondary  $\Lambda$  and, for instance, a  $K^+$  will be sensitive to,  
 355 and dependent upon, the interaction between the parent of the  $\Lambda$  and the  $K^+$ . In effect, the correlation  
 356 between the parent of the  $\Lambda$  and the  $K^+$  (ex.  $\Sigma^0 K^+$ ) will be visible, although smeared out, in the  $\Lambda K^+$   
 357 data; we call this a residual correlation resulting from feed-down. The contributions from the primary  
 358 correlation, residual correlations, and fake pairs on the finally measure data is shown schematically in  
 359 Figure 19. Residual correlations are important in an analysis when three criteria are met [6]: i) the parent  
 360 correlation signal is large, ii) a large fraction of pairs in the sample originate from the particular parent  
 361 system, and iii) the decay momenta are comparable to the expected correlation width in  $k^*$ .

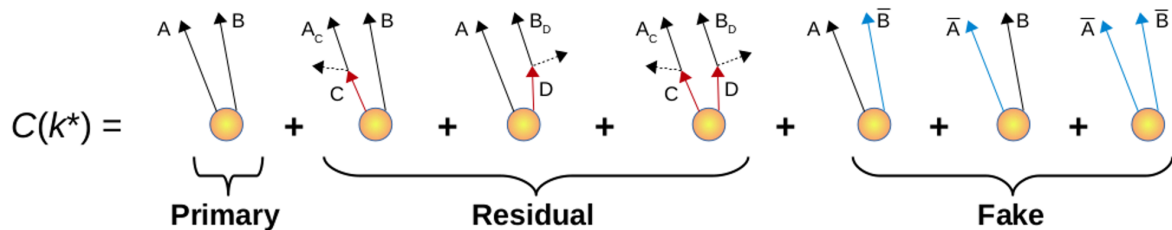


Fig. 19: A schematic representation of the contributions to the finally measured data from the primary correlation, residual correlations, and fake pairs.

362 As it is difficult for us to eliminate these residual correlations in our analyses, we must attempt to account  
 363 for them in our fit. To achieve this, we will simultaneously fit the data for both the primary correlation  
 364 function and the residual correlations. For example, in the simple case of a  $\Lambda K^+$  analysis with residuals  
 365 arising solely from  $\Sigma^0 K^+$  feed-down:

$$C_{measured}(k_{\Lambda K^+}^*) = 1 + \lambda_{\Lambda K^+}[C_{\Lambda K^+}(k_{\Lambda K^+}^*) - 1] + \lambda_{\Sigma^0 K^+}[C_{\Sigma^0 K^+}(k_{\Lambda K^+}^*) - 1]$$

$$C_{\Sigma^0 K^+}(k_{\Lambda K^+}^*) \equiv \frac{\sum_{k_{\Sigma^0 K^+}^*} C_{\Sigma^0 K^+}(k_{\Sigma^0 K^+}^*) T(k_{\Sigma^0 K^+}^*, k_{\Lambda K^+}^*)}{\sum_{k_{\Sigma^0 K^+}^*} T(k_{\Sigma^0 K^+}^*, k_{\Lambda K^+}^*)} \quad (15)$$

366  $C_{\Sigma^0 K^+}(k_{\Sigma^0 K^+}^*)$  is the  $\Sigma^0 K^+$  correlation function from, for instance, Equation 5, and  $T$  is the transform  
 367 matrix generated with THERMINATOR. The transform matrix is formed for a given parent pair, AB,  
 368 by taking all  $\Lambda K$  pairs originating from AB, calculating the relative momentum of the parents ( $k_{AB}^*$ )  
 369 and daughters ( $k_{\Lambda K}^*$ ), and filling a two-dimensional histogram with the values. The transform matrix  
 370 is essentially an unnormalized probability distribution mapping the  $k^*$  of the parent pair to that of the  
 371 daughter pair when one or both parents decay. An example of such transform matrices can be found in  
 372 Figures 20 and 21.

373 The above equation can be easily extended to include feed-down from more sources:

$$\begin{aligned}
C_{measured}(k_{\Lambda K}^*) &= 1 + \lambda_{\Lambda K}[C_{\Lambda K}(k_{\Lambda K}^*) - 1] + \lambda_{\Sigma^0 K}[C_{\Sigma^0 K}(k_{\Lambda K}^*) - 1] + \dots \\
&\quad + \lambda_{P_1 P_2}[C_{P_1 P_2}(k_{\Lambda K}^*) - 1] + \lambda_{other}[C_{other}(k_{\Lambda K}^*) - 1]
\end{aligned}
\tag{16}$$

$$C_{P_1 P_2}(k_{\Lambda K}^*) \equiv \frac{\sum_{k_{P_1 P_2}^*} C_{P_1 P_2}(k_{P_1 P_2}^*) T(k_{P_1 P_2}^*, k_{\Lambda K}^*)}{\sum_{k_{P_1 P_2}^*} T(k_{P_1 P_2}^*, k_{\Lambda K}^*)}$$

<sup>374</sup> Or, more compactly:

$$C_{measured}(k_{\Lambda K}^*) = 1 + \sum_i \lambda_i [C_i(k_{\Lambda K}^*) - 1] \tag{17}$$

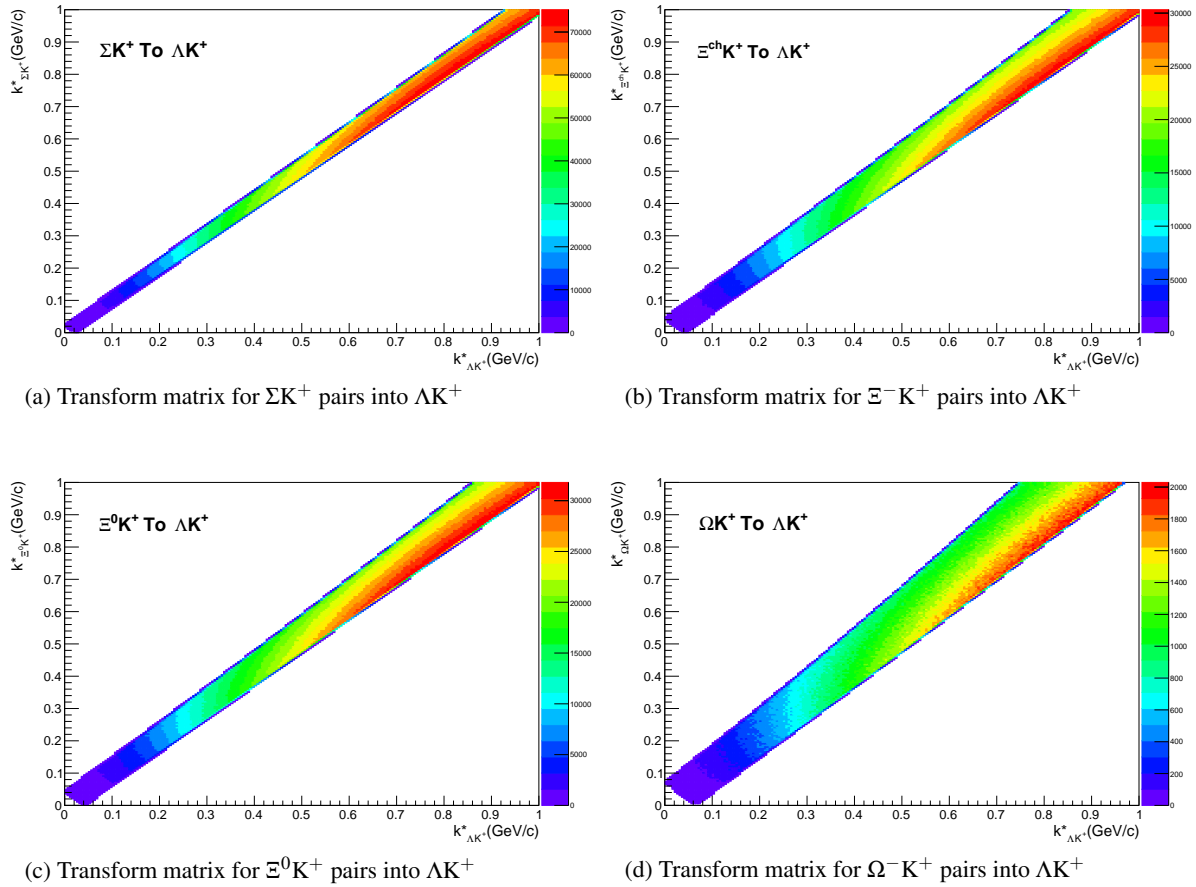


**Fig. 20:** Sample Transform Matrices generated with THERMINATOR for  $\Lambda K^+$  Analysis

<sup>375</sup> So, in practice, we model the correlation function of the parents (ex.  $\Sigma^0 K^+$ ), and run the correlation  
<sup>376</sup> function through the appropriate transform matrix to determine the contribution to the daughter correla-  
<sup>377</sup> tion function (ex.  $\Lambda K^+$ ). A few questions still remain. First, what  $\lambda$  values should be used in the above  
<sup>378</sup> equation? One option would be to leave all of these  $\lambda$ -parameters free during the fit process. However,  
<sup>379</sup> this would introduce a huge number of new parameters into the fitter, and would make the fit results less  
<sup>380</sup> trustworthy. The  $\lambda$  parameters roughly dictate the strength of the parent contribution to the daughter pair.  
<sup>381</sup> Additionally, as found in [7], the reconstruction efficiency for primary  $\Lambda$  particles is nearly equal to that  
<sup>382</sup> of  $\Lambda$  particles originating from  $\Sigma$ ,  $\Sigma^*$ ,  $\Xi^0$ ,  $\Xi^-$ , and  $\Omega$  hyperons. Therefore, the  $\lambda$  parameter for parent

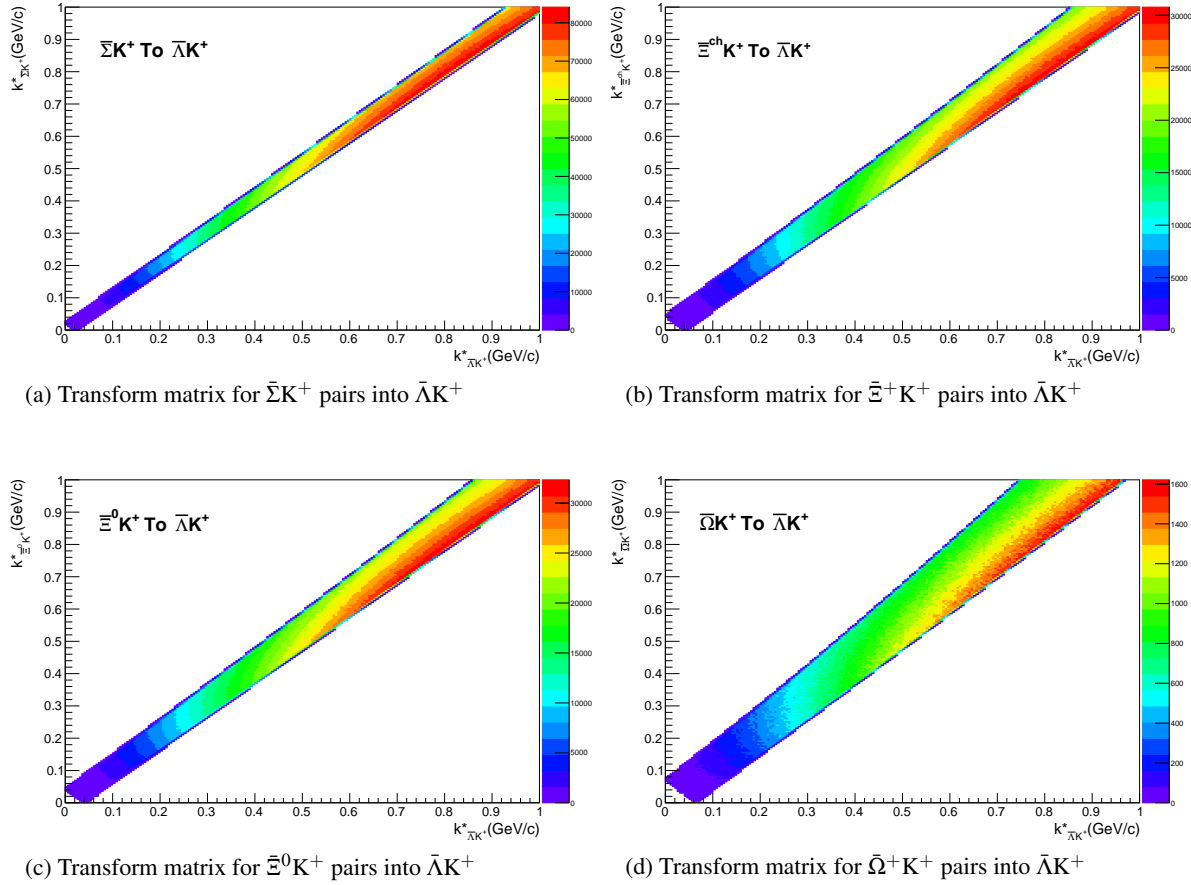


**Fig. 21:** Sample Transform Matrices generated with THERMINATOR for  $\bar{\Lambda}K^+$  Analysis

383 system AB can be estimated as the total number of  $\Lambda K$  pairs in our experimental sample originating from  
 384 AB ( $N_{AB}$ ) divided by the total number of  $\Lambda K$  pairs ( $N_{Total}$ ):

$$\lambda_{AB} = \frac{N_{AB}}{N_{Total}} \quad (18)$$

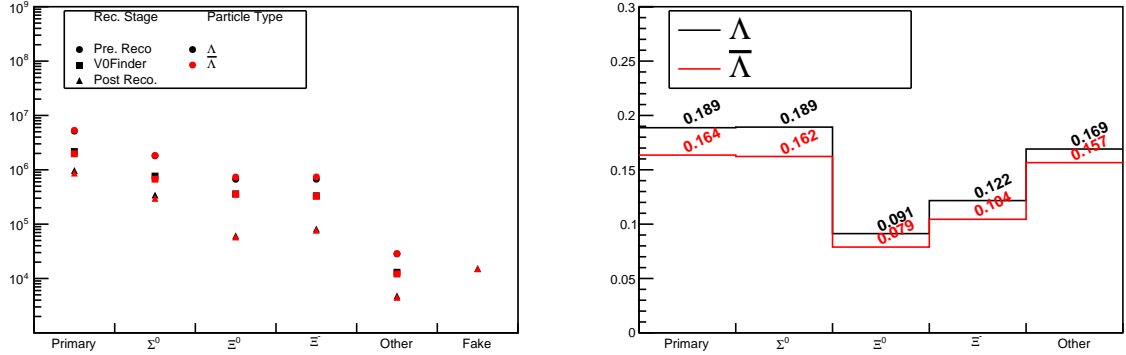
385 The particle yields can be estimated using THERMINATOR simulation, while the reconstruction effi-  
 386 ciencies ( $RE_{AB}$ ) are estimated with MC HIJING data (Fig. 22), which has been run through GEANT to  
 387 simulate the detector response. Thus, the  $\lambda$  parameters are estimated as:

$$\lambda_{AB} = \frac{N_{AB}}{N_{Total}} = \frac{N_{AB}^{THERM} RE_{AB}^{HIJING}}{\sum_{ij} N_{ij}^{THERM} RE_{ij}^{HIJING}} \quad (19)$$

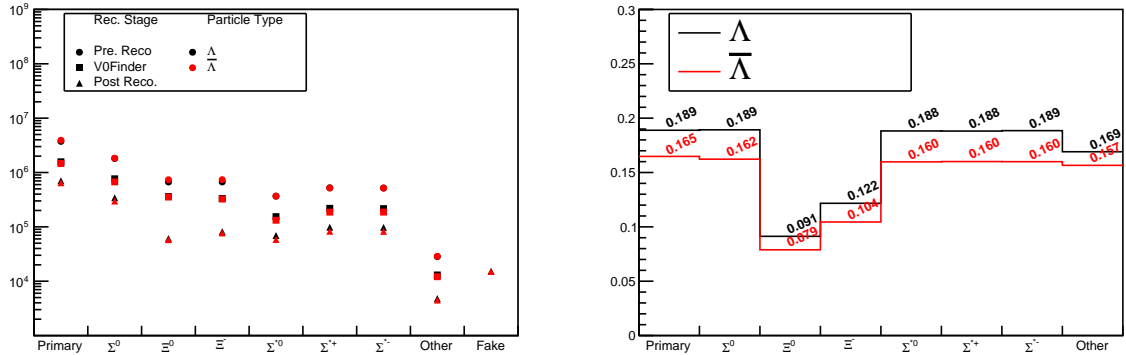
388 Note, for our study, when including three residual contributors, we consider a particle to be primary if  
 389 its parent has a proper decay length of  $c\tau < 10$  fm. When including ten residual contributors, we must  
 390 reduce this number to  $c\tau < 4$  fm for consistency. Moving to ten contributors, we introduce feed-down  
 391 from  $\Sigma^*$  and  $K^*$  resonances, with proper decay lengths of  $c\tau \approx 5$  fm and  $c\tau \approx 4$  fm, respectively. As  
 392 these are considered non-primary for the case of ten contributors, so must any resonance with  $c\tau > 4$  fm.

393 The  $\lambda$  values used can be found in Table 5, for the case of both three and ten residual contributors. In the  
 394 table, we also list the  $\lambda$  values used for “Other” and “Fakes”. The “Other” category contains pairs which  
 395 are not primary, and which do not originate from the (3 or 10) residual pairs included in the fit. The

396 “Fakes” category represents pairs that are mistakenly identified as  $\Lambda$ . To estimate this  $\lambda_{\text{Fakes}}$  value, we  
 397 assumed that the number of fake pairs was equal to the total number of pairs multiplied by the  $\Lambda$  purity  
 398 (i.e. assuming perfect purity for the kaons); or, more simply,  $\lambda_{\text{Fakes}} = 1.0 - \text{Purity}(\Lambda)$ . For both of these  
 399 contributors (“Other” and “Fakes”), we assume that these correlations average to unity, and therefore do  
 400 not contribute to the final correlation function.



(a) Reconstruction Efficiencies (3 Residuals)



(b) Reconstruction Efficiencies (10 Residuals)

**Fig. 22:** Reconstruction Efficiencies

$\Lambda K^+$ residuals		$\bar{\Lambda}K^-$ residuals		$\Lambda K^-$ residuals		$\bar{\Lambda}K^+$ residuals		$\Lambda K_S^0$ residuals		$\bar{\Lambda}K_S^0$ residuals	
Pair System	$\lambda$ value	Pair System	$\lambda$ value	Pair System	$\lambda$ value	Pair System	$\lambda$ value	Pair System	$\lambda$ value	Pair System	$\lambda$ value
3 Residuals (Max Parent $c\tau_{\text{decay}} = 10$ fm)											
$\Lambda K^+$	0.527	$\bar{\Lambda}K^-$	0.526	$\Lambda K^-$	0.526	$\bar{\Lambda}K^+$	0.527	$\Lambda K_S^0$	0.543	$\bar{\Lambda}K_S^0$	0.544
$\Sigma^0 K^+$	0.111	$\bar{\Sigma}^0 K^-$	0.110	$\Sigma^0 K^-$	0.110	$\bar{\Sigma}^0 K^+$	0.111	$\Sigma^0 K_S^0$	0.120	$\bar{\Sigma}^0 K_S^0$	0.120
$\Xi^0 K^+$	0.039	$\bar{\Xi}^0 K^-$	0.035	$\Xi^0 K^-$	0.038	$\bar{\Xi}^0 K^+$	0.036	$\Xi^0 K_S^0$	0.042	$\bar{\Xi}^0 K_S^0$	0.039
$\Xi^- K^+$	0.050	$\bar{\Xi}^+ K^-$	0.046	$\Xi^- K^-$	0.050	$\bar{\Xi}^+ K^+$	0.046	$\Xi^- K_S^0$	0.054	$\bar{\Xi}^+ K_S^0$	0.050
Other	0.226	Other	0.235	Other	0.228	Other	0.233	Other	0.194	Other	0.199
Fakes	0.048	Fakes	0.048	Fakes	0.048	Fakes	0.048	Fakes	0.048	Fakes	0.048
10 Residuals (Max Parent $c\tau_{\text{decay}} = 4$ fm)											
$\Lambda K^+$	0.180	$\bar{\Lambda}K^-$	0.180	$\Lambda K^-$	0.179	$\bar{\Lambda}K^+$	0.181	$\Lambda K_S^0$	0.192	$\bar{\Lambda}K_S^0$	0.193
$\Sigma^0 K^+$	0.116	$\bar{\Sigma}^0 K^-$	0.114	$\Sigma^0 K^-$	0.115	$\bar{\Sigma}^0 K^+$	0.116	$\Sigma^0 K_S^0$	0.125	$\bar{\Sigma}^0 K_S^0$	0.124
$\Xi^0 K^+$	0.040	$\bar{\Xi}^0 K^-$	0.037	$\Xi^0 K^-$	0.040	$\bar{\Xi}^0 K^+$	0.037	$\Xi^0 K_S^0$	0.043	$\bar{\Xi}^0 K_S^0$	0.040
$\Xi^- K^+$	0.052	$\bar{\Xi}^+ K^-$	0.047	$\Xi^- K^-$	0.052	$\bar{\Xi}^+ K^+$	0.048	$\Xi^- K_S^0$	0.056	$\bar{\Xi}^+ K_S^0$	0.052
$\Sigma^{*+} K^+$	0.054	$\bar{\Sigma}^{*-} K^-$	0.051	$\Sigma^{*+} K^-$	0.053	$\bar{\Sigma}^{*-} K^+$	0.051	$\Sigma^{*+} K_S^0$	0.058	$\bar{\Sigma}^{*-} K_S^0$	0.055
$\Sigma^{*-} K^+$	0.048	$\bar{\Sigma}^{*+} K^-$	0.050	$\Sigma^{*-} K^-$	0.048	$\bar{\Sigma}^{*+} K^+$	0.050	$\Sigma^{*-} K_S^0$	0.052	$\bar{\Sigma}^{*+} K_S^0$	0.054
$\Sigma^{*0} K^+$	0.048	$\bar{\Sigma}^{*0} K^-$	0.045	$\Sigma^{*0} K^-$	0.048	$\bar{\Sigma}^{*0} K^+$	0.045	$\Sigma^{*0} K_S^0$	0.052	$\bar{\Sigma}^{*0} K_S^0$	0.048
$\Lambda K^{*0}$	0.046	$\bar{\Lambda}K^{*0}$	0.047	$\Lambda \bar{K}^{*0}$	0.046	$\bar{\Lambda}K^{*0}$	0.047	$\Lambda K^{*0}$	0.022	$\bar{\Lambda}K^{*0}$	0.022
$\Sigma^0 K^{*0}$	0.041	$\bar{\Sigma}^0 \bar{K}^{*0}$	0.041	$\Sigma^0 \bar{K}^{*0}$	0.041	$\bar{\Sigma}^0 K^{*0}$	0.041	$\Sigma^0 K^{*0}$	0.019	$\bar{\Sigma}^0 K^{*0}$	0.019
$\Xi^0 K^{*0}$	0.014	$\bar{\Xi}^0 \bar{K}^{*0}$	0.013	$\Xi^0 \bar{K}^{*0}$	0.014	$\bar{\Xi}^0 K^{*0}$	0.013	$\Xi^0 K^{*0}$	0.007	$\bar{\Xi}^0 K^{*0}$	0.006
$\Xi^- K^{*0}$	0.018	$\bar{\Xi}^+ \bar{K}^{*0}$	0.017	$\Xi^- \bar{K}^{*0}$	0.018	$\bar{\Xi}^+ K^{*0}$	0.017	$\Xi^- K^{*0}$	0.009	$\bar{\Xi}^+ K^{*0}$	0.008
Other	0.295	Other	0.310	Other	0.299	Other	0.307	Other	0.318	Other	0.330
Fakes	0.048	Fakes	0.048	Fakes	0.048	Fakes	0.048	Fakes	0.048	Fakes	0.048

**Table 5:**  $\lambda$  values for the individual components of the  $\Lambda K$  correlation functions for the case of 3 and 10 residual contributions.

401 Now, the remaining question is how do we model the parent correlation functions? In an ideal world, we  
 402 would simply look up the parent interaction in some table, and input this into our Lednicky equation (for  
 403 the case of one or more charge neutral particle in the pair), or run it through the CoulombFitter machinery  
 404 described in Sec.5.2. Unfortunately, the world in which we live is not perfect, such a table does not exists,  
 405 and little is know about the interaction between the residual pairs in this study. One solution would be  
 406 to introduce a set of scattering parameters and radii for each residual system. However, as was the case  
 407 of the  $\lambda$ -parameters above, this would introduce a large number of additional fit parameters, and would  
 408 make our fitter too unconstrained and would yield untrustworthy results. The second option, which is  
 409 adopted in this analysis, is to assume all residual pairs have the same source size as the daughter pair,  
 410 and all Coulomb-neutral residual pairs also share the same scattering parameters as the daughter pair (the  
 411 case of charged pairs, such as  $\Xi^- K^\pm$  or  $\Sigma^{*\pm} K^\pm$ , will be described below).

412 Concerning the radii of the residual parent pairs, it was suggested that these should be set to smaller  
 413 values than those of the daughter pair. In the interest of minimizing the number of parameters in the  
 414 fitter, we tested this by introducing an  $m_T$ -scaling of the parents' radii. The motivation for this scaling  
 415 comes from the approximate  $m_T$ -scaling of the radii observed in 31. To achieve this scaling, we assume  
 416 the radii follow an inverse-square-root distribution:  $R_{AB} = \alpha m_T^{-1/2}$ . Then, it follows that we should scale  
 417 the parent radii as:

$$R_{AB} = R_{\Lambda K} \left( \frac{m_{T,AB}}{m_{T,\Lambda K}} \right)^{-1/2} \quad (20)$$

418 The values of  $m_T$  for each pair system were taken from THERMINATOR. As the fitter dances around  
 419 parameter space and selects a new radius for the  $\Lambda K$  system, the radii of the residuals is simply the  $\Lambda K$   
 420 radius scaled by the appropriate factor, given above (Eq.20). In the end, this scaling factor made no  
 421 significant difference in our fit results, so this complication is excluded from our final results. Note that  
 422 this is not surprising, as the most extreme scaling factor was, in the case of using 10 residual systems,  
 423 between  $\Lambda K^+$  with  $m_{T,\Lambda K^+} \approx 1.4 \text{ GeV}/c^2$  and  $\Xi^- K^{*0}$  with  $m_{T,\Xi^- K^{*0}} \approx 1.8 \text{ GeV}/c^2$ , resulting in a scale  
 424 factor of  $\approx 0.9$ .

425 Now, as hinted above, accounting for charged residuals adds a complication in that they necessitate the  
 426 inclusion of the CoulombFitter (described in Sec. 5.7) into the process. The complication of combining  
 427 the two fitters is not troubling; however, the substantial increase in the fitting time is (the parallelization  
 428 of the CoulombFitter across a large number of GPU cores, to drastically decrease run-time, is currently  
 429 underway). We have two solutions to bypass such a large increase in run time. First, we can use our  
 430 experimental  $\Xi^{ch} K^{ch}$  data to represent all charged parent pair system. In this case, there is no need to  
 431 make any assumption about scattering parameters or source sizes, as we already have the experimental  
 432 data. The downside is that, especially in the 30-50% centrality bin, the statistics are low and error bars  
 433 large. Alternatively, we can assume the strong interaction is negligible in the charged residual, and  
 434 generate the parent correlation function given radius and  $\lambda$  parameters. We find in our  $\Xi^{ch} K^{ch}$  study  
 435 that a Coulomb-only description of the system describes, reasonably well, the broad features of the  
 436 correlation. The strong interaction is necessary for the fine details. However, as these correlations are  
 437 run through a transform matrix, which largely flattens out and fine details, a Coulomb-only description  
 438 should be sufficient. In practice, this Coulomb-only scenario is achieved by first building a large number  
 439 of Coulomb-only correlations for various radii and  $\lambda$  parameter values, and interpolating from this grid  
 440 during the fitting process. We find consistent results between using the  $\Xi K$  data and the Coulomb-only  
 441 interpolation method. When quantifying the  $\Xi^- K^\pm$  residual contribution, the experimental  $\Xi^- K^\pm$  data  
 442 is always used. When the number of residual pairs used is increased to 10, so that contributors such  
 443 as  $\Sigma^{*+} K^-$  enter the picture, the Coulomb-only interpolation method is used. In other words, the  $\Xi K$   
 444 experimental data is only used to model the  $\Xi K$  residual contribution, all other charged pairs are treated  
 445 with the Coulomb-only interpolation method.

446 Two examples of how very different transform matrices can alter a correlation function are shown in  
 447 Figures 23 and 24 below. These figures were taken using parameter values obtained from fits to the data.  
 448 In the top left corner of the figures, the input correlation function (closed symbols) is shown together  
 449 with the output, transformed, correlation function (open symbols). In the bottom left, the transformed  
 450 correlation is shown by itself (with zoomed y-axis). This is especially helpful when the  $\lambda$  parameter is  
 451 very small, in which case the contribution in the top left can look flat, but the zoomed in view in the  
 452 bottom left shows the structure. The right two plots in each figure show the transform matrix without  
 453 (top right) and with (bottom right) a log-scale on the z-axis. Note, more examples of these transforms  
 454 can be found in Sec. 9.

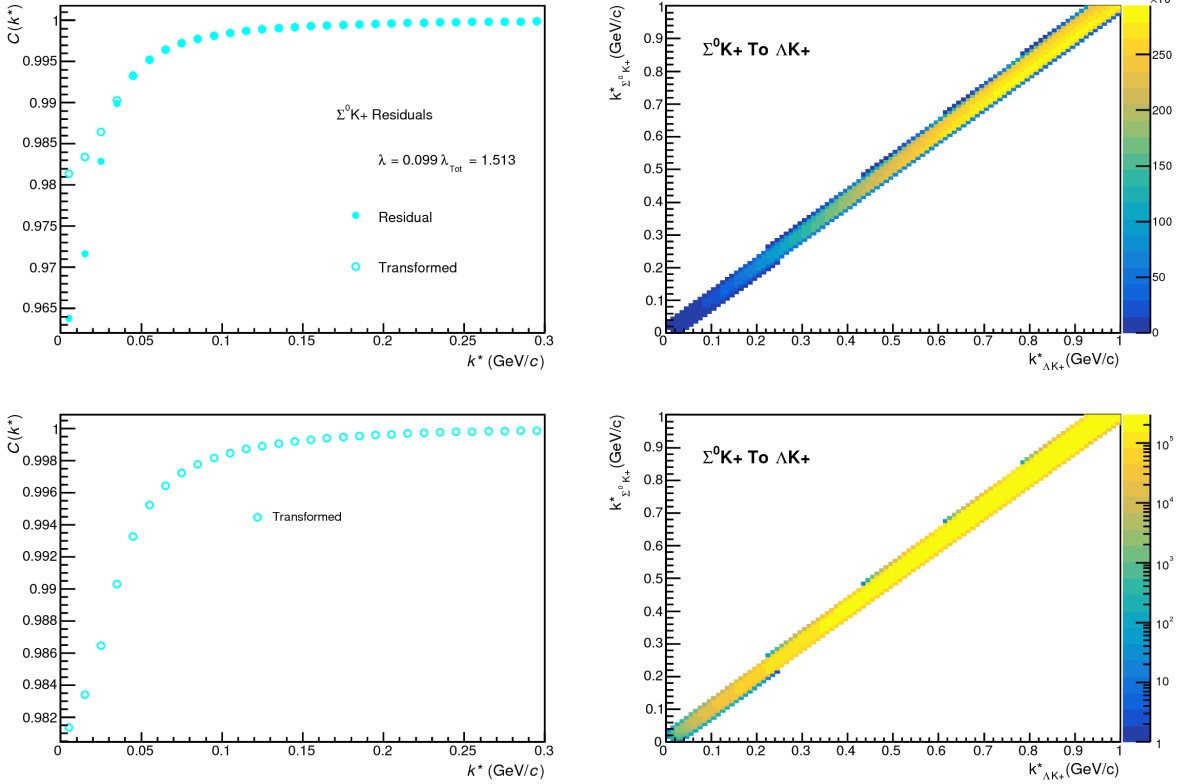


**Fig. 23:**  $\Sigma^0 K^+$  Transform. These figures were taken using parameter values obtained from fits to the data. In the top left corner of the figures, the input correlation function (closed symbols) is shown together with the output, transformed, correlation function (open symbols). In the bottom left, the transformed correlation is shown by itself. The right two plots in each figure show the transform matrix without (top right) and with (bottom right) a log-scale on the z-axis.

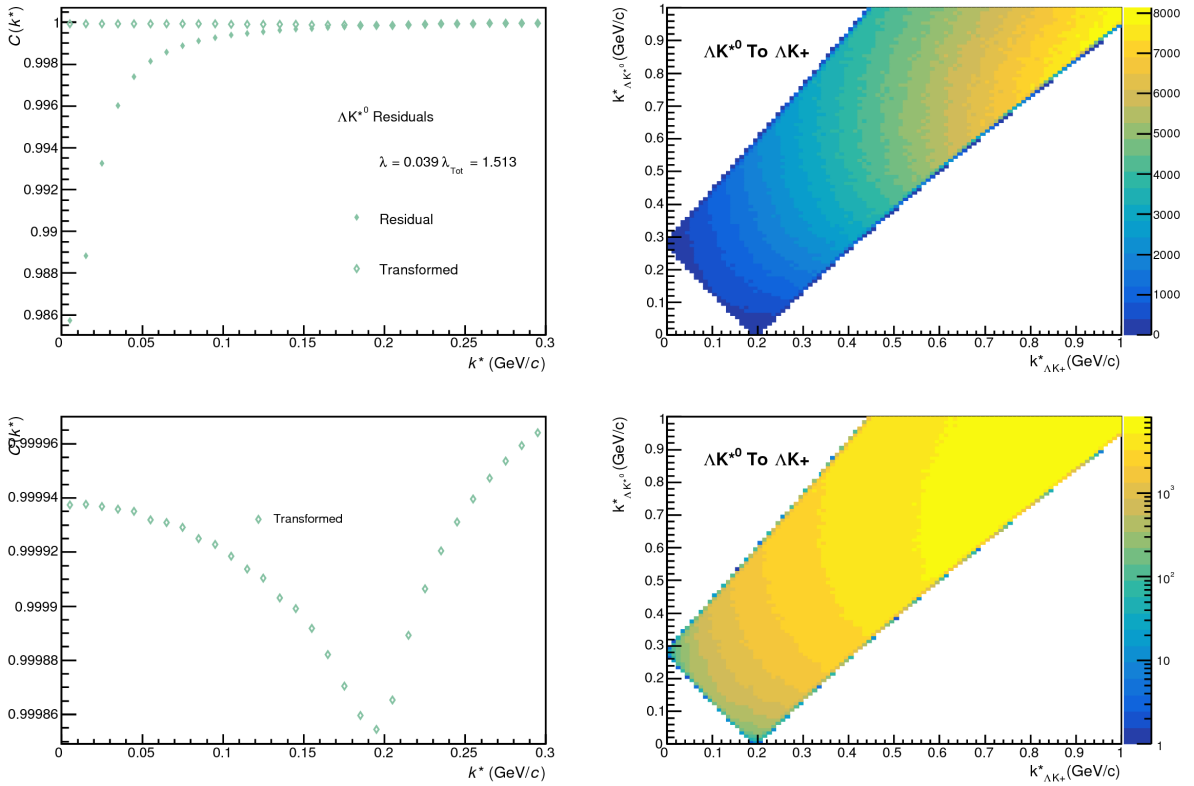


**Fig. 24:**  $\Delta K^{*0}$  Transform. These figures were taken using parameter values obtained from fits to the data. In the top left corner of the figures, the input correlation function (closed symbols) is shown together with the output, transformed, correlation function (open symbols). In the bottom left, the transformed correlation is shown by itself. The right two plots in each figure show the transform matrix without (top right) and with (bottom right) a log-scale on the z-axis.

## 455 5.5 Non-Flat Background

456 We observe a significant non-femtoscopic, non-flat, background in all of our correlations at large  $k^*$ .  
 457 This background increases with decreasing centrality, is the same amongst all  $\Lambda K^\pm$  pairs, and is more  
 458 pronounced in the  $\Lambda K_S^0$  system, as can be seen in Fig. 25. Figure 26a shows that THERMINATOR 2  
 459 simulation does a good job of describing the difference in backgrounds between  $\Lambda K^\pm$  and  $\Lambda K_S^0$ .

460 Before beginning, it is important to note that the difference in  $\Lambda K^\pm$  and  $\Lambda K_S^0$  backgrounds is due mainly  
 461 to the difference in kinematic cuts, not due to any interesting physics. Figure 26b shows that, for THER-  
 462 MINATOR simulation, when restrictions are imposed on the  $p_T$  of the  $K_S^0$  to more closely match the  
 463  $K^\pm$  cuts, the backgrounds align much better. Therefore, we conclude that the difference in background  
 464 between  $\Lambda K^\pm$  and  $\Lambda K_S^0$  observed in our experimental data is simply due to a difference in kinematic cuts  
 465 between  $K^\pm$  and  $K_S^0$  particles.

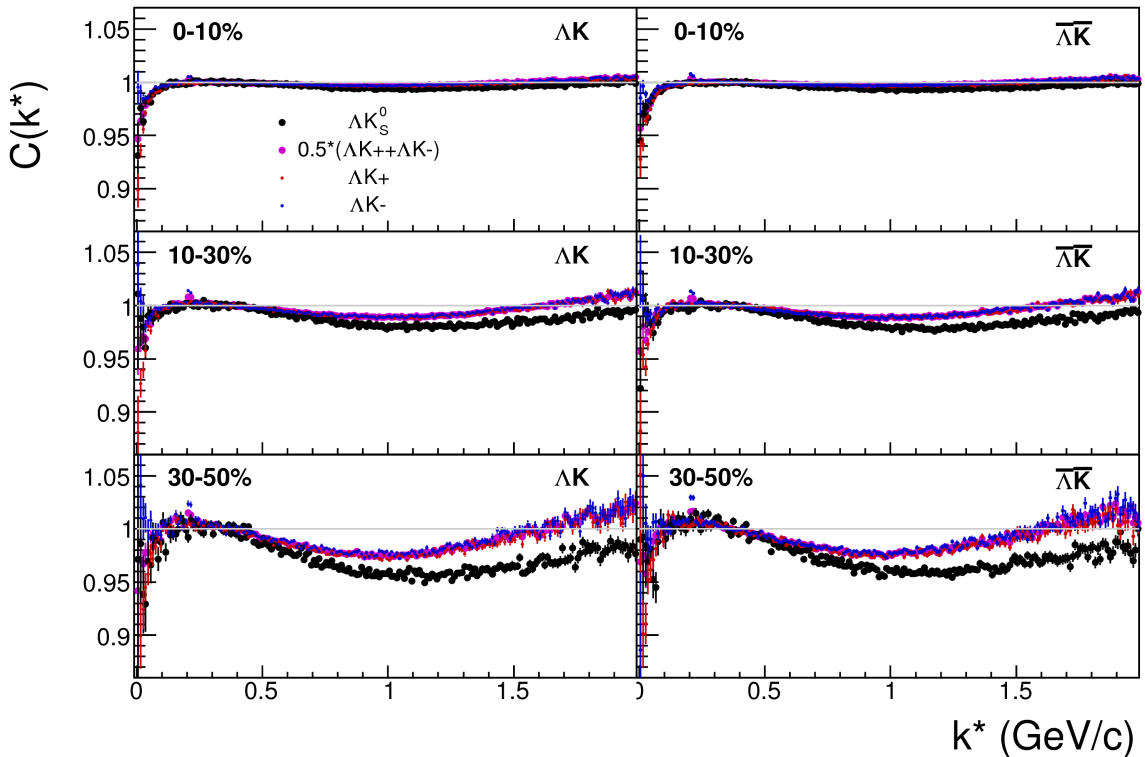


**Fig. 25:** A comparison on the non-femtoscopic backgrounds observed in our  $\Lambda K$  experimental data.

466 It is suggested that this background effect is due primarily to particle collimation associated with elliptic  
 467 flow [8]. More specifically, these backgrounds result from mixing events with unlike event-plane angles  
 468 ( $\Psi_{EP}$ ). As explained in [8], when elliptic flow is present, all particles are more likely to be emitted  
 469 in a specific direction (in-plane), as opposed to a perpendicular direction. Therefore, the difference in  
 470 momenta for pairs of particles tends to be smaller, compared to the case of no flow. In the case of mixed-  
 471 event pairs, the two events used do not share an event-plane, and therefore there is no collimation effect  
 472 in the pairs from flow. As a result, pairs with larger momentum are more likely when mixed-events are  
 473 used, causing the correlation function to be observed below unity. In general, a dip below unity, at a given  
 474  $k^*$ , means it is more probable to find a pair at that  $k^*$  when the daughters are taken from mixed-events, as  
 475 compared to when they are taken from the same event.

476 This same reasoning suggests that the background should lead to an enhancement at low- $k^*$ . The en-  
 477 hancement at high- $k^*$  ( $k^* \gtrsim 1.5$  GeV/c) does not result from the collective flow of the system. We are not

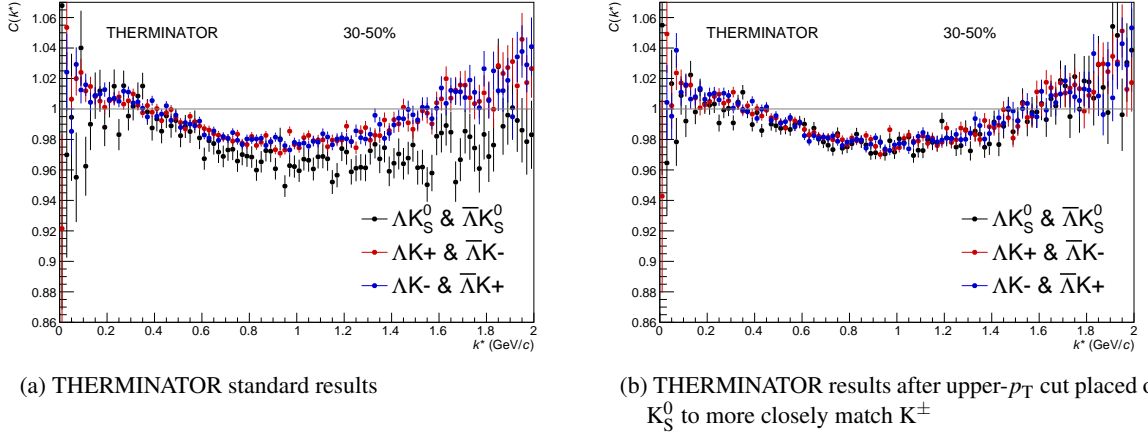


**Fig. 26:** THERMINATOR 2 simulation for  $\Lambda K^+$  (red),  $\Lambda K^-$  (blue), and  $\Lambda K_S^0$  (black). In 26a, we show the standard THERMINATOR 2 results. THERMINATOR 2 does a good job describing qualitatively the difference between the  $\Lambda K^\pm$  and  $\Lambda K_S^0$  backgrounds. In 26b, an upper- $p_T$  cut was placed on the  $K_S^0$  particles to more closely match the  $K^\pm$  kinematic cuts. After this tweak, the  $\Lambda K^\pm$  and  $\Lambda K_S^0$  backgrounds agree much better.

478 certain what causes this enhancement, but typical suspects are jet-like correlations and resonance decays.

479 We can split our correlation functions into three main regions. First, the low- $k^*$  region ( $k^* \lesssim 0.3$  GeV/c)  
480 contains the femtoscopic correlations, as well as a likely enhancement from the background. The  
481 intermediate- $k^*$  region ( $0.3 \lesssim k^* \gtrsim 1.5$  GeV/c) contains a suppression from the background. Finally,  
482 the high- $k^*$  region ( $k^* \gtrsim 1.5$  GeV/c) contains an enhancement with unknown origin.

483 THERMINATOR 2 simulation has been shown to reproduce the background features in a  $\pi K$  analysis  
484 [8]. As the background effect can be attributed mainly to elliptic flow, which is a global feature of the  
485 system, we suspected THERMINATOR 2 could also, at least qualitatively, describe our backgrounds.  
486 After ensuring each simulated event received a random event-plane angle ( $\Psi_{EP}$ )<sup>1</sup>, we found THERMI-  
487 NATOR 2 did a good job of describing our data qualitatively, and, in many cases, quantitatively. Figure  
488 27 shows the THERMINATOR 2 simulation (gold) together with experimental data (red, blue, or black).  
489 The figure also shows a 6<sup>th</sup>-order polynomial fit to the simulation (gold), as well as the fit polynomial  
490 scaled to match the data (red, blue, black).

491 Figure 28 shows three different correlation function generated using THERMINATOR 2 simulation (“Cf  
492 w/o Bgd (A)”, “Cf w. Bgd (B)”, “Bgd(C)”), as well as two histograms describing the relation between  
493 the three (“Ratio (B/C)”, “1+Diff(B-C)”). “Cf w/o Bgd (A)” shows a correlation function with a femto-  
494 scopic correlation, but without background. When THERMINATOR 2 is run without randomizing event  
495 planes, and therefore having all events share a common event plane, no background is observed, as ex-  
496 pected. The femtoscopic correlation effect was introduced by assuming a set of scattering parameters for  
497 the system, and weighting the numerators appropriately. The second correlation, ”Cf w. Bgd (B)”, shows  
498 a correlation function with both a femtoscopic correlation and a background (most closely matches our  
499 situation in experiment). To generate the background, each event was given a random event-plane angle,  
500 as is given to us in experiment. To generate the femtoscopic correlation, the same numerator weighting  
501 procedure was used. Finally, ”Bgd (C)”, shows a correlation function with a non-femtoscopic back-  
502 ground, but no femtoscopic correlation, i.e. background only. This is generated just as ”Cf w. Bgd (B)”,  
503 with randomized event planes, but unit weights are used when filling the numerators, so no femtoscopic  
504 effects are included.

<sup>1</sup>default was for all events to share a common event plane

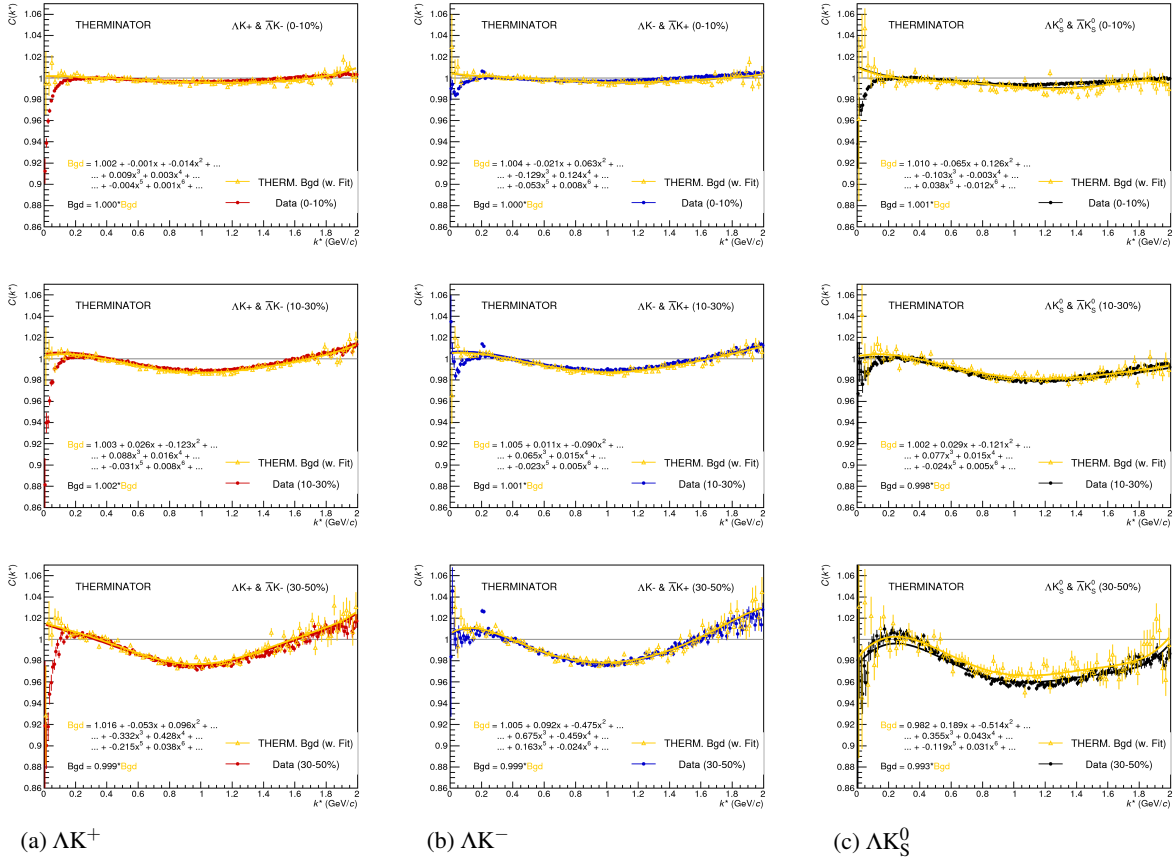


**Fig. 27:** THERMINATOR 2 simulation (gold) together with experimental data (red, blue, or black). The left column shows results for  $\Lambda K^+$  (27a), middle for  $\Lambda K^-$  (27b), and right for  $\Lambda K_S^0$  (27c). A 6<sup>th</sup>-order polynomial fit to the simulation is shown as a solid gold line, and whose fit parameters are printed on the lower left of each plot. This polynomial is scaled to match the experimental data; the value of this scale is printed in the lower left corner of each plot. The polynomial fit with scale factor applied is drawn in a color matching the experimental data (red, blue, black).

505 The main point of Fig. 28 is that the black points match the blue (and purple) points; or, equivalently:

$$C_{fw/oBgd} = \frac{C_{fw.Bgd}}{Bgd} \rightarrow C_{theory} = \frac{C_{exp}}{F_{Bgd}} \rightarrow C_{exp} = C_{theory} \cdot F_{Bgd} \quad (21)$$

506 As shown and described in Fig 28 and Eq. 21, THERMINATOR 2 simulation shows the non-femtoscopic  
507 background affects the correlation function as a separable scale factor. We expect this behavior to be  
508 roughly the same in the experimental data.

509 Figure 29 demonstrates the use of the Stavinskiy method with THERMINATOR 2. In the figure, unit  
510 weights were used for all numerators, so no femtoscopic signal is included, only background effects.  
511 The black points show an ideal, experimentally unreachable, situation of aligning all of the event-plane  
512 angles. With THERMINATOR 2, when the event-planes are aligned, the background signal is killed.  
513 The green points show the case of random event-plane angles, a situation more closely matching that  
514 of experiment. The purple points show the affect of applying the Stavinskiy method to the case of  
515 random event-planes. The figure shows that this method effectively kills the non-flat background (i.e.  
516 the procedure takes the green points to the purple). Finally, the blue points show the effect of applying  
517 the Stavinskiy method when all of the event-planes are aligned. This shows that the Stavinskiy method

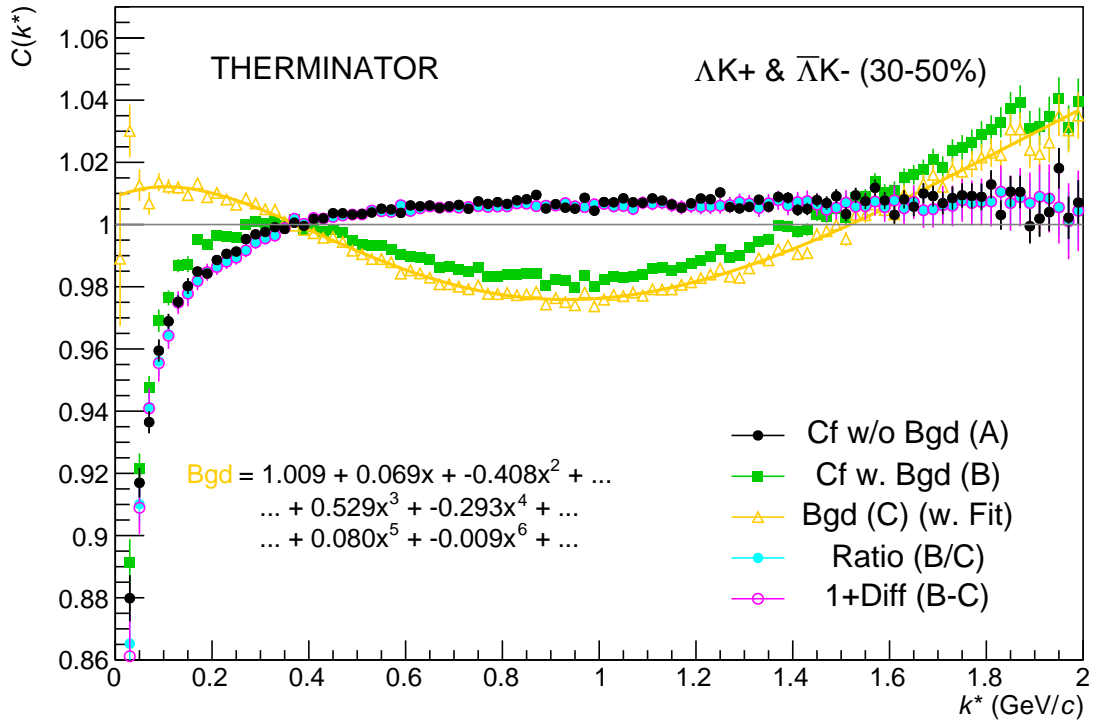


**Fig. 28:** Correlation with background decomposition with THERMINATOR. "Cf w/o Bgd (A)" shows a correlation function with a femtoscopic correlation, but without background. "Cf w. Bgd (B)", shows a correlation function with both a femtoscopic correlation and a background (most closely matches our situation in experiment). "Bgd (C)", shows a correlation function with a non-femtoscopic background, but no femtoscopic correlation, i.e. background only.

518 does not introduce any signal to an already flat background.

## 519 5.6 LednickyFitter

520 The code developed to fit the data is called "LednickyFitter", and utilizes the ROOT TMinuit implemen-  
 521 tation of the MINUIT fitting package. In short, given a function with a number of parameters, the fitter  
 522 explores the parameter space searching for the minimum of the function. In this implementation, the  
 523 function to be minimized should represent the difference between the measured and theoretical corre-  
 524 lation functions. However, a simple  $\chi^2$  test is inappropriate for fitting correlation functions, as the ratio of  
 525 two Poisson distributions does not result in a Poisson distribution. Instead, a log-likelihood fit function  
 526 of the following form is used [2]:

$$\chi_{PML}^2 = -2 \left[ A \ln \left( \frac{C(A+B)}{A(C+1)} \right) + B \ln \left( \frac{A+B}{B(C+1)} \right) \right] \quad (22)$$

527 where  $A$  is the experimental signal distribution (numerator),  $B$  is the experimental background distribu-  
 528 tion (denominator), and  $C$  is the theoretical fit correlation function.

529 The LednickyFitter uses Equations 5 – 7 to build the theoretical fit, and Equation 22 as the statistic  
 530 quantifying the quality of the fit. The parameters to be varied by MINUIT are:  $\lambda$ ,  $R$ ,  $f_0$  ( $\mathbb{R}f_0$  and  $\mathbb{I}f_0$   
 531 separately),  $d_0$ , and normalization  $N$ . The fitter currently includes methods to correct for momentum  
 532 resolution and a non-flat background. These corrections are applied to the fit function, the data is never

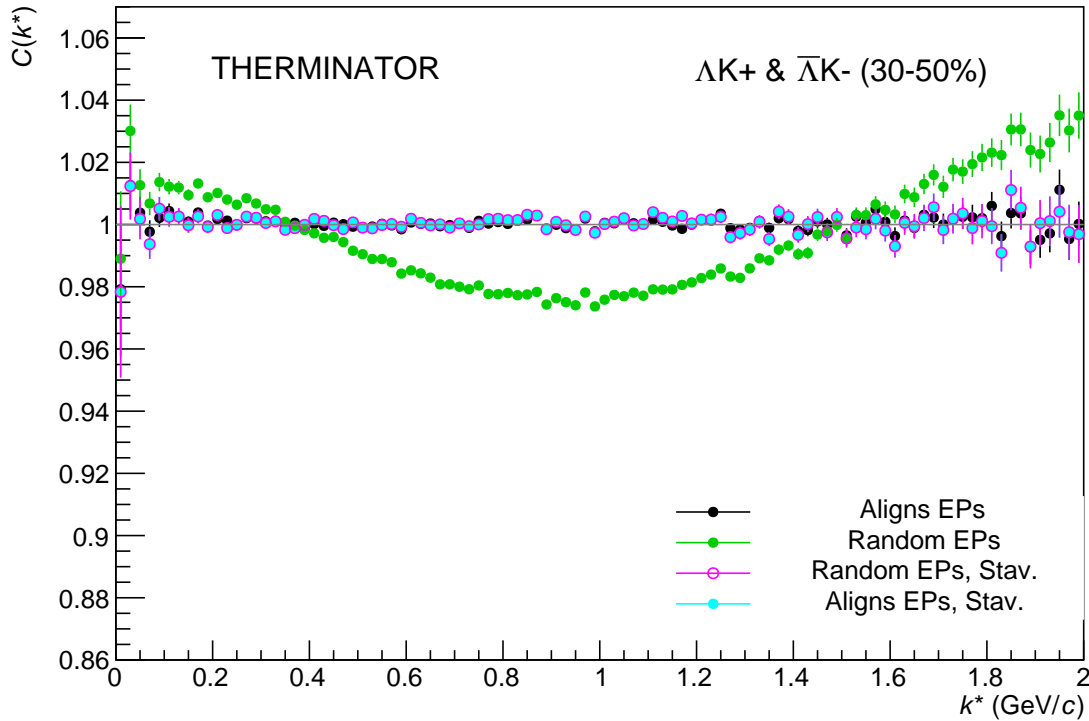


**Fig. 29:** The use of the Stavinskiy method with THERMINATOR 2. Unit weights were used for all numerators, so no femtoscopic signal is included, only background effects. The black points show an ideal, experimentally unreachable, situation of aligning all of the event-plane angles. The green points show the experimental situation of random event-plane angles. The purple points shown the affect of applying the Stavinskiy method to the case of random event-planes. Finally, the blue points show the effect of applying the Stavinskiy method when all of the event-planes are aligned.

533 touched. The fitter is able to share parameters between different analyses and fit all simultaneously.

534 In a typical fit, a given pair is fit with its conjugate (ex.  $\Lambda K^+$  with  $\bar{\Lambda} K^-$ ) across all centralities (0-10%,  
535 10-30%, 30-50%), for a total of 6 simultaneous analyses. Each analysis has a unique  $\lambda$  and normalization  
536 parameter. The radii are shared between analyses of like centrality, as these should have similar source  
537 sizes. The scattering parameters ( $\mathbb{R}f_0$ ,  $\mathbb{I}f_0$ ,  $d_0$ ) are shared amongst all.

538 Initially, we left open the possibility for the  $\Lambda K^+(\bar{\Lambda} K^-)$  and  $\Lambda K^-(\bar{\Lambda} K^+)$  systems to have different source  
539 radii. After always finding these two be consistent, we decided to join the radii parameters between these  
540 systems. So, now, in a typical fit of our  $\Lambda K^\pm$  data, all  $\Lambda K^\pm$  analyses ( $\Lambda K^+$ ,  $\bar{\Lambda} K^-$ ,  $\Lambda K^-$ ,  $\bar{\Lambda} K^+$ ) are fit  
541 simultaneously across all centralities. Scattering parameters are shared between pair-conjugate systems  
542 (i.e. a parameter set describing the  $\Lambda K^+$  &  $\bar{\Lambda} K^-$  system, and a separate set describing the  $\Lambda K^-$  &  $\bar{\Lambda} K^+$   
543 system). For each centrality, a radius and  $\lambda$  parameters are shared amongst all pairs. Each analysis has a  
544 unique normalization parameter.

545 In the case of fitting with residuals, the  $\lambda_{Fit}$  parameter serves as an overall normalization shared by all  
546 contributors, such that Eqn 17 becomes:

$$\begin{aligned}
C_{measured}(k_{\Lambda K}^*) &= 1 + \sum_i \lambda'_i [C_i(k_{\Lambda K}^*) - 1] \\
\lambda'_i &= \lambda_{Fit} \lambda_i \\
\sum_i \lambda'_i &= \lambda_{Fit} \sum_i \lambda_i = \lambda_{Fit}
\end{aligned} \tag{23}$$

547 where  $\lambda_i$  is obtained from THERMINATOR, as explained in Section 5.4, and whose values are presented  
548 in Table 5. For Coulomb-neutral pairs, such as  $\Lambda K$ ,  $\Sigma^0 K$ , and  $\Xi^0 K$ ,  $C_i(k_{\Lambda K}^*)$  is calculated from Eqn.  
549 5, with the help of Eqn. 7. For those residual pairs which include a Coulomb interaction,  $C_i(k_{\Lambda K}^*)$  is  
550 either calculated using the CoulombFitter method (Sections 5.2 and 5.7) with no strong interaction, or  
551 by using the  $\Xi^{ch} K^{ch}$  data directly. Unless otherwise stated, the  $\Xi^{ch} K^{ch}$  residual contribution is modeled  
552 using the experimental  $\Xi^{ch} K^{ch}$  data, and all other charged contributors (ex.  $\Sigma^{*ch} K^{ch}$ ) are modeled using  
553 the CoulombFitter technique with no strong interaction contribution.

554 To summarize, the complete fit function is constructed as follows:

- 555 1. The uncorrected, primary, correlation function,  $C_{\Lambda K}(k_{True}^*)$ , is constructed using Eq. 23 (with the  
556 help of Eqns. 5 and 7)
- 557 2. If residuals are included:
  - 558 – the parent correlation functions are obtained using:
    - 559 – Eq. 23 (with the help of Eqns. 5 and 7) for the case of Coulomb-neutral pairs
    - 560 –  $\Xi^- K^\pm$  experimental data for  $\Xi^- K^\pm$  contributions
    - 561 – a Coulomb-only curve, with the help of Secs. 5.2 and 5.7, for pairs including the  
562 Coulomb interaction
    - 563 – the contribution to the  $\Lambda K$  correlation function is found by running the parent correlation  
564 function through the appropriate transform, via Eq.16
  - 565 3. The primary and residual correlations are combined, via Eq.17, to form  $C'_{Fit}(k_{True}^*)$ 
    - 566 – in the case of no residual contributions included in the fit,  $\lambda_i = \lambda_{\Lambda K}$  in Eq. 23 is set equal to  
567 1. Then, the extracted  $\lambda_{Fit}$  parameter should be roughly equal to the pair purity
    - 568 – when residuals are included, the  $\lambda_i$  values are presented in Table 5
  - 569 4. The correlation function is corrected to account for momentum resolution effects using Eq. 14

$$C'_{fit}(k_{Rec}^*) = \frac{\sum_{k_{True}^*} M_{k_{Rec}, k_{True}^*} C'_{fit}(k_{True}^*)}{\sum_{k_{True}^*} M_{k_{Rec}, k_{True}^*}}$$

- 571 5. Finally, the non-flat background correction is applied, and the final fit function is obtained
- 572 –  $C_{Fit}(k_{Rec}^*) = C'_{Fit}(k_{Rec}^*) * F_{Bgd}(k_{Rec}^*)$

573 Figures 46, 47, and 48 (32, 33, and 34, or 39, 40, and 41), in Section 7, show experimental data with fits  
574 for all studied centralities for  $\Lambda K_S^0 (\bar{\Lambda} K_S^0)$ ,  $\Lambda K^+ (\bar{\Lambda} K^-)$ , and  $\Lambda K^- (\bar{\Lambda} K^+)$ , respectively. In the figures, the  
575 black solid line represents the “raw” fit, i.e. not corrected for momentum resolution effects nor non-flat  
576 background. The green line shows the fit to the non-flat background. The purple points show the fit after  
577 momentum resolution, non-flat background, and residual correlations (if applicable) corrections have  
578 been applied. The extracted fit values with uncertainties are also printed on the figures.

## 579 5.7 Coulomb Fitter

580 When fitting the  $\Xi^-(\bar{\Xi}^+)K^\pm$  results, it is necessary to include both strong and Coulomb effects. In this  
 581 case, Equation 5 is no longer valid, and, in fact, there is no analytical form with which to fit. We therefore  
 582 must take a more basic approach, and integrate out Eq.4 by hand. To achieve this, one has two options.  
 583 The first option is to numerically integrate Eq.4. The second option is to simulate a large sample of  
 584 particle pairs, calculate the wave function describing the interaction, and average to obtain the integral.  
 585 Having no experience with either of these options, we elected the latter of simulating pairs. The code  
 586 developed to achieve this functionality is called “CoulombFitter”. Currently, in order to generate the  
 587 statistics needed for a stable fit, we find that  $\sim 10^4$  simulated pairs per 10 MeV bin are necessary. The  
 588 nature of this process means that the “CoulombFitter” takes much longer to run than the “LednickyFitter”  
 589 of Section 5.1.

590 Unfortunately, with this analysis, we are not sensitive to, and therefore not able to distinguish between,  
 591 the iso-spin singlet and triplet states. We proceed with our analysis, but the results must be interpreted  
 592 as iso-spin averaged scattering parameters.

593 As stated before, to generate a fit correlation function, we must simulate a large number of pairs, calculate  
 594 the wave-function, and average  $\Psi^2$  over all pairs in a given  $k^*$  bin. Essentially, we calculate Equation 9  
 595 by hand:

$$\begin{aligned} C(\mathbf{k}^*) &= \sum_S \rho_S \int S(\mathbf{r}^*) |\Psi_{\mathbf{k}^*}^S(\mathbf{r}^*)|^2 d^3 \mathbf{r}^* \\ &\longrightarrow C(|\mathbf{k}^*|) \equiv C(k^*) = \sum_S \rho_S \langle |\Psi^S(\mathbf{k}_i^*, \mathbf{r}_i^*)|^2 \rangle_i \\ &\longrightarrow C(k^*) = \lambda \sum_S \rho_S \langle |\Psi^S(\mathbf{k}_i^*, \mathbf{r}_i^*)|^2 \rangle_i + (1 - \lambda) \end{aligned} \quad (24)$$

596 where  $\langle \rangle_i$  represents an average over all pairs in a given  $k^*$  bin.

597 In summary, for a given  $k^*$  bin, we must draw  $N_{pairs} \sim 10^4$  pairs, and for each pair:

- 598 1. Draw a random  $\mathbf{r}^*$  vector according to our Gaussian source distribution  $S(\mathbf{r}^*)$
- 599 2. Draw a random  $\mathbf{k}^*$  vector satisfying the  $|\mathbf{k}^*|$  restriction of the bin
  - 600 – We draw from real  $k^*$  vectors obtained from the data
  - 601 – However, we find that drawing from a distribution flat in  $k^*$  gives similar results
- 602 3. Construct the wave-function  $\Psi$

603 After all pairs for a given  $k^*$  bin are simulated and wave-functions obtained, the results are averaged to  
 604 give the fit result.

605 Construction of the wave-functions, Equation 10, involves a number of complex functions not included  
 606 in standard C++ or ROOT libraries (namely,  $h(\eta)$ ,  $\tilde{G}(\rho, \eta)$ ), and  $F(-i\eta, 1, i\xi)$ . These functions were  
 607 even difficult to find and implement from elsewhere. Our solution was to embed a Mathematica kernel  
 608 into our C++ code to evaluate these functions. However, having Mathematica work on-the-fly with the  
 609 fitter was far too time consuming (fitter would have taken days, maybe weeks to finish). Our solution  
 610 was to use Mathematica to create matrices representing these functions for different parameter values.  
 611 During fitting, these matrices were then interpolated and the results used to build the wave-functions.  
 612 This method decreased the running time dramatically, and we are not able to generate results in under  $\sim$   
 613 1 hour. This process will be explained in more detail in future versions of the note.

614 **6 Systematic Errors**

615 In order to understand my systematic uncertainties, the analysis code was run many times using slightly  
 616 different values for a number of important cuts, and the results were compared. To quantify the systematic  
 617 errors on the data, all correlation functions built using all varied cut values were bin-by-bin averaged,  
 618 and the resulting variance of each bin was taken as the systematic error. The cuts which were utilized in  
 619 this study are presented in Sections 6.1.1 ( $\Lambda K_S^0$ ) and 6.2.1 ( $\Lambda K^\pm$ ).

620 Similarly, the fit parameters extracted from all of these correlation functions were averaged, and the  
 621 resulting variances were taken as the systematic errors for the fit parameters. As with the systematic  
 622 errors on the data, this was performed for all varied cut values. Additionally, a systematic analysis was  
 623 done on our fit method (which, for now, just includes our choice of fit range and functional form used to  
 624 model the non-femtoscopic background). These two sources of uncertainty were combined in quadrature  
 625 to obtain the final systematic uncertainties on the extracted fit parameters.

626 **6.1 Systematic Errors:  $\Lambda K_S^0$**

627 **6.1.1 Particle and Pair Cuts**

628 The cuts included in the systematic study, as well as the values used in the variations, are listed below.  
 629 Note, the central value corresponds to that used in the analysis.

$\Lambda K_S^0$ systematics	
DCA $\Lambda(\bar{\Lambda})$	4, 5, 6 mm
DCA $K_S^0$	2, 3, 4 mm
DCA $\Lambda(\bar{\Lambda})$ Daughters	3, 4, 5 mm
DCA $K_S^0$ Daughters	2, 3, 4 mm
$\Lambda(\bar{\Lambda})$ Cosine of Pointing Angle	0.9992, 0.9993, 0.9994
$K_S^0$ Cosine of Pointing Angle	0.9992, 0.9993, 0.9994
DCA to Primary Vertex of $p(\bar{p})$ Daughter of $\Lambda(\bar{\Lambda})$	0.5, 1, 2 mm
DCA to Primary Vertex of $\pi^-(\pi^+)$ Daughter of $\Lambda(\bar{\Lambda})$	2, 3, 4 mm
DCA to Primary Vertex of $\pi^+$ Daughter of $K_S^0$	2, 3, 4 mm
DCA to Primary Vertex of $\pi^-$ Daughter of $K_S^0$	2, 3, 4 mm
Average Separation of Like-Charge Daughters	5, 6, 7 cm

Table 6:  $\Lambda K_S^0$  systematics

630 **6.1.2 Non-Flat Background**

631 We fit our non-flat background with a linear function. To study the contribution of this choice to our sys-  
 632 tematic errors, we also fit with a quadratic and Gaussian form. The resulting uncertainties are combined  
 633 with the uncertainties arising from our particle cuts.

634 **6.1.3 Fit Range**

635 Our choice of  $k^*$  fit range was varied by  $\pm 25\%$ . The resulting uncertainties in the extracted parameter  
 636 sets were combined with our uncertainties arising from our particle and pair cuts.

637 **6.2 Systematic Errors:  $\Lambda K^\pm$**

638 **6.2.1 Particle and Pair Cuts**

639 The cuts included in the systematic study, as well as the values used in the variations, are listed below.

640 Note, the central value corresponds to that used in the analysis.

$\Lambda K^\pm$  systematics

$\Lambda K^\pm$ systematics	
DCA $\Lambda(\bar{\Lambda})$	4, 5, 6 mm
DCA $\Lambda(\bar{\Lambda})$ Daughters	3, 4, 5 mm
$\Lambda(\bar{\Lambda})$ Cosine of Pointing Angle	0.9992, 0.9993, 0.9994
DCA to Primary Vertex of $p(\bar{p})$ Daughter of $\Lambda(\bar{\Lambda})$	0.5, 1, 2 mm
DCA to Primary Vertex of $\pi^-(\pi^+)$ Daughter of $\Lambda(\bar{\Lambda})$	2, 3, 4 mm
Average Separation of $\Lambda(\bar{\Lambda})$ Daughter with Same Charge as $K^\pm$	7, 8, 9 cm
Max. DCA to Primary Vertex in Transverse Plane of $K^\pm$	1.92, 2.4, 2.88
Max. DCA to Primary Vertex in Longitudinal Direction of $K^\pm$	2.4, 3.0, 3.6

Table 7:  $\Lambda K^\pm$  systematics

641 **6.2.2 Non-Flat Background**

642 We fit our non-flat background with a linear function. To study the contribution of this choice to our sys-  
643 tematic errors, we also fit with a quadratic and Gaussian form. The resulting uncertainties are combined  
644 with the uncertainties arising from our particle cuts.

645 **6.2.3 Fit Range**

646 Our choice of  $k^*$  fit range was varied by  $\pm 25\%$ . The resulting uncertainties in the extracted parameter  
647 sets were combined with our uncertainties arising from our particle and pair cuts.

648 **6.3 Systematic Errors:  $\Xi K^\pm$**

649 **6.3.1 Particle and Pair Cuts**

650 The cuts included in the systematic study, as well as the values used in the variations, are listed below.

651 Note, the central value corresponds to that used in the analysis.

$\Xi^- K^\pm$  systematics

$\Xi^- K^\pm$ systematics	
Max. DCA $\Xi(\bar{\Xi})$	2, 3, 4 mm
Max. DCA $\Xi(\bar{\Xi})$ Daughters	2, 3, 4 mm
Min. $\Xi(\bar{\Xi})$ Cosine of Pointing Angle to Primary Vertex	0.9991, 0.9992, 0.9993
Min. $\Lambda(\bar{\Lambda})$ Cosine of Pointing Angle to $\Xi(\bar{\Xi})$ Decay Vertex	0.9992, 0.9993, 0.9994
Min. DCA Bachelor $\pi$	0.5, 1, 2 mm
Min. DCA $\Lambda(\bar{\Lambda})$	1, 2, 3 mm
Max. DCA $\Lambda(\bar{\Lambda})$ Daughters	3, 4, 5 mm
Min. DCA to Primary Vertex of $p(\bar{p})$ Daughter of $\Lambda(\bar{\Lambda})$	0.5, 1, 2 mm
Min. DCA to Primary Vertex of $\pi^-(\pi^+)$ Daughter of $\Lambda(\bar{\Lambda})$	2, 3, 4 mm
Min. Average Separation of $\Lambda(\bar{\Lambda})$ Daughter and $K^\pm$ with like charge	7, 8, 9 cm
Min. Average Separation of Bachelor $\pi$ and $K^\pm$ with like charge	7, 8, 9 cm
Max. DCA to Primary Vertex in Transverse Plane of $K^\pm$	1.92, 2.4, 2.88
Max. DCA to Primary Vertex in Longitudinal Direction of $K^\pm$	2.4, 3.0, 3.6

**Table 8:**  $\Xi^- K^\pm$  systematics

## 652 7 Results and Discussion

### 653 7.1 Results: $\Lambda K_S^0$ and $\Lambda K^\pm$

654 In the following sections, we present results assuming (i) three residual contributors (Sec. 7.1.1), (ii) ten  
 655 residual contributors (Sec. 7.1.2), and (iii) no residual correlations (Sec. 7.1.3).

656 For the results shown, unless otherwise noted, the following hold true: All correlation functions were  
 657 normalized in the range  $0.32 < k^* < 0.40 \text{ GeV}/c$ , and fit in the range  $0.0 < k^* < 0.30 \text{ GeV}/c$ . For the  $\Lambda K^-$   
 658 and  $\bar{\Lambda} K^+$  analyses, the region  $0.19 < k^* < 0.23 \text{ GeV}/c$  was excluded from the fit to exclude the bump  
 659 caused by the  $\Omega^-$  resonance. The non-femtoscopic backgrounds for the  $\Lambda K^+$  and  $\Lambda K^-$  systems were  
 660 modeled by a (6<sup>th</sup>-order polynomial fit to THERMINATOR simulation, while those for the  $\Lambda K_S^0$  were  
 661 fit with a simple linear form. The  $\Lambda K^+(\bar{\Lambda} K^-)$  radii are shared with  $\Lambda K^-(\bar{\Lambda} K^+)$ , while the  $\Lambda K_S^0(\bar{\Lambda} K_S^0)$   
 662 radii are unique. In the figures showing experimental correlation functions with fits, the black solid line  
 663 represents the primary ( $\Lambda K$ ) correlation's contribution to the fit. The green line shows the fit to the non-  
 664 flat background. The purple points show the fit after all residuals' contributions have been included, and  
 665 momentum resolution and non-flat background corrections have been applied.

666 Before beginning, I first collect a summary of my final results in Figure 30. In the summary plot, we  
 667 show the extracted scattering parameters in the form of a  $\text{Im}[f_0]$  vs  $\text{Re}[f_0]$  plot, which includes the  $d_0$   
 668 values to the right side. We also show the  $\lambda$  vs. radius parameters for all three of our studied centrality  
 669 bins. In Fig. 30, three residual contributors were used. For the  $\Lambda K_S^0$  results shown in the figure, the  $\Lambda K_S^0$   
 670 and  $\bar{\Lambda} K_S^0$  analyses were fit simultaneously across all centralities (0-10%, 10-30%, 30-50%); scattering  
 671 parameters and a single  $\lambda$  parameter were shared amongst all, the radii were shared amongst results  
 672 of like-centrality, and each has a unique normalization parameter. For the  $\Lambda K^\pm$  results shown, all four  
 673 pair combinations were fit simultaneously ( $\Lambda K^+, \bar{\Lambda} K^-, \Lambda K^-, \bar{\Lambda} K^+$ ) across all centralities. Scattering  
 674 parameters were shared between pair-conjugate systems (i.e. a parameter set describing  $\Lambda K^+$  &  $\bar{\Lambda} K^-$ ,  
 675 and a separate set describing  $\Lambda K^-$  &  $\bar{\Lambda} K^+$ ). For each centrality, a radius and  $\lambda$  parameters were shared  
 676 between all pairs. Each analysis has a unique normalization parameter.

677 **7.1.1 3 Residual Correlations Included in Fit**

678 Figure 30 nicely collects and summarizes all of our extracted fit parameters for the case of 3 included  
 679 residual contributors. Figure 31 presents our extracted fit radii, along with those of other systems previ-  
 680 ously analyzed by ALICE [9], as a function of pair transverse mass ( $m_T$ ). Figures 32, 33, and 34 show the  
 681 experimental correlation functions with fits, assuming 3 residual contributors, for all studied centralities  
 682 for  $\Lambda K_S^0$  with  $\bar{\Lambda} K_S^0$ ,  $\Lambda K^+$  with  $\bar{\Lambda} K^-$ , and  $\Lambda K^-$  with  $\bar{\Lambda} K^+$ , respectively. The parameter sets extracted  
 683 from the fits can be found in Tables 13 and 14.

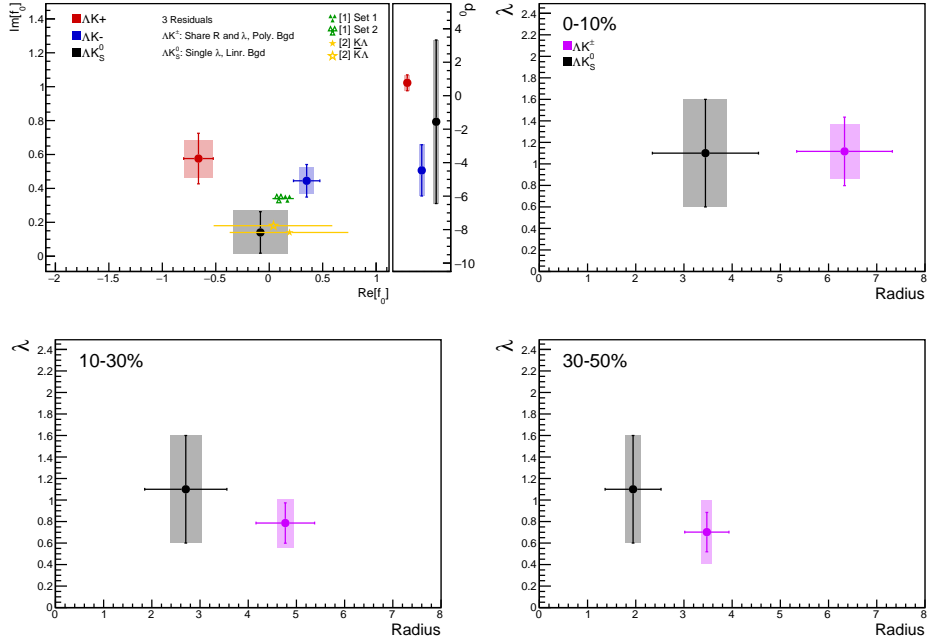


**Fig. 30:** Extracted scattering parameters for the case of 3 residual contributors for all of our  $\Lambda K$  systems. [Top Left]:  $\Im f_0$  vs.  $\Re f_0$ , together with  $d_0$  to the right. [Top Right (Bottom Left, Bottom Right)]:  $\lambda$  vs. Radius for the 0-10% (10-30%, 30-50%) bin. The green [10] and yellow [11] points show theoretical predictions made using chiral perturbation theory.

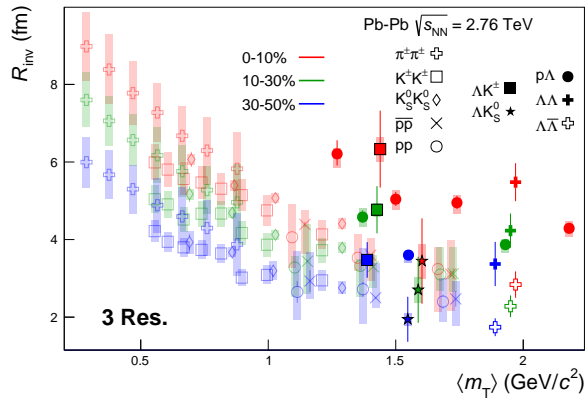
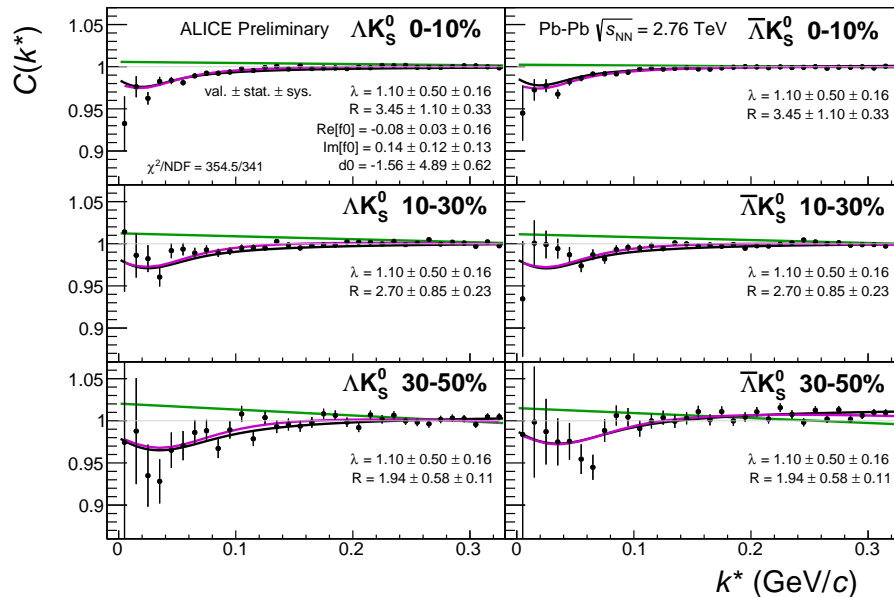
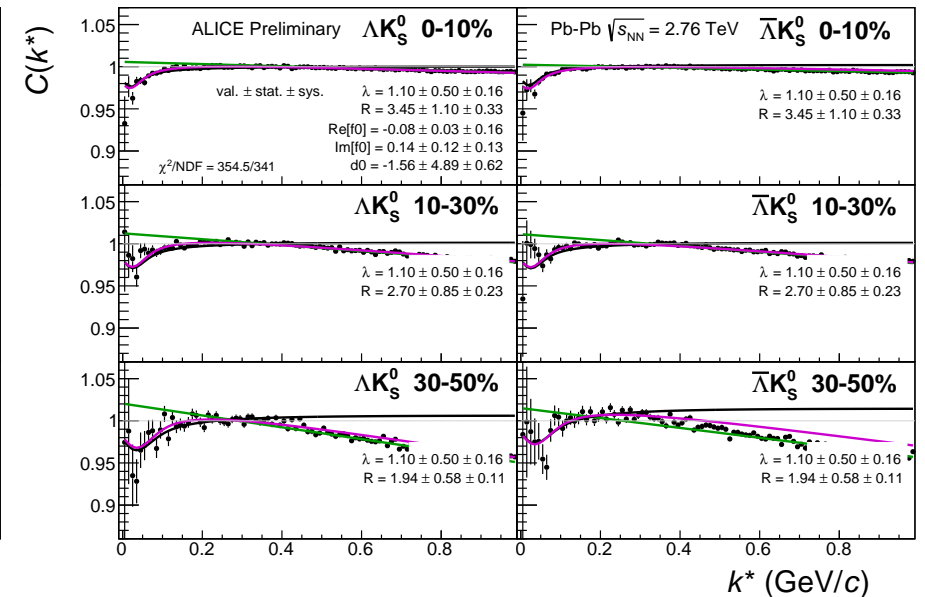


**Fig. 31:** 3 residual correlations in  $\Lambda K$  fits. Extracted fit  $R_{\text{inv}}$  parameters as a function of pair transverse mass ( $m_T$ ) for various pair systems over several centralities. The ALICE published data [9] is shown with transparent, open symbols. The new  $\Lambda K$  results are shown with opaque, filled symbols. In the left, the  $\Lambda K^+$  (with its conjugate pair) results are shown separately from the  $\Lambda K^-$  (with its conjugate pair) results. In the right, all  $\Lambda K^\pm$  results are averaged.

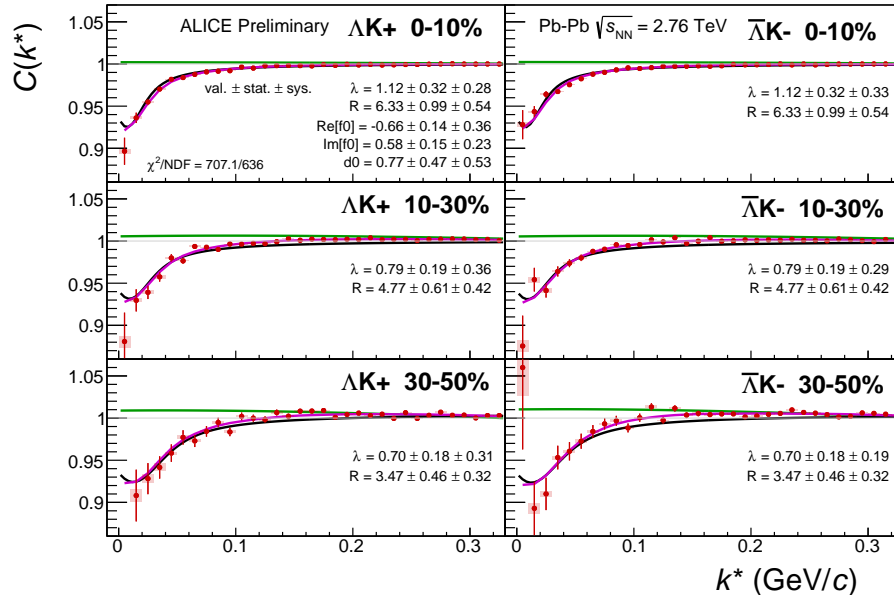


(a) Signal region view ( $k^* \lesssim 0.3$  GeV/c)

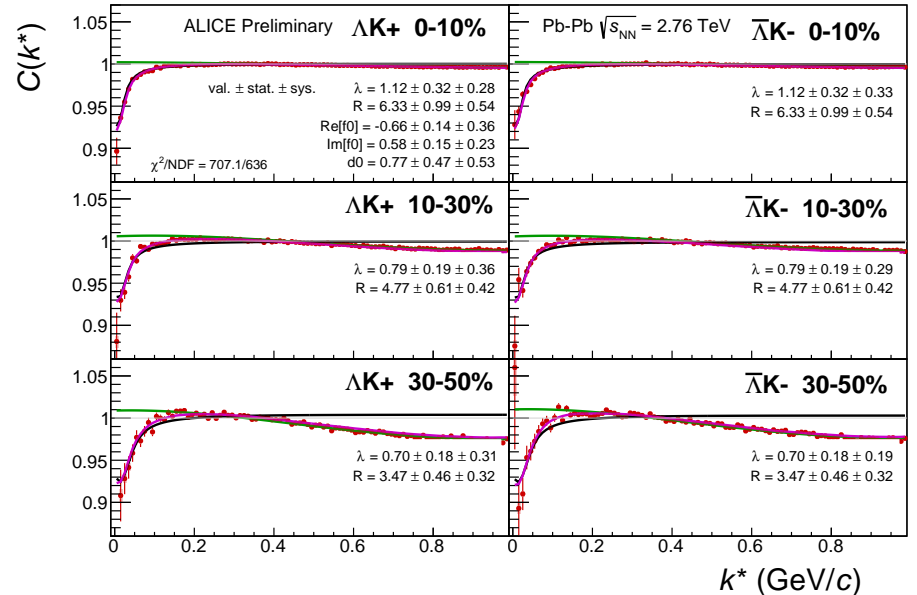


(b) Wide view ( $k^* \lesssim 1.0$  GeV/c)

**Fig. 32:** Fits, with 3 residual correlations included, to the  $\Lambda K_s^0$  (left) and  $\bar{\Lambda} K_s^0$  (right) data for the centralities 0-10% (top), 10-30% (middle), and 30-50% (bottom). The lines represent the statistical errors, while the boxes represent the systematic errors. A single  $\lambda$  parameter is shared amongst all. Each analysis has a unique normalization parameter. The radii are shared between analyses of like centrality, as these should have similar source sizes. The scattering parameters ( $\mathbb{R} f_0$ ,  $\mathbb{I} f_0$ ,  $d_0$ ) are shared amongst all. The background is modeled by a (6<sup>th</sup>-degree polynomial fit to THERMINATOR simulation. The black solid line represents the primary ( $\Lambda K$ ) correlation's contribution to the fit. The green line shows the fit to the non-flat background. The purple points show the fit after all residuals' contributions have been included, and momentum resolution and non-flat background corrections have been applied. The extracted fit values with uncertainties are printed.

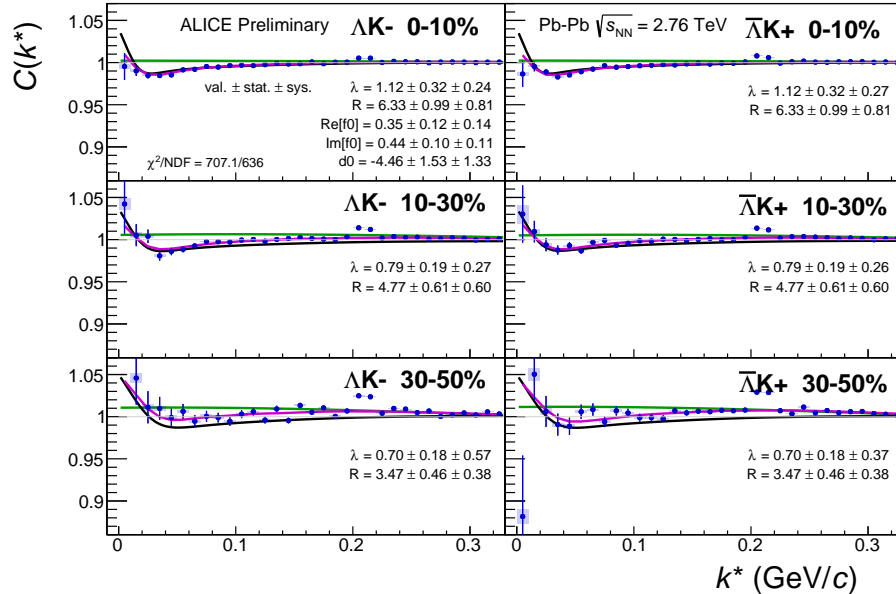


(a) Signal region view ( $k^* \lesssim 0.3 \text{ GeV}/c$ )

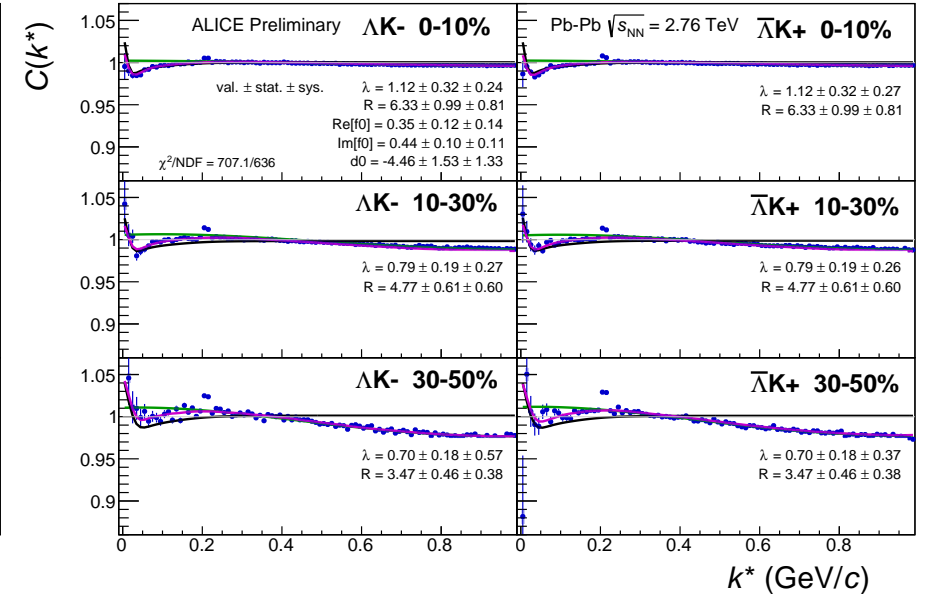


(b) Wide view ( $k^* \lesssim 1.0 \text{ GeV}/c$ )

**Fig. 33:** Fits, with 3 residual correlations included, to the  $\Delta K^+$  (left) and  $\bar{\Delta} K^-$  (right) data for the centralities 0-10% (top), 10-30% (middle), and 30-50% (bottom). The lines represent the statistical errors, while the boxes represent the systematic errors. All  $\Delta K^\pm$  analyses are fit simultaneously across all centralities (0-10%, 10-30%, 30-50%). Scattering parameters ( $\text{Re}[f_0]$ ,  $\text{Im}[f_0]$ ,  $d_0$ ) are shared between pair-conjugate systems (i.e. a parameter set describing the  $\Delta K^+$  &  $\bar{\Delta} K^-$  system, and a separate set describing the  $\Delta K^-$  &  $\bar{\Delta} K^+$  system). For each centrality, a radius and  $\lambda$  parameters are shared between all pairs ( $\Delta K^+$ ,  $\bar{\Delta} K^-$ ,  $\Delta K^-$ ,  $\bar{\Delta} K^+$ ). Each analysis has a unique normalization parameter. The background is modeled by a (6<sup>th</sup>-degree polynomial fit to THERMINATOR simulation. The black solid line represents the primary ( $\Delta K$ ) correlation's contribution to the fit. The green line shows the fit to the non-flat background. The purple points show the fit after all residuals' contributions have been included, and momentum resolution and non-flat background corrections have been applied. The extracted fit values with uncertainties are printed.



(a) Signal region view ( $k^* \lesssim 0.3 \text{ GeV}/c$ )



(b) Wide view ( $k^* \lesssim 1.0 \text{ GeV}/c$ )

**Fig. 34:** Fits, with 3 residual correlations included, to the  $\Lambda K^-$  (left) with  $\bar{\Lambda} K^+$  (right) data for the centralities 0-10% (top), 10-30% (middle), and 30-50% (bottom). The lines represent the statistical errors, while the boxes represent the systematic errors. All  $\Lambda K^\pm$  analyses are fit simultaneously across all centralities (0-10%, 10-30%, 30-50%). Scattering parameters ( $\mathbb{R}f_0$ ,  $\mathbb{I}f_0$ ,  $d_0$ ) are shared between pair-conjugate systems (i.e. a parameter set describing the  $\Lambda K^+$  &  $\bar{\Lambda} K^-$  system, and a separate set describing the  $\Lambda K^-$  &  $\bar{\Lambda} K^+$  system). For each centrality, a radius and  $\lambda$  parameters are shared between all pairs ( $\Lambda K^+$ ,  $\bar{\Lambda} K^-$ ,  $\Lambda K^-$ ,  $\bar{\Lambda} K^+$ ). Each analysis has a unique normalization parameter. The background is modeled by a (6<sup>th</sup>-)degree polynomial fit to THERMINATOR simulation. The black solid line represents the “raw” fit, i.e. not corrected for momentum resolution effects nor non-flat background. The green line shows the fit to the non-flat background. The purple points show the fit after momentum resolution and non-flat background corrections have been applied. The extracted fit values with uncertainties are printed.

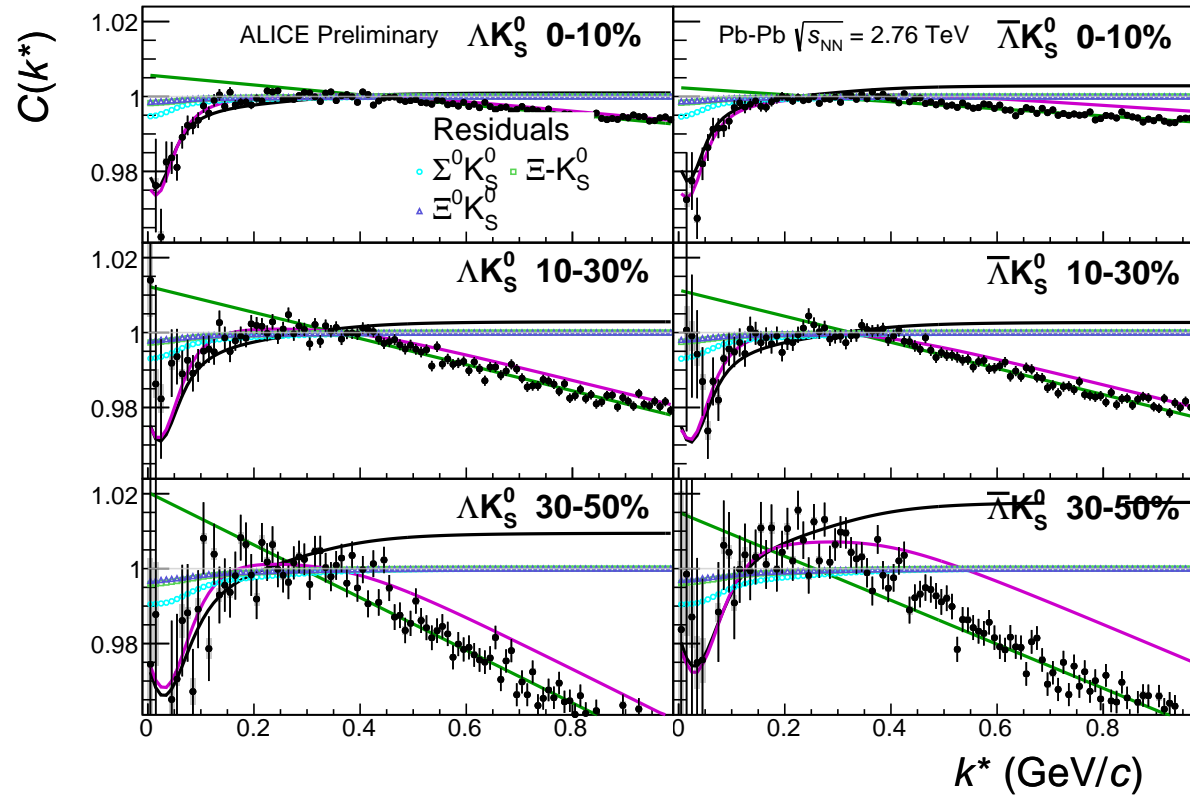
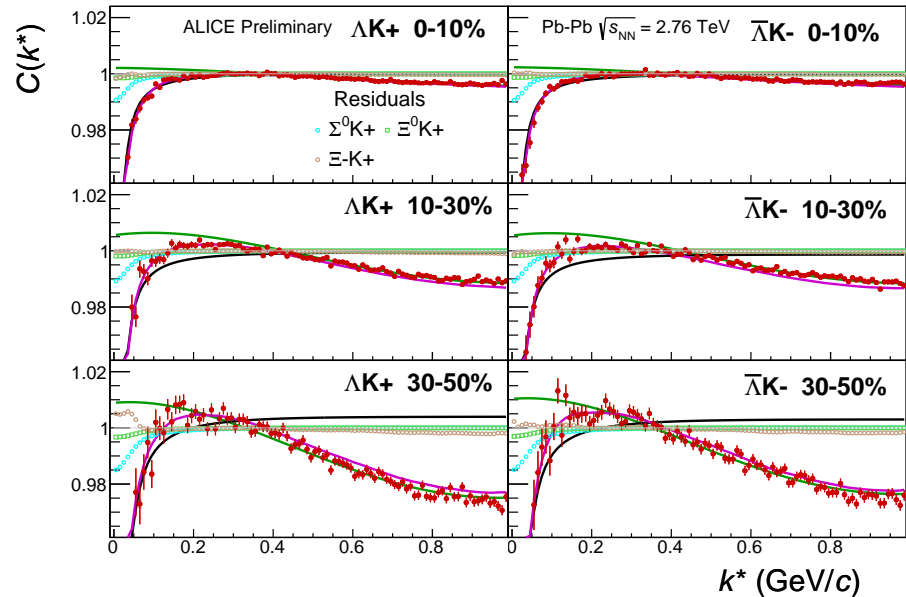
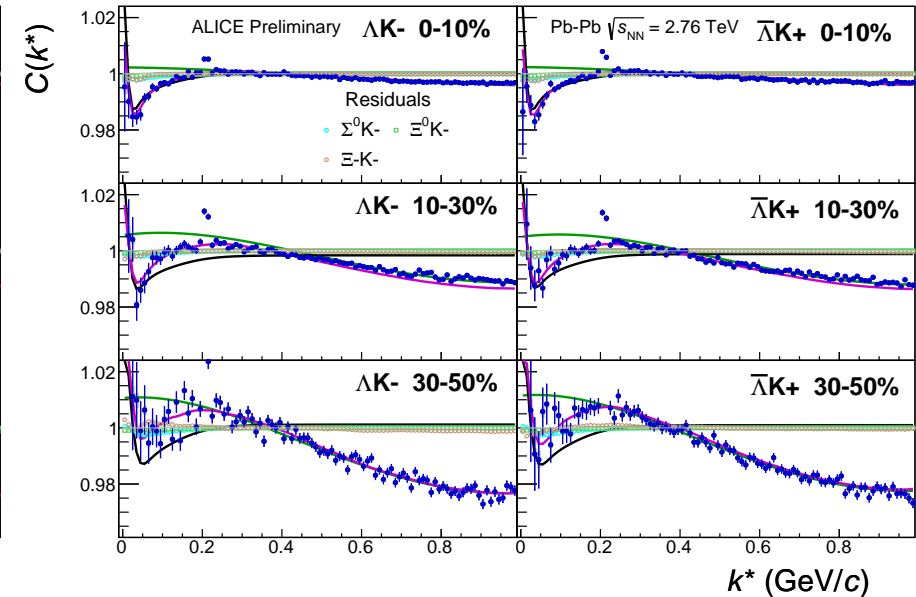


**Fig. 35:** Fits, with 3 residual correlations included and shown, to the  $\Lambda K_S^0$  (left) and  $\bar{\Lambda} K_S^0$  (right) data for the centralities 0-10% (top), 10-30% (middle), and 30-50% (bottom). The three parent pairs used for the residual correction to the  $\Lambda K_S^0$  ( $\bar{\Lambda} K_S^0$ ) fit are  $\Sigma^0 K_S^0$ ,  $\Xi^0 K_S^0$ , and  $\Xi^- K_S^0$  ( $\bar{\Sigma}^0 K_S^0$ ,  $\bar{\Xi}^0 K_S^0$ , and  $\bar{\Xi}^+ K_S^0$ ).



(a)  $\Lambda K^+(\bar{\Lambda}K^-)$  fits with residual contributions shown for the centralities 0-10% (top), 10-30% (middle), and 30-50% (bottom)



(b)  $\Lambda K^-(\bar{\Lambda}K^+)$  fits with residual contributions shown for the centralities 0-10% (top), 10-30% (middle), and 30-50% (bottom)

**Fig. 36:** Fits, with 3 residual correlations included and shown, to the  $\Lambda K^+$  &  $\bar{\Lambda}K^-$  (left) and  $\Lambda K^-$  &  $\bar{\Lambda}K^+$  (right) data for the centralities 0-10% (top), 10-30% (middle), and 30-50% (bottom). The three parent pairs used for the residual correction to the  $\Lambda K^+(\bar{\Lambda}K^-)$  fit are  $\Sigma^0 K^+$ ,  $\Xi^0 K^+$ , and  $\Xi^- K^-$  ( $\bar{\Sigma}^0 K^-$ ,  $\bar{\Xi}^0 K^-$ , and  $\bar{\Xi}^+ K^-$ ).

Fit Results $\Lambda(\bar{\Lambda})K_S^0$						
System	Centrality	Fit Parameters				
		$\lambda$	$R$	$\mathbb{R}f_0$	$\mathbb{I}f_0$	$d_0$
$\Lambda K_S^0 \text{ & } \bar{\Lambda} K_S^0$	0-10%			$3.45 \pm 1.10 \text{ (stat.)} \pm 0.45 \text{ (sys.)}$		
	10-30%	$1.10 \pm 0.50 \text{ (stat.)} \pm 0.50 \text{ (sys.)}$	$2.70 \pm 0.85 \text{ (stat.)} \pm 0.32 \text{ (sys.)}$	$-0.08 \pm 0.03 \text{ (stat.)} \pm 0.25 \text{ (sys.)}$	$0.14 \pm 0.12 \text{ (stat.)} \pm 0.13 \text{ (sys.)}$	$-1.56 \pm 4.89 \text{ (stat.)} \pm 3.53 \text{ (sys.)}$
	30-50%			$1.94 \pm 0.58 \text{ (stat.)} \pm 0.16 \text{ (sys.)}$		

**Table 9:** Fit Results  $\Lambda(\bar{\Lambda})K_S^0$ , with 3 residual correlations included. Each pair is fit simultaneously with its conjugate (ie.  $\Lambda K_S^0$  with  $\bar{\Lambda} K_S^0$ ) across all centralities (0-10%, 10-30%, 30-50%), for a total of 6 simultaneous analyses in the fit. A single  $\lambda$  parameter is shared amongst all. Each analysis has a unique normalization parameter. The radii are shared between analyses of like centrality, as these should have similar source sizes. The scattering parameters ( $\mathbb{R}f_0$ ,  $\mathbb{I}f_0$ ,  $d_0$ ) are shared amongst all. The background is fit with a linear form in the range  $0.6 < k^* < 0.9 \text{ GeV}/c$ . The fit is done on the data with only statistical error bars. The errors marked as “stat.” are those returned by MINUIT. The errors marked as “sys.” are those which result from my systematic analysis (as outlined in Section 6).

Fit Results $\Lambda(\bar{\Lambda})K^\pm$						
System	Centrality	Fit Parameters				
		$\lambda$	$R$	$\mathbb{R}f_0$	$\mathbb{I}f_0$	$d_0$
$\Lambda K^+ \text{ & } \bar{\Lambda} K^-$	0-10%	$1.12 \pm 0.32 \text{ (stat.)} \pm 0.25 \text{ (sys.)}$	$6.33 \pm 0.99 \text{ (stat.)} \pm 0.31 \text{ (sys.)}$	$-0.66 \pm 0.14 \text{ (stat.)} \pm 0.13 \text{ (sys.)}$	$0.58 \pm 0.15 \text{ (stat.)} \pm 0.11 \text{ (sys.)}$	$0.77 \pm 0.47 \text{ (stat.)} \pm 1.66 \text{ (sys.)}$
	10-30%	$0.79 \pm 0.19 \text{ (stat.)} \pm 0.23 \text{ (sys.)}$	$4.77 \pm 0.61 \text{ (stat.)} \pm 0.17 \text{ (sys.)}$			
$\Lambda K^+ \text{ & } \bar{\Lambda} K^-$	30-50%	$0.70 \pm 0.18 \text{ (stat.)} \pm 0.30 \text{ (sys.)}$	$3.47 \pm 0.46 \text{ (stat.)} \pm 0.10 \text{ (sys.)}$	$0.35 \pm 0.12 \text{ (stat.)} \pm 0.07 \text{ (sys.)}$	$0.44 \pm 0.10 \text{ (stat.)} \pm 0.08 \text{ (sys.)}$	$-4.46 \pm 1.53 \text{ (stat.)} \pm 1.36 \text{ (sys.)}$

**Table 10:** Fit Results  $\Lambda(\bar{\Lambda})K^\pm$ , with 3 residual correlations included. All  $\Lambda K^\pm$  analyses are fit simultaneously across all centralities (0-10%, 10-30%, 30-50%). Scattering parameters ( $\mathbb{R}f_0$ ,  $\mathbb{I}f_0$ ,  $d_0$ ) are shared between pair-conjugate systems (i.e. a parameter set describing the  $\Lambda K^+ \text{ & } \bar{\Lambda} K^-$  system, and a separate set describing the  $\Lambda K^- \text{ & } \bar{\Lambda} K^+$  system). For each centrality, a radius and  $\lambda$  parameters are shared between all pairs ( $\Lambda K^+, \bar{\Lambda} K^-, \Lambda K^-, \bar{\Lambda} K^+$ ). Each analysis has a unique normalization parameter. The background is modeled by a (6<sup>th</sup>-)degree polynomial fit to THERMINATOR simulation. The fit is done on the data with only statistical error bars. The errors marked as “stat.” are those returned by MINUIT. The errors marked as “sys.” are those which result from my systematic analysis (as outlined in Section 6).

### 7.1.2 10 Residual Correlations Included in Fit

Figure 37 nicely collects and summarizes all of our extracted fit parameters for the case of 10 included residual contributors. Figure 38 presents our extracted fit radii, along with those of other systems previously analyzed by ALICE [9], as a function of pair transverse mass ( $m_T$ ). Figures 39, 40, and 41 show the experimental correlation functions with fits, assuming 10 residual contributors, for all studied centralities for  $\Lambda K_S^0$  with  $\bar{\Lambda} K_S^0$ ,  $\Lambda K^+$  with  $\bar{\Lambda} K^-$ , and  $\Lambda K^-$  with  $\bar{\Lambda} K^+$ , respectively. The parameter sets extracted from the fits can be found in Tables 11 and 12.

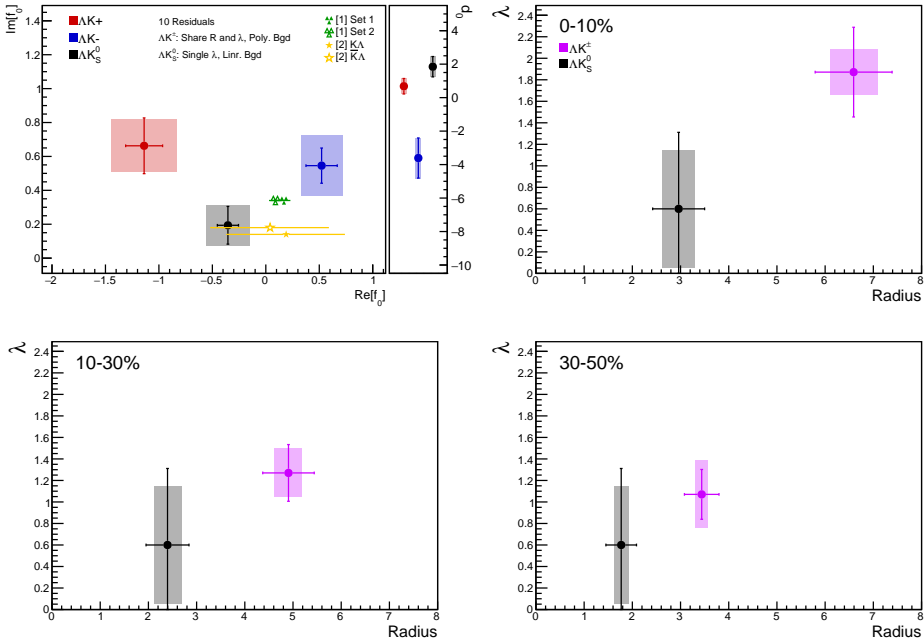


**Fig. 37:** Extracted scattering parameters for the case of 10 residual contributors for all of our AK systems. [Top Left]:  $\text{Im}[f_0]$  vs.  $\text{Re}[f_0]$ , together with  $d_0$  to the right. [Top Right (Bottom Left, Bottom Right)]:  $\lambda$  vs. Radius for the 0-10% (10-30%, 30-50%) bin. The green [10] and yellow [11] points show theoretical predictions made using chiral perturbation theory.

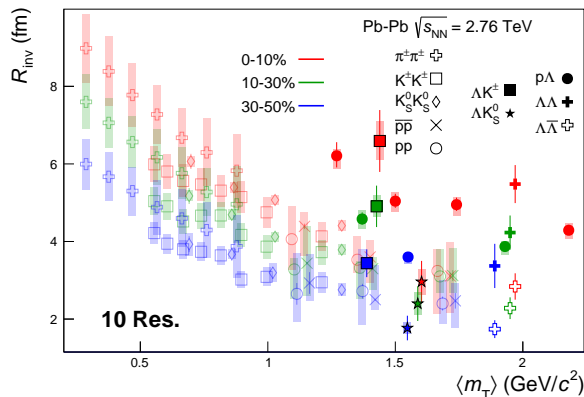
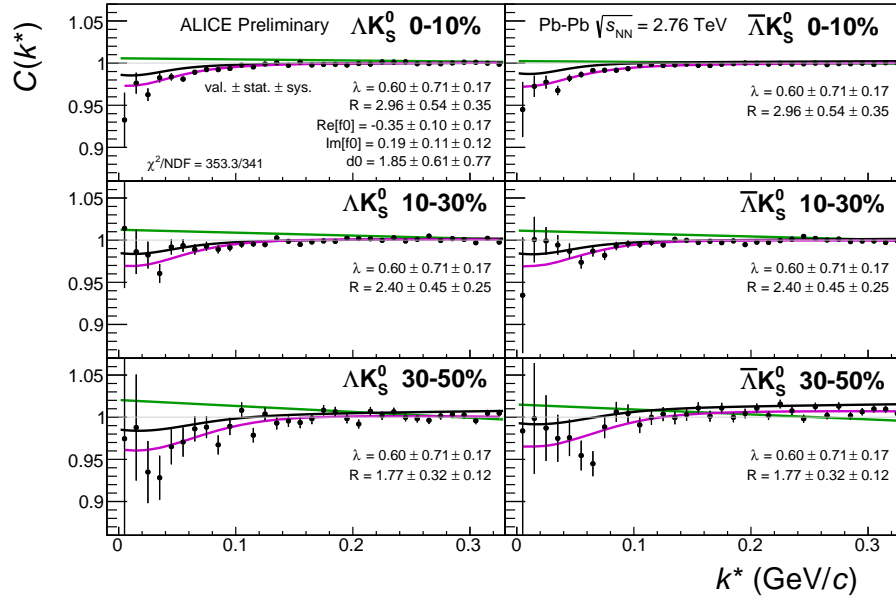
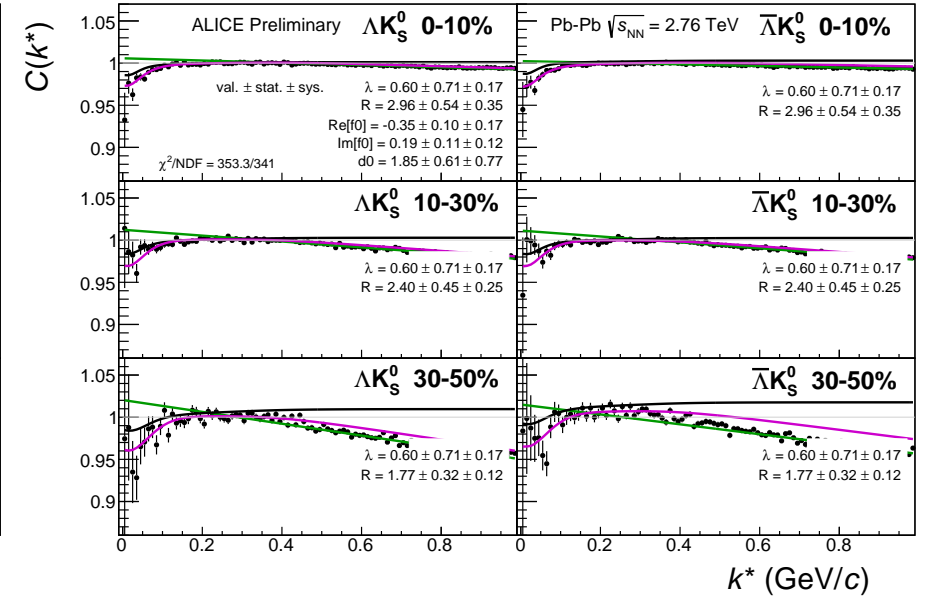


**Fig. 38:** 10 residual correlations in AK fits. Extracted fit  $R_{\text{inv}}$  parameters as a function of pair transverse mass ( $m_T$ ) for various pair systems over several centralities. The ALICE published data [9] is shown with transparent, open symbols. The new AK results are shown with opaque, filled symbols. In the left, the  $\Lambda K^+$  (with its conjugate pair) results are shown separately from the  $\Lambda K^-$  (with its conjugate pair) results. In the right, all  $\Lambda K^\pm$  results are averaged.

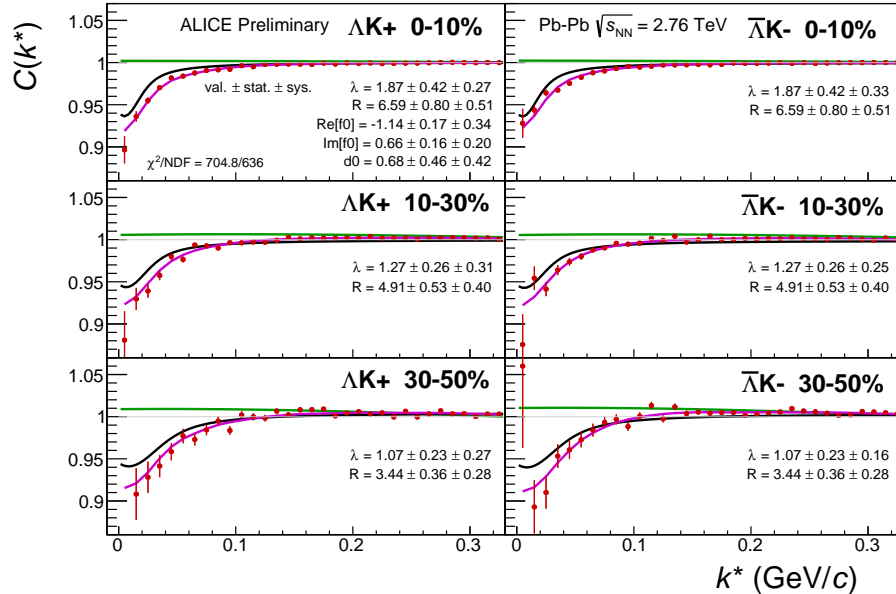


(a) Signal region view ( $k^* \lesssim 0.3 \text{ GeV}/c$ )

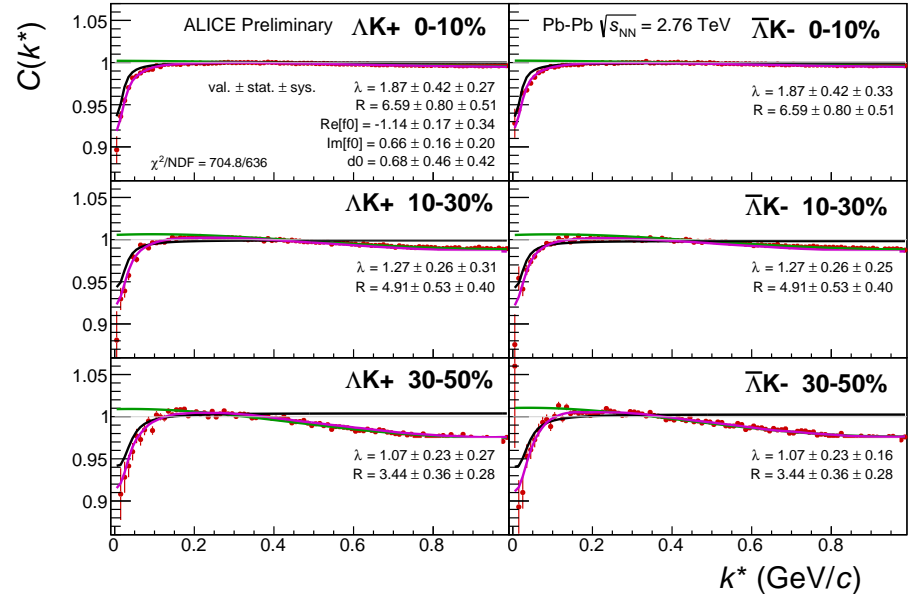


(b) Wide view ( $k^* \lesssim 1.0 \text{ GeV}/c$ )

**Fig. 39:** Fits, with 10 residual correlations included, to the  $\Lambda K_s^0$  (left) and  $\bar{\Lambda} K_s^0$  (right) data for the centralities 0-10% (top), 10-30% (middle), and 30-50% (bottom). The lines represent the statistical errors, while the boxes represent the systematic errors. A single  $\lambda$  parameter is shared amongst all. Each analysis has a unique normalization parameter. The radii are shared between analyses of like centrality, as these should have similar source sizes. The scattering parameters ( $\mathbb{R} f_0$ ,  $\mathbb{I} f_0$ ,  $d_0$ ) are shared amongst all. The background is modeled by a (6<sup>th</sup>-degree polynomial fit to THERMINATOR simulation. The black solid line represents the primary ( $\Lambda K$ ) correlation's contribution to the fit. The green line shows the fit to the non-flat background. The purple points show the fit after all residuals' contributions have been included, and momentum resolution and non-flat background corrections have been applied. The extracted fit values with uncertainties are printed.

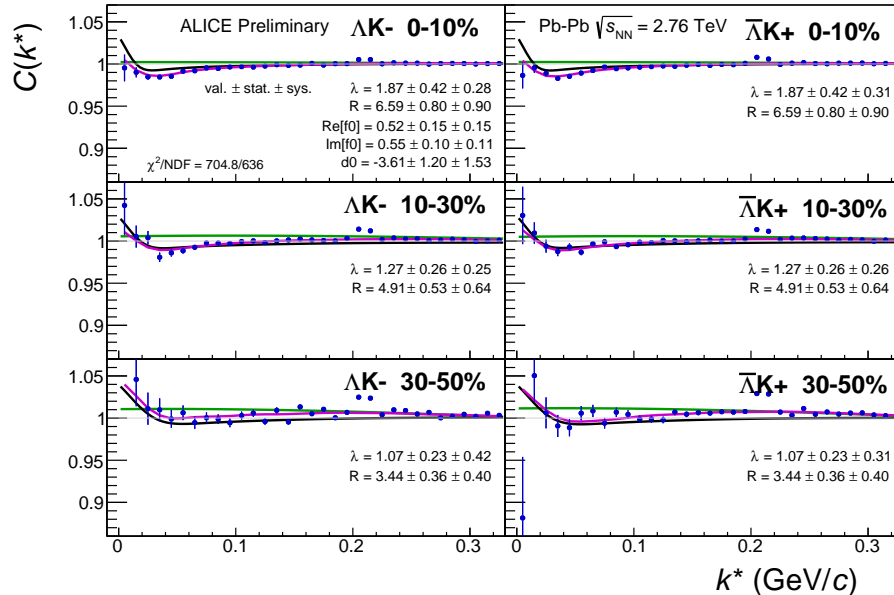


(a) Signal region view ( $k^* \lesssim 0.3 \text{ GeV}/c$ )

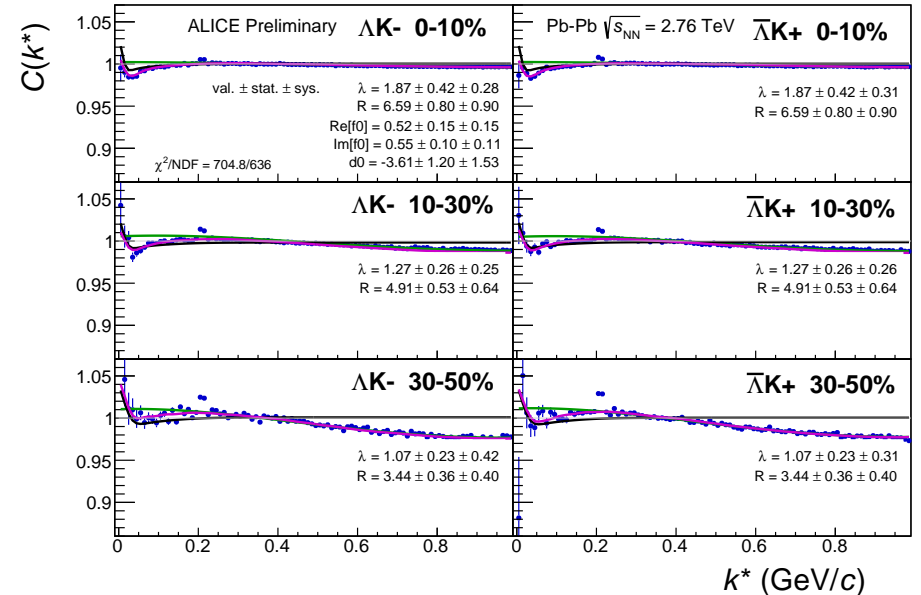


(b) Wide view ( $k^* \lesssim 1.0 \text{ GeV}/c$ )

**Fig. 40:** Fits, with 10 residual correlations included, to the  $\Lambda K^+$  (left) and  $\bar{\Lambda}K^-$  (right) data for the centralities 0-10% (top), 10-30% (middle), and 30-50% (bottom). The lines represent the statistical errors, while the boxes represent the systematic errors. All  $\Lambda K^\pm$  analyses are fit simultaneously across all centralities (0-10%, 10-30%, 30-50%). Scattering parameters ( $\text{Re}[f_0]$ ,  $\text{Im}[f_0]$ ,  $d_0$ ) are shared between pair-conjugate systems (i.e. a parameter set describing the  $\Lambda K^+$  &  $\bar{\Lambda}K^-$  system, and a separate set describing the  $\Lambda K^-$  &  $\bar{\Lambda}K^+$  system). For each centrality, a radius and  $\lambda$  parameters are shared between all pairs ( $\Lambda K^+$ ,  $\bar{\Lambda}K^-$ ,  $\Lambda K^-$ ,  $\bar{\Lambda}K^+$ ). Each analysis has a unique normalization parameter. The background is modeled by a (6<sup>th</sup>-degree polynomial fit to THERMINATOR simulation. The black solid line represents the primary ( $\Lambda K$ ) correlation's contribution to the fit. The green line shows the fit to the non-flat background. The purple points show the fit after all residuals' contributions have been included, and momentum resolution and non-flat background corrections have been applied. The extracted fit values with uncertainties are printed.



(a) Signal region view ( $k^* \lesssim 0.3 \text{ GeV}/c$ )



(b) Wide view ( $k^* \lesssim 1.0 \text{ GeV}/c$ )

**Fig. 41:** Fits, with 10 residual correlations included, to the  $\Lambda K^-$  (left) with  $\bar{\Lambda} K^+$  (right) data for the centralities 0-10% (top), 10-30% (middle), and 30-50% (bottom). The lines represent the statistical errors, while the boxes represent the systematic errors. All  $\Lambda K^\pm$  analyses are fit simultaneously across all centralities (0-10%, 10-30%, 30-50%). Scattering parameters ( $\Re f_0$ ,  $\Im f_0$ ,  $d_0$ ) are shared between pair-conjugate systems (i.e. a parameter set describing the  $\Lambda K^+$  &  $\bar{\Lambda} K^-$  system, and a separate set describing the  $\Lambda K^-$  &  $\bar{\Lambda} K^+$  system). For each centrality, a radius and  $\lambda$  parameters are shared between all pairs ( $\Lambda K^+$ ,  $\bar{\Lambda} K^-$ ,  $\Lambda K^-$ ,  $\bar{\Lambda} K^+$ ). Each analysis has a unique normalization parameter. The background is modeled by a (6<sup>th</sup>-degree polynomial fit to THERMINATOR simulation. The black solid line represents the primary ( $\Lambda K$ ) correlation's contribution to the fit. The green line shows the fit to the non-flat background. The purple points show the fit after all residuals' contributions have been included, and momentum resolution and non-flat background corrections have been applied. The extracted fit values with uncertainties are printed.

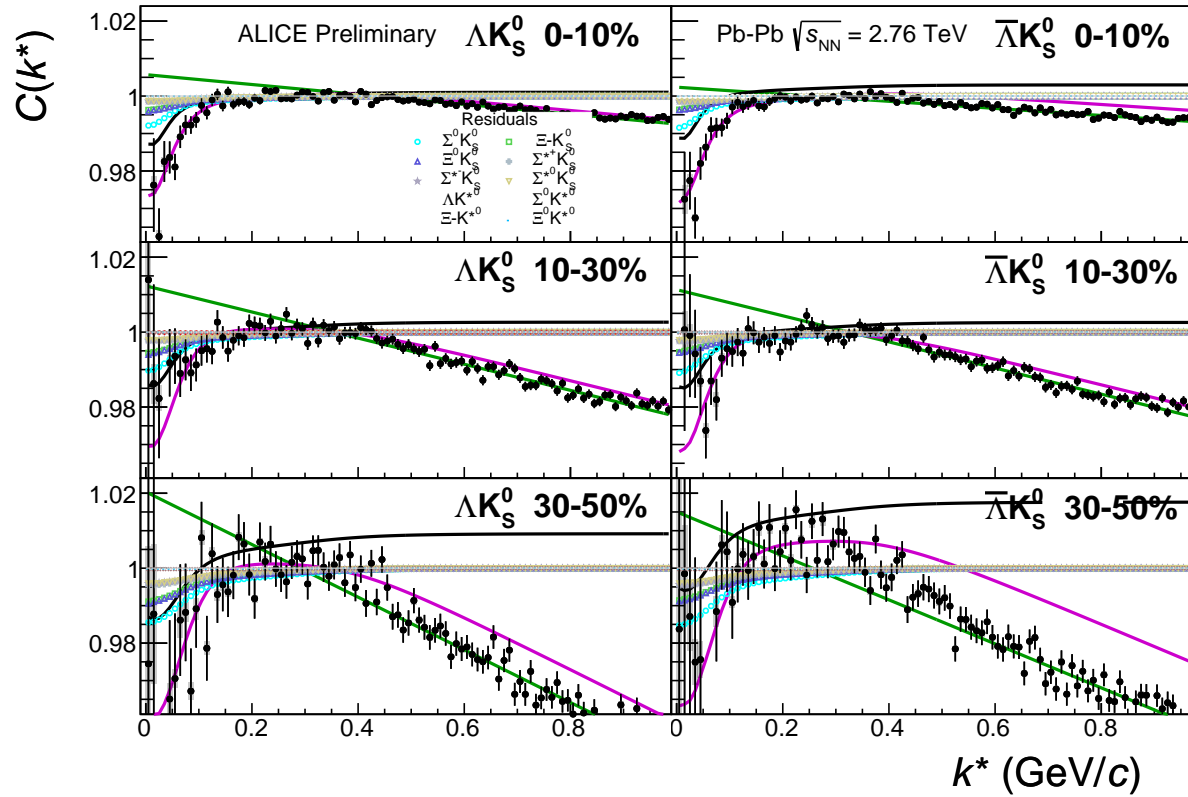
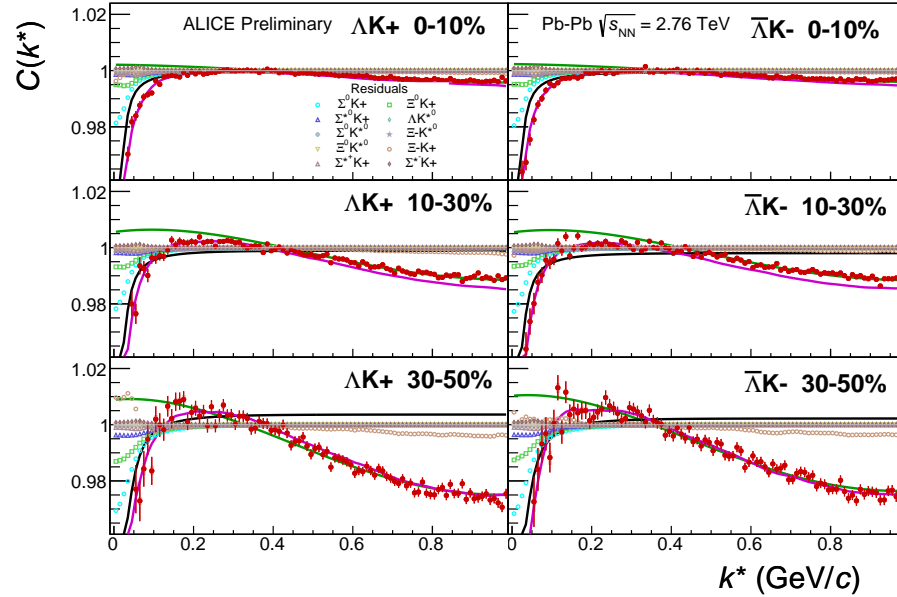
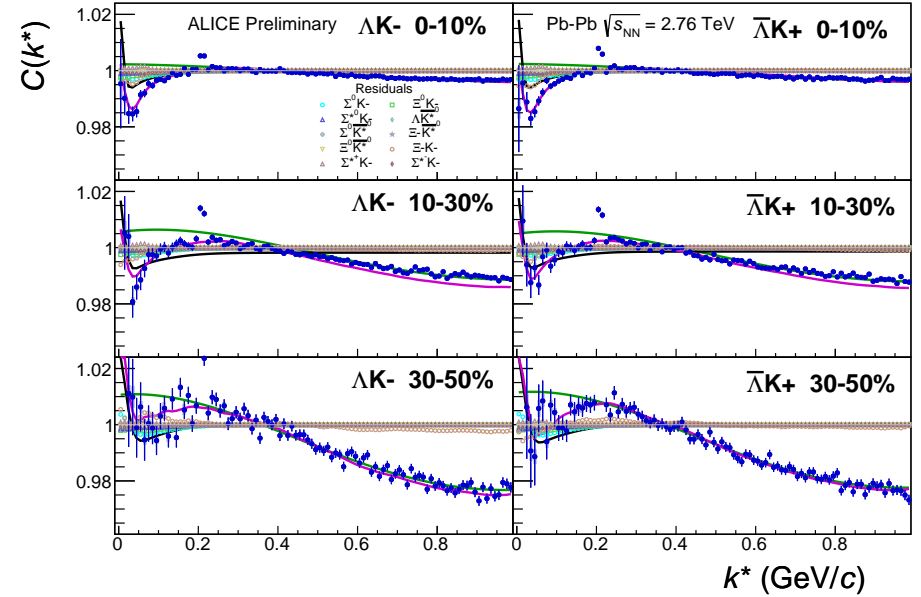


**Fig. 42:** Fits, with 10 residual correlations included and shown, to the  $\Lambda K_s^0$  (left) and  $\bar{\Lambda} K_s^0$  (right) data for the centralities 0-10% (top), 10-30% (middle), and 30-50% (bottom). The ten parent pairs used for the residual correction to the  $\Lambda K_s^0$  ( $\bar{\Lambda} K_s^0$ ) fit are  $\Sigma^0 K_S^0$ ,  $\Xi^0 K_S^0$ ,  $\Xi^- K_S^0$ ,  $\Sigma^{*(+,-,0)} K_S^0$ ,  $\Lambda K^{*0}$ ,  $\Sigma^0 K^{*0}$ ,  $\Xi^0 K^{*0}$ , and  $\Xi^- K^{*0}$  ( $\bar{\Sigma}^0 K_S^0$ ,  $\bar{\Xi}^0 K_S^0$ ,  $\bar{\Xi}^+ K_S^0$ ,  $\bar{\Sigma}^{*(+,-,0)} K_S^0$ ,  $\bar{\Lambda} \bar{K}^{*0}$ ,  $\bar{\Sigma}^0 \bar{K}^{*0}$ ,  $\bar{\Xi}^0 \bar{K}^{*0}$ , and  $\bar{\Xi}^+ \bar{K}^{*0}$ ).



(a)  $\Lambda K^+(\bar{\Lambda}K^-)$  fits with residual contributions shown for the centralities 0-10% (top), 10-30% (middle), and 30-50% (bottom)



(b)  $\Lambda K^-(\bar{\Lambda}K^+)$  fits with residual contributions shown for the centralities 0-10% (top), 10-30% (middle), and 30-50% (bottom)

**Fig. 43:** Fits, with 10 residual correlations included and shown, to the  $\Lambda K^+$  &  $\bar{\Lambda}K^-$  (left) and  $\Lambda K^-$  &  $\bar{\Lambda}K^+$  (right) data for the centralities 0-10% (top), 10-30% (middle), and 30-50% (bottom). The ten parent pairs used for the residual correction to the  $\Lambda K^+$  ( $\bar{\Lambda}K^-$ ) fit are  $\Sigma^0 K^+$ ,  $\Xi^0 K^+$ ,  $\Xi^- K^+$ ,  $\Sigma^{*(+,-,0)} K^+$ ,  $\Lambda K^{*0}$ ,  $\Sigma^0 K^{*0}$ ,  $\Xi^0 K^{*0}$ , and  $\Xi^- K^{*0}$  ( $\bar{\Sigma}^0 K^-$ ,  $\bar{\Xi}^0 K^-$ ,  $\bar{\Xi}^+ K^-$ ,  $\bar{\Sigma}^{*(+,-,0)} K^-$ ,  $\bar{\Lambda}K^{*0}$ ,  $\bar{\Sigma}^0 \bar{K}^{*0}$ ,  $\bar{\Xi}^0 \bar{K}^{*0}$ , and  $\bar{\Xi}^+ \bar{K}^{*0}$ ).

Fit Results $\Lambda(\bar{\Lambda})K_S^0$						
System	Centrality	Fit Parameters				
		$\lambda$	$R$	$\mathbb{R}f_0$	$\mathbb{I}f_0$	$d_0$
$\Lambda K_S^0 \& \bar{\Lambda} K_S^0$	0-10%					
	10-30%	$0.60 \pm 0.71$ (stat.) $\pm 0.54$ (sys.)	$2.96 \pm 0.54$ (stat.) $\pm 0.33$ (sys.)	$2.40 \pm 0.45$ (stat.) $\pm 0.29$ (sys.)	$-0.35 \pm 0.10$ (stat.) $\pm 0.21$ (sys.)	$0.19 \pm 0.11$ (stat.) $\pm 0.12$ (sys.)
	30-50%			$1.77 \pm 0.32$ (stat.) $\pm 0.15$ (sys.)		$1.85 \pm 0.61$ (stat.) $\pm 2.68$ (sys.)

**Table 11:** Fit Results  $\Lambda(\bar{\Lambda})K_S^0$ , with 10 residual correlations included. Each pair is fit simultaneously with its conjugate (ie.  $\Lambda K_S^0$  with  $\bar{\Lambda} K_S^0$ ) across all centralities (0-10%, 10-30%, 30-50%), for a total of 6 simultaneous analyses in the fit. A single  $\lambda$  parameter is shared amongst all. Each analysis has a unique normalization parameter. The radii are shared between analyses of like centrality, as these should have similar source sizes. The scattering parameters ( $\mathbb{R}f_0$ ,  $\mathbb{I}f_0$ ,  $d_0$ ) are shared amongst all. The background is fit with a linear form in the range  $0.6 < k^* < 0.9$  GeV/c. The fit is done on the data with only statistical error bars. The errors marked as “stat.” are those returned by MINUIT. The errors marked as “sys.” are those which result from my systematic analysis (as outlined in Section 6).

Fit Results $\Lambda(\bar{\Lambda})K^\pm$						
System	Centrality	Fit Parameters				
		$\lambda$	$R$	$\mathbb{R}f_0$	$\mathbb{I}f_0$	$d_0$
$\Lambda K^+ \& \bar{\Lambda} K^-$	0-10%	$1.87 \pm 0.42$ (stat.) $\pm 0.21$ (sys.)	$6.59 \pm 0.80$ (stat.) $\pm 0.49$ (sys.)	$-1.14 \pm 0.17$ (stat.) $\pm 0.31$ (sys.)	$0.66 \pm 0.16$ (stat.) $\pm 0.15$ (sys.)	$0.68 \pm 0.46$ (stat.) $\pm 0.53$ (sys.)
	10-30%	$1.27 \pm 0.26$ (stat.) $\pm 0.23$ (sys.)	$4.91 \pm 0.53$ (stat.) $\pm 0.28$ (sys.)			
$\Lambda K^+ \& \bar{\Lambda} K^-$	30-50%	$1.07 \pm 0.23$ (stat.) $\pm 0.32$ (sys.)	$3.44 \pm 0.36$ (stat.) $\pm 0.13$ (sys.)	$0.52 \pm 0.15$ (stat.) $\pm 0.19$ (sys.)	$0.55 \pm 0.10$ (stat.) $\pm 0.18$ (sys.)	$-3.61 \pm 1.20$ (stat.) $\pm 1.02$ (sys.)

**Table 12:** Fit Results  $\Lambda(\bar{\Lambda})K^\pm$ , with 10 residual correlations included. All  $\Lambda K^\pm$  analyses are fit simultaneously across all centralities (0-10%, 10-30%, 30-50%). Scattering parameters ( $\mathbb{R}f_0$ ,  $\mathbb{I}f_0$ ,  $d_0$ ) are shared between pair-conjugate systems (i.e. a parameter set describing the  $\Lambda K^+$  &  $\bar{\Lambda} K^-$  system, and a separate set describing the  $\Lambda K^-$  &  $\bar{\Lambda} K^+$  system). For each centrality, a radius and  $\lambda$  parameters are shared between all pairs ( $\Lambda K^+$ ,  $\bar{\Lambda} K^-$ ,  $\Lambda K^-$ ,  $\bar{\Lambda} K^+$ ). Each analysis has a unique normalization parameter. The background is modeled by a (6<sup>th</sup>-)degree polynomial fit to THERMINATOR simulation. The fit is done on the data with only statistical error bars. The errors marked as “stat.” are those returned by MINUIT. The errors marked as “sys.” are those which result from my systematic analysis (as outlined in Section 6).

691 **7.1.3 No Residual Correlations Included in Fit**

692 Figure 44 nicely collects and summarizes all of our extracted fit parameters for the case of no included  
 693 residual contributors. Figure 45 presents our extracted fit radii, along with those of other systems pre-  
 694 viously analyzed by ALICE [9], as a function of pair transverse mass ( $m_T$ ). Figures 46, 47, and 48  
 695 show the experimental correlation functions with fits, assuming no residual contributors, for all studied  
 696 centralities for  $\Lambda K_S^0$  with  $\bar{\Lambda} K_S^0$ ,  $\Lambda K^+$  with  $\bar{\Lambda} K^-$ , and  $\Lambda K^-$  with  $\bar{\Lambda} K^+$ , respectively. The parameter sets  
 697 extracted from the fits can be found in Tables 13 and 14.

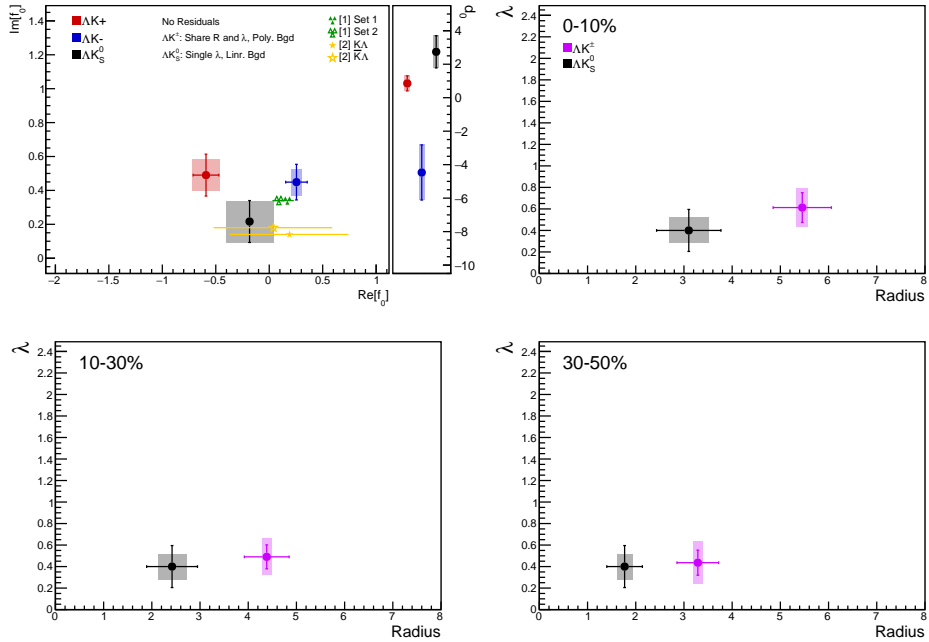


**Fig. 44:** Extracted scattering parameters for the case of NO residual contributors for all of our  $\Lambda K$  systems. [Top Left]:  $\Im f_0$  vs.  $\Re f_0$ , together with  $d_0$  to the right. [Top Right (Bottom Left, Bottom Right)]:  $\lambda$  vs. Radius for the 0-10% (10-30%, 30-50%) bin. The green [10] and yellow [11] points show theoretical predictions made using chiral perturbation theory.

698 Figure 45 shows extracted  $R_{\text{inv}}$  parameters as a function of tranverse mass ( $m_T$ ) for various pair systems  
 699 over several centralities. The published ALICE data [9] is shown with transparent, open symbols. The  
 700 new  $\Lambda K$  results are shown with opaque, filled symbols. The radii shown an increasing size with increas-  
 701 ing centrality, as is expected from the simple geometric picture of the collisions. The radii decrease  
 702 in size with increasing  $m_T$ , and we see an approximate scaling of the radii with transverse mass, as is  
 703 expected in the presence of collective flow in the system.

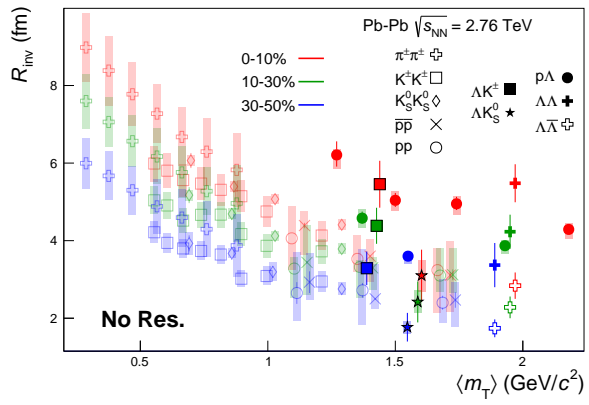
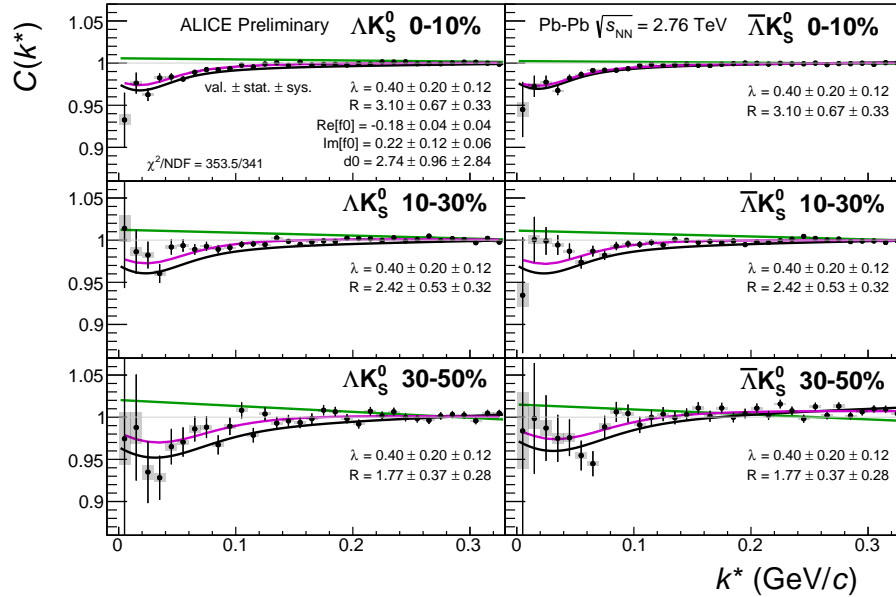
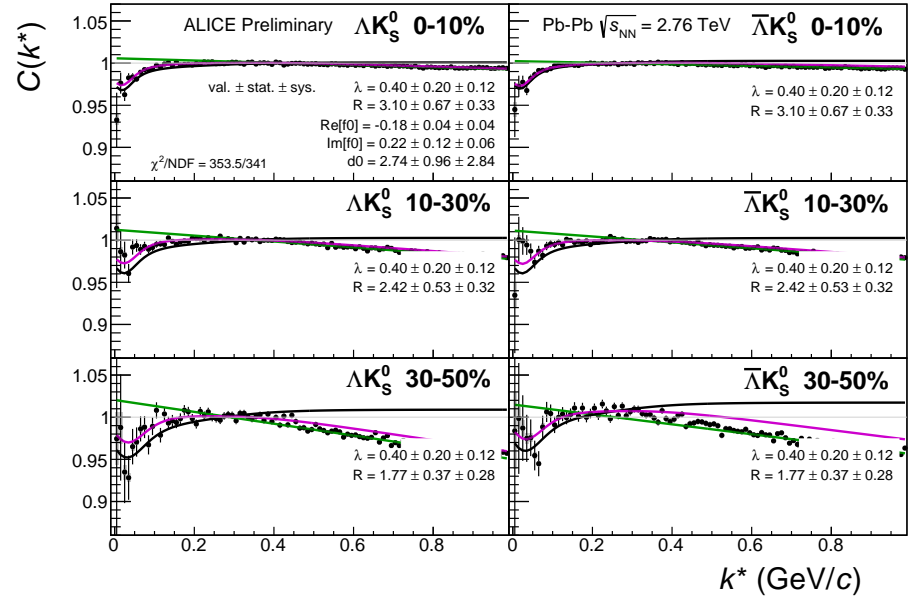


**Fig. 45:** No residual correlations in  $\Lambda K$  fits. Extracted fit  $R_{\text{inv}}$  parameters as a function of pair transverse mass ( $m_T$ ) for various pair systems over several centralities. The ALICE published data [9] is shown with transparent, open symbols. The new  $\Lambda K$  results are shown with opaque, filled symbols. In the left, the  $\Lambda K^+$  (with its conjugate pair) results are shown separately from the  $\Lambda K^-$  (with its conjugate pair) results. In the right, all  $\Lambda K^\pm$  results are averaged.

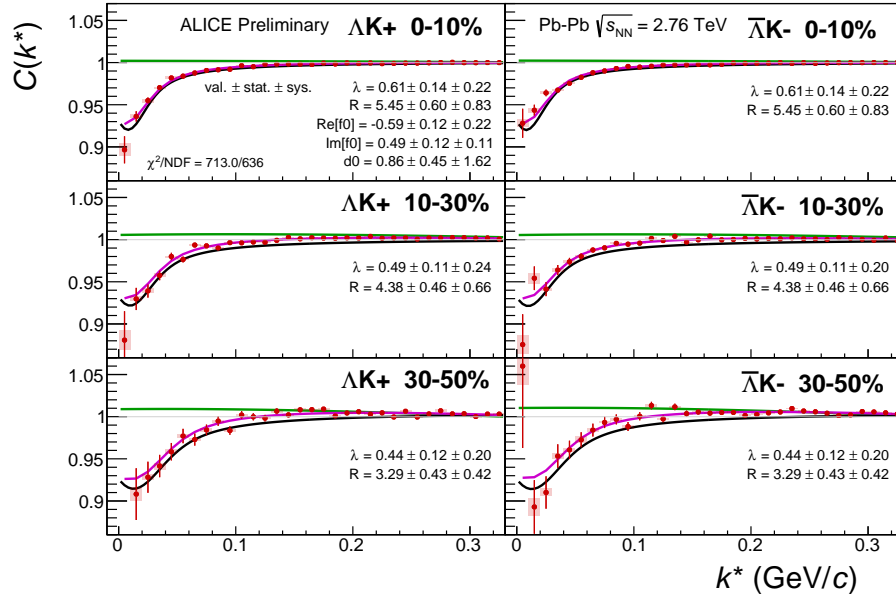


(a) Signal region view ( $k^* \lesssim 0.3 \text{ GeV}/c$ )

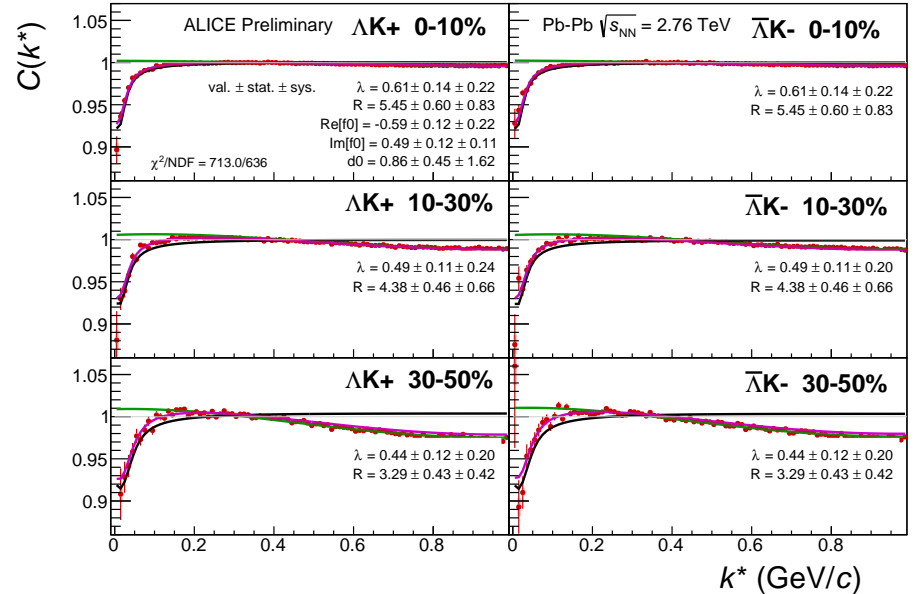


(b) Wide view ( $k^* \lesssim 1.0 \text{ GeV}/c$ )

**Fig. 46:** Fits, with NO residual correlations included, to the  $\Lambda K_s^0$  (left) and  $\bar{\Lambda} K_s^0$  (right) data for the centralities 0-10% (top), 10-30% (middle), and 30-50% (bottom). The lines represent the statistical errors, while the boxes represent the systematic errors. A single  $\lambda$  parameter is shared amongst all. Each analysis has a unique normalization parameter. The radii are shared between analyses of like centrality, as these should have similar source sizes. The scattering parameters ( $\mathbb{R} f_0, \mathbb{I} f_0, d_0$ ) are shared amongst all. The background is modeled by a (6<sup>th</sup>-)degree polynomial fit to THERMINATOR simulation. The black solid line represents the “raw” primary fit, i.e. not corrected for momentum resolution effects nor non-flat background. The green line shows the fit to the non-flat background. The purple points show the fit after momentum resolution and non-flat background corrections have been applied. The extracted fit values with uncertainties are printed.

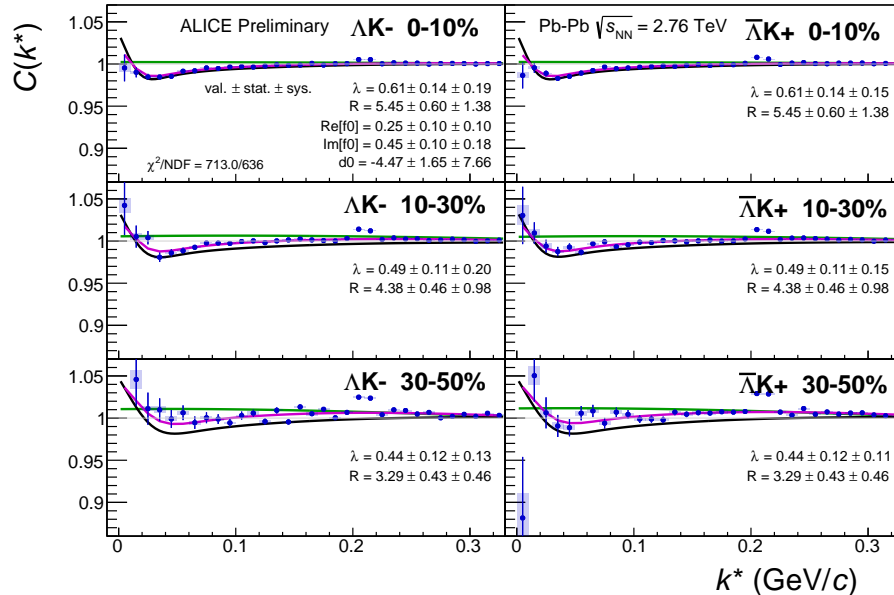


(a) Signal region view ( $k^* \lesssim 0.3 \text{ GeV}/c$ )

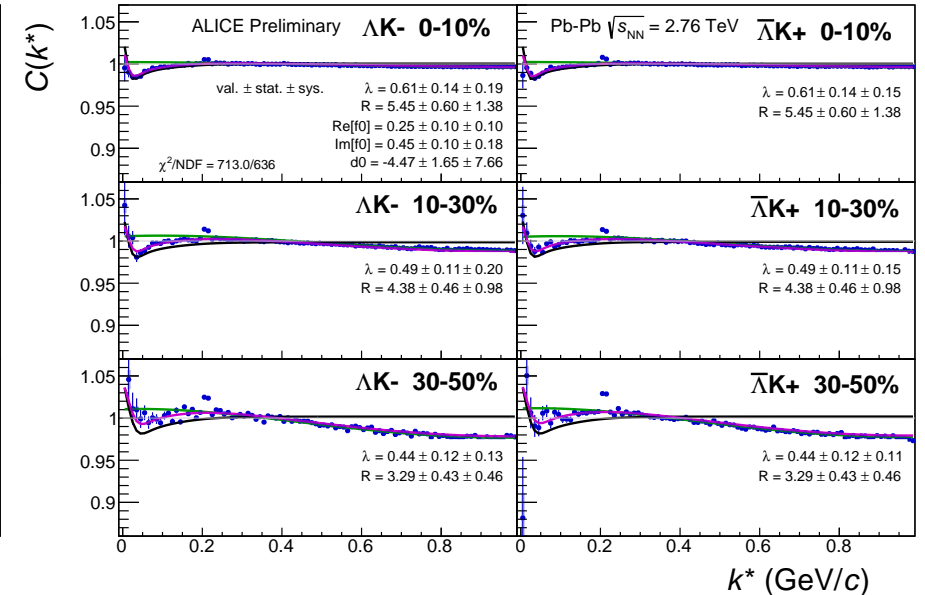


(b) Wide view ( $k^* \lesssim 1.0 \text{ GeV}/c$ )

**Fig. 47:** Fits to the  $\Delta K^+$  (left) and  $\bar{\Delta}K^-$  (right) data for the centralities 0-10% (top), 10-30% (middle), and 30-50% (bottom). The lines represent the statistical errors, while the boxes represent the systematic errors. All  $\Delta K^\pm$  analyses are fit simultaneously across all centralities (0-10%, 10-30%, 30-50%). Scattering parameters ( $\text{Re}[f_0]$ ,  $\text{Im}[f_0]$ ,  $d_0$ ) are shared between pair-conjugate systems (i.e. a parameter set describing the  $\Delta K^+$  &  $\bar{\Delta}K^-$  system, and a separate set describing the  $\Delta K^-$  &  $\bar{\Delta}K^+$  system). For each centrality, a radius and  $\lambda$  parameters are shared between all pairs ( $\Delta K^+$ ,  $\bar{\Delta}K^-$ ,  $\Delta K^-$ ,  $\bar{\Delta}K^+$ ). Each analysis has a unique normalization parameter. The background is modeled by a (6<sup>th</sup>-degree polynomial fit to THERMINATOR simulation. The black solid line represents the “raw” primary fit, i.e. not corrected for momentum resolution effects nor non-flat background. The green line shows the fit to the non-flat background. The purple points show the fit after momentum resolution and non-flat background corrections have been applied. The extracted fit values with uncertainties are printed.



(a) Signal region view ( $k^* \lesssim 0.3 \text{ GeV}/c$ )



(b) Wide view ( $k^* \lesssim 1.0 \text{ GeV}/c$ )

**Fig. 48:** Fits, with NO residual correlations included, to the  $\Lambda K^-$  (left) with  $\bar{\Lambda} K^+$  (right) data for the centralities 0-10% (top), 10-30% (middle), and 30-50% (bottom). The lines represent the statistical errors, while the boxes represent the systematic errors. All  $\Lambda K^\pm$  analyses are fit simultaneously across all centralities (0-10%, 10-30%, 30-50%). Scattering parameters ( $\Re f_0$ ,  $\Im f_0$ ,  $d_0$ ) are shared between pair-conjugate systems (i.e. a parameter set describing the  $\Lambda K^+$  &  $\bar{\Lambda} K^-$  system, and a separate set describing the  $\Lambda K^-$  &  $\bar{\Lambda} K^+$  system). For each centrality, a radius and  $\lambda$  parameters are shared between all pairs ( $\Lambda K^+$ ,  $\bar{\Lambda} K^-$ ,  $\Lambda K^-$ ,  $\bar{\Lambda} K^+$ ). Each analysis has a unique normalization parameter. The background is modeled by a (6<sup>th</sup>-degree polynomial fit to THERMINATOR simulation. The black solid line represents the “raw” primary fit, i.e. not corrected for momentum resolution effects nor non-flat background. The green line shows the fit to the non-flat background. The purple points show the fit after momentum resolution and non-flat background corrections have been applied. The extracted fit values with uncertainties are printed.

Fit Results $\Lambda(\bar{\Lambda})K_S^0$						
System	Centrality	Fit Parameters				
		$\lambda$	$R$	$\mathbb{R}f_0$	$\mathbb{I}f_0$	$d_0$
$\Lambda K_S^0 \& \bar{\Lambda} K_S^0$	0-10%			$3.10 \pm 0.67$ (stat.) $\pm 0.41$ (sys.)		
	10-30%	$0.40 \pm 0.20$ (stat.) $\pm 0.12$ (sys.)	$2.42 \pm 0.53$ (stat.) $\pm 0.29$ (sys.)	$-0.18 \pm 0.04$ (stat.) $\pm 0.22$ (sys.)	$0.22 \pm 0.12$ (stat.) $\pm 0.12$ (sys.)	$2.74 \pm 0.96$ (stat.) $\pm 1.28$ (sys.)
	30-50%			$1.77 \pm 0.37$ (stat.) $\pm 0.16$ (sys.)		

**Table 13:** Fit Results  $\Lambda(\bar{\Lambda})K_S^0$ , with no residual correlations included. Each pair is fit simultaneously with its conjugate (ie.  $\Lambda K_S^0$  with  $\bar{\Lambda} K_S^0$ ) across all centralities (0-10%, 10-30%, 30-50%), for a total of 6 simultaneous analyses in the fit. A single  $\lambda$  parameter is shared amongst all. Each analysis has a unique normalization parameter. The radii are shared between analyses of like centrality, as these should have similar source sizes. The scattering parameters ( $\mathbb{R}f_0$ ,  $\mathbb{I}f_0$ ,  $d_0$ ) are shared amongst all. The background is fit with a linear form in the range  $0.6 < k^* < 0.9$  GeV/c. The fit is done on the data with only statistical error bars. The errors marked as “stat.” are those returned by MINUIT. The errors marked as “sys.” are those which result from my systematic analysis (as outlined in Section 6).

Fit Results $\Lambda(\bar{\Lambda})K^\pm$						
System	Centrality	Fit Parameters				
		$\lambda$	$R$	$\mathbb{R}f_0$	$\mathbb{I}f_0$	$d_0$
$\Lambda K^+ \& \bar{\Lambda} K^-$	0-10%	$0.61 \pm 0.14$ (stat.) $\pm 0.18$ (sys.)	$5.45 \pm 0.60$ (stat.) $\pm 0.12$ (sys.)	$-0.59 \pm 0.12$ (stat.) $\pm 0.13$ (sys.)	$0.49 \pm 0.12$ (stat.) $\pm 0.09$ (sys.)	$0.86 \pm 0.45$ (stat.) $\pm 1.63$ (sys.)
	10-30%	$0.49 \pm 0.11$ (stat.) $\pm 0.17$ (sys.)	$4.38 \pm 0.46$ (stat.) $\pm 0.10$ (sys.)			
$\Lambda K^+ \& \bar{\Lambda} K^+$	30-50%	$0.44 \pm 0.12$ (stat.) $\pm 0.20$ (sys.)	$3.29 \pm 0.43$ (stat.) $\pm 0.10$ (sys.)	$0.25 \pm 0.10$ (stat.) $\pm 0.05$ (sys.)	$0.45 \pm 0.10$ (stat.) $\pm 0.08$ (sys.)	$-4.47 \pm 1.65$ (stat.) $\pm 1.60$ (sys.)

**Table 14:** Fit Results  $\Lambda(\bar{\Lambda})K^\pm$ , with no residual correlations included. All  $\Lambda K^\pm$  analyses are fit simultaneously across all centralities (0-10%, 10-30%, 30-50%). Scattering parameters ( $\mathbb{R}f_0$ ,  $\mathbb{I}f_0$ ,  $d_0$ ) are shared between pair-conjugate systems (i.e. a parameter set describing the  $\Lambda K^+ \& \bar{\Lambda} K^-$  system, and a separate set describing the  $\Lambda K^- \& \bar{\Lambda} K^+$  system). For each centrality, a radius and  $\lambda$  parameters are shared between all pairs ( $\Lambda K^+, \bar{\Lambda} K^-, \Lambda K^-, \bar{\Lambda} K^+$ ). Each analysis has a unique normalization parameter. The background is modeled by a (6<sup>th</sup>-)degree polynomial fit to THERMINATOR simulation. The fit is done on the data with only statistical error bars. The errors marked as “stat.” are those returned by MINUIT. The errors marked as “sys.” are those which result from my systematic analysis (as outlined in Section 6).

704 **7.1.4 Fit Method Comparisons**

705 In Figure 49, we show extracted fit parameters for the case of  $\Lambda K^+(\bar{\Lambda} K^-)$  sharing radii with  $\Lambda K^-(\bar{\Lambda} K^+)$ .  
 706 The figure shows results for three different treatments of the non-femtoscopic background: a polynomial  
 707 fit to THERMINATOR 2 simulation to model the background (circles), a linear fit to the data to model  
 708 the background (squares), and the Stavinskiy method (crosses).

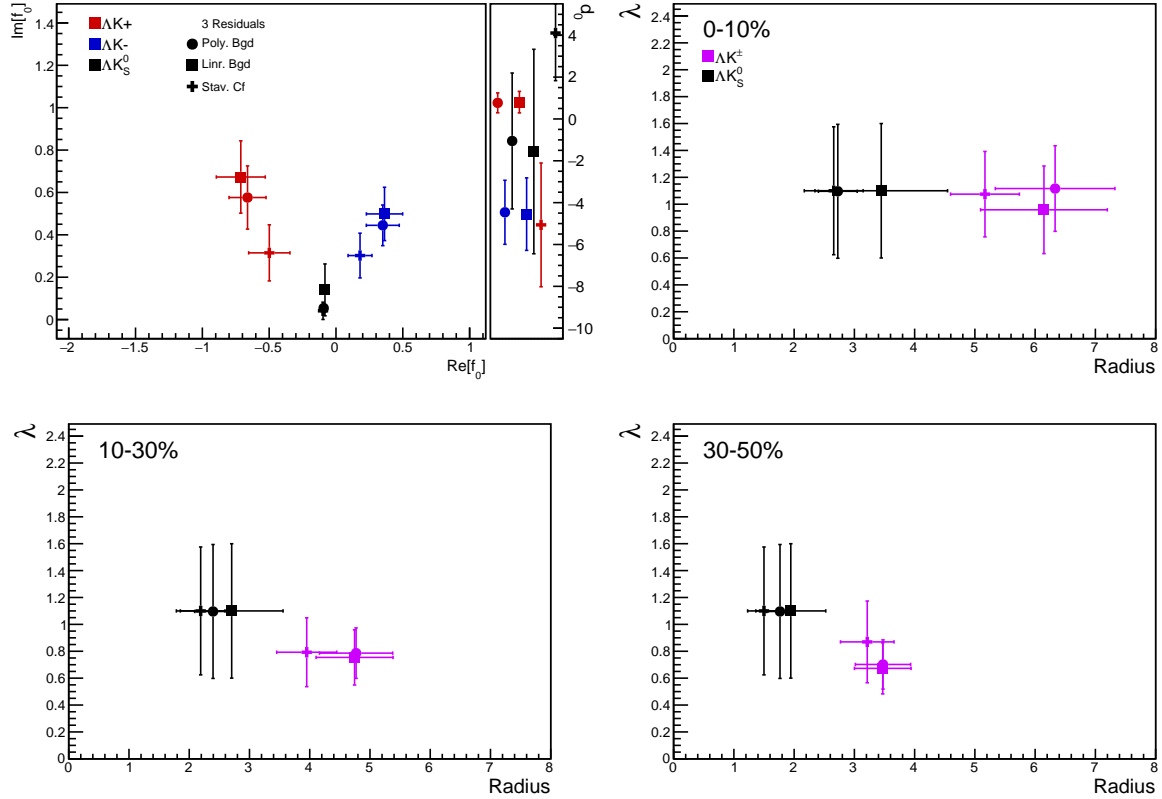


**Fig. 49:** Compare Fit Parameters: Background treatment: Extracted fit results for all of our  $\Lambda(\bar{\Lambda})K^\pm$  systems across all studied centrality bins (0-10%, 10-30%, 30-50%). The  $\Lambda K^+(\bar{\Lambda} K^-)$  and  $\Lambda K^-(\bar{\Lambda} K^+)$  systems share both a radius and a  $\lambda$  parameter for each centrality bin (i.e. 3 total radius parameters, 3 total  $\lambda$  parameters). The figure shows results for three different treatments of the non-femtoscopic background: a polynomial fit to THERMINATOR 2 simulation to model the background (circles), a linear fit to the data to model the background (squares), and the Stavinskiy method (crosses). The green [10] and yellow [11] points show theoretical predictions made using chiral perturbation theory.

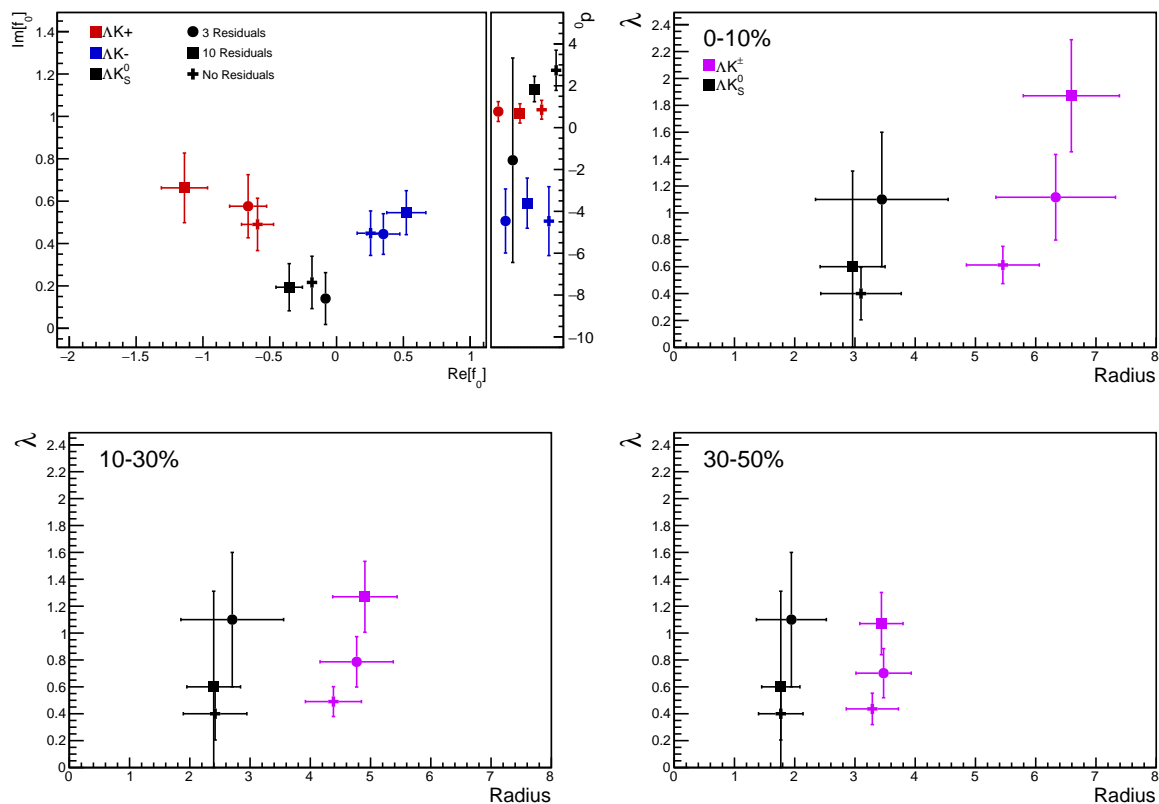


**Fig. 50:** Compare Fit Parameters: Number of residuals: Results shown for the case of 3 (+), 10 (X), and no (circles) residual contributors.

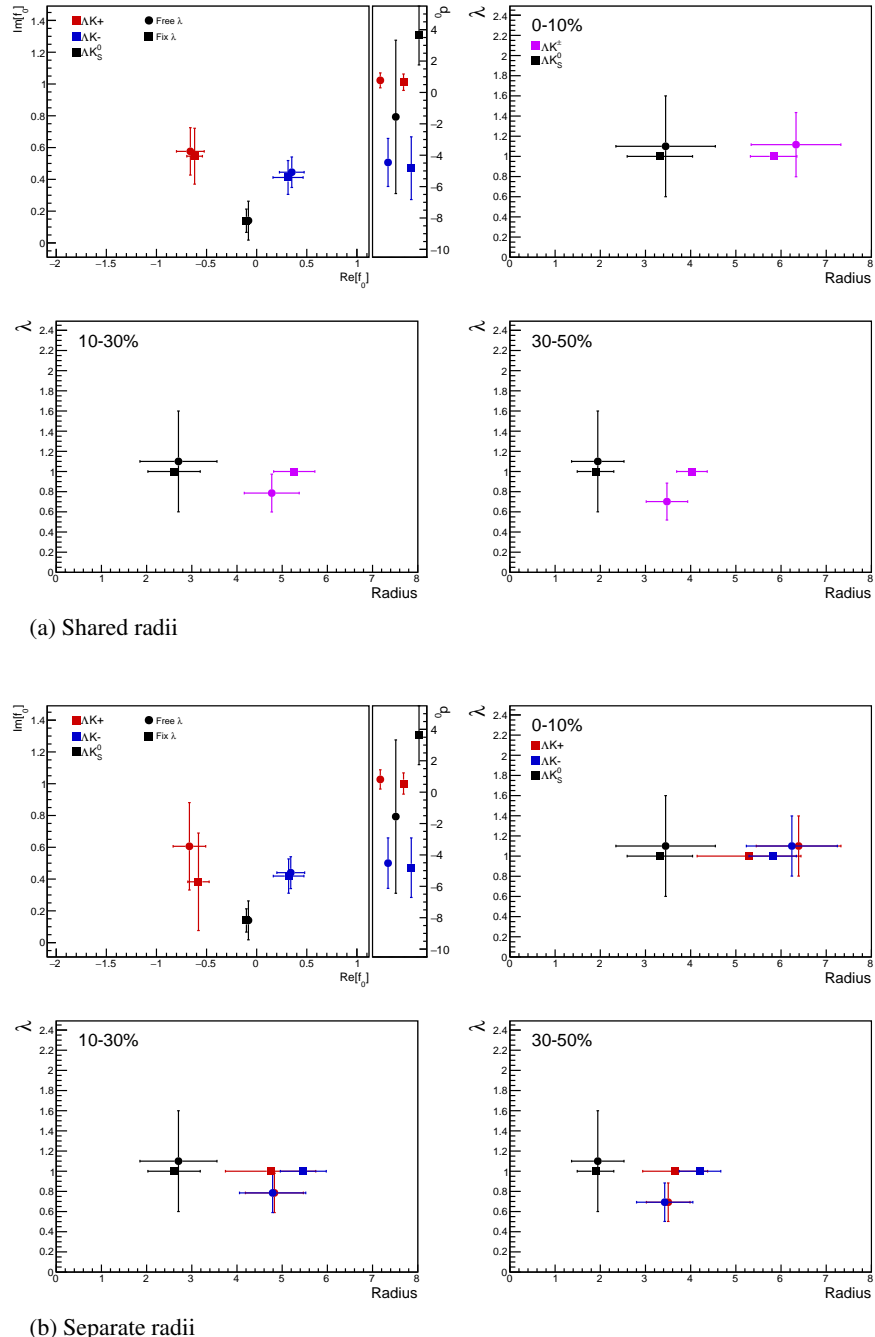


**Fig. 51:** Compare Fit Parameters: Free vs fixed  $\lambda$ : Results shown for  $\lambda$  parameters left free (filled symbols) and fixed to 1 (open symbols). In the top plot (51a), the  $\Lambda K^+$  and  $\Lambda K^-$  analyses share radii, whereas in the bottom (51b) they have unique radii.

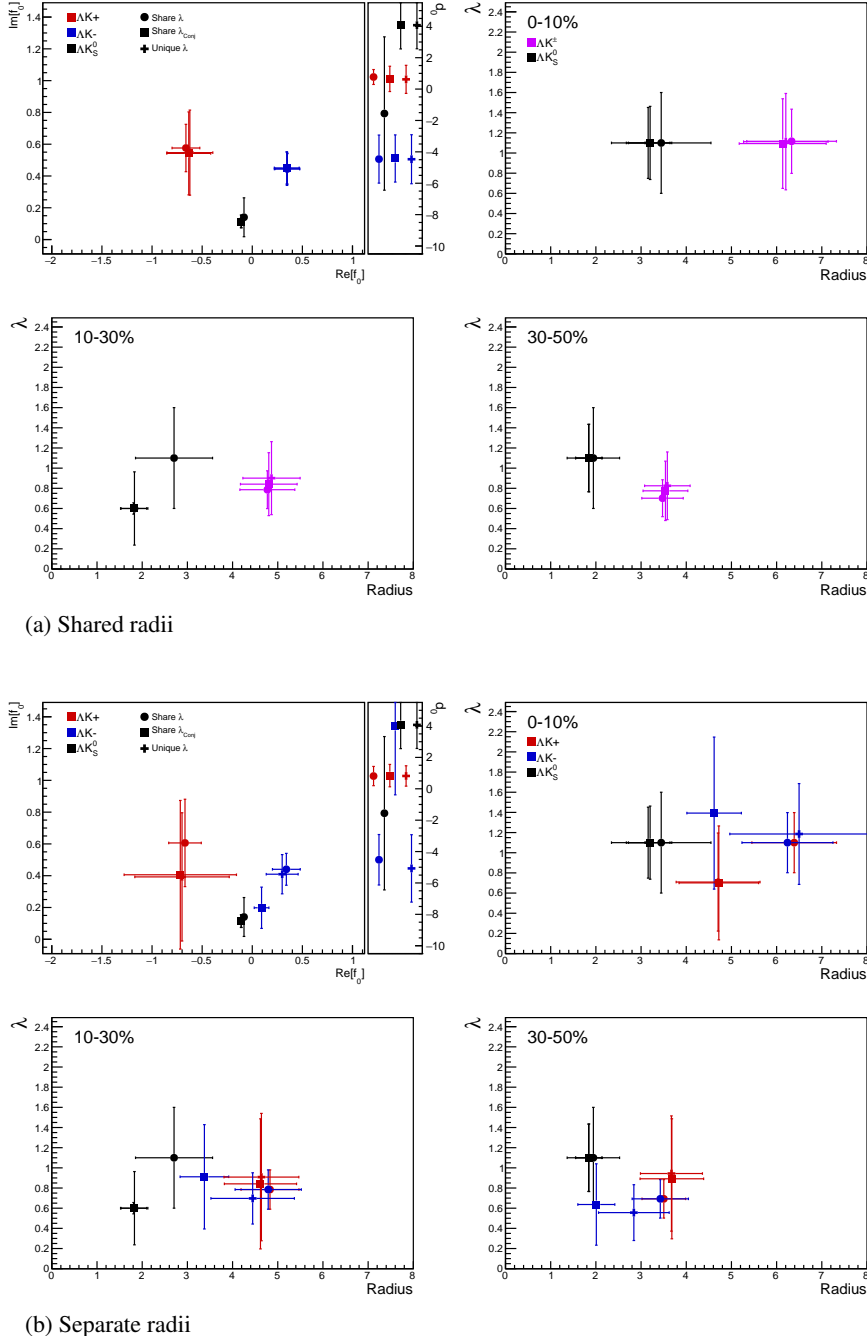


**Fig. 52:** Compare Fit Parameters: Shared vs unique  $\lambda$ : Results shown for different sharing of the  $\lambda$  parameters between analyses and systems. In the top (52a), the  $\Lambda K^+$  and  $\bar{\Lambda} K^-$  analyses share radii, whereas in the bottom (52b), they do not. “Share  $\lambda$ ” (circles) is the case where a single  $\lambda$  is shared amongst all analyses for a given centrality bin (i.e., in 52a, 3 radius parameters and 3  $\lambda$  parameters). “Share  $\lambda_{Conj}$ ” (squares) means that conjugate pairs (ex.  $\Lambda K^+$  and  $\bar{\Lambda} K^-$ ) share a  $\lambda$  parameter for each centrality. This corresponds to 6 total  $\lambda$  parameters (for each of the 3 centrality bins, the  $\Lambda K^+(\bar{\Lambda} K^-)$  receives a unique  $\lambda$ , as does  $\Lambda K^-(\bar{\Lambda} K^+)$ ). Finally, in “Unique  $\lambda$ ” (+), each analysis received its own unique  $\lambda$  parameter. This corresponds to 12  $\lambda$  parameters (for each of the 3 centrality bins, each  $\Lambda K^+$ ,  $\bar{\Lambda} K^-$ ,  $\Lambda K^-$ , and  $\bar{\Lambda} K^+$  receives a unique  $\lambda$ ).

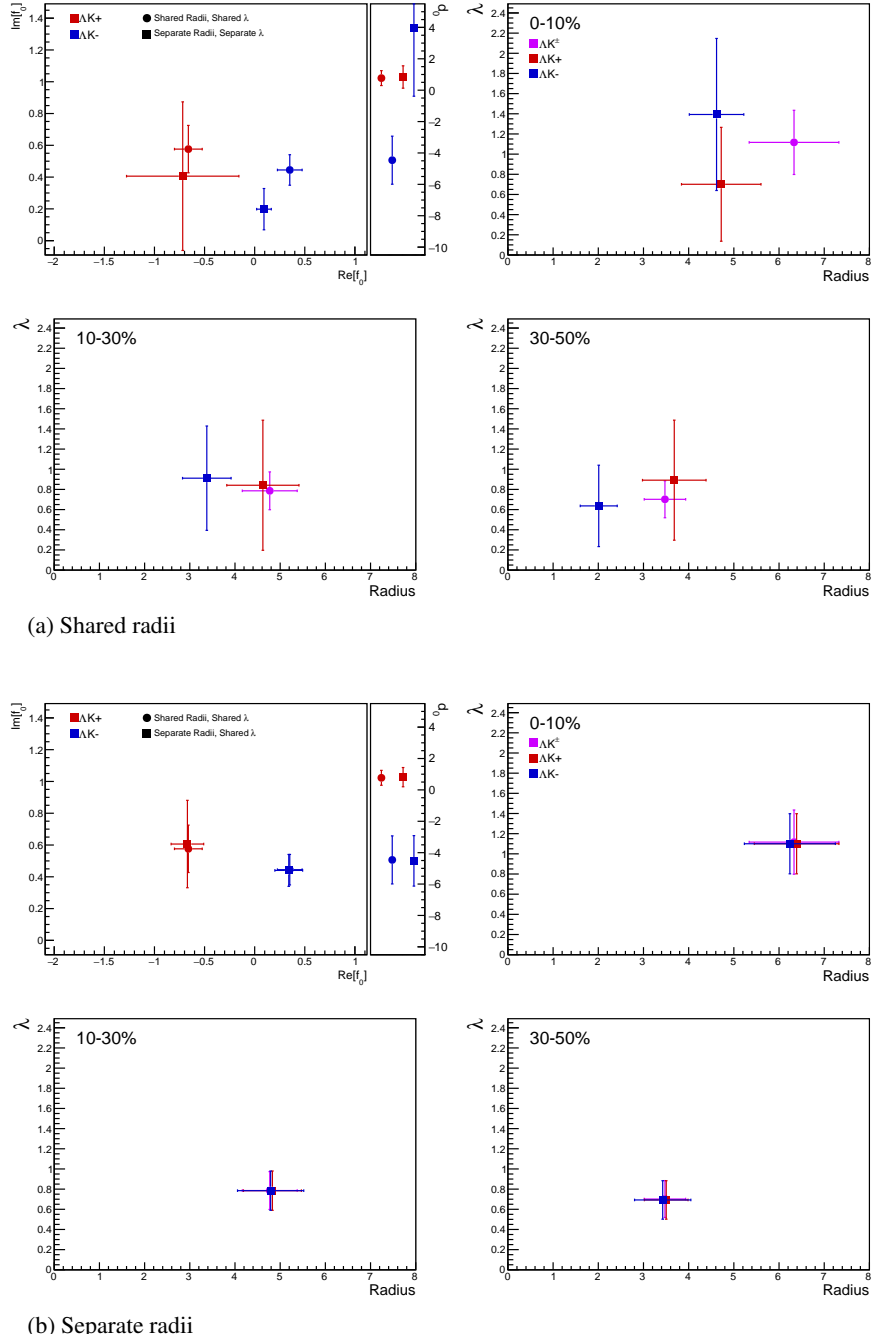


**Fig. 53:** Compare Fit Parameters: Shared vs. Separate Radii: Results shown for the case of radii being shared between  $\Lambda K^+$  and  $\Lambda K^-$  (circles) vs not shared (squares). In (a), when the radii are not shared between  $\Lambda K^+$  and  $\Lambda K^-$ , neither are the  $\lambda$  parameters. In (b), the  $\lambda$  parameters are always shared between  $\Lambda K^+$  and  $\Lambda K^-$

709 **7.1.5 Discussion of  $m_T$ -Scaling**

710 It is clear from the results presented in the previous sections, that the  $\Lambda\bar{\Lambda}$  systems do not conform to the  
 711 approximate  $m_T$ -scaling of the pair source sizes. At first thought, this may appear to be a troubling result;  
 712 the approximate scaling is an observed consequence of the collective behavior of the soft (low- $p_T$ ) sector  
 713 of the produced system. The  $\Lambda$  and  $K$  particles certainly participate in the collective expansion of the  
 714 QGP medium, so why do their extracted femtoscopic radii not behave as expected? To get straight to the  
 715 point: the  $\Lambda\bar{\Lambda}$  systems are (obviously) comprised on non-identical particles, each with its own and unique  
 716 single particle source. Each source is, in general, unique in both its overall size, and in its space-time po-  
 717 sition within the produced medium. The hydrodynamic nature of the medium produces the approximate  
 718  $m_T$ -scaling with respect to these single-particle sources, not the pair sources. The combination of these  
 719 effects, when probing correlations between non-identical particle pairs, leads to extracted radii falling  
 720 outside of the (identical particle femtoscopy)  $m_T$ -scaling trend. Figure 54 (which contains the same data  
 721 as Fig.31), shows again the  $R_{inv}$  vs  $m_T$  plot, but also highlights (with arrows) the approximate individual  
 722  $\langle m_T \rangle$  values of the single particle distributions. The grey circles show how to single particle sizes change  
 723 with  $m_T$ .

724 Taking a close look at Fig. 54, one can see that the previously published data (transparent points) are  
 725 for identical particle analyses only. For these cases, the pair source, probed through femtoscopy, is  
 726 comprised of two identical sources laying on top of each other. The extracted femtoscopic radii are  
 727 related to the single particle source sizes by a factor of  $\sqrt{2}$ , and of course follow the  $m_T$ -scaling trend.  
 728 The other (unpublished) non-identical particle femtoscopy study ( $p\Lambda$ ) included in the figure, also shows  
 729 radii deviating from the  $m_T$ -scaling band. Drawing a comparison with the  $\Lambda\bar{\Lambda}$  study shown in Fig. 31  
 730 is a bit more complicated; the  $\Lambda\bar{\Lambda}$  system, although containing non-identical particles, does contain a  
 731 particle with its antiparticle, for which annihilation could conceivably alter the pair source distribution.  
 732 It would be more surprising if the non-identical analyses did happen to conform to the scaling; although,  
 733 this could occur for a non-identical analysis in which the particles have similar masses as well as similar  
 734  $m_T$  distributions. For the case presented here, the result differing from  $m_T$ -scaling is not surprising.

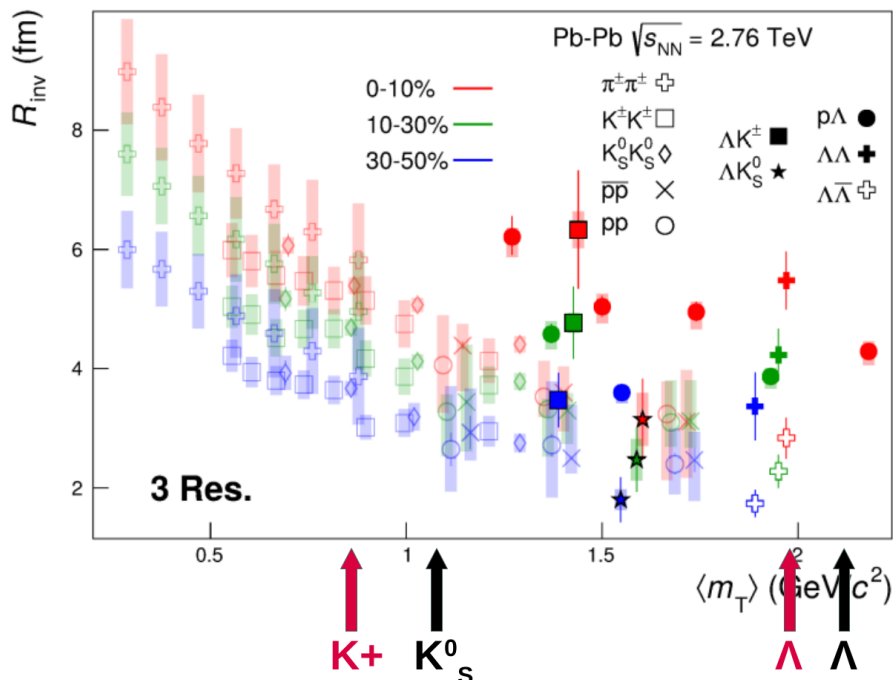


**Fig. 54:** Same as Fig. 31, but with the individual  $m_T$  values for the single particle distributions identified. The grey circles show how the single particle sizes are expected to change with  $m_T$ .

735 I will also briefly point out that it is not automatically clear where a non-identical study should be placed  
 736 on such a  $R_{\text{inv}}$  vs  $m_T$  plot. Each single particle distribution has a well-defined  $\langle m_T \rangle$ , which, to a large  
 737 extent, determines the single particle region of homogeneity. When combining two sources with different  
 738 spatio-temporal characteristics, originating from particles of different  $m_T$ , how should one define the pair  
 739  $m_T$ ? A simple mathematical expression for the pair  $m_T$  is easy to come up with, but that's not exactly  
 740 what I'm hinting at here. With respect to this  $m_T$ -scaling picture, the  $m_T$  value dictates the source size,  
 741 and one desires the same for non-identical particles. However, do the two unequal sized sources both  
 742 contribute equally to the extracted femtoscopic size? Or does the larger (smaller) source more closely  
 743 dictate the femtoscopic signal? If the contribution is equal, then it seems natural to simply more-or-less  
 744 average the two, single particle,  $m_T$  values. If the contribution is unequal, then there should be introduced  
 745 some sort of weighting in the pair  $m_T$  calculation reflecting this fact. In any case, in our study we use  
 746 the most straightforward definition of pair  $m_T$ , defined as:

$$m_{T,\text{pair}}^2 = \left(\frac{m_{\text{inv}}}{2}\right)^2 + \left(\frac{1}{2}|\mathbf{p}_{T,1} + \mathbf{p}_{T,2}|\right)^2 \quad (25)$$

747 Many times, the equation for non-identical particle pair  $m_T$  is defined with the average mass replacing  
 748  $m_{\text{inv}}/2$ . However, the above Eq. 25 is more directly analogous to the single particle  $m_T$ :

$$m_T^2 = m^2 + \mathbf{p}_T^2 = (p^0)^2 - (p^3)^2 \quad (26)$$

749 as, Eq. 25 may be rewritten as:

$$\begin{aligned} m_{T,\text{pair}}^2 &= (K^0)^2 - (K^3)^2 \\ K^\mu &\equiv \frac{1}{2}(p_1^\mu + p_2^\mu) \end{aligned} \quad (27)$$

750 Identical particle femtoscopic studies are able to probe only the size of the emitting region, or, more  
 751 precisely, the second moments of the emission function. In addition to this, non-identical particle studies  
 752 are able to measure the relative emission shifts, the first moments of the emission function. One method  
 753 to extract information about the emission asymmetries in the system is via a spherical decomposition  
 754 of the correlation function. With this method, one can draw a wealth of information from just a few  
 755 components of the decomposition. More specifically, the  $C_{00}$  component is similar to the 1D correlation  
 756 functions typically studied, and probes the overall size of the source. The  $\Im C_{11}$  component probes the  
 757 asymmetry in the system; a non-zero value reveals the asymmetry.

758 In Fig. 55 we show results for the  $C_{00}$  and  $\Im C_{11}$  components from the spherical decomposition of our  
 759  $\Lambda K^+$  system in the 0-10% centrality bin (red circles). Results from a number of other components  
 760 within the decomposition, as well as for our  $\Lambda K_S^0$  and  $\Lambda K^-$  systems, are contained in 9.2. Along with  
 761 the experimental data in Fig. 55, we have also included results from THERMINATOR simulation for an  
 762 impact parameter of  $b = 2$  fm (gold stars). As THERMINATOR does not include any final state effects,  
 763 we assumed scattering parameters  $(\Re f_0, \Im f_0, d_0) = (-1.16, 0.51, 1.08)$  and weighted the numerator pairs  
 764 with  $|\Psi|^2$ , as discussed previously. As seen in the figure, the  $C_{00}$  signal is similar to that observed in our  
 765 one-dimensional study. The  $\Im C_{11}$  component shows a clear deviation from zero, and the negative value  
 766 signifies that the  $\Lambda$  particles are, on average, emitted further out and/or earlier than the K mesons.

767 Fig. 56 shows a closer look at the THERMINATOR simulation, whose spherical harmonic decompositon  
 768 was shown along with the data in Fig. 55. The top left of Fig. 56a shows a fit to the one-dimensional  
 769 correlation function from THERMINATOR. The scattering parameters are known precisely here, as they  
 770 served as the weights used in the simulation, and are kept constant in the fit. We are interested in looking

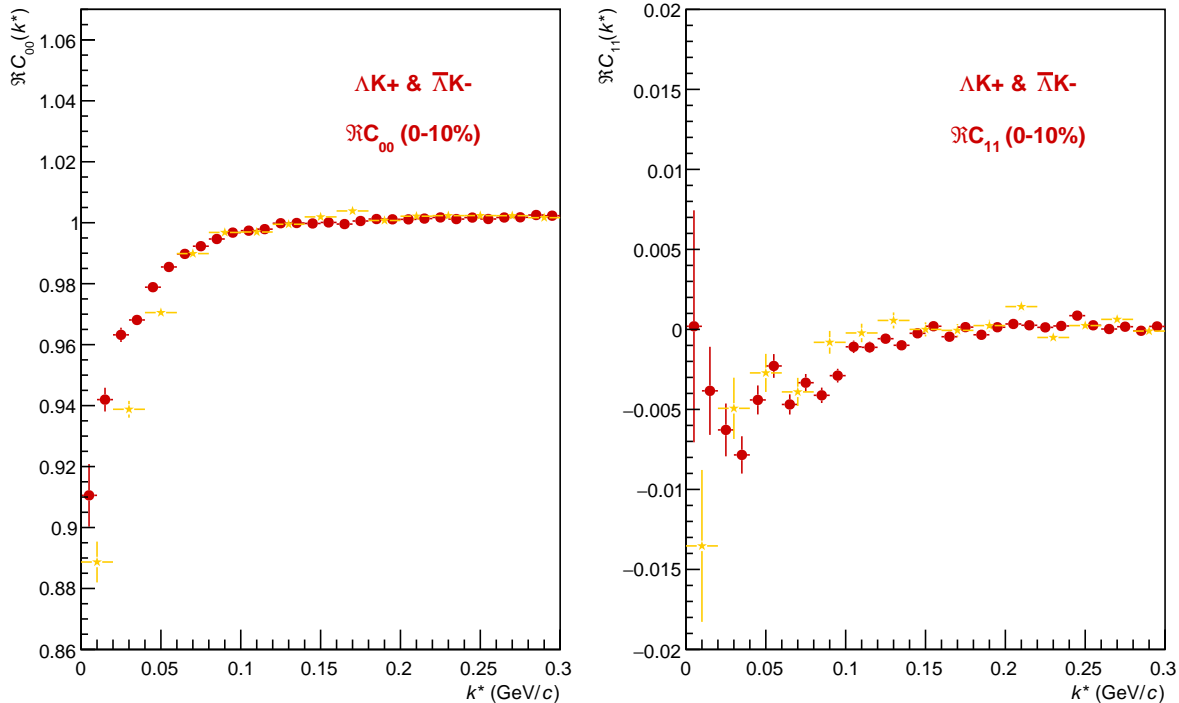
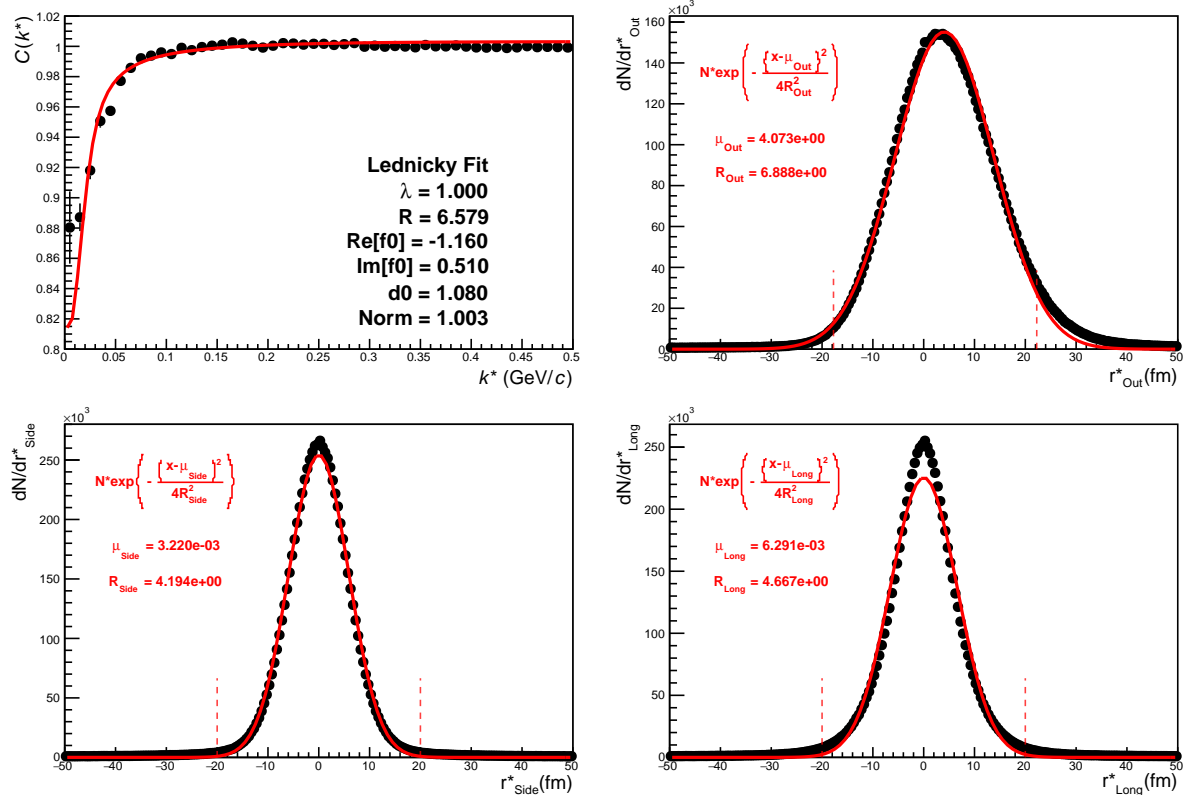


**Fig. 55:**  $C_{00}$  (left) and  $\Im C_{11}$  (right) components of a spherical harmonic decomposition of the  $\Lambda K^+$  correlation function for the 0-10% centrality bin. The  $C_{00}$  component is similar to the 1D correlation functions typically studied, and probes the overall size of the source. The  $\Im C_{11}$  component probes the asymmetry in the system; a non-zero value reveals the asymmetry

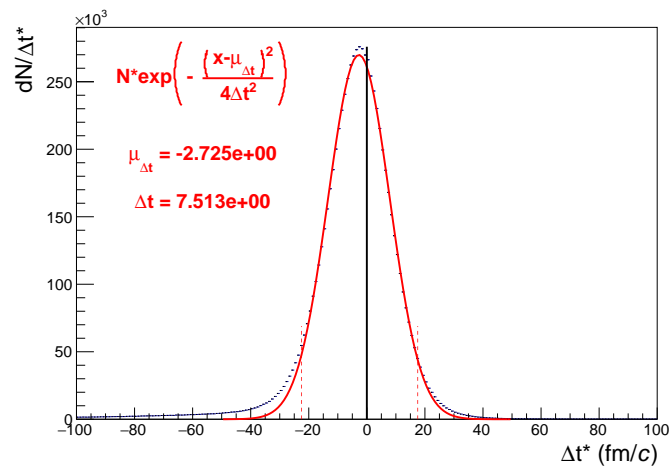
at the extracted one-dimensional source size here, so the  $\lambda$  parameter is also fixed at unity. The other three plots in Fig. 56a show the source distribution in the out (top right), side (bottom left), and long (bottom right) directions (all in the PRF). The source distributions have all been fitted with a Gaussian form, the result of which is printed within the respective plot. One immediately sees a significant shift in the out direction,  $\mu_{\text{out}} \approx 4$  fm, and negligible shift in the other two directions,  $\mu_{\text{side}} \approx \mu_{\text{long}} \approx 0$  fm. The figure demonstrates that, within the THERMINATOR model, the  $\Lambda$  is, on average, emitted further out than its K partner. Finally, Fig. 56b shows the distribution of the relative time of emittance, again in the PRF. The figure shows that the  $\Lambda$  is, on average, emitted earlier than its K partner.

We end this section with a brief look at how a spatial separation of the single particle sources affects the radii extracted from a femtoscopic analysis. To achieve this, we use THERMINATOR in a similar fashion as described above, but with one important difference. Instead of taking the source information from THERMINATOR, we instead draw the source from a pre-determined Gaussian distribution. In all cases, we take  $R_{\text{out}} = R_{\text{side}} = R_{\text{long}} = 5$  fm, and  $\mu_{\text{side}} = \mu_{\text{long}} = 0$  fm. Figure 57 shows an example of results obtained from THERMINATOR following this procedure, where  $\mu_{\text{out}} = 3$  fm.

In Figure 58, we show results for the case of  $\mu_{\text{out}} = 1$  fm,  $\mu_{\text{out}} = 3$  fm, and  $\mu_{\text{out}} = 6$  fm. In this figure, we do not show the side and long distributions, as they appear identical to those shown in Fig. 57. The figure demonstrates that as the separation  $\mu_{\text{out}}$  increases, so do the extracted femtoscopic radii.



(a) Caption 1



(b) Caption 2

**Fig. 56:** Long Overall

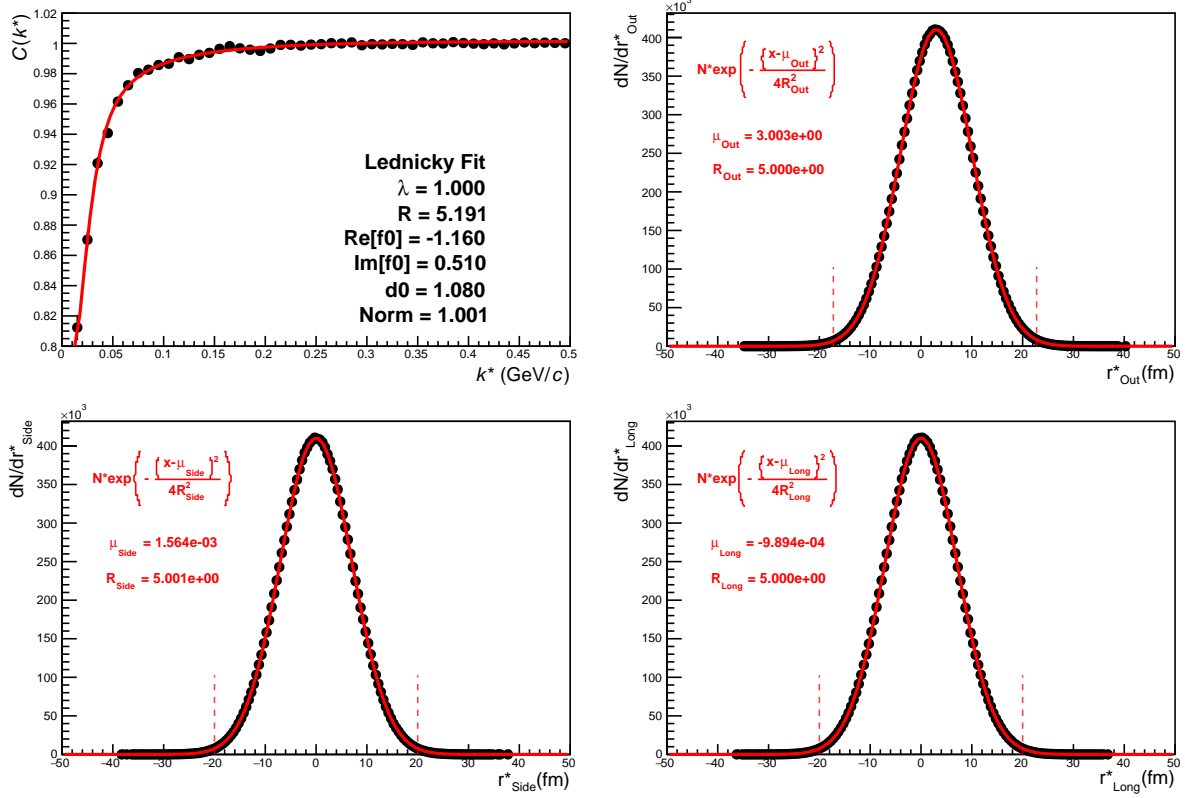


Fig. 57: Long Caption

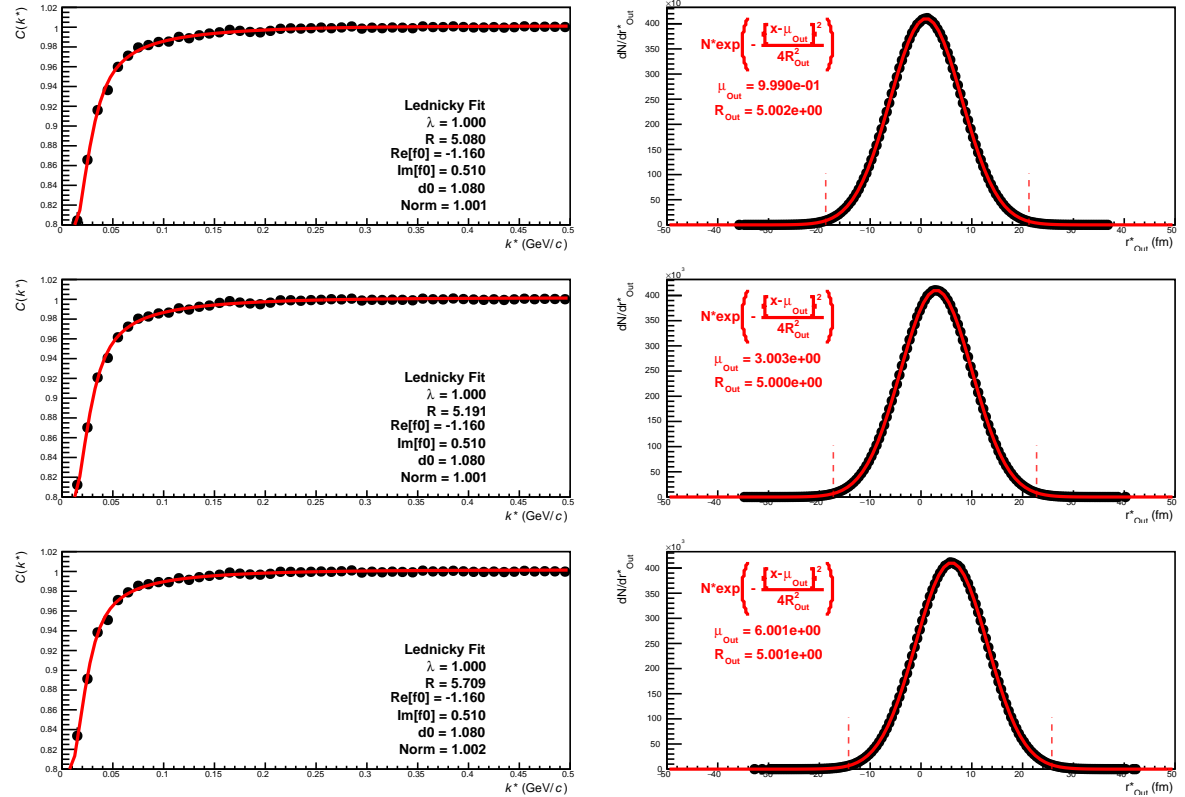
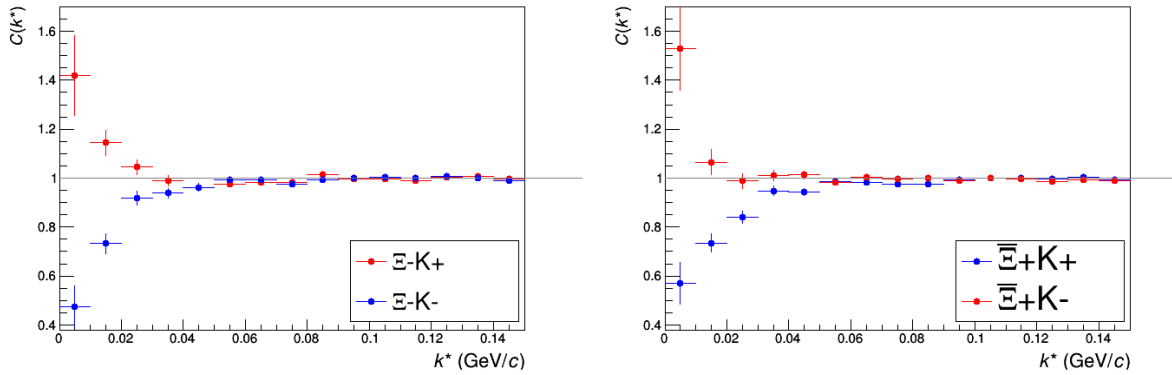


Fig. 58: Long Caption

788 **7.2 Results:  $\Xi K^\pm$** 

789 Even without any fits to the data, the fact that the  $\Xi^- K^+$  data dips below unity (Fig. 59) is exciting, as  
 790 this cannot occur purely from a Coulomb interaction. We hope that this dip signifies that we are able to  
 791 peer through the overwhelming contribution from the Coulomb interaction to see the effects arising from  
 792 the strong interaction.

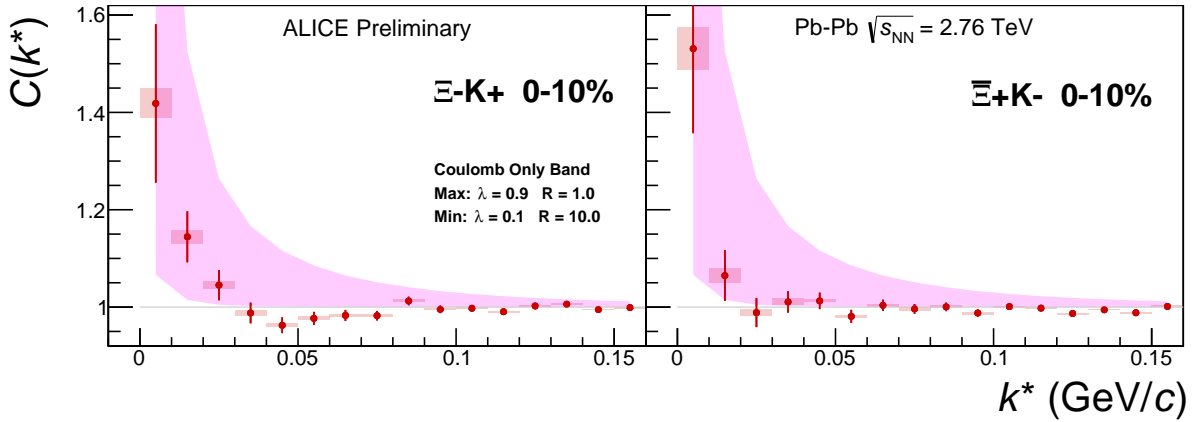
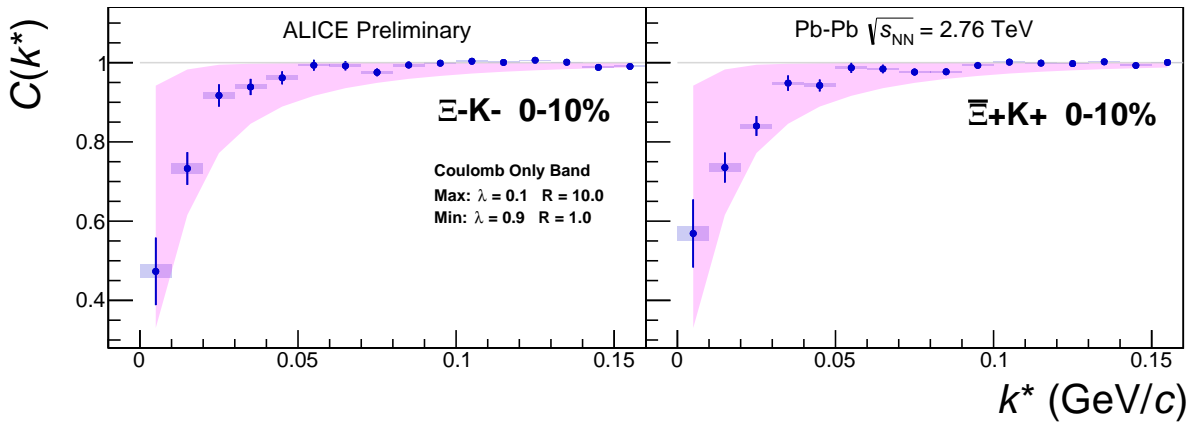


**Fig. 59:**  $\Xi K^\pm$  Results for 0-10% Centrality. (Left)  $\Xi^- K^+$  and  $\Xi^- K^-$  (Right)  $\Xi^+ K^+$  and  $\Xi^+ K^-$

793 Figure 60 demonstrates graphically, that the  $\Xi^- K^+$  results cannot be described by solely the Coulomb  
 794 interaction. In this figure, we present the data along with a Coulomb-only band. The Coulomb-only  
 795 band is spanned by two Coulomb-only curves, whose parameters are given in the figure. The Coulomb-only  
 796 curves were generated using a technique identical to the generation of the fit function, described  
 797 in Sec. 5.2, except, of course, with the nuclear scattering parameters all set to zero. The Coulomb-only  
 798 curves change monotonically with varying  $\lambda$  or varyin radius parametres, therefore, any curves built with  
 799 parameter sets intermediate to those use in the Coulomb-only band will be contained in the band.

800 Including the strong interaction into the simulation can change, sometimes dramatically, the resulting  
 801 correlation function, as shown in Figure 61. In the figure, the solid line represents a Coulomb-only curve,  
 802 i.e. a simulated correlation function with the strong interaction turned off. The dashed lines represent a  
 803 full simulation, including both the strong and Coulomb interactions. The two dashed lines differ only in  
 804 the real part of the assumed scattering length: positive in Set 1, and negative in Set 2. In the top figure,  
 805 for the  $\Xi^- K^+$  simulation, we see that parameter set 2, with a negative real part of the scattering length,  
 806 causes the simulated curve to dip below unity, as is seen in the data. If there is a parallel to be drawn  
 807 between this analysis and the  $\Lambda K$  analysis, we expect to see similar effects in the  $\Lambda K^+$  system and the  
 808  $\Xi^- K^+$  systems. In these systems, we could have an  $s\bar{s}$  annihilation picture. Or, another possible way of  
 809 thinking about these systems is in terms of net strangeness. The  $\Lambda K^+$  system has  $S=0$ , while the  $\Lambda K^-$   
 810 has  $S=-2$ . The  $\Xi^- K^+$  has  $S=-1$ , while the  $\Xi^- K^-$  has  $S=-3$ .

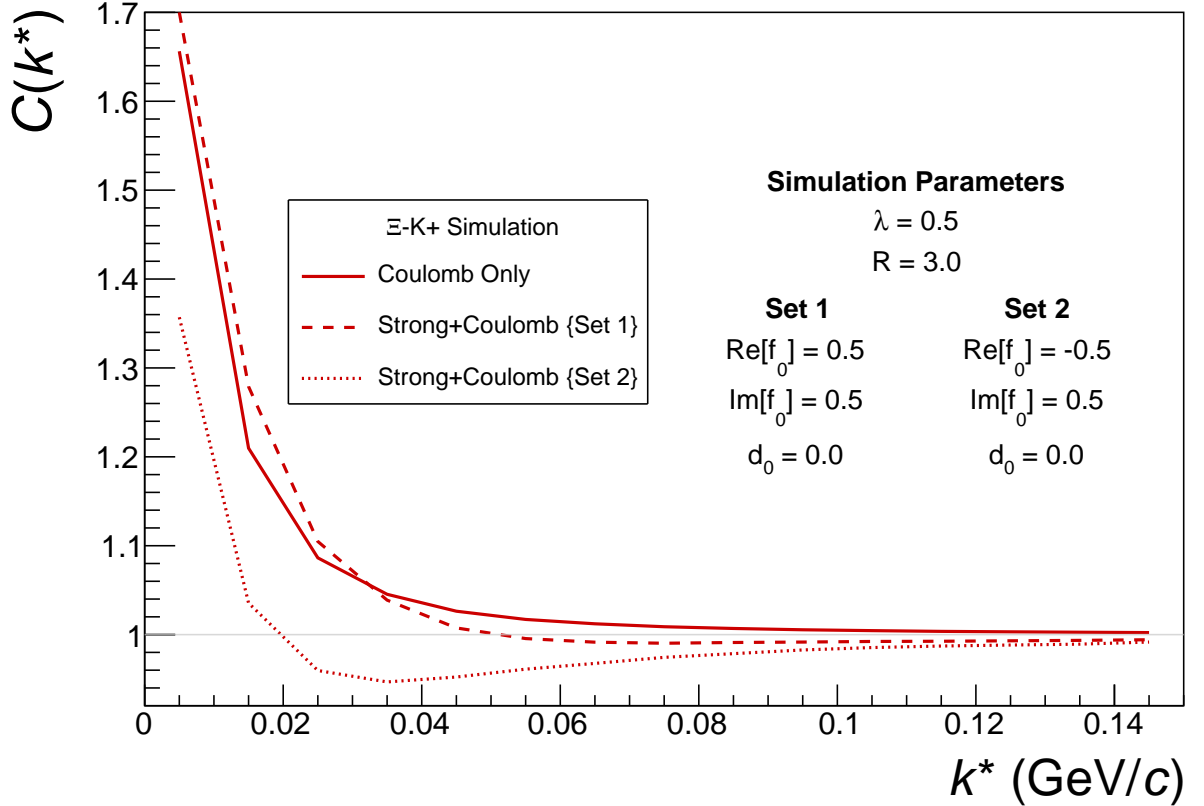
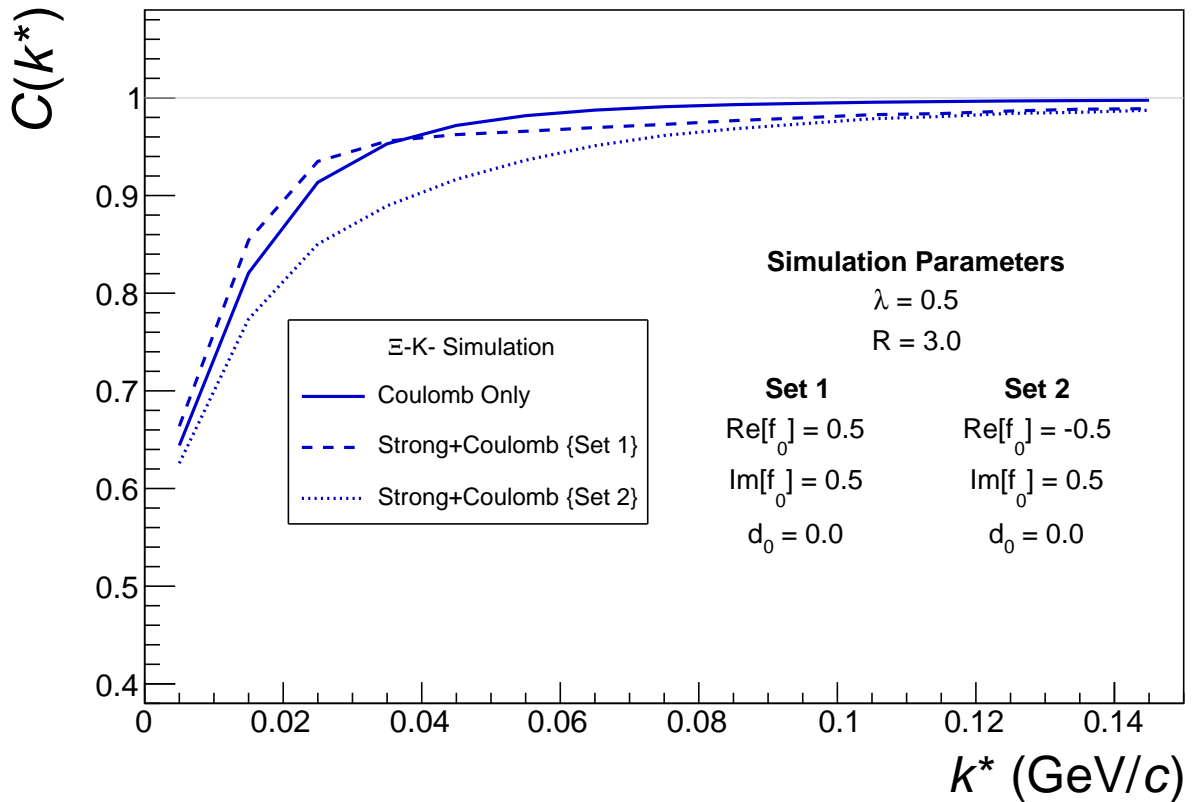
811 The author was asked to perform a global Coulomb-only fit to the data, to ensure that the system truly  
 812 could not be described simply by the Coulomb interaction. In order words, in the fit, the strong force was  
 813 turned off, and the  $\Xi^- K^+$ ,  $\Xi^+ K^-$ ,  $\Xi^- K^-$ ,  $\Xi^+ K^+$  systems all share one sinlge radius parameter, while the  
 814 pair and conjugate pair systems share a  $\lambda$  parameter. The results of this fit are shown in Figures 62 and  
 815 63. In Fig. 62, there was a lower limit of 0.1 fm placed on the radius parameter, and the radius parameter  
 816 was initialized to 3 fm (as seems reasonable, when considering the transverse mass of the system and  
 817 looking at Fig. 31). As is shown in the results, the radius parameter reached this unrealistic lower bound  
 818 of 0.1 fm. In Fig. 63, the parameters were all unbounded, and the radius parameter was initialized to 10  
 819 fm. In this case, the radius parameters reamins high, and ends at an unrealistic value of 10.84 fm. In both  
 820 cases, the  $\lambda$  parameters are too low. From these figures, we conclude that a global Coulomb-only fit is  
 821 not suitable for the data.

(a) (Left)  $\Xi\text{K}^+$  and (Right)  $\Xi\text{K}^-$ (b) (Left)  $\Xi\text{K}^-$  and (Right)  $\Xi\text{K}^+$ 

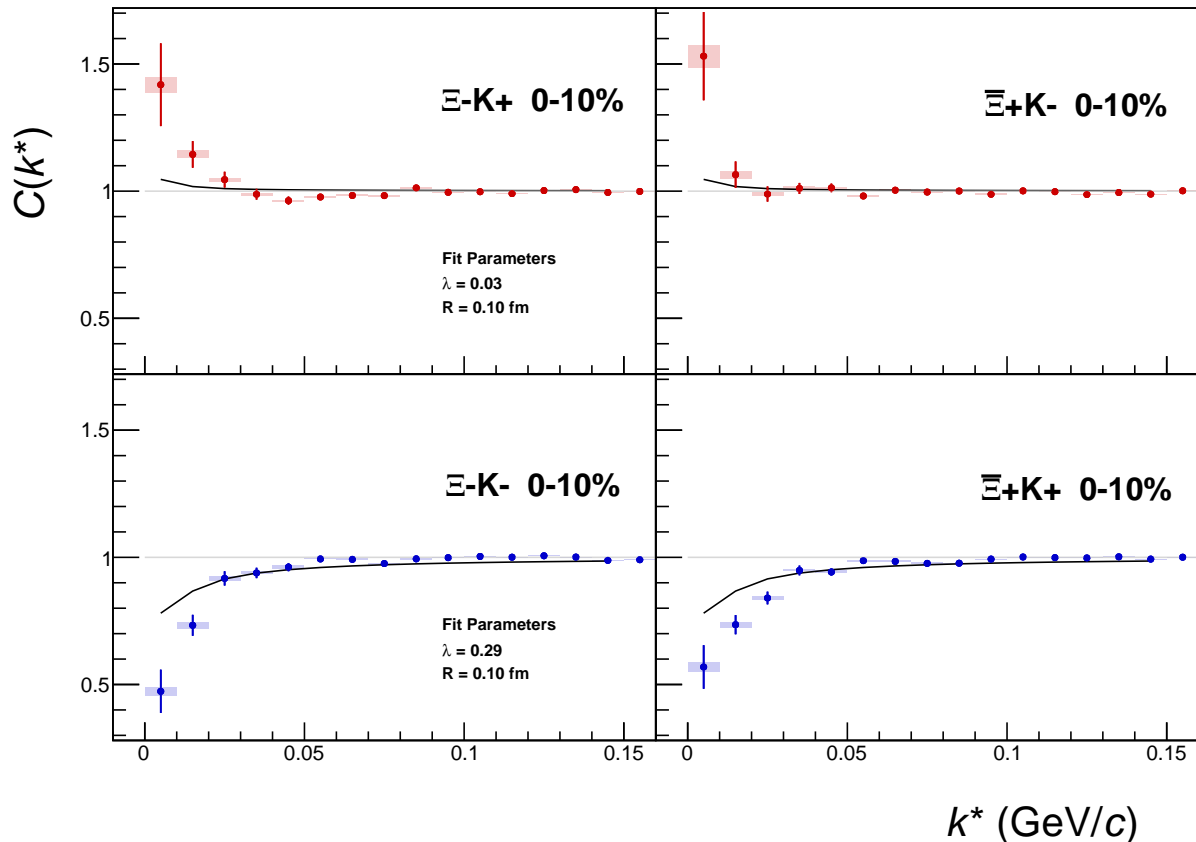
**Fig. 60:**  $\Xi\text{K}^\pm$  data with Coulomb-only bands for the 0-10% centrality bin. The Coulomb-only bands span two sets of Coulomb-only curves: (1)  $\lambda = 0.9$ , R = 1.0 fm and (2)  $\lambda = 0.1$ , R = 10.0 fm. The Coulomb-only curves are simulated correlation functions for the respective pair system assuming only a Coulomb interaction, i.e. ignoring the strong interaction. The Coulomb-only curves change monotonically with varying  $\lambda$  and varying R, therefore, any intermediate parameter set will fall within this Coulomb-only band.

822 Although the global Coulomb-only fit failed, it is possible that a Coulomb-only fit performed on  $\Xi\text{-K}^+$   
 823 and  $\Xi\text{+K}^-$  separately from  $\Xi\text{-K}^-$  and  $\Xi\text{+K}^+$  could be suitable. The result of such fits are shown in  
 824 Figures 64 and 65. Figure 64, shows that the fit is not able to describe the dip in the  $\Xi\text{-K}^+$  data below  
 825 unity. Of course, this is obviously true for an attractive Coulomb-only fit. The radius parameter of  
 826 8.43 fm extracted from this fit is unrealistically large. In Figure 65 shows the Coulomb-only fit can  
 827 described the  $\Xi\text{-K}^-$  data reasonable well; although the extracted radius of 3.73 fm is somewhat larger  
 828 than expected.

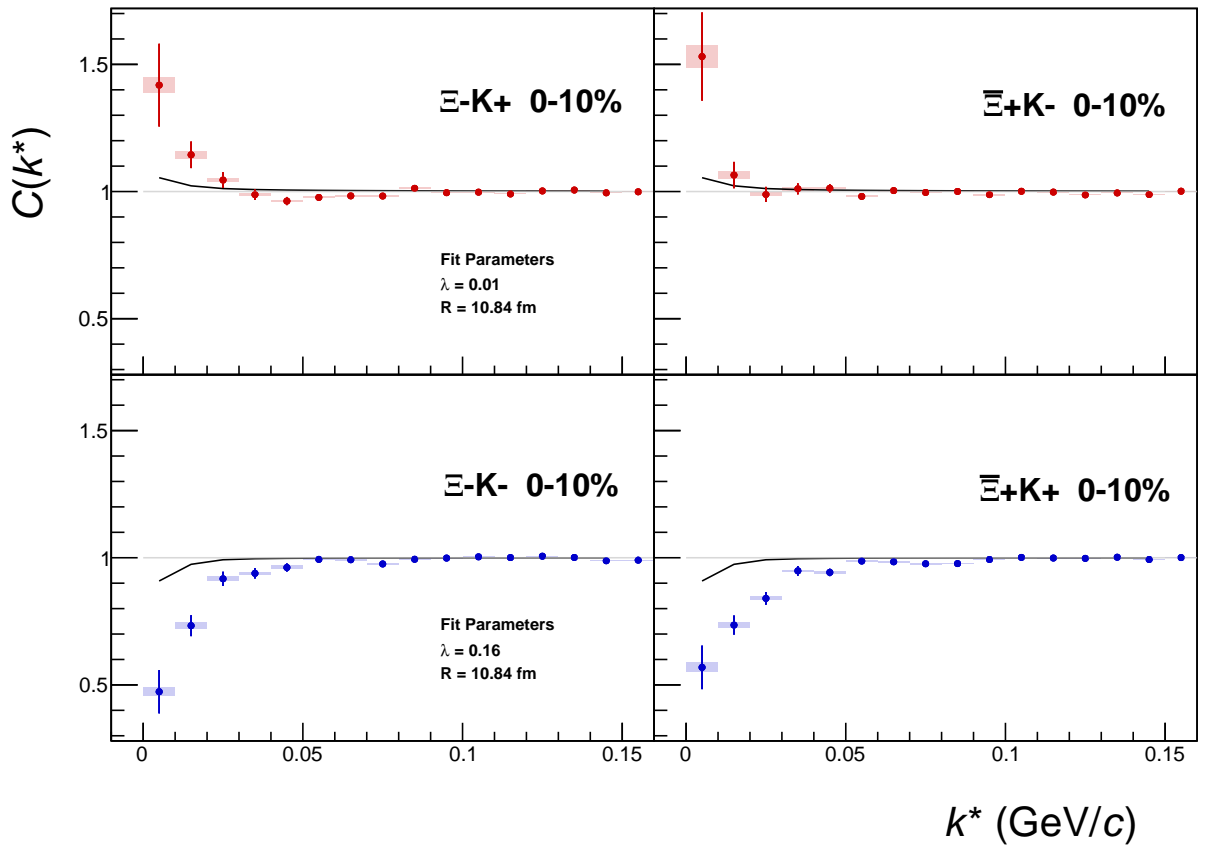
## 8 To Do


 (a)  $\Xi K^+$  and  $\bar{\Xi} K^-$  simulation

 (b)  $\Xi K^-$  and  $\bar{\Xi} K^+$  simulation

**Fig. 61:** Effect on the Coulomb-only curve of including the strong interaction for  $\Xi K^\pm$  systems. The solid line represents a Coulomb-only curve, i.e. a simulated correlation function with the strong interaction turned off. The dashed lines represent a full simulation, including both the strong and Coulomb interactions. The two dashed lines differ only in the real part of the assumed scattering length: positive in Set 1, and negative in Set 2.



**Fig. 62:**  $\Xi K^\pm$  Global Coulomb-only fit (Set 1) for 0-10% centrality. In this fit, there was a lower limit of 0.1 fm placed on the radius parameter, and the radius parameter was initialized to 3 fm (as seems reasonable, when considering the transverse mass of the system and looking at Fig. 31). As is shown in the results, the radius parameter reached this unrealistic lower bound of 0.1 fm. Also, the extracted  $\lambda$  parameters are too low.



**Fig. 63:**  $\Xi K^\pm$  Global Coulomb-only fit (Set 2) for 0-10% centrality. In this fit, the parameters were all unbounded, and the radius parameter was initialized to 10 fm. In this case, the radius parameters remain high, and ends at an unrealistic value of 10.84 fm. Also, the extracted  $\lambda$  parameters are too low.

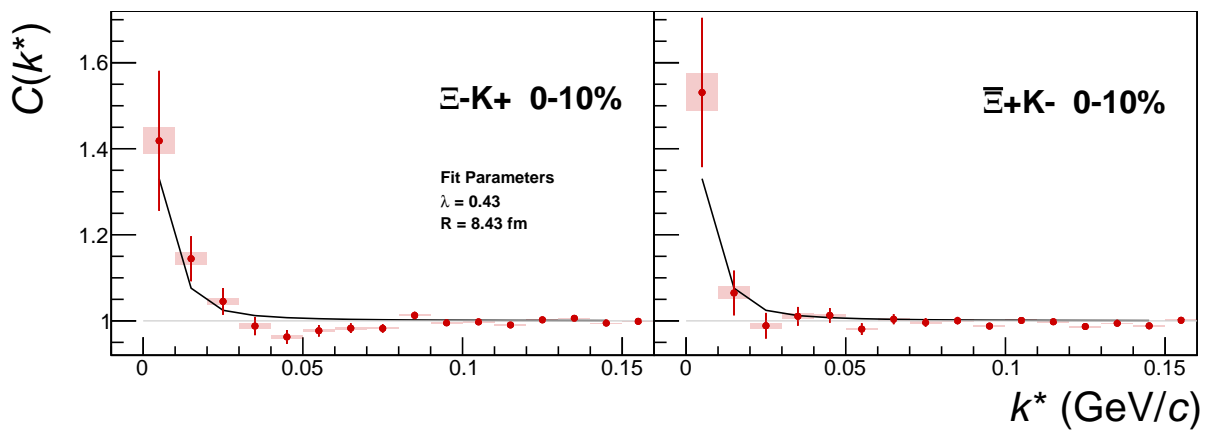


**Fig. 64:**  $\Xi^- K^+$  Coulomb-only fit for 0-10% centrality

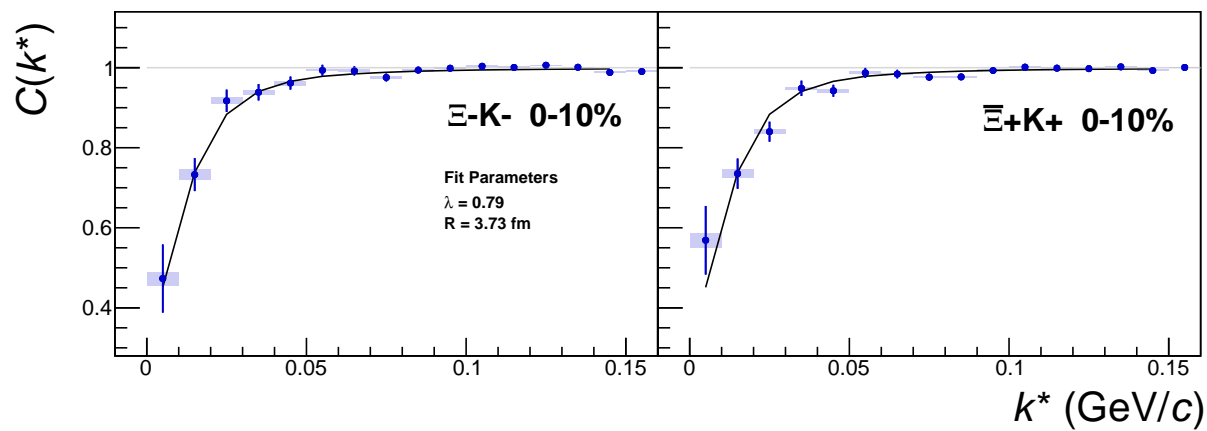
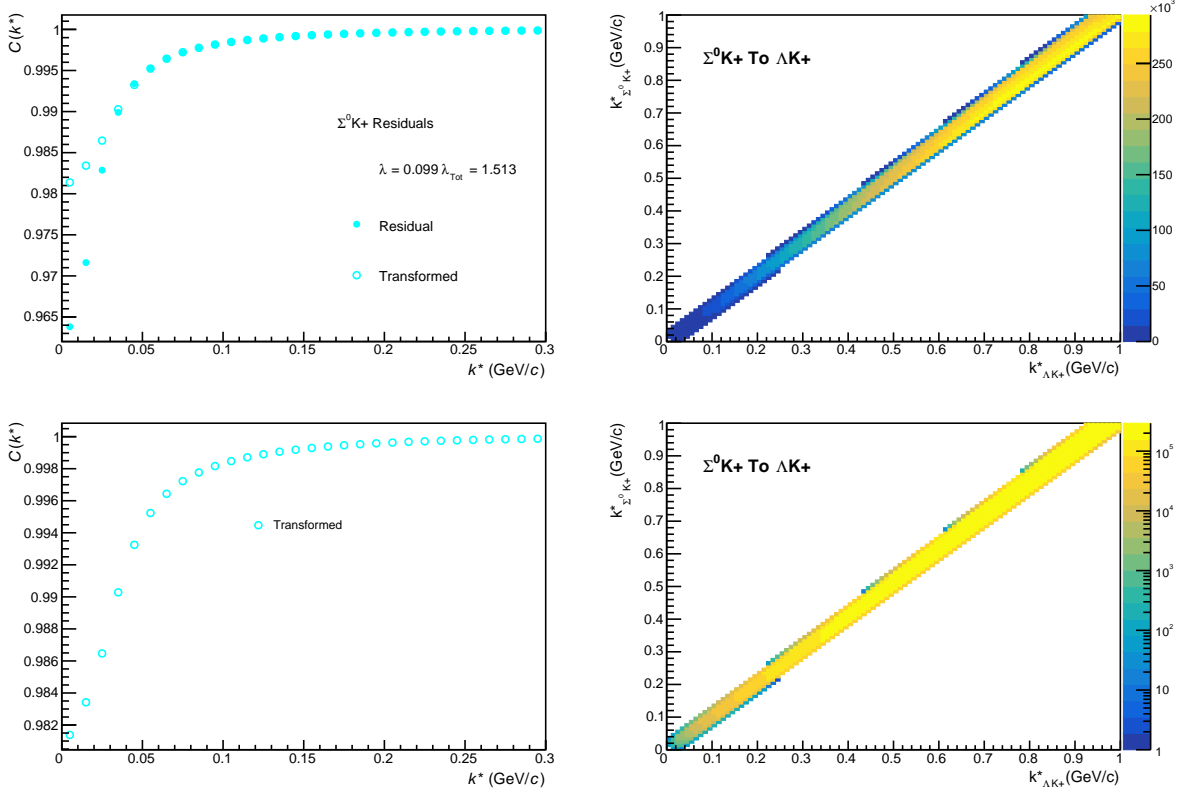


**Fig. 65:**  $\Xi^- \text{K}^-$  Coulomb-only fit for 0-10% centrality

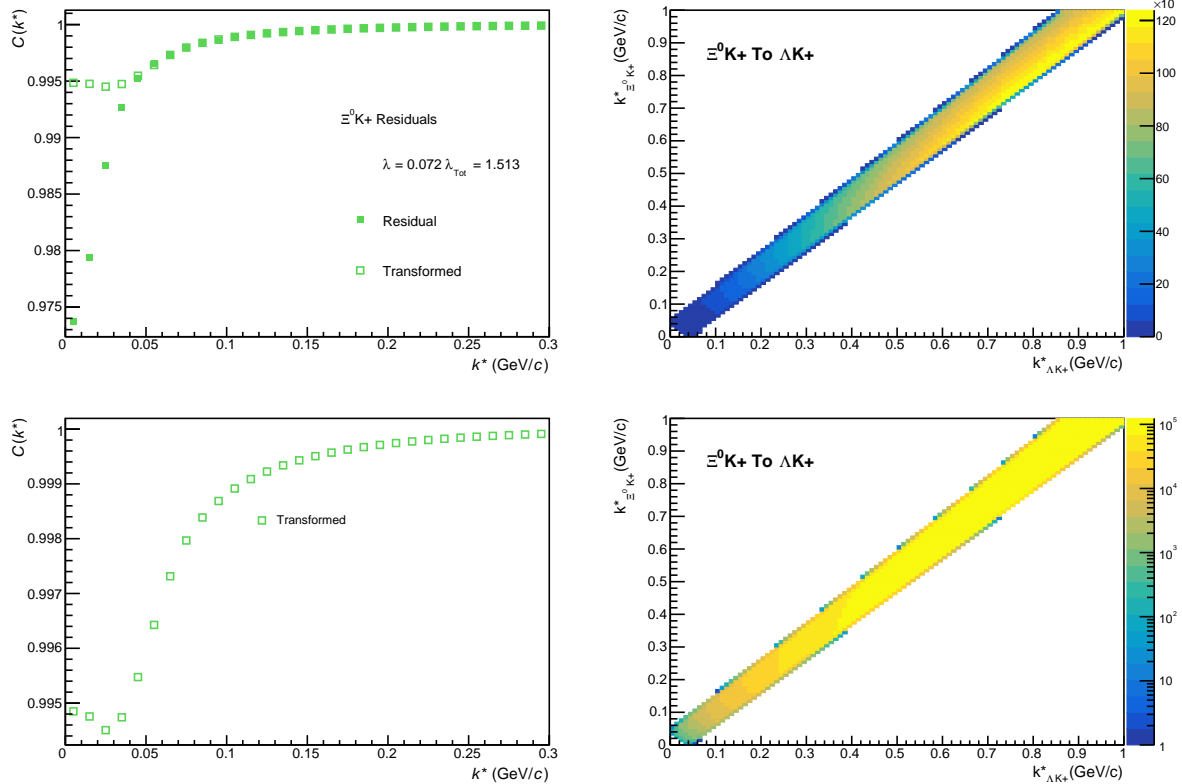
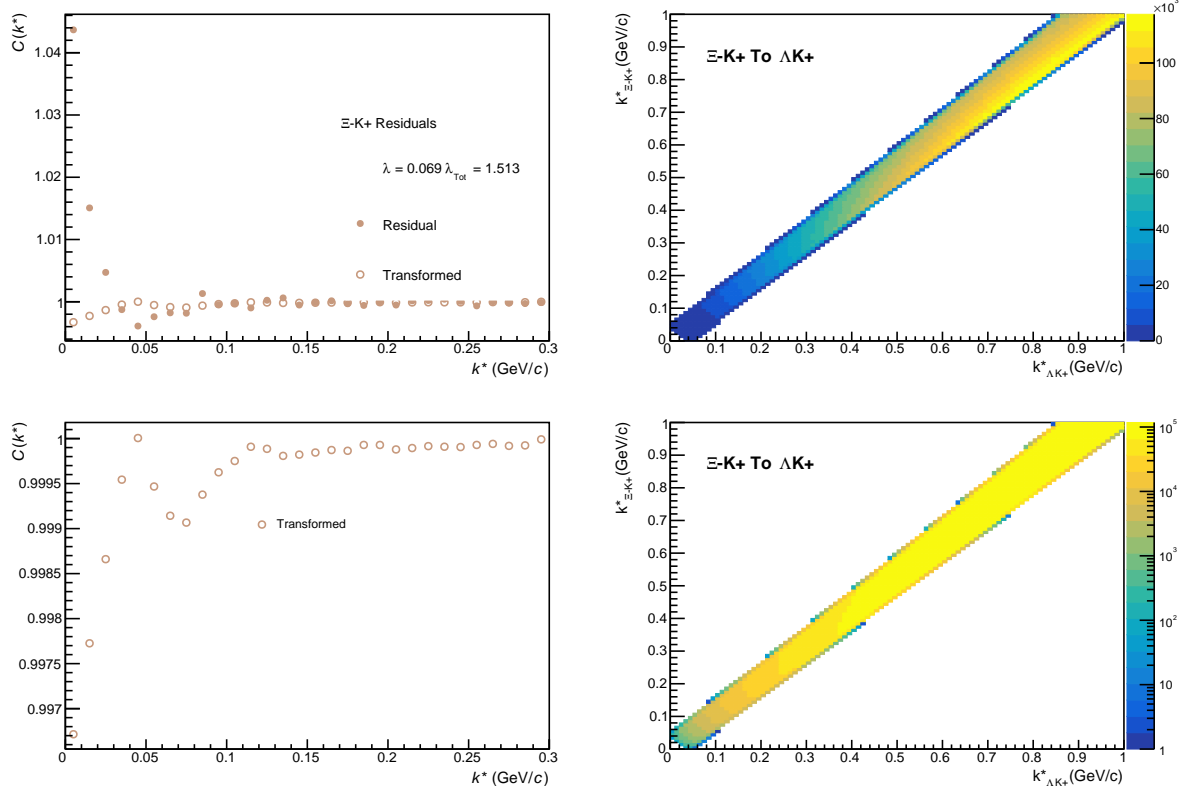
830 **9 Additional Figures**

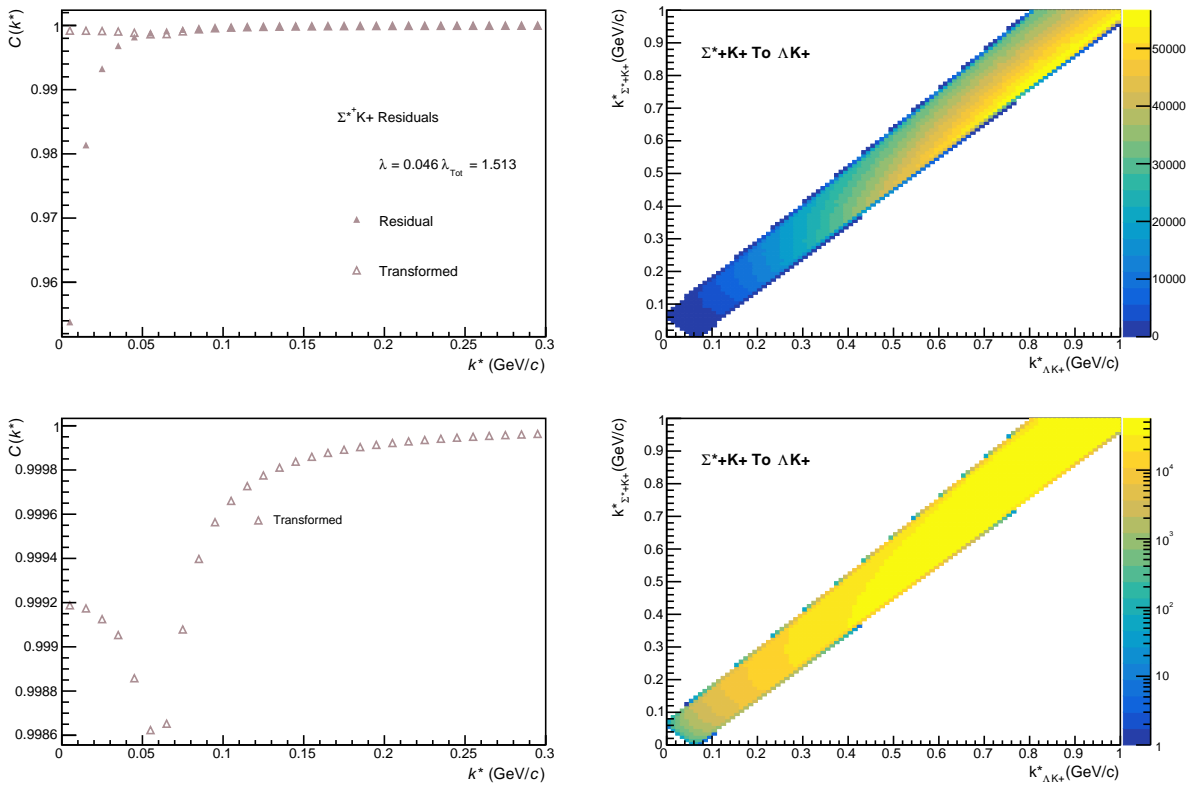
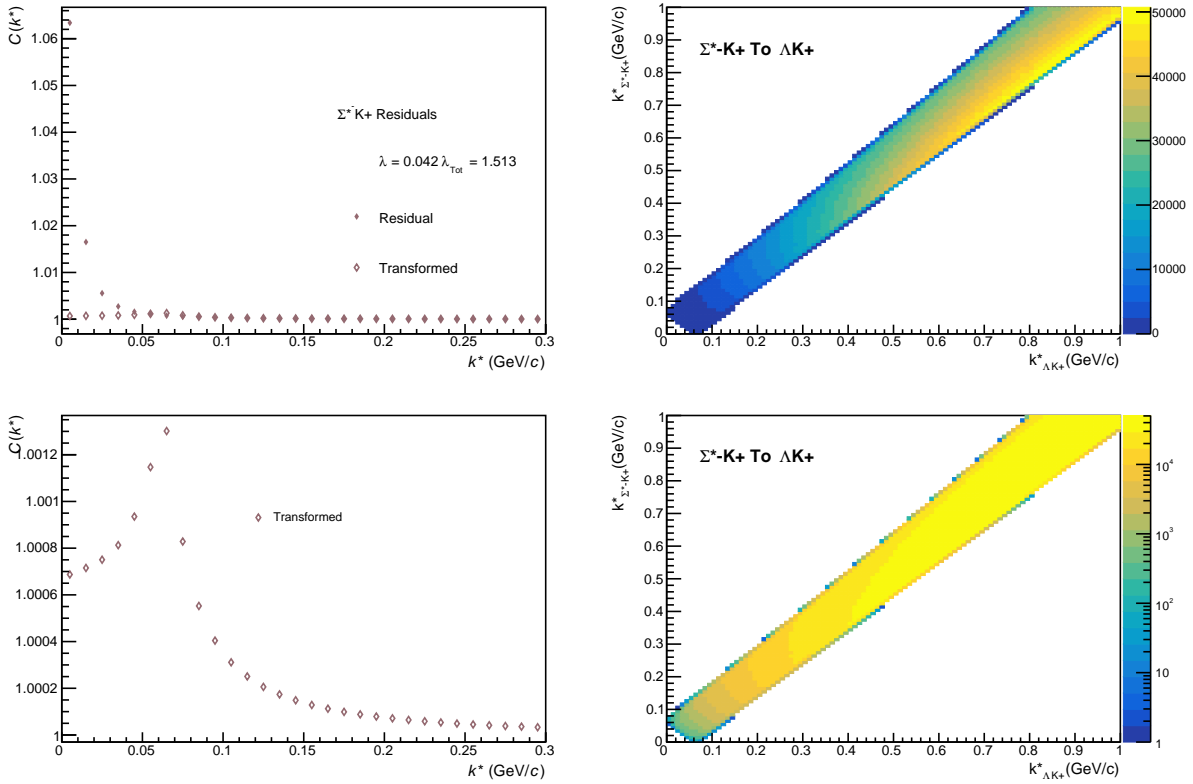
831 **9.1 Residuals**

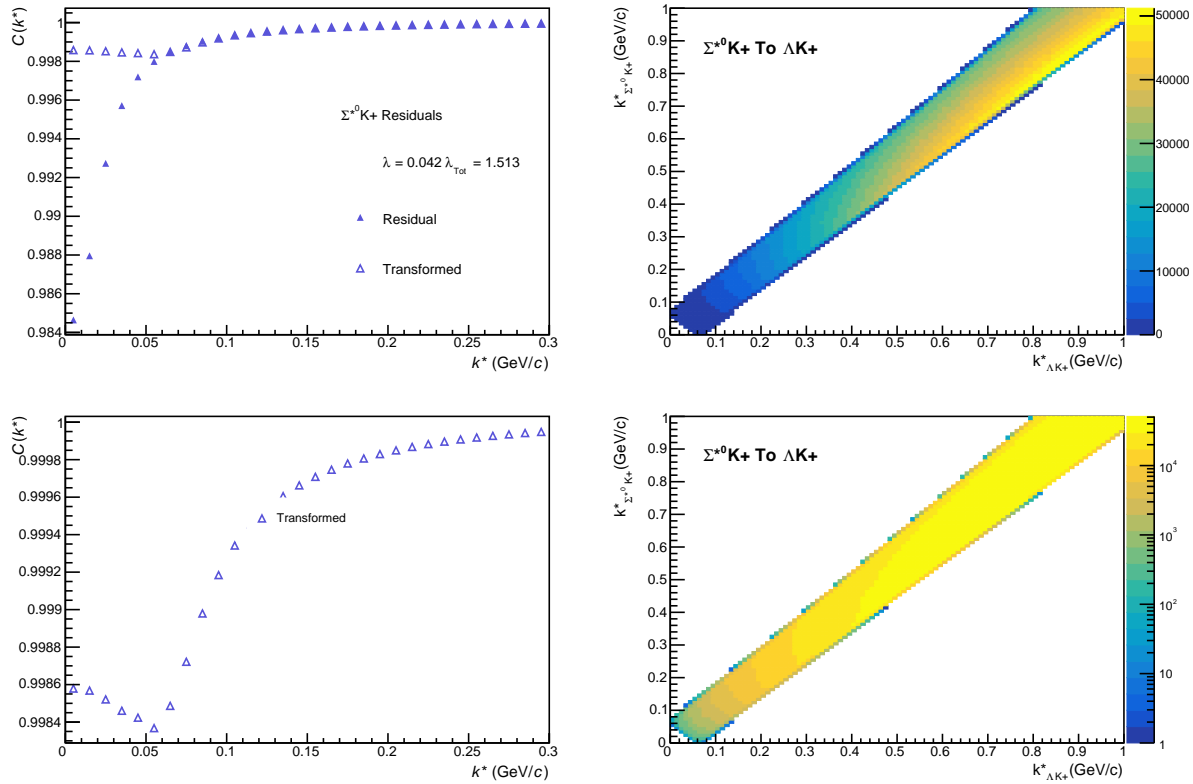
832 **9.1.1  $\Lambda K^+$  Residuals**



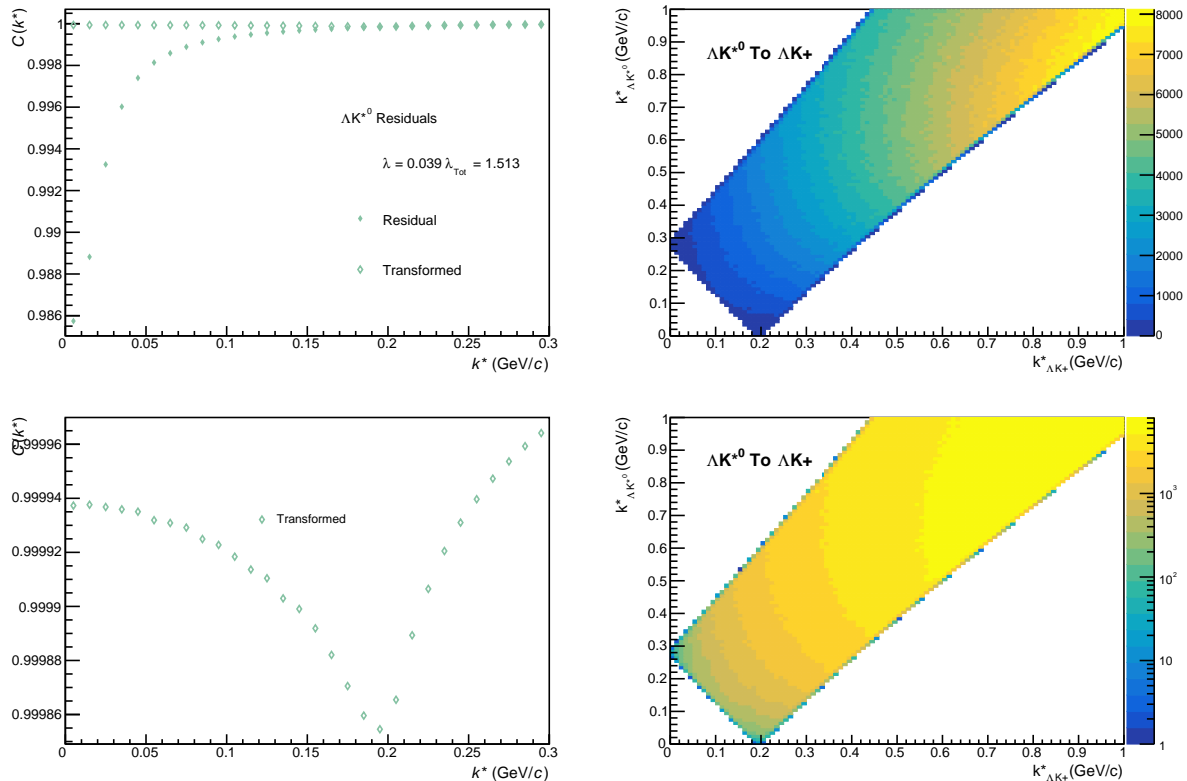
**Fig. 66:** Residuals:  $\Sigma^0 K^+$  to  $\Lambda K^+$  (0-10% Centrality)

Fig. 67: Residuals:  $\Xi^0 \text{K}^+$  to  $\Lambda \text{K}^+$  (0-10% Centrality)Fig. 68: Residuals:  $\Xi^- \text{K}^+$  to  $\Lambda \text{K}^+$  (0-10% Centrality)

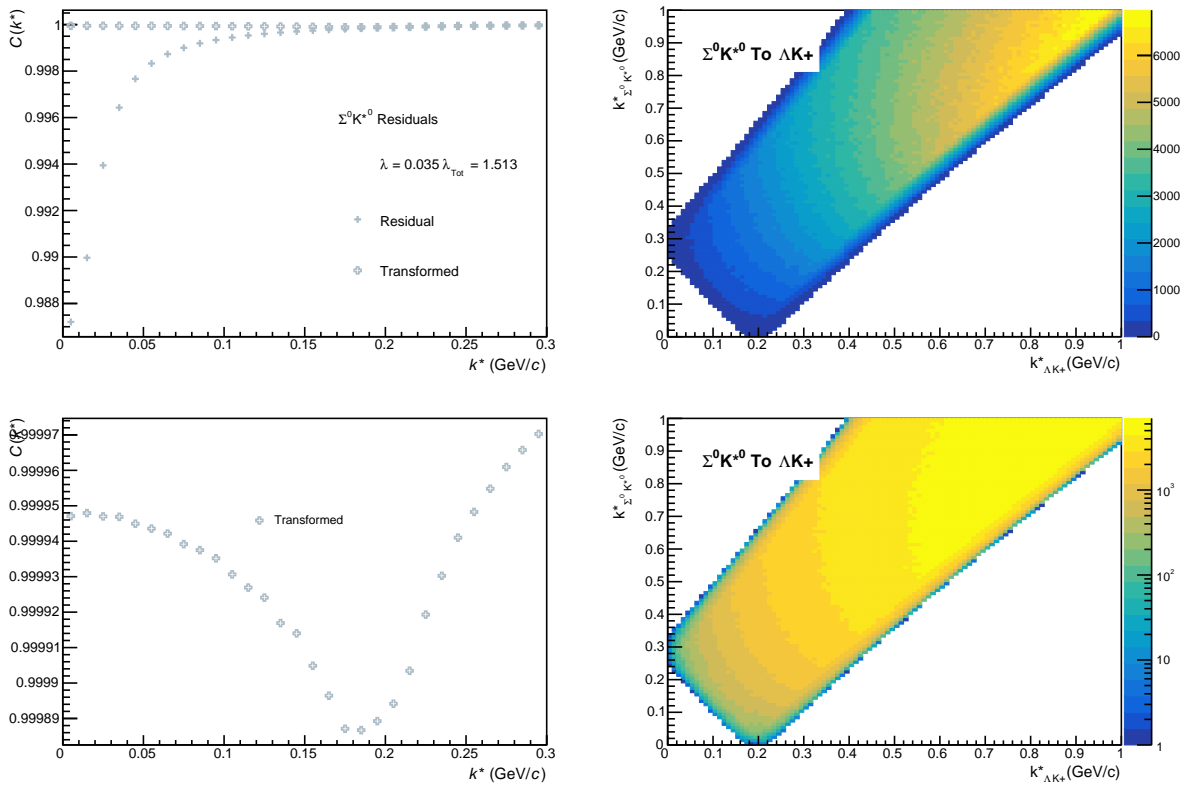

 Fig. 69: Residuals:  $\Sigma^{*+}K^+$  to  $\Lambda K^+$  (0-10% Centrality)

 Fig. 70: Residuals:  $\Sigma^{*-}K^+$  to  $\Lambda K^+$  (0-10% Centrality)



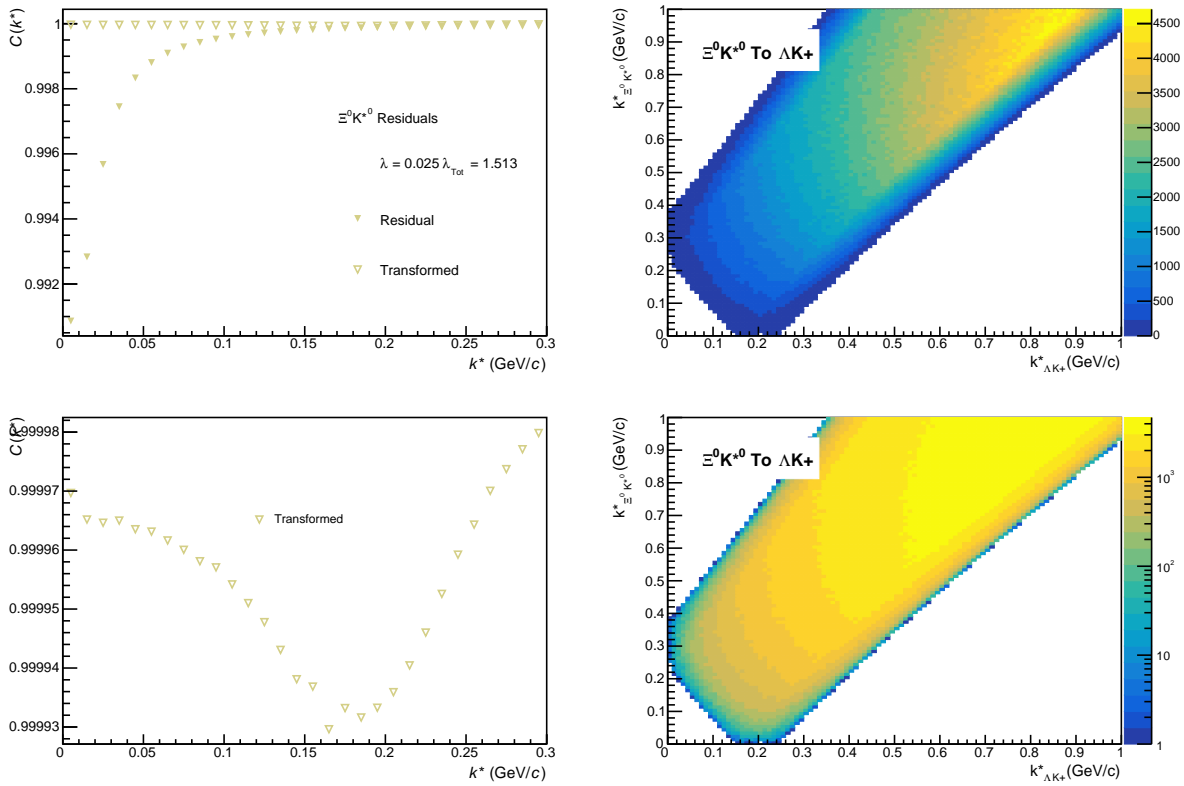
**Fig. 71:** Residuals:  $\Sigma^{*0} \text{K}^+$  to  $\Lambda \text{K}^+$  (0-10% Centrality)



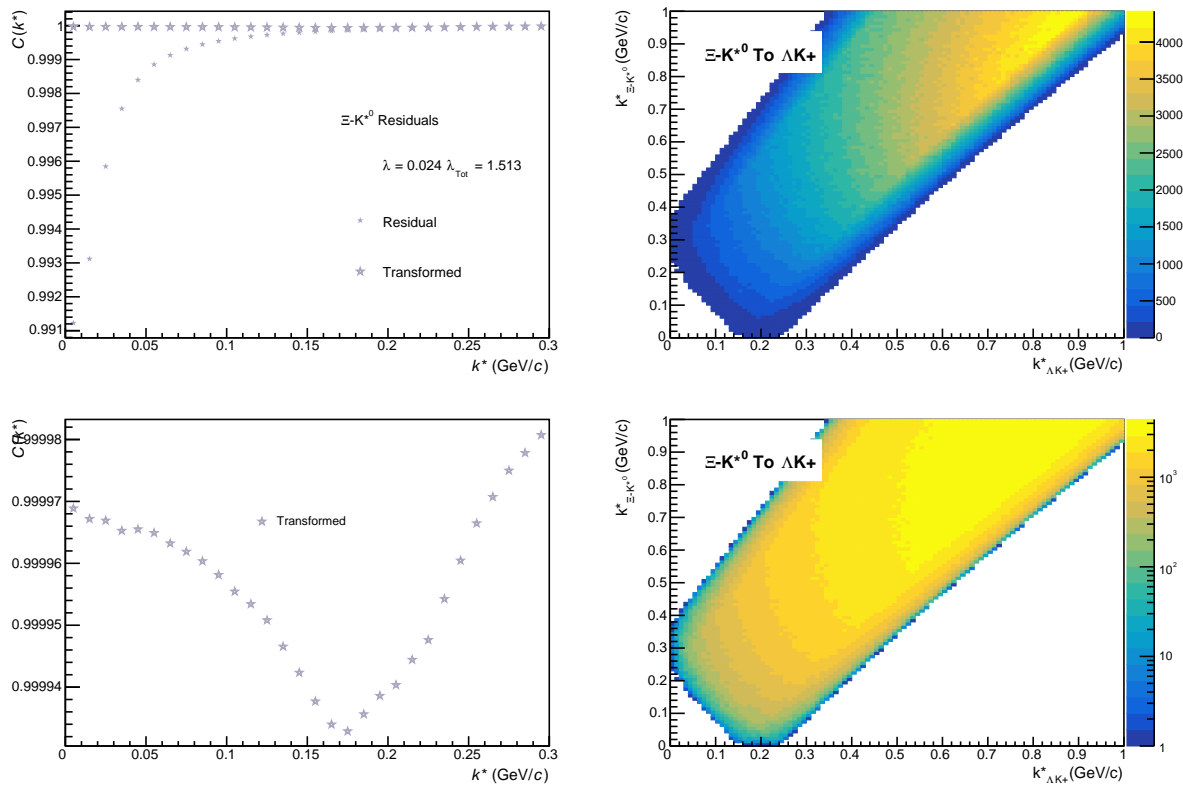
**Fig. 72:** Residuals:  $\Lambda \text{K}^{*0}$  to  $\Lambda \text{K}^+$  (0-10% Centrality)



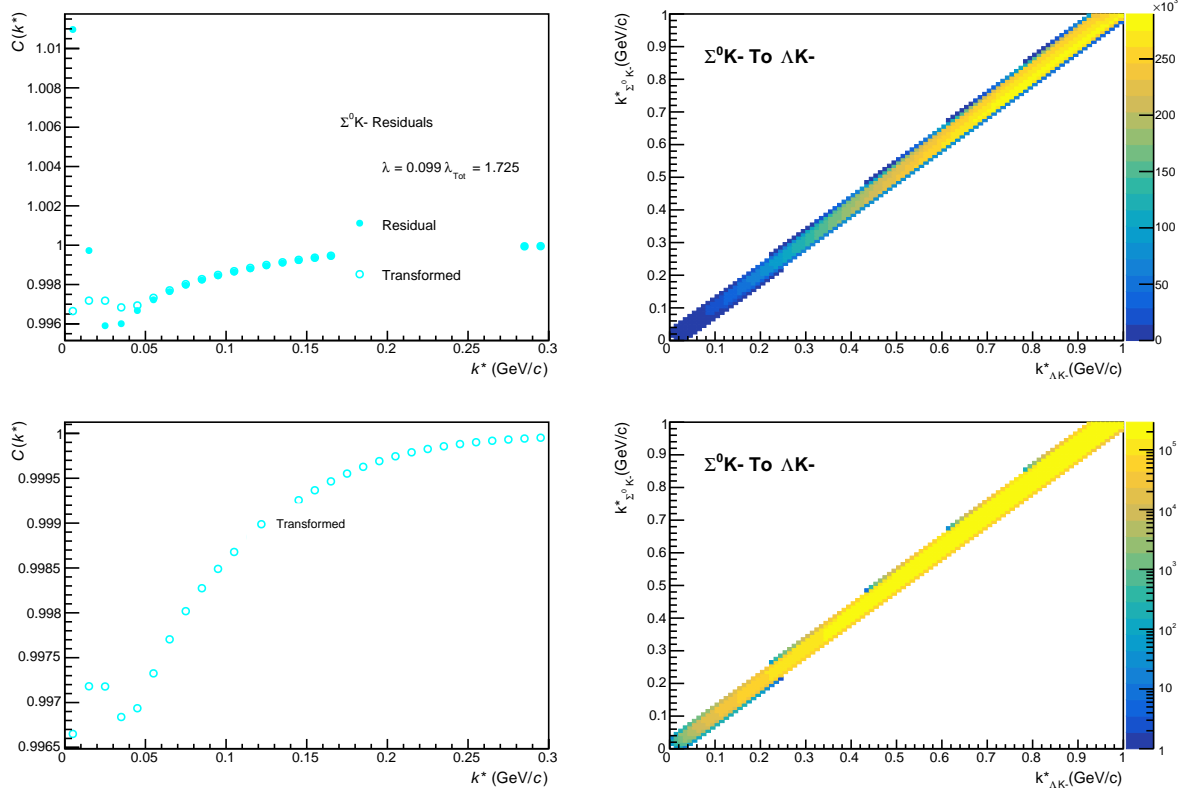
**Fig. 73:** Residuals:  $\Sigma^0 K^{*0}$  to  $\Lambda K^+$  (0-10% Centrality)



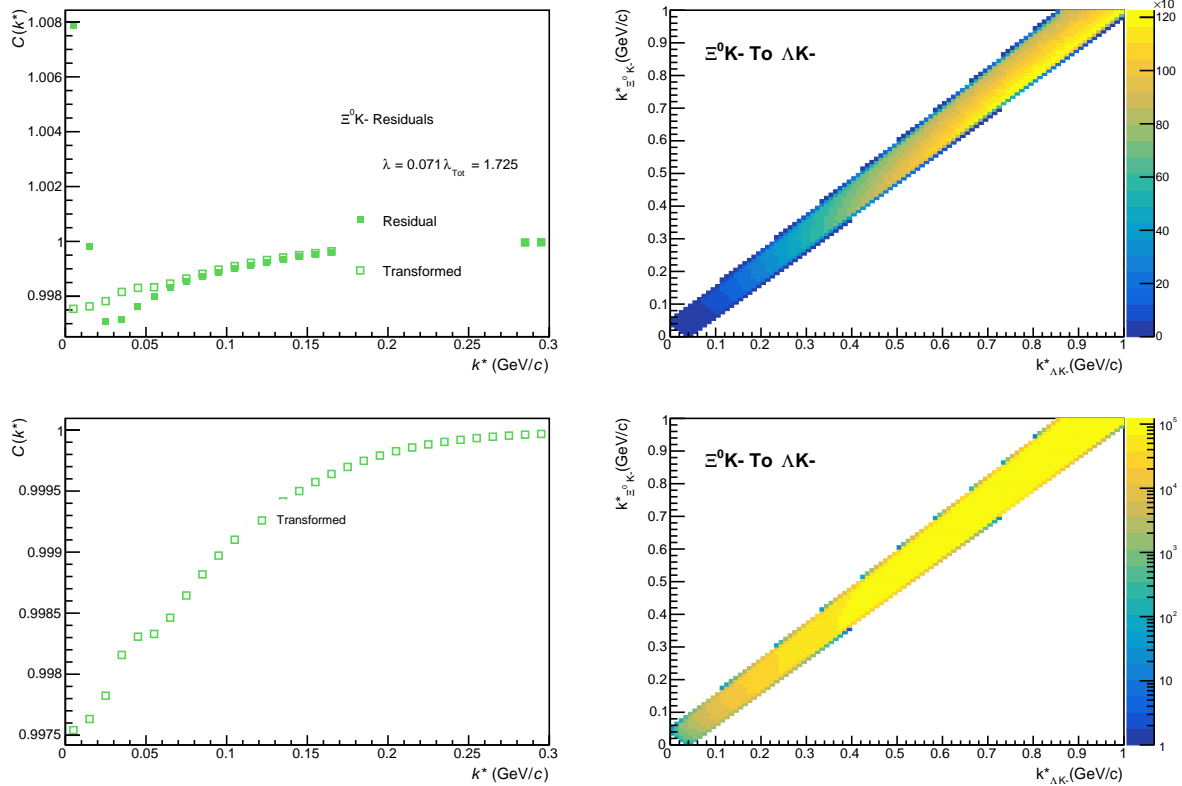
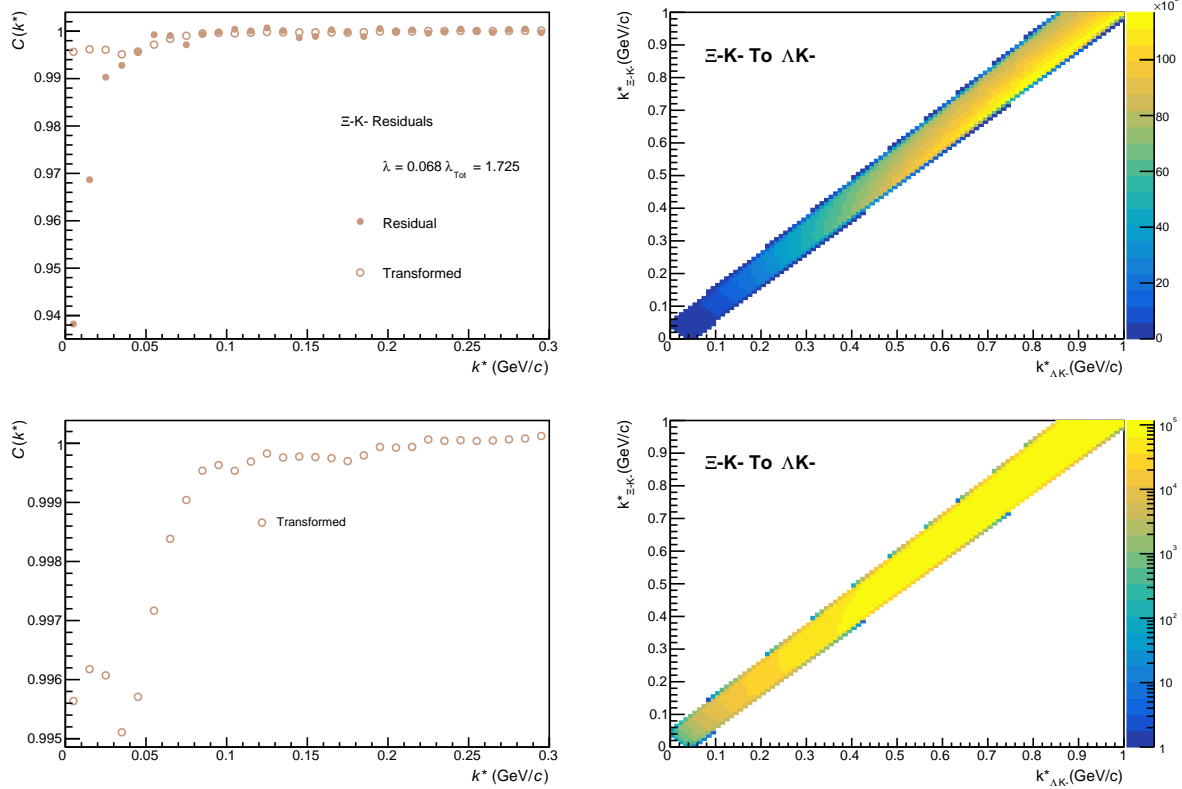
**Fig. 74:** Residuals:  $\Xi^0 K^{*0}$  to  $\Lambda K^+$  (0-10% Centrality)

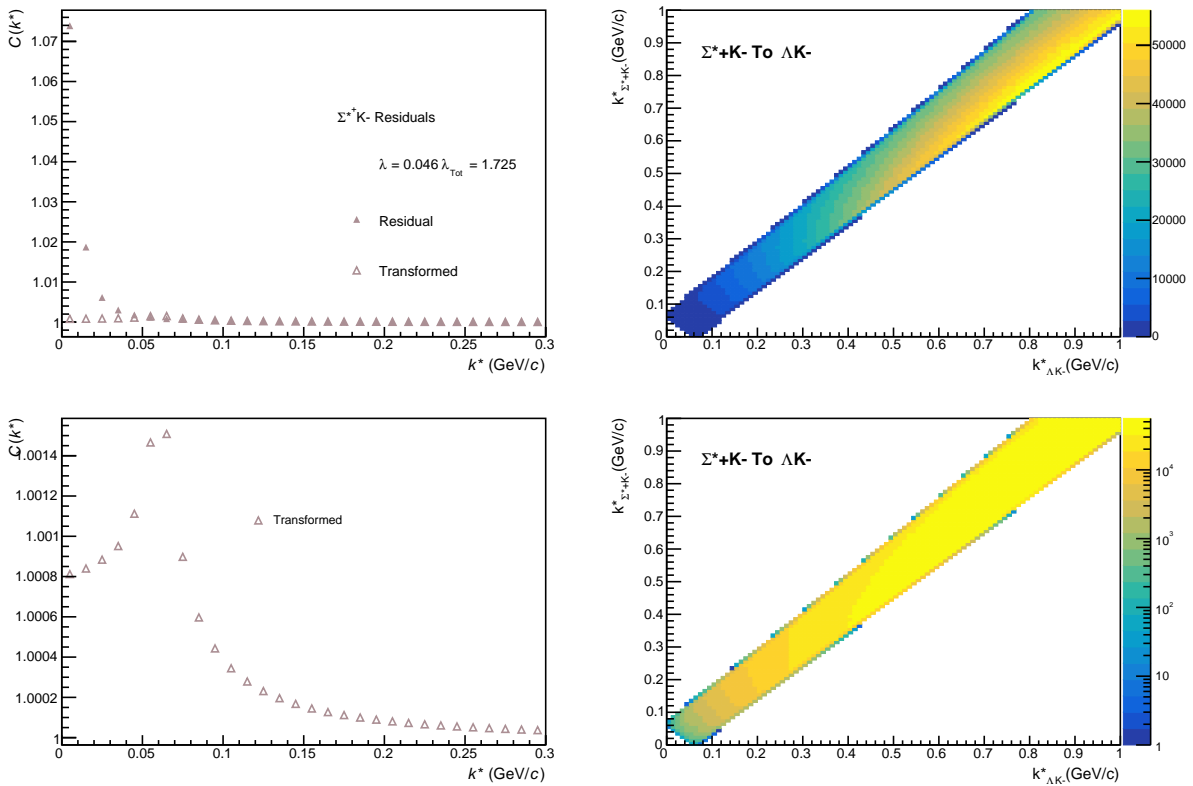


**Fig. 75:** Residuals:  $\Xi^-K^{*0}$  to  $\Lambda K^+$  (0-10% Centrality)

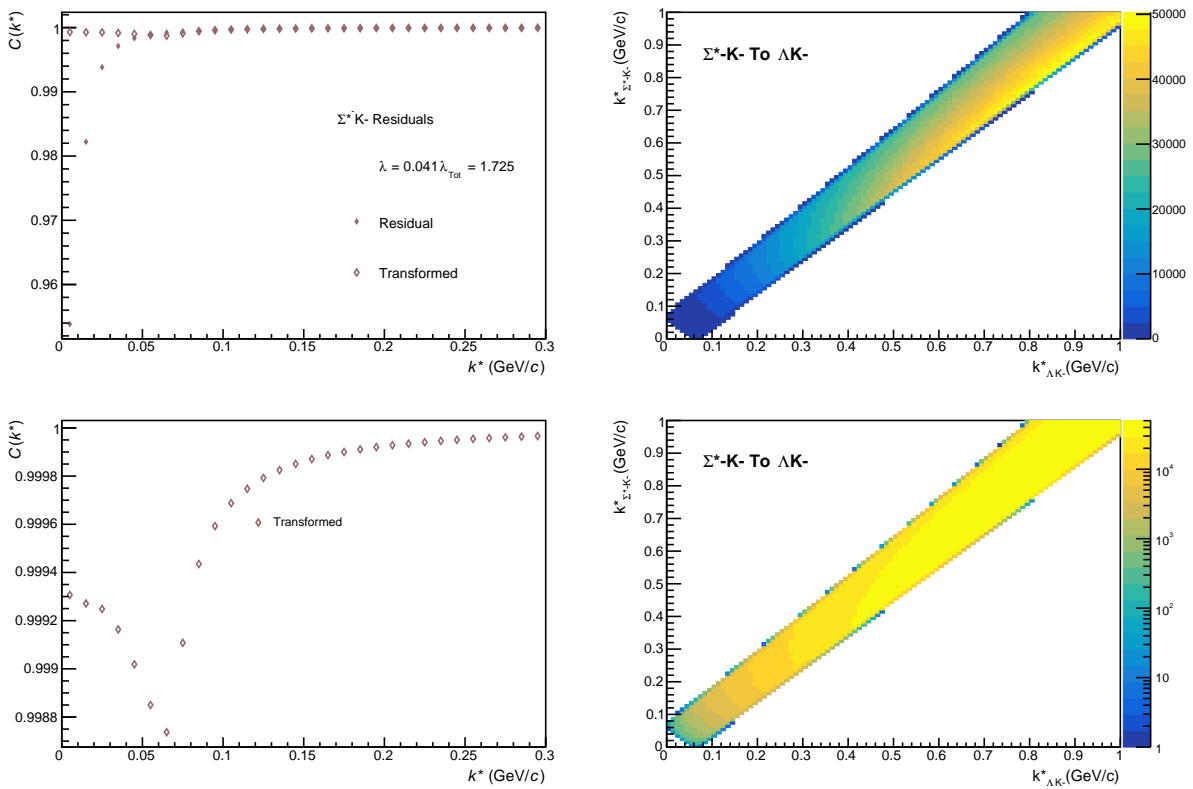
833 9.1.2  $\Lambda K^-$  Residuals


**Fig. 76:** Residuals:  $\Sigma^0 K^-$  to  $\Lambda K^-$  (0-10% Centrality)

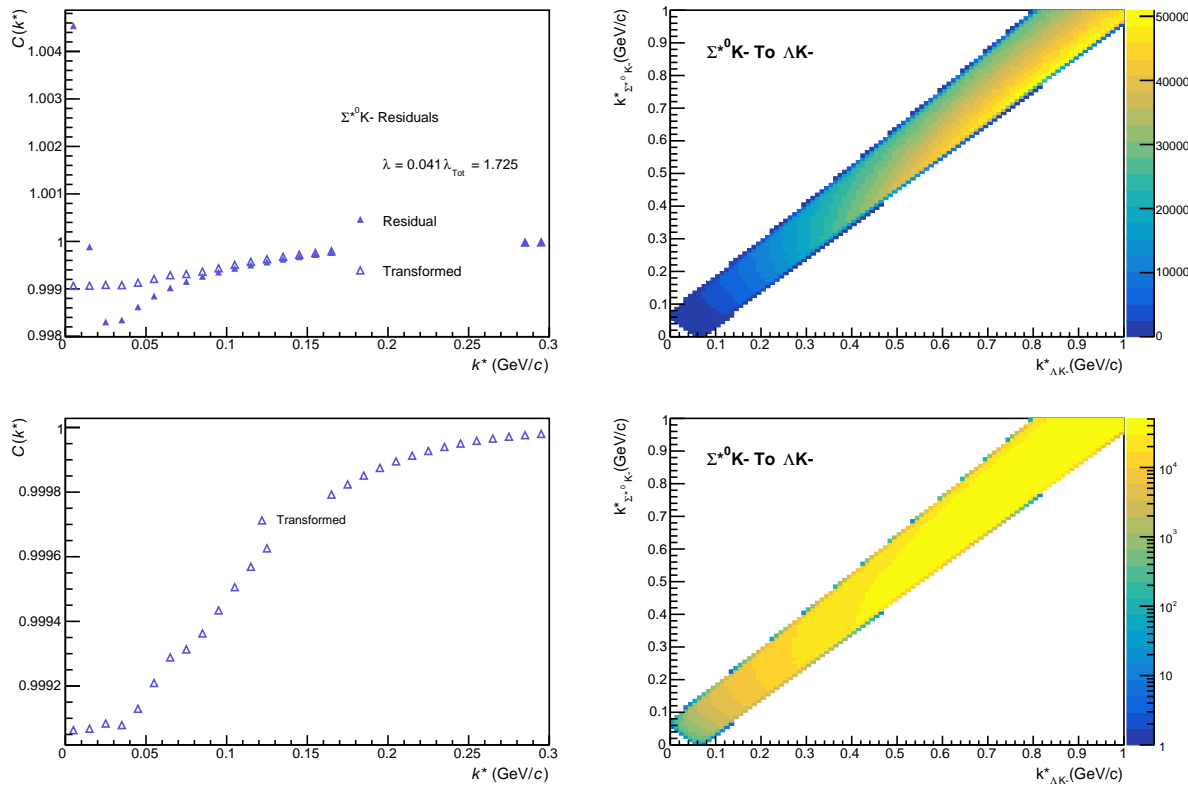
Fig. 77: Residuals:  $\Xi^0 \text{K}^-$  to  $\Lambda \text{K}^-$  (0-10% Centrality)Fig. 78: Residuals:  $\Xi^- \text{K}^-$  to  $\Lambda \text{K}^-$  (0-10% Centrality)



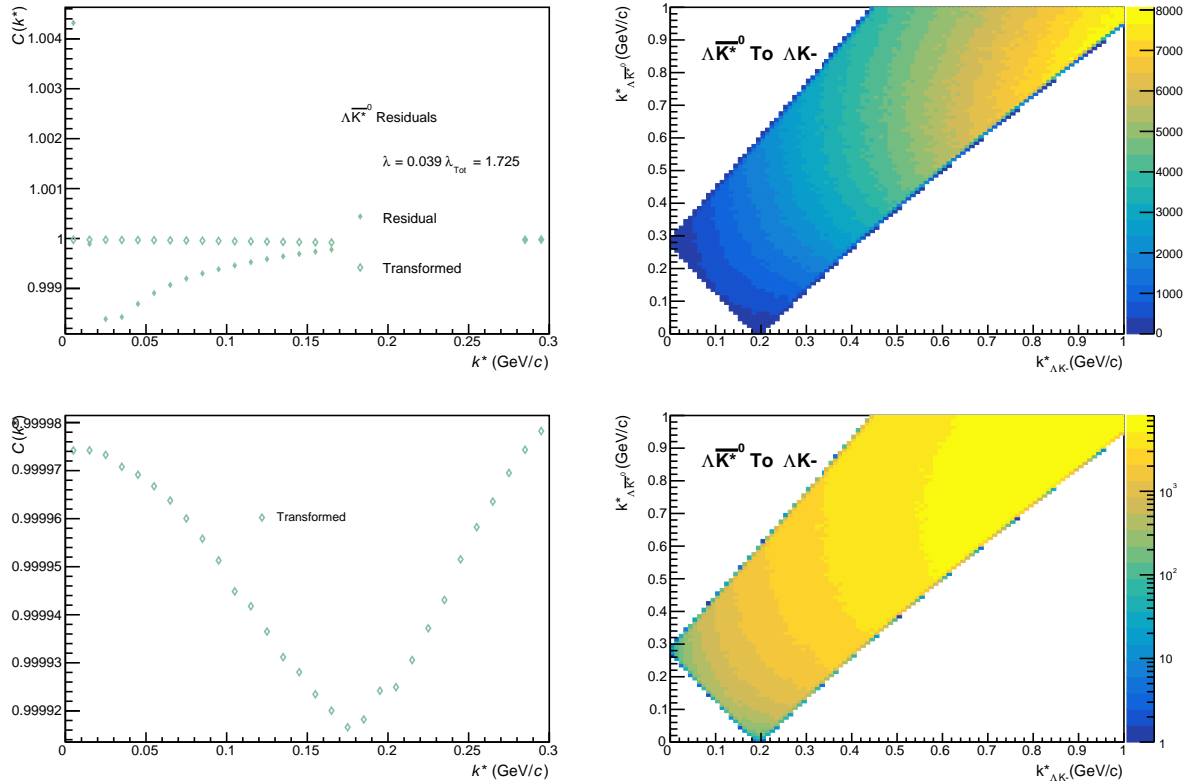
**Fig. 79:** Residuals:  $\Sigma^{*+} K^-$  to  $\Lambda K^-$  (0-10% Centrality)



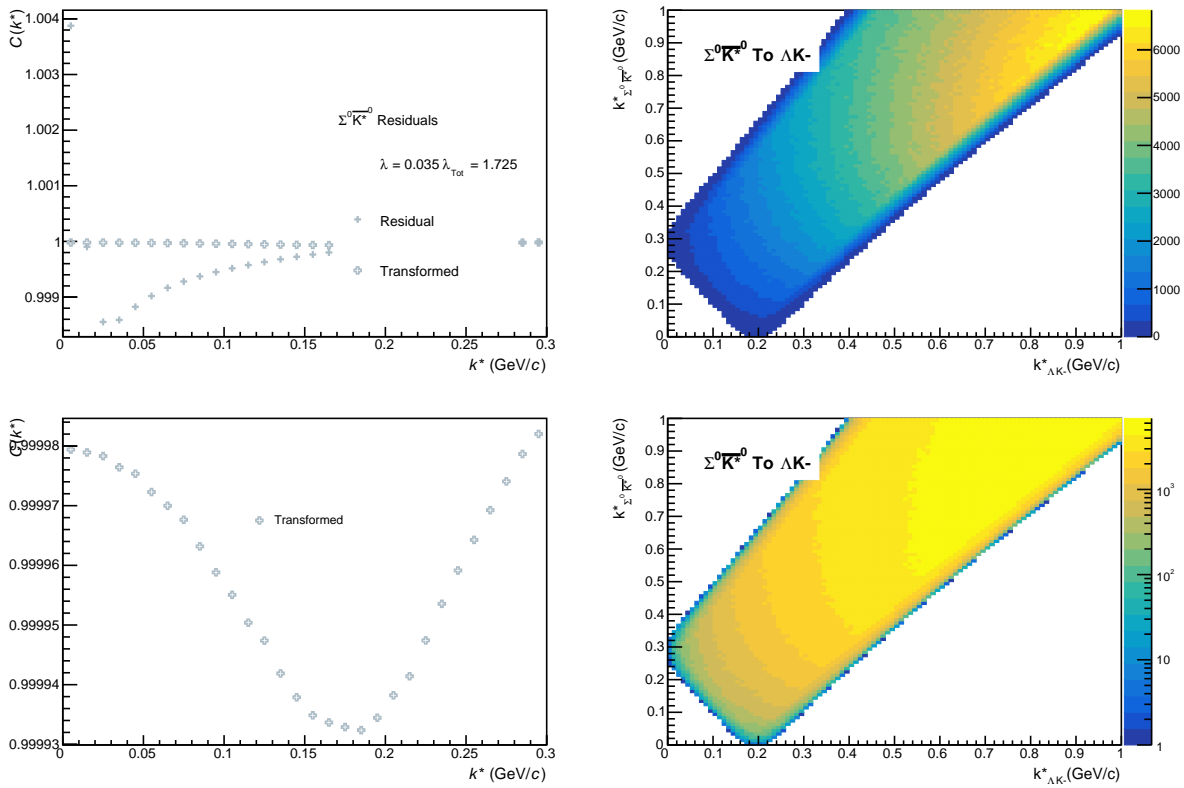
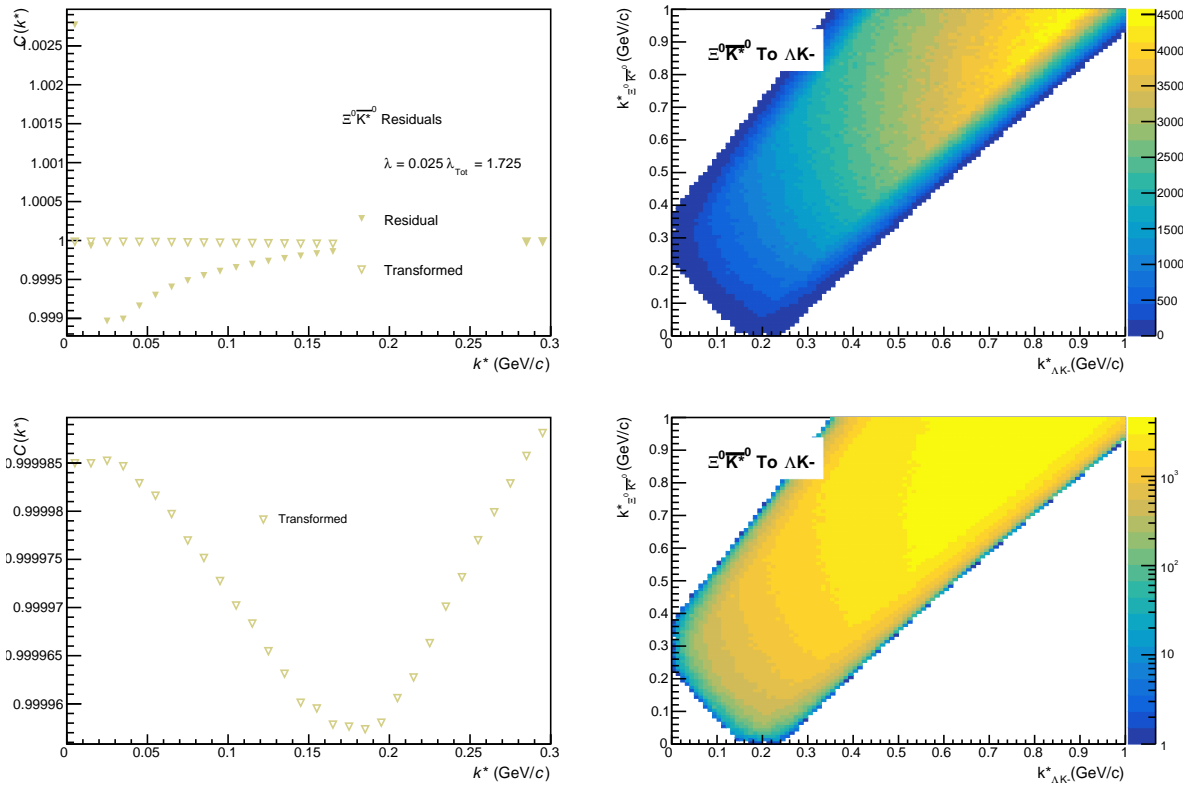
**Fig. 80:** Residuals:  $\Sigma^{*-} K^-$  to  $\Lambda K^-$  (0-10% Centrality)

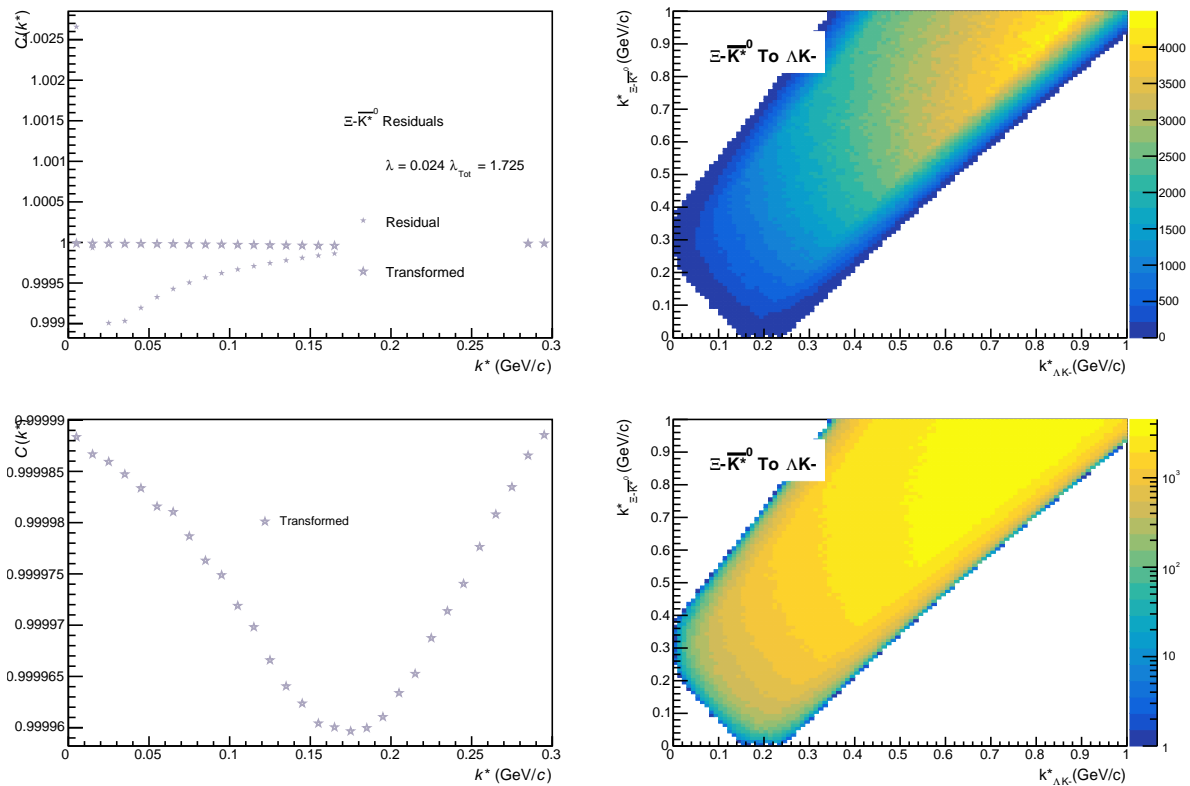


**Fig. 81:** Residuals:  $\Sigma^0 \text{K}^-$  to  $\Lambda \text{K}^-$  (0-10% Centrality)

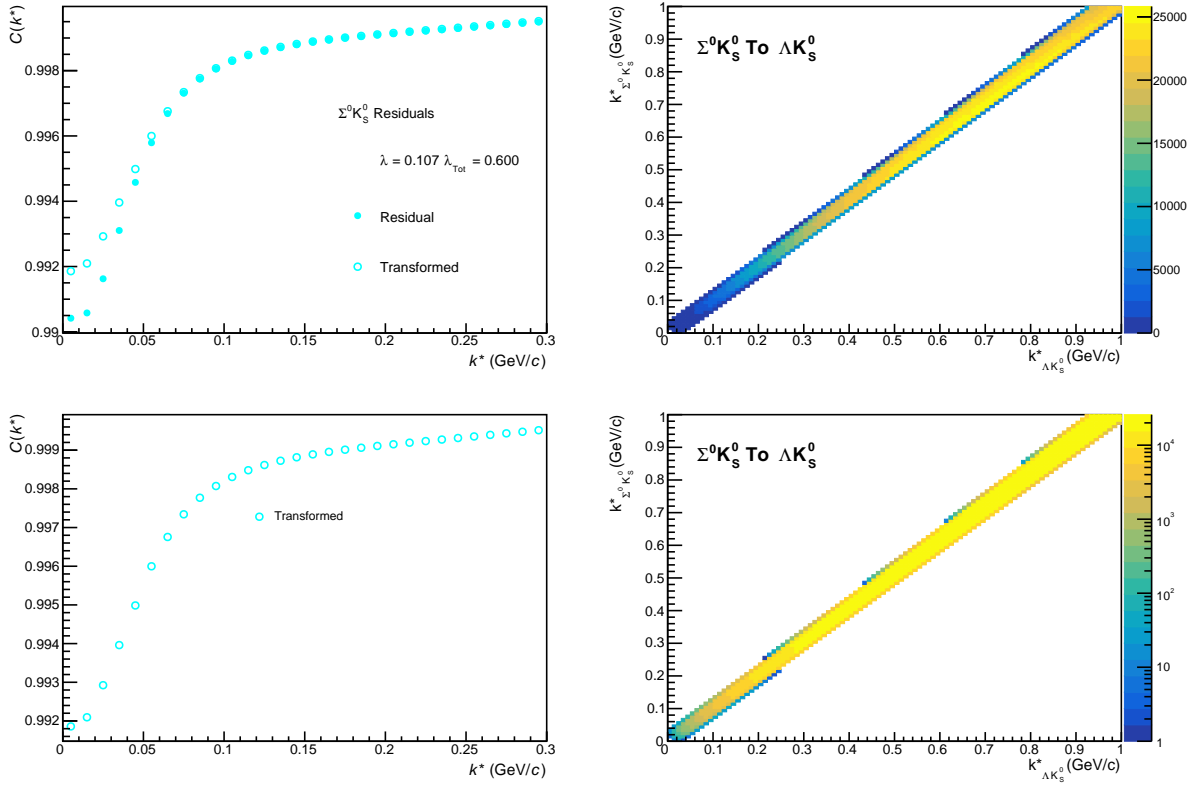


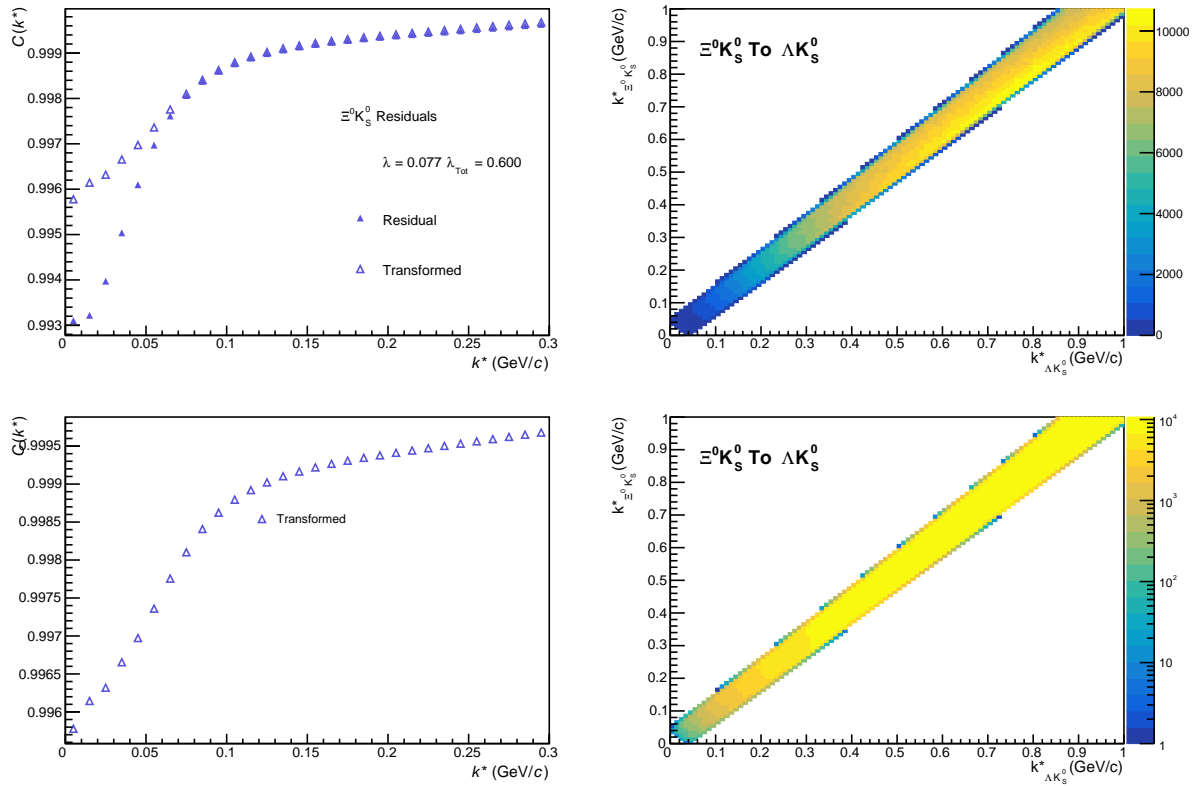
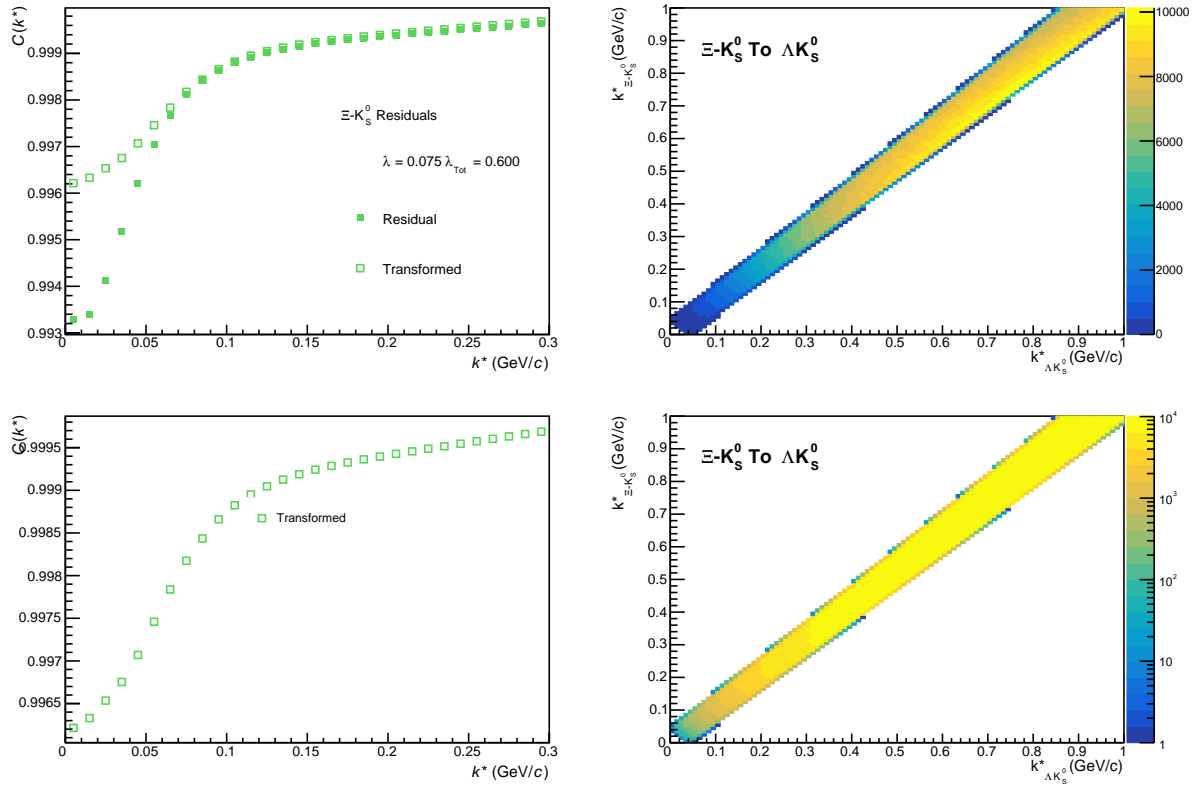
**Fig. 82:** Residuals:  $\Lambda \bar{K}^0$  to  $\Lambda \text{K}^-$  (0-10% Centrality)

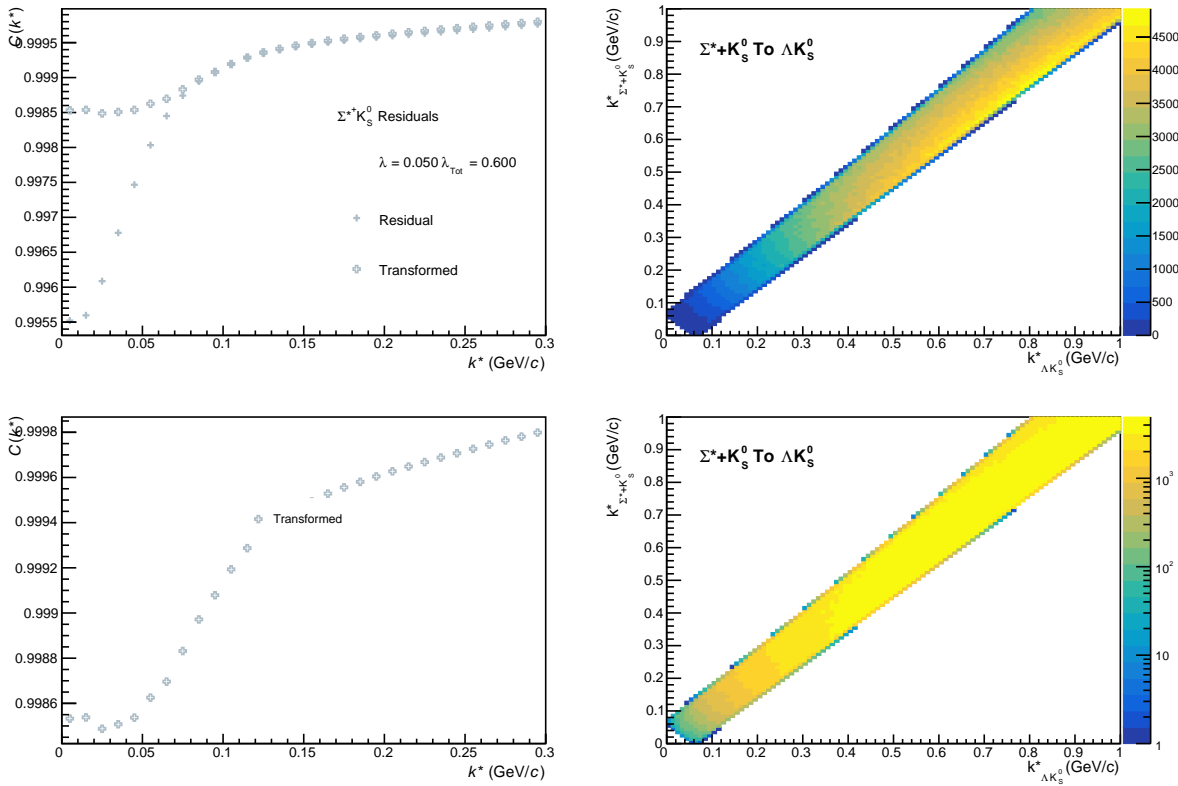
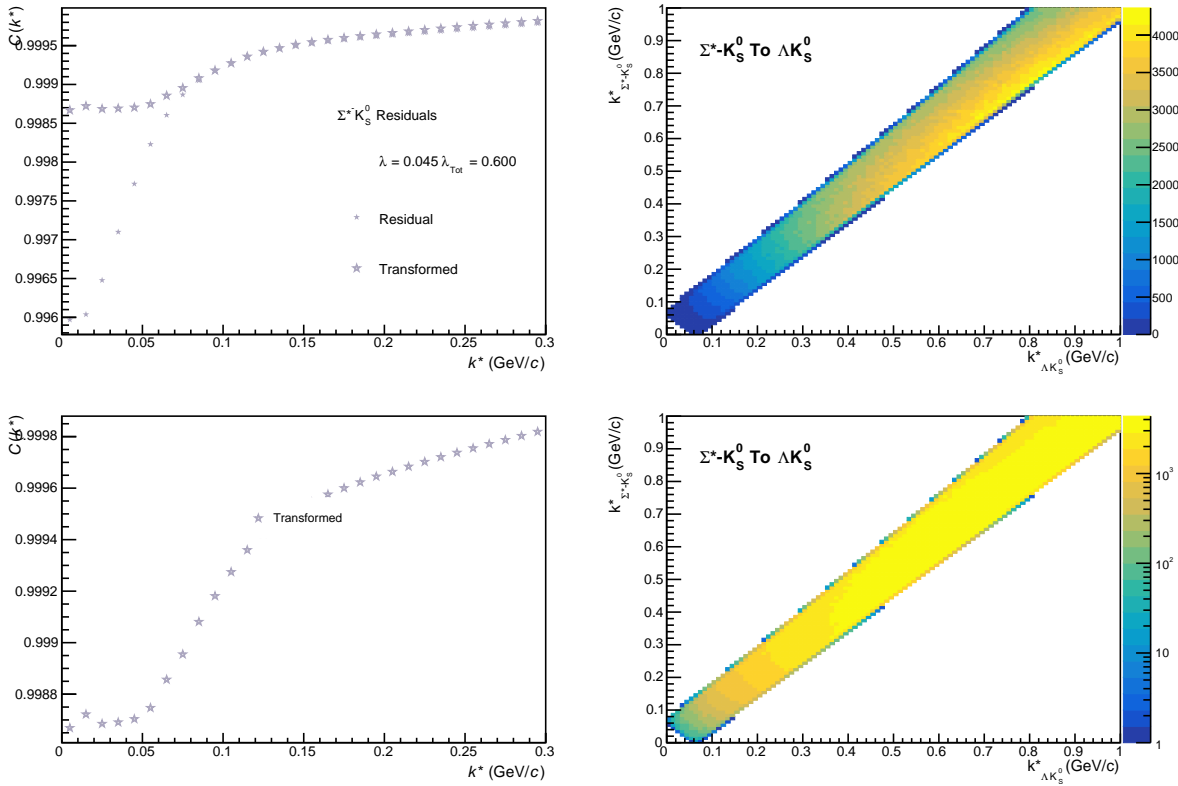

**Fig. 83:** Residuals:  $\Sigma^0 \bar{K}^{*0}$  to  $\Lambda K^-$  (0-10% Centrality)

**Fig. 84:** Residuals:  $\Xi^0 \bar{K}^{*0}$  to  $\Lambda K^-$  (0-10% Centrality)

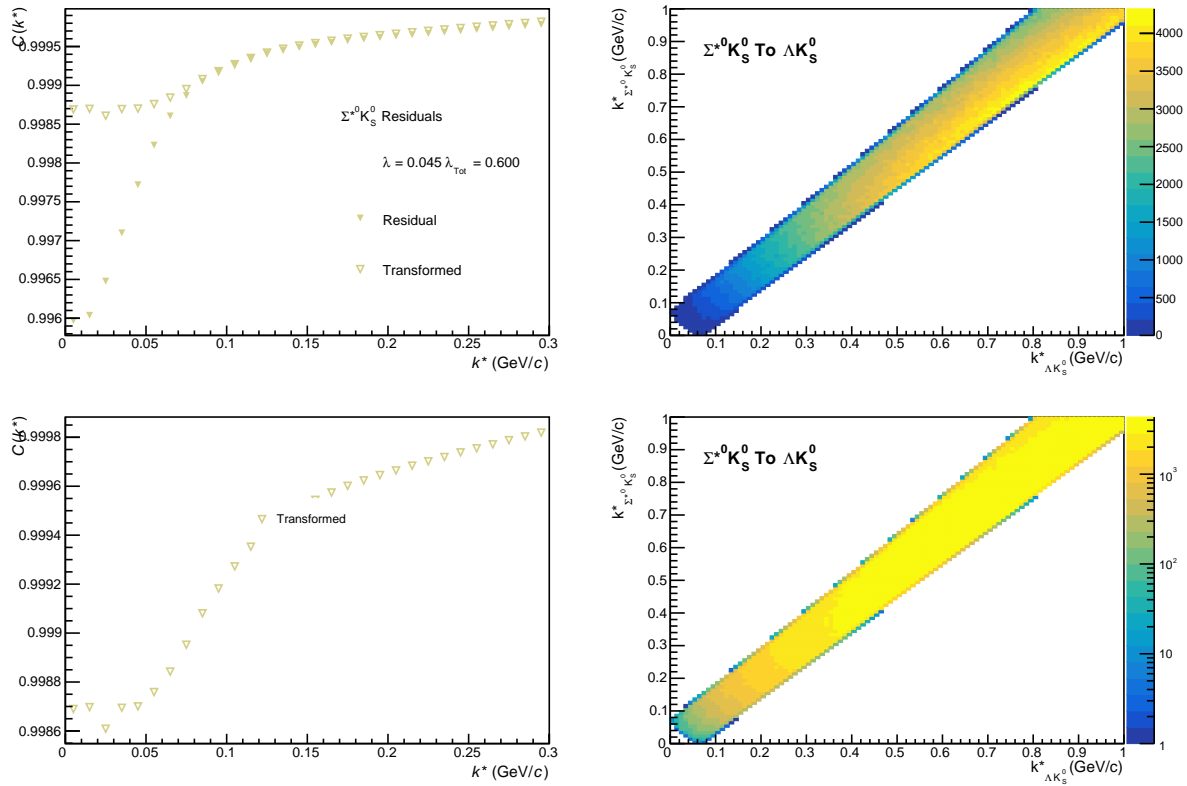


**Fig. 85:** Residuals:  $\Xi^-\bar{K}^{*0}$  to  $\Lambda K^-$  (0-10% Centrality)

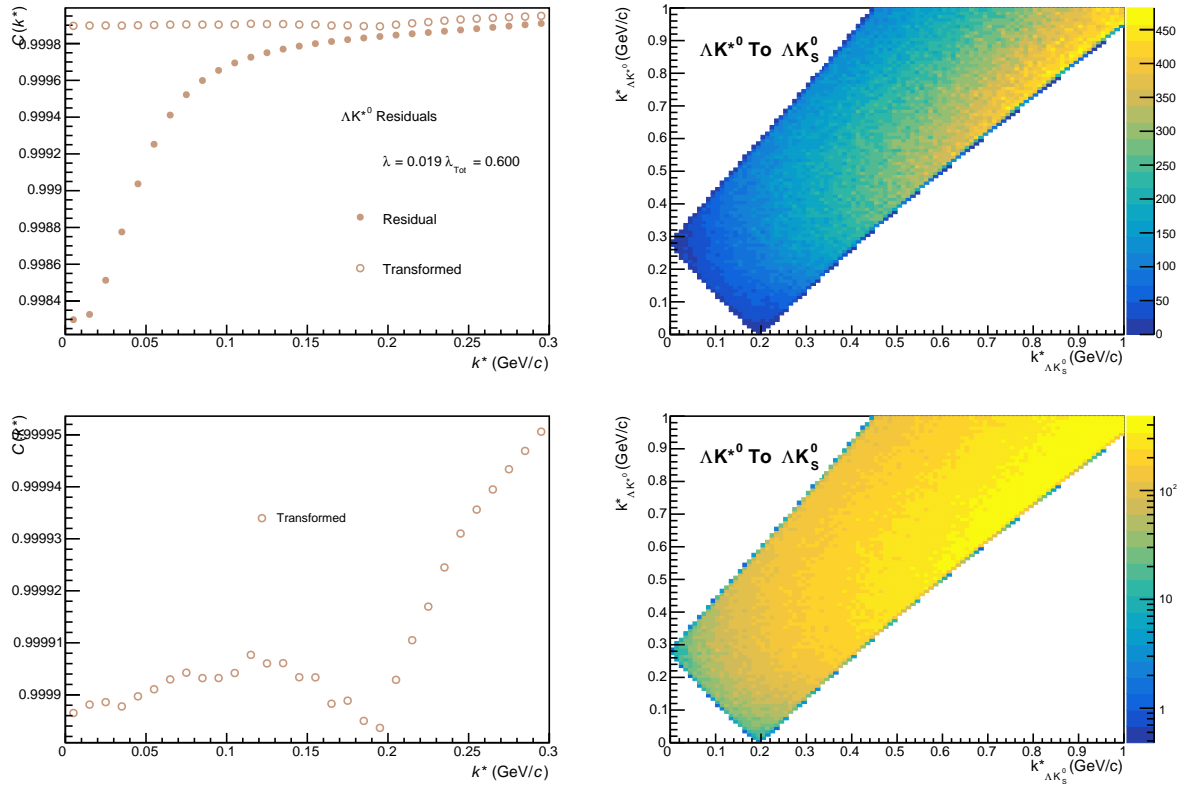
834 **9.1.3  $\Lambda K_S^0$  Residuals****Fig. 86:** Residuals:  $\Sigma^0 K_S^0$  to  $\Lambda K_S^0$  (0-10% Centrality)

Fig. 87: Residuals:  $\Xi^0 K_s^0$  to  $\Lambda K_s^0$  (0-10% Centrality)Fig. 88: Residuals:  $\Xi^- K_s^0$  to  $\Lambda K_s^0$  (0-10% Centrality)

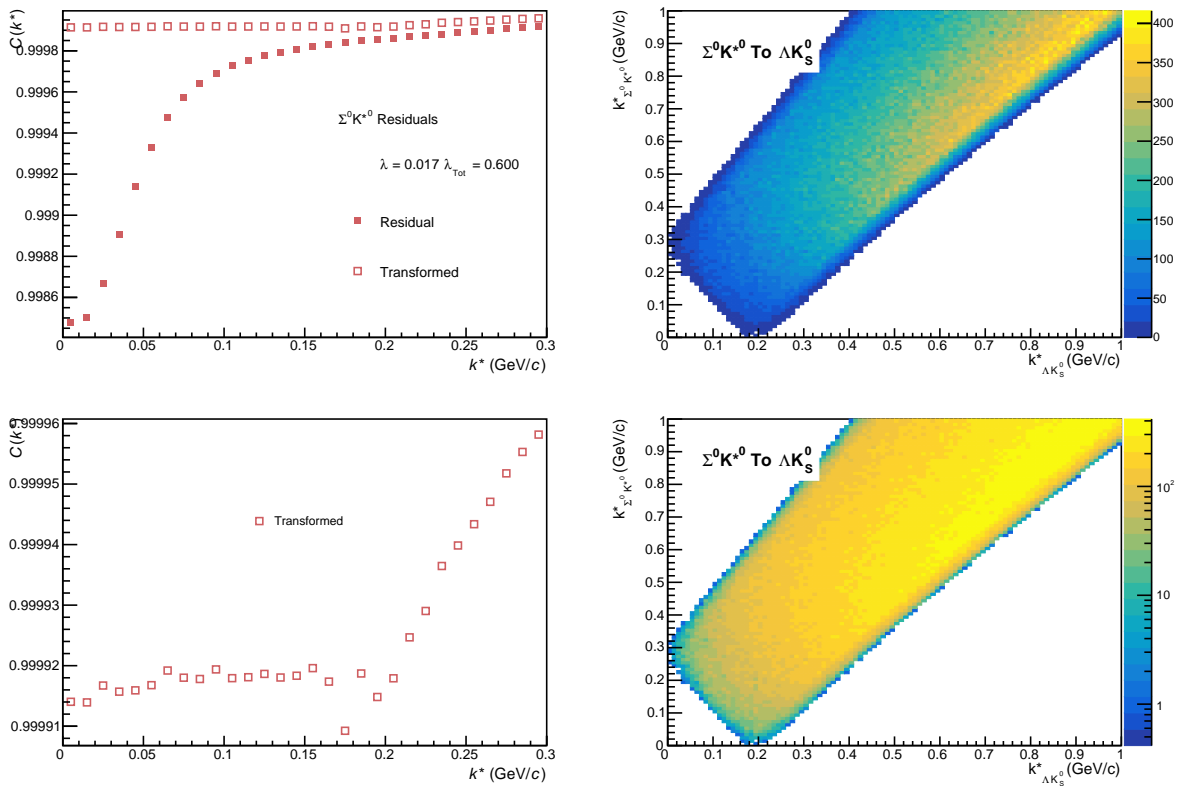
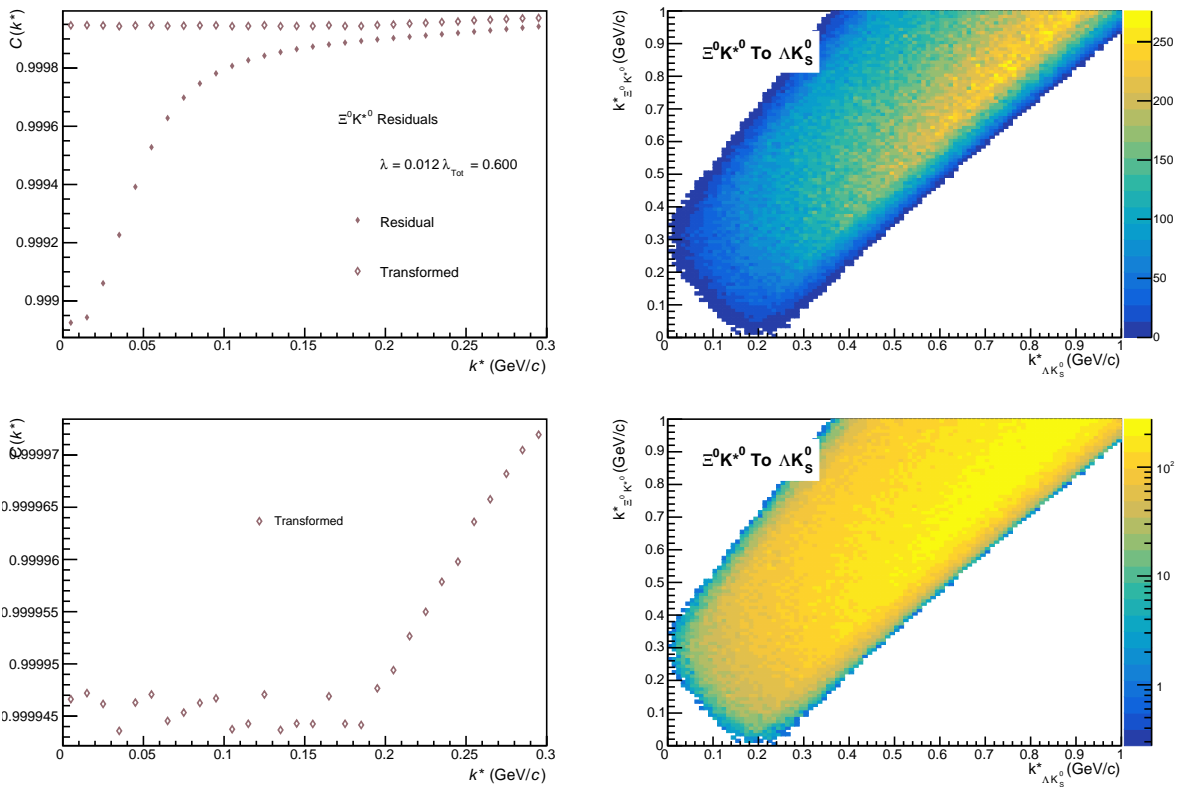

**Fig. 89:** Residuals:  $\Sigma^* + K_S^0 \rightarrow \Lambda K_S^0$  (0-10% Centrality)

**Fig. 90:** Residuals:  $\Sigma^* - K_S^0 \rightarrow \Lambda K_S^0$  (0-10% Centrality)

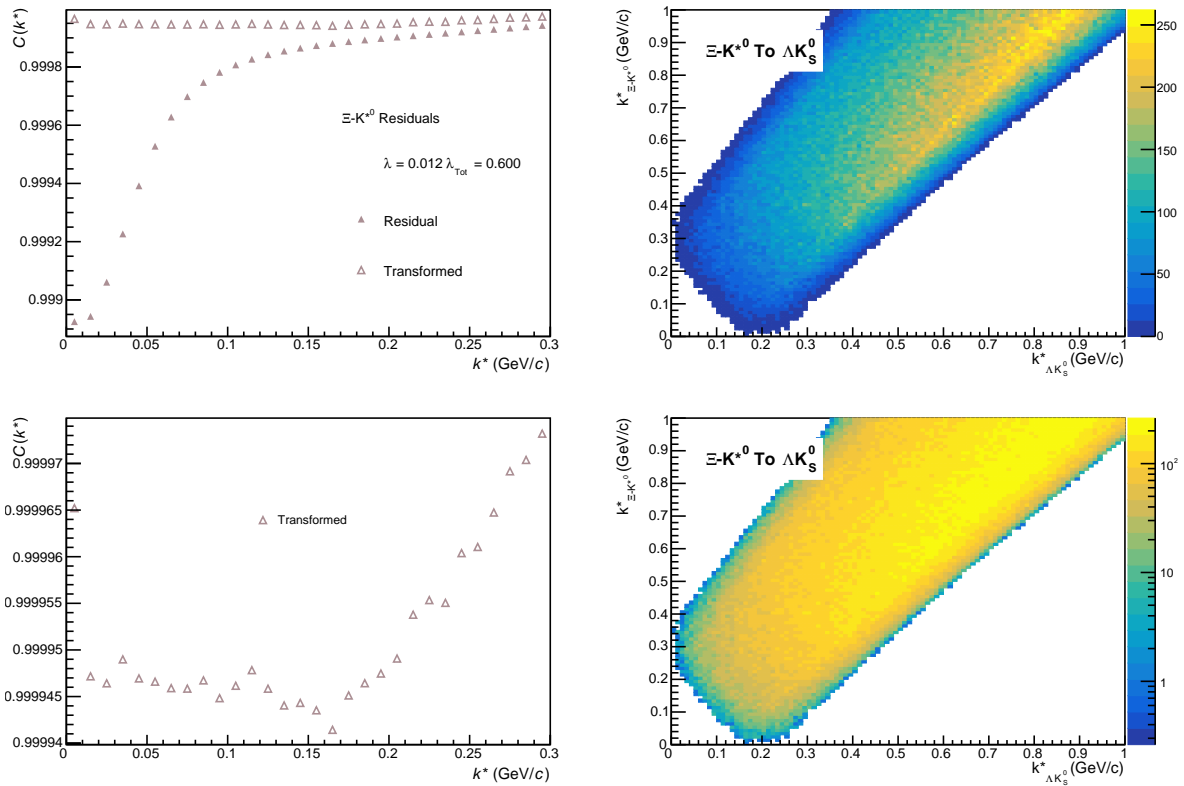


**Fig. 91:** Residuals:  $\Sigma^{*0} K_S^0$  to  $\Lambda K_S^0$  (0-10% Centrality)



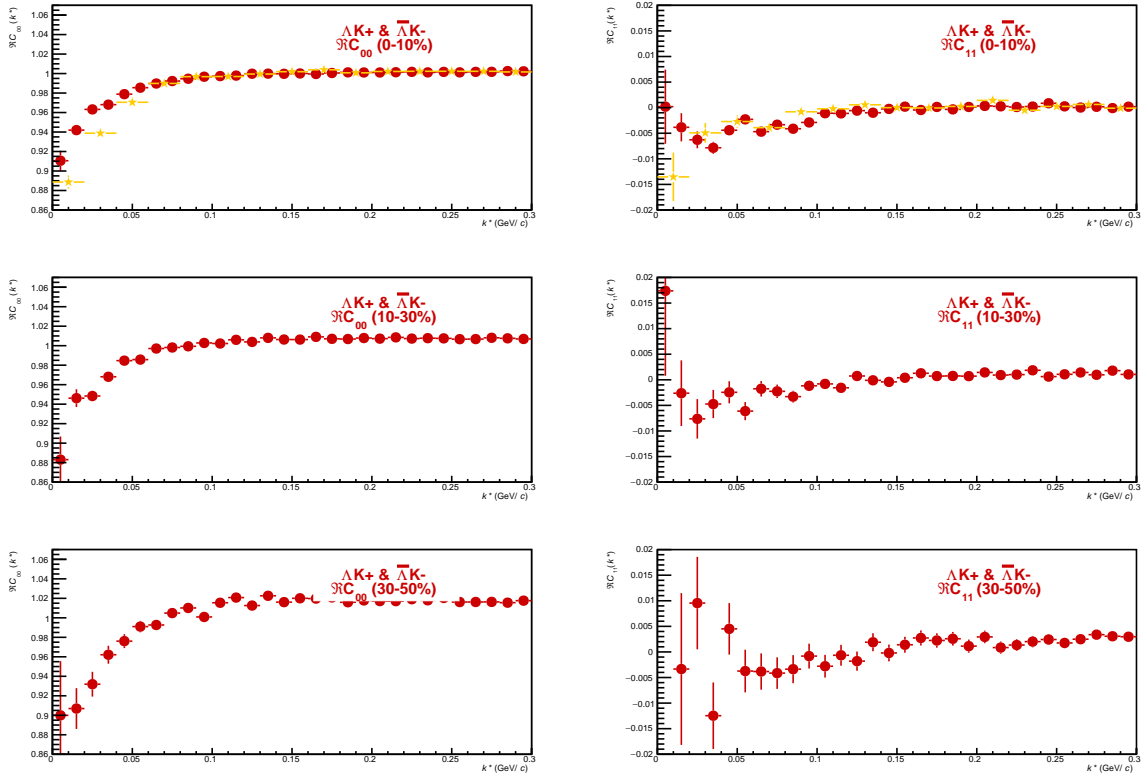
**Fig. 92:** Residuals:  $\Delta K^{*0}$  to  $\Lambda K_S^0$  (0-10% Centrality)


**Fig. 93:** Residuals:  $\Sigma^0 K^{*0}$  to  $\Lambda K_S^0$  (0-10% Centrality)

**Fig. 94:** Residuals:  $\Xi^0 K^{*0}$  to  $\Lambda K_S^0$  (0-10% Centrality)



**Fig. 95:** Residuals:  $\Xi^- K^{*0}$  to  $\Lambda K_s^0$  (0-10% Centrality)

## 835 9.2 Spherical Harmonics



**Fig. 96:**  $C_{00}$  (left) and  $\Im C_{11}$  (right) components of a spherical harmonic decomposition of the  $\Lambda K^+$  correlation function for the 0-10% (top), 10-30% (middle), and 30-50% (bottom) centrality bins

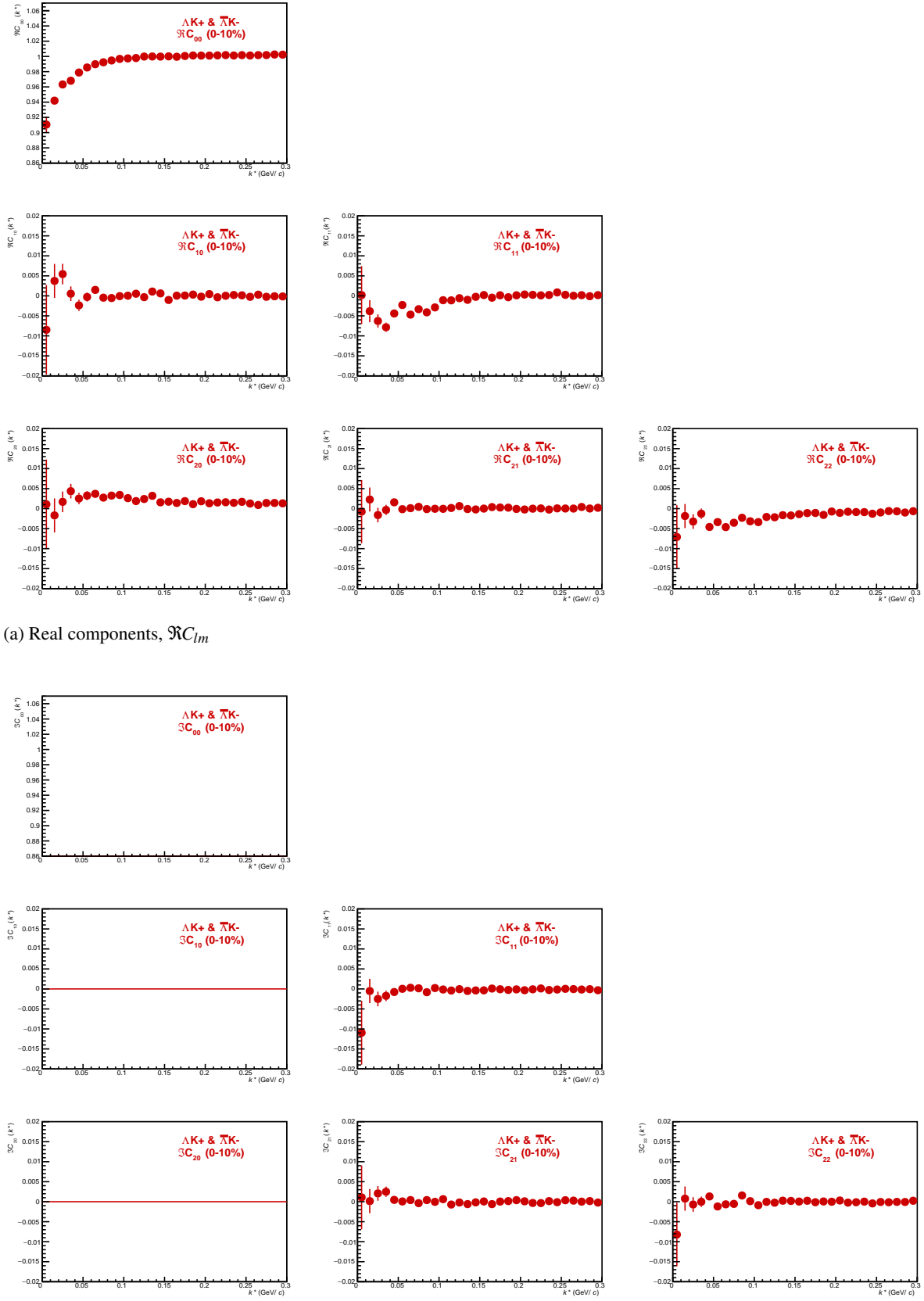


**Fig. 97:** First six components ( $C_{00}, C_{10}, C_{11}, C_{20}, C_{21}, C_{22}$ ) of the spherical harmonic decomposition of the  $\Lambda K^+$  correlation function for the 0-10% centrality bin. Note,  $\Im C_{00}$ ,  $\Im C_{10}$ , and  $\Im C_{20}$  are zero by definition.

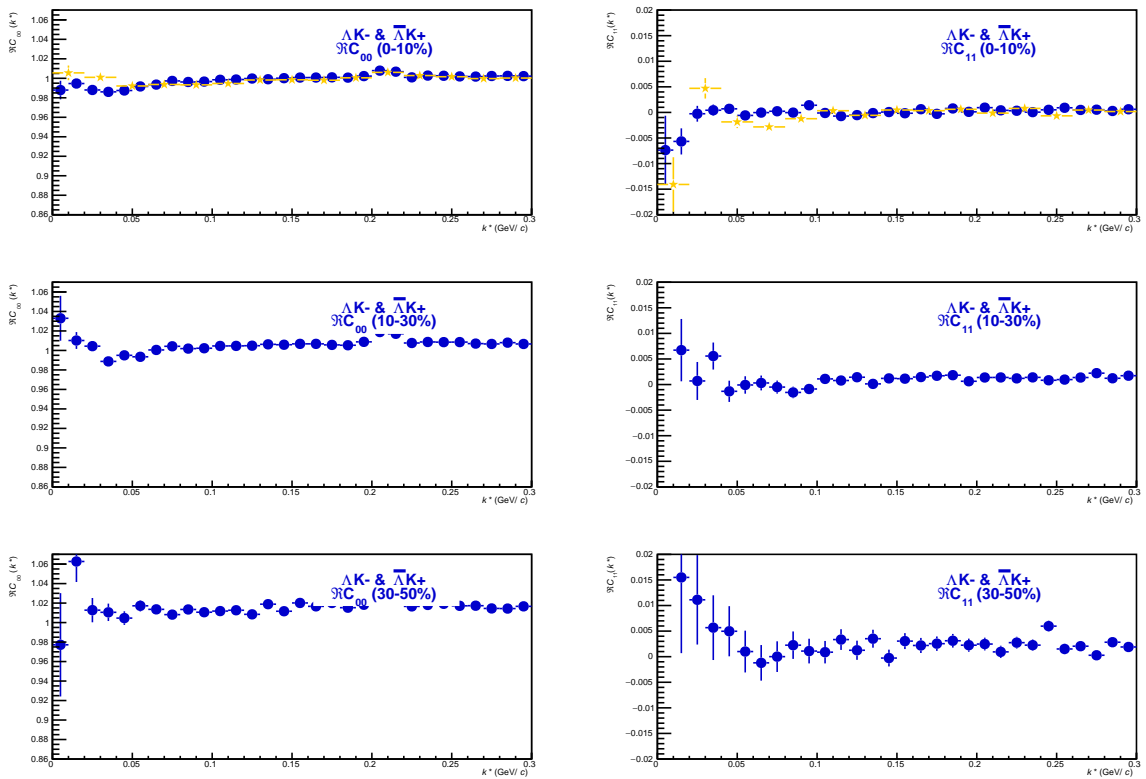


**Fig. 98:**  $C_{00}$  (left) and  $\Im C_{11}$  (right) components of a spherical harmonic decomposition of the  $\Lambda K^-$  correlation function for the 0-10% (top), 10-30% (middle), and 30-50% (bottom) centrality bins

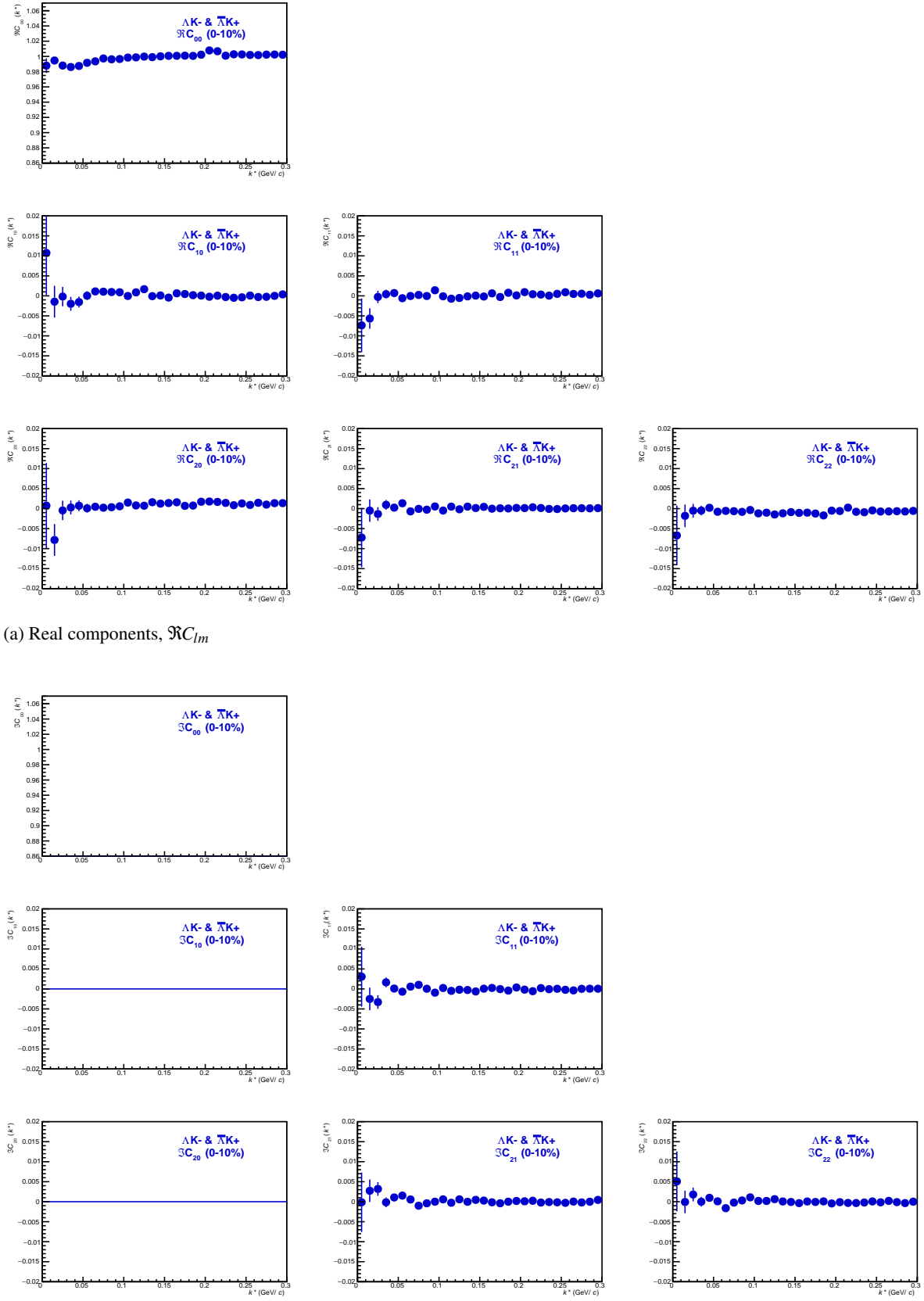


**Fig. 99:** First six components ( $C_{00}, C_{10}, C_{11}, C_{20}, C_{21}, C_{22}$ ) of the spherical harmonic decomposition of the  $\Lambda K^-$  correlation function for the 0-10% centrality bin. Note,  $\Im C_{00}$ ,  $\Im C_{10}$ , and  $\Im C_{20}$  are zero by definition.

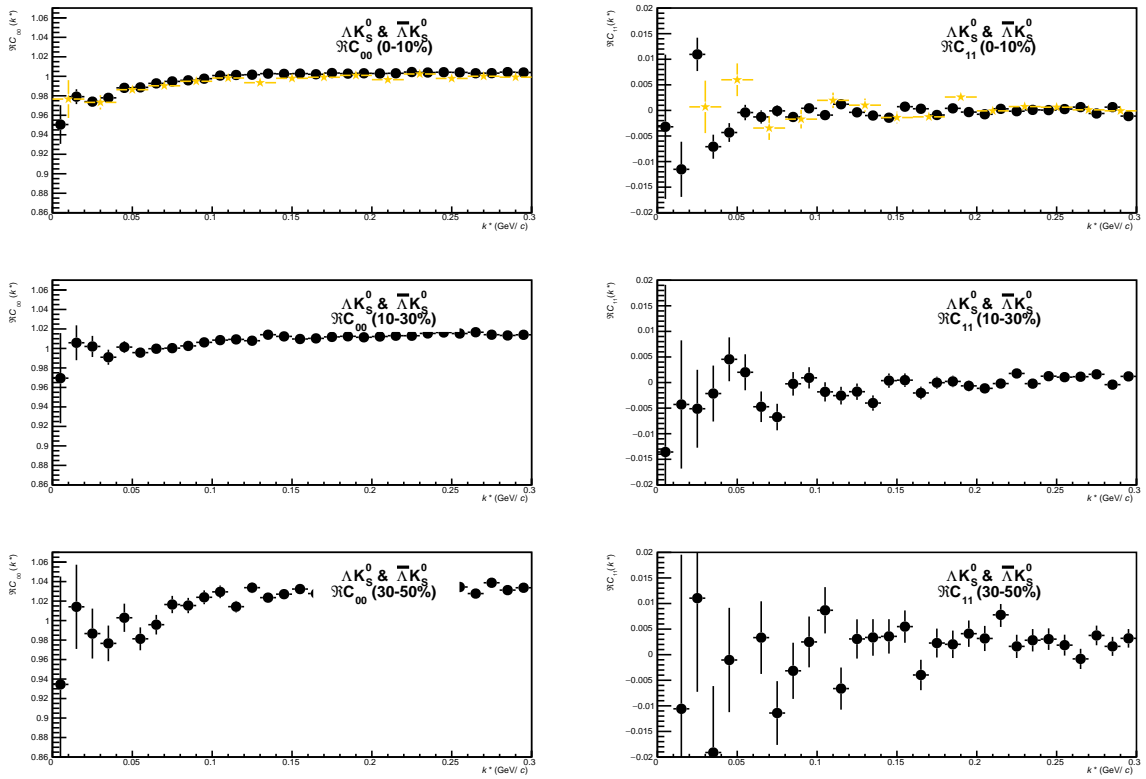


**Fig. 100:**  $C_{00}$  (left) and  $\Im C_{11}$  (right) components of a spherical harmonic decomposition of the  $\Lambda K_s^0$  correlation function for the 0-10% (top), 10-30% (middle), and 30-50% (bottom) centrality bins

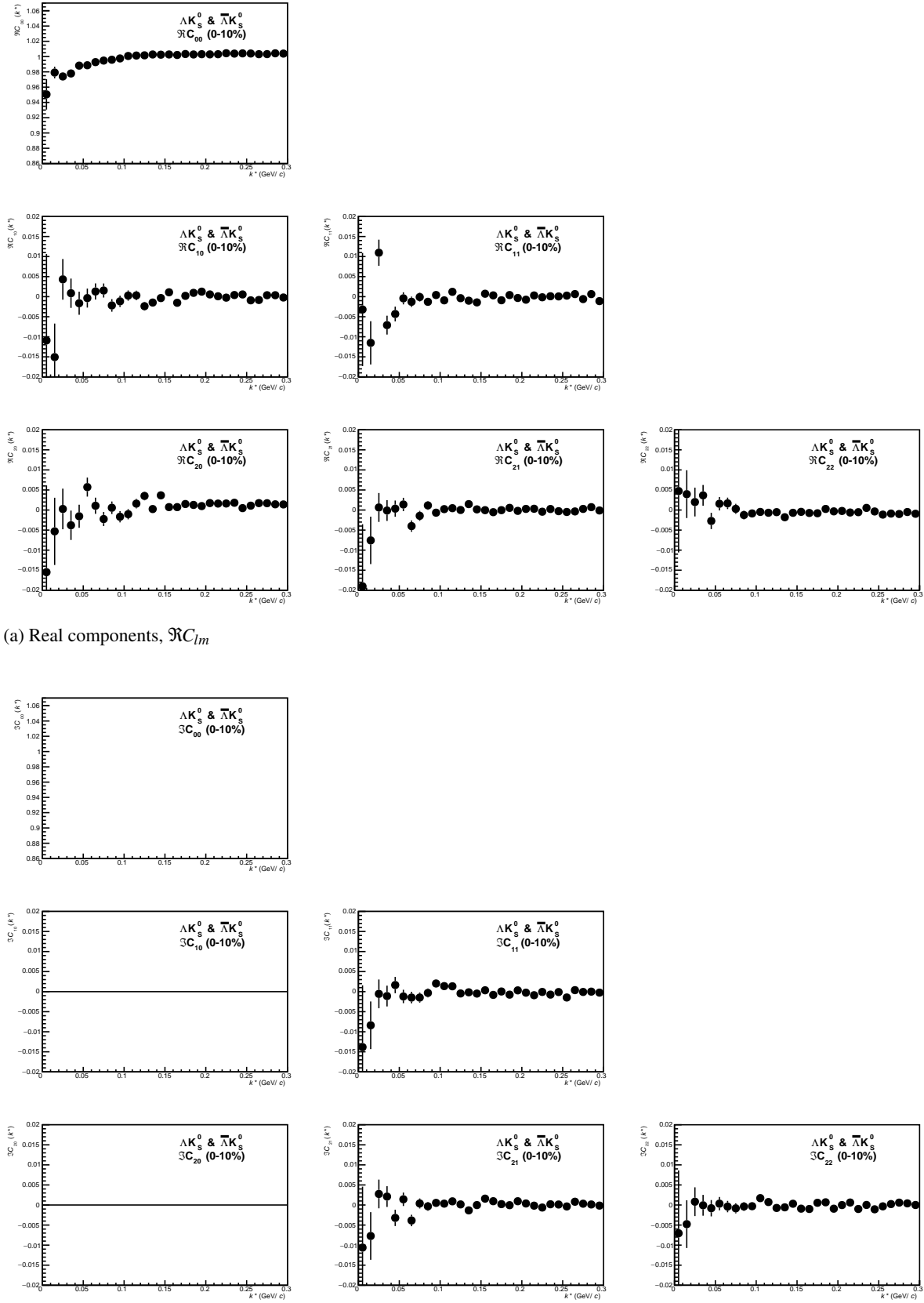


**Fig. 101:** First six components ( $C_{00}, C_{10}, C_{11}, C_{20}, C_{21}, C_{22}$ ) of the spherical harmonic decomposition of the  $\Lambda K_s^0$  correlation function for the 0-10% centrality bin. Note,  $\Im C_{00}$ ,  $\Im C_{10}$ , and  $\Im C_{20}$  are zero by definition.

## References

- [1] R. Lednicky and V. L. Lyuboshitz. *Sov. J. Nucl. Phys.*, 35:770, 1982.
- [2] Michael Annan Lisa, Scott Pratt, Ron Soltz, and Urs Wiedemann. Femtoscopy in relativistic heavy ion collisions. *Ann. Rev. Nucl. Part. Sci.*, 55:357–402, 2005.
- [3] S. E. Koonin. Proton Pictures of High-Energy Nuclear Collisions. *Phys. Lett.*, B70:43–47, 1977.
- [4] S. Pratt, T. Csorgo, and J. Zimanyi. Detailed predictions for two pion correlations in ultrarelativistic heavy ion collisions. *Phys. Rev.*, C42:2646–2652, 1990.
- [5] Richard Lednicky. Finite-size effects on two-particle production in continuous and discrete spectrum. *Phys. Part. Nucl.*, 40:307–352, 2009.
- [6] Adam Kisiel, Hanna Zbroszczyk, and Maciej Szymaski. Extracting baryon-antibaryon strong interaction potentials from  $p\bar{\Lambda}$  femtoscopic correlation functions. *Phys. Rev.*, C89(5):054916, 2014.
- [7] Jai Salzwedel and Thomas Humanic. Lambda femtoscopy in  $\sqrt{s_{NN}} = 2.76$  TeV Pb-Pb collisions at ALICE, Jan 2017. Presented 15 Dec 2016.
- [8] A Kisiel. Non-identical particle correlation analysis in the presence of non-femtoscopic correlations. *Acta Physica Polonica B*, 48:717, 04 2017.
- [9] Jaroslav Adam et al. One-dimensional pion, kaon, and proton femtoscopy in Pb-Pb collisions at  $\sqrt{s_{NN}} = 2.76$  TeV. *Phys. Rev.*, C92(5):054908, 2015.
- [10] Yan-Rui Liu and Shi-Lin Zhu. Meson-baryon scattering lengths in HB chi PT. *Phys. Rev.*, D75:034003, 2007.
- [11] Maxim Mai, Peter C. Bruns, Bastian Kubis, and Ulf-G. Meissner. Aspects of meson-baryon scattering in three and two-flavor chiral perturbation theory. *Phys. Rev.*, D80:094006, 2009.